Università degli Studi di Torino

Facoltà di Scienze Matematiche, Fisiche e Naturali
Dipartimento di Fisica Sperimentale
Dottorato di Ricerca in Fisica ed Astrofisica - XX ciclo

Study and Development of the CMS High Level Trigger and Muon Reconstruction Algorithms and Their Effects on the $pp \rightarrow \mu^+\mu^- jjjj$ Vector Boson Fusion Process

Coordinatore
Prof. Stefano Sciuto

Tutore
Dott. Ernesto Migliore

Candidato
Dott. Riccardo Bellan

A.A. 2004/05
A.A. 2005/06
A.A. 2006/07

*A tutti coloro che mi
hanno insegnato qualcosa;
al primo giorno di scuola.*

Contents

Introduction

The particle interactions are described, in modern physics, by the Standard Model (SM). Although the SM perfectly reproduces the low-energy phenomenology and has been tested with very high accuracy, the electroweak symmetry breaking (EWSB) mechanism is not yet fully understood. This weak spot of the theory has led to the design of the Large Hadron Collider (LHC), a proton-proton collider installed at the European Laboratory for Particle Physics (CERN).

The LHC running conditions are very challenging and impose strict requirements to the detector performance. At the design luminosity, the interesting events are surrounded by more than 25 background events per bunch crossing, so the detector must be finely segmented. A *discovery* signal event is expected to be produced with a rate of 10^{-11} smaller than the background rate, which is of about 1 GHz. A fast response detector capable of providing precise measurement is required to select the signal candidates out of the uninteresting events. As in an hadron collider the largest fraction of the minimum bias events have hadrons in the final state, a detector capable to reconstruct leptons with high resolution, high efficiency and purity is of fundamental importance.

The work presented in this thesis has been done within the Compact Muon Solenoid (CMS) collaboration, one of the four experimental communities present at LHC. In particular my principal activity in the CMS collaboration has been oriented to the preparation of the CMS tools for the data analysis, mainly focusing on the muon reconstruction and the simulation of the Drift Tubes (DT) response to the passage of the particle radiation.

In Chapter 3 a description of the simulation of the DT cell response to the particle radiation [1], which I developed and of which I have been responsible for, is given. The simulated data and the 2004 Test Beam data have been compared and found in agreement among themselves.

In Chapter 4 the first step of the muon reconstruction is described. Particular emphasis is given to the reconstruction inside each individual DT chamber, as I developed and I was responsible of the DT local reconstruction [2].

In Chapter 5 the muon track reconstruction [3] and identification using the whole CMS detector is analysed and studied in detail. I developed in collaboration with an international group, of which I have been the coordinator, the muon reconstruction software. The starting date of my work on muon reconstruction coincided with the transition to the final configuration of the CMS framework infrastructure. This implied not only the development of new components but also a revision of the whole reconstruction strategies. The work resulted in an overall improvement of the muon reconstruction performance.

The tools developed in these two years were successfully tested on real data during the *CMS Magnet Test and Cosmic Challenge* [4], held during summer 2006.

The Chapter 6 describes the *Vector Boson Fusion* (VVF) process analysis [5, 6]. The VVF processes holds the key to investigate the electroweak symmetry breaking without any assumption on the breaking mechanism. Our model-independent analysis was the first attempt done on this subject and its main aim was the exploration of the high energy region of the vector boson scattering process. In particular I studied the $pp \to ZZ/W \to \mu^+\mu^- jjjj$ channel, determining resolution, efficiencies and significances. I also worked together with the Torino theoretical group on the comparison among different Monte Carlo generators [7, 8], required to validate the dedicated generator developed by the Torino group. I produced within the official production task of the CMS experiment the VVF signal events and the the main backgrounds. Both of them are the principal background to the most important analyses at CMS.

In Chapter 7 the muon reconstruction performance is tested on a $Z \to \mu\mu$ sample. This test is of fundamental importance as it is the direct link between the work done on the muon reconstruction and the VVF process analysis, as the latter has been carried out with an (old) fast simulation of the CMS detector which does not benefit of the improvements in the muon reconstruction. The study it is also the starting point for a future analysis of the Z boson resonance [9].

Chapter 1

The Large Hadron Collider Physics

The Large Hadron Collider (LHC) is presently under installation at CERN and the start-up operations will begin in 2008. The accelerator will provide two *proton* beams, with an energy of 7 TeV per proton, as well as *heavy ions* beams with an energy of $Z/A \cdot 7$ TeV per nucleon. The design luminosity for the p-p collision will be $10^{34}\text{cm}^{-2}\text{s}^{-1}$, but for the first three years LHC will run at lower luminosities. The design lifespan of LHC is of 10 years.

1.1 Motivation for the LHC

The Standard Model (SM) describes three fundamental interactions with two gauge theories: the theory of the electroweak interaction, that unifies the electromagnetic and the weak interactions, and the theory of strong interactions or Quantum Chromodynamics (QCD). The SM for weak and electromagnetic interactions is constructed on a gauge theory with four gauge fields corresponding to massless bosons. Since only the photon is massless, whereas Ws and Z are massive, something has to happen in order to preserve the electroweak unification.

The masses of the gauge fields, as well as the fermions, in the SM are generated by spontaneous symmetry breaking. Electroweak symmetry breaking (EWSB) in the SM is described by the Higgs mechanism. Although a renormalizable theory which perfectly reproduces the low-energy phenomenology is then obtained, at present the Higgs mechanism is the weak spot of the theory, as it implies the rising of a new scalar particle, the Higgs boson, which has not yet been observed. If the Higgs boson does not exist, some processes could violate unitarity and then renormalizability could be lost. However, even the discovery of the Higgs boson could imply the necessity of new physics, depending on its mass. In fact only a limited range of masses around 160 GeV/$c^2$are compatible with the stability of the Standard Model up to the Planck mass scale. A very different mass would imply a breakdown of the Standard Model and give an indication of the scale at which new physics would become evident.

LHC was conceived to accomplish the important task to shed light on the consistency of the Standard Model at energy scales up to about 1 TeV and finally solve the EWSB puzzle. Although EWSB investigation is the LHC main goal, a wide research programme, both in the SM and beyond it, has been developed. In Section 1.3 a brief description of the possible physics study at LHC is given.

1.2 Design Concept of the LHC

The Large Hadron Collider is under installation in the 27 km long tunnel, built for the previous LEP (Large Electron Positron) collider. Some advantages were obtained as the tunnel and several infrastructures, including injectors, already exist. However, the radius of LHC limits the centre-of-mass energy to 14 TeV, since the beams must be bent by dipole magnets whose maximum reliable field is currently limited at about 8 T.

The choice of proton beams is mainly dictated by the following considerations.

- The hadrons allow exploration of a wide range of energies with fixed-energy beams: they are the natural choice for a discovery machine. The protons are not elementary particles, and in hard collisions the interaction involves their constituents (quarks and gluons), which carry a non fixed fraction of the proton energy.

- The protons allow the accelerator to reach higher luminosities with respect to anti-protons machine, as their production and storage is easier.

- In a circular collider of radius R, the energy loss per turn due to synchrotron radiation is proportional to $(E/m)^4/R$, where E and m are respectively the energy and mass of the particles accelerated. Therefore, due to their higher mass, the usage of protons imply a smaller energy loss for synchrotron radiation with respect to the electrons.

The LHC shall have very high luminosity to compensate for the low cross section of the interesting processes. The cross section of different processes as a function of the centre-of-mass energies for p-p collisions is shown in Fig. 1.1. The Higgs cross section increases steeply with the centre-of-mass energy, while the total cross section (*i.e.* the background) remains almost constant. This leads to use the highest possible centre-of-mass energy.

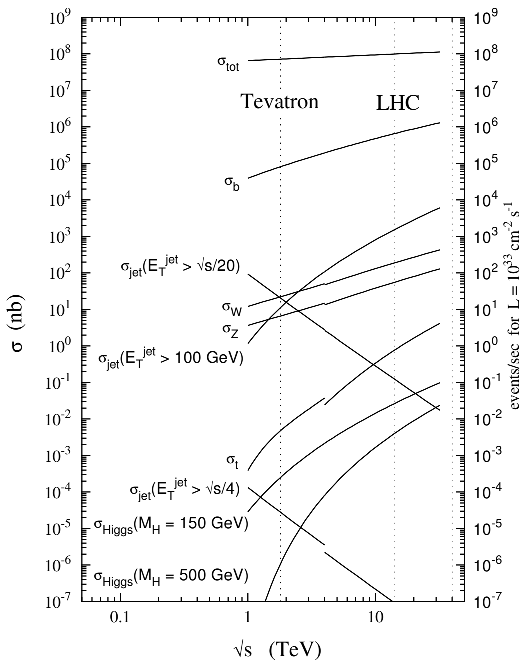

Figure 1.1: *Expected cross sections and event rates of several processes as a function of the centre-of-mass energy of proton-proton collisions [10].*

1.2.1 The LHC Parameters

The LHC machine comprises 1232 dipole magnets, with radio frequency cavities providing an increase in the proton energy of 0.5 MeV/turn. The injected beams, from the Super Proton Synchrotron (SPS), have an energy of 450 GeV. The beams are injected in bunches separated in time by 25 ns (or multiple of 25 ns). The bunch structure is such that, at design luminosity, only about 80% of the bunches are filled [11]. The machine parameters are listed in Table 1.1.

The luminosity is given by:

$$\mathcal{L} = \frac{\gamma\, f\, k_B\, N_p^2}{4\pi\, \varepsilon_n\, \beta^*} F, \tag{1.1}$$

where γ is the Lorentz factor, f is the crossing frequency, k_B is the number of bunches, N_p is the number of protons per bunch, ε_n is the normalised transverse emittance (with a design value of 3.75μm), β^* is the betatron function at the interaction point, and F is the reduction factor due to the crossing angle. The event rate R of a given process with cross section σ is given by $R = \mathcal{L}\sigma$

This design has the drawback that the total interaction rate becomes high and several interactions overlap in the same bunch crossing (*pile up*). As the total non-diffractive inelastic p-p cross section predicted by PYTHIA is 80 mb,

Table 1.1: *LHC parameters for p-p and Pb–Pb collisions.*

Parameter		p-p	$^{208}Pb^{82+}$
Energy per nucleon (TeV)	E	7	2.76
Dipole field at 7 TeV (T)	B	8.33	8.33
Design Luminosity ($\mathrm{cm^{-2}s^{-1}}$)	$\mathcal{L}$	10^{34}	10^{27}
Bunch time separation (ns)		25	100
No. of bunches	k_B	2808	592
No. particles per bunch	N_p	1.15×10^{11}	7.0×10^7
β-value at IP (m)	β^*	0.55	0.5
RMS beam radius at IP (μm)	σ^*	16.7	15.9
Luminosity lifetime (h)	τ_L	15	6

on average 22 events will occur at every bunch crossing. With about 50 charged tracks per interaction, this pile-up poses several experimental problems, as discussed in Section 1.2.2.

The first beam will be a commissioning run with reduced luminosity (10^{32} $\mathrm{cm^{-2}s^{-1}}$). The operation will start at 75 ns bunch spacing and subsequently the design 25 ns spacing will be reached. During the first year of physics running the LHC should reach the peak luminosity of $2 \times 10^{33}\mathrm{cm^{-2}s^{-1}}$ while the design luminosity of $10^{34}\mathrm{cm^{-2}s^{-1}}$ should be reached within the fourth year of operation. These two luminosity regimes are commonly called "Low luminosity" and "High Luminosity", respectively.

1.2.2 LHC Experiments

LHC detectors will operate in a very difficult environment: the high bunch crossing frequency, the high event rate and the pile-up of several interactions in the same bunch crossing impose strict requirements on the detector design. To cope with a bunch crossing rate of 25 ns and a pile-up of about 20 interactions per bunch crossing, the detectors shall have a very fast time response and the readout electronics shall also be very fast. Due to the presence of pile-up, high granularity and a large number of electronic channels are required to avoid the overlap of particles in the same sensitive elements. LHC detectors will also have to withstand an extremely high radiation dose and special radiation-hard electronics must be used.

Additional requirements apply to the on-line trigger selection, that has to deal with a background rate several orders of magnitude higher than the signal rate. These requirements are discussed in Section 2.6 and Section 5.5.

Four experiments will be installed at the LHC. Two of them are devoted to specific topics: Alice to heavy ions and LHC-b to b-physics. The other two are the general-purpose experiments ATLAS and CMS.

1.3 Physics with the LHC

1.3.1 Phenomenology of the Proton-Proton Collisions

In high-energy inelastic proton-proton collisions the interaction involves the partons inside the proton. The effective centre-of-mass energy of the hard scattering, $\sqrt{\hat{s}}$, is proportional to the fractional energies x_a and x_b carried by the two interacting partons: $\sqrt{\hat{s}} = \sqrt{x_a x_b s}$, where $\sqrt{s}$ is the centre-of-mass energy of the proton beams.

The distribution of the partons inside the proton are called Parton Density Functions (PDFs). They are different for gluons, u and d valence quarks and for low-momentum quark-antiquark pairs produced and annihilated as virtual particles (sea quarks). They are functions of Q^2, the negative of the four-momentum squared of the virtual photon exchanged during the scattering. For higher Q^2 a shorter distance scale is probed and the contribution of gluons and sea quarks increases. PDFs are obtained from experimental data covering the widest possible range of (x, Q^2); their accuracy is important for several precision measurements as the luminosity determination. In Fig. 1.2, the CTEQ4M PDFs [12] at two different values of Q^2 are shown.

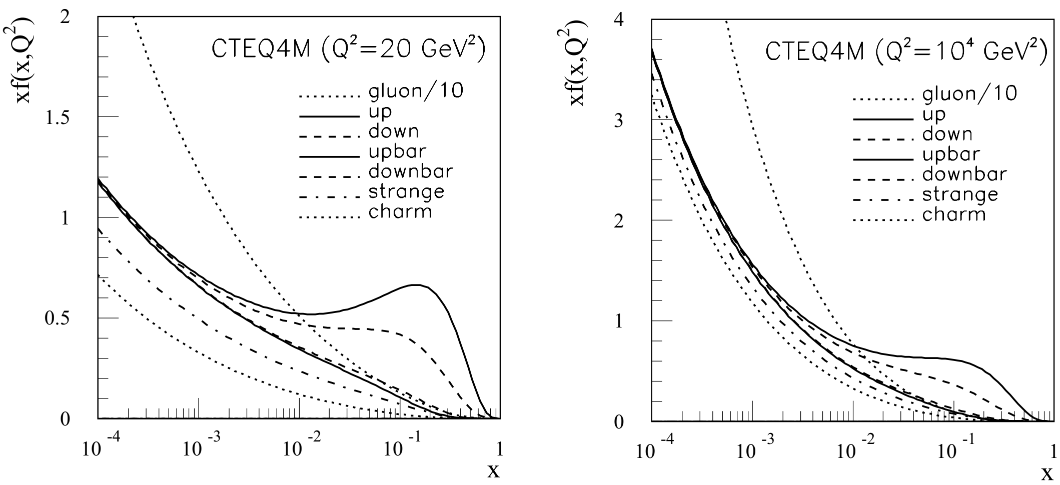

Figure 1.2: *Parton density functions for $Q^2 = 20\ GeV^2c^{-2}$ and $Q^2 = 10^4\ GeV^2c^{-2}$.*

The fact that the two partons interact with unknown energies has two fundamental consequences. First of all the total energy of an event is unknown, because the proton remnants, that carry a sizeable fraction of the proton energy, are scattered at small angles and are predominantly lost in the beam pipe, escaping detection. Moreover, the centre of mass may be boosted along the beam direction. Experimentally, it is therefore not possible to define the total and missing energy of the event, but only the total and missing transverse [1] energies.

In an hadron collider the usage of experimental quantities that are invariant under boost along the beam direction, as the transverse momentum (p_T) or the *rapidity* (y), are very useful. The rapidity, choosing the beam direction as z axis, is defined as:

$$y = \frac{1}{2} \ln \frac{E + p_z}{E - p_z} \tag{1.2}$$

and it is often used to describe angular distributions. The shape of dN/dy distributions is invariant under boosts along the z direction. For ultra-relativistic particles ($p \gg m$) the rapidity is approximated by the *pseudorapidity*:

$$\eta = -\ln \tan \frac{\theta}{2}, \tag{1.3}$$

where θ is the angle between the particle momentum and the z axis. The pseudorapidity is more practical to be used as it can be evaluated from the measurement of the θ angle and can be applied also to particles with unmeasured mass and momentum.

A very remarkable aspect of LHC physics is the wide cross section range of the processes involved (Fig. 1.1). The total p-p cross-section is about 100 mb and it is calculated taking into account processes of the elastic, inelastic, single an double diffractive type (the so called *minimum bias events*). The bulk of the events produced in proton-proton collisions is either due to low-$\hat{p}_T$ scattering, where the protons collide at large distances, or to QCD high-$\hat{p}_T$ processes of the type:

$$\begin{cases} q_i\bar{q}_i \rightarrow q_k\bar{q}_k \\ q_iq_j \rightarrow q_iq_j \\ q_ig \rightarrow q_ig \\ q_i\bar{q}_i \rightarrow gg \\ gg \rightarrow q_k\bar{q}_k \\ gg \rightarrow gg \end{cases}$$

All these events are in general considered of no interest as they constitute a background for other processes, where massive particles are created in the hard scattering. However this classification is somewhat arbitrary; for example, this definition of minimum bias events includes $b\bar{b}$ production that is of interest for b-physics studies.

[1] In the plane transverse to the beam.

1.3.2 Standard Model Physics

Several precision electroweak measurements will be possible with the two experiments ATLAS and CMS. Thanks to the high statistics available (*e.g.* 10^8 $W \to e\nu$ decays, 10^7 $t\bar{t}$ pairs produced in the first year of operation), for most measurements the statistical uncertainty will be very small. High statistics control samples will allow a good understanding of the detector response, thus reducing the systematic uncertainty.

In the following, we shortly discuss the experimental challenges of some electroweak measurements to be performed at LHC. A more comprehensive discussion can be found elsewhere [10, 13].

1.3.2.1 Measurement of the W and Top Mass

The values of the top and Higgs masses enter in the prediction of the W mass through radiative corrections. Precise measurements of m_t and m_W allow therefore to set limits on m_H and, if the Higgs is found, they will allow stringent tests of the Standard Model (SM) or its extensions like the Minimal Supersymmetric Standard Model (MSSM).

The most promising channel for the measurement of the top mass is $t\bar{t} \to W^+W^-b\bar{b}$ with one leptonic and one hadronic W decay, where the hadronic part is used to reconstruct the top mass and the leptonic part to select the event. The main source of uncertainty will be the jet energy scale, which is affected by the accuracy of the fragmentation model, the knowledge of the gluon radiation and the response of the detectors. The same sample of $t\bar{t}$ events will provide a large number of hadronic W decays to be used for the calibration of the hadron calorimeters.

The final uncertainty on m_t will be better than 2 GeV/c^2. This will constrain the Higgs mass to better than 30% but, in order not to become the dominant source of uncertainty, the W mass will have to be measured with a precision of about 15 MeV.

Since the longitudinal component of the neutrino momentum cannot be measured in hadron colliders, the W mass is obtained from a fit to the distribution of the W transverse mass. The main source of uncertainty is the lepton energy and momentum scale, which should be known with a precision of $\sim 0.02\%$ to achieve the mentioned precision on m_W. This is a challenging goal that could be reached thanks to the high statistics of $Z \to \ell\ell$ decays. Other sources of systematic uncertainty include the p_T^W spectrum, Γ_W and the proton structure functions. Since pile-up deteriorates the shape of the W transverse mass distribution, this measurement will probably be feasible only in the low luminosity mode.

Several other measurements will be possible in the top quark sector, including rare top decays, the determination of the $t\bar{t}$ and single top production cross section.

1.3.2.2 Drell-Yan Production of Lepton Pairs

The Drell-Yan production of lepton pairs is a process with clean signature and low experimental background. The interesting quantities are the cross section and the forward-backward asymmetry, both functions of the rapidity y and of the invariant mass of the di-lepton system.

The measurement of the cross section can provide evidence of new physics (new resonances, contact terms etc.) and probe electroweak radiative corrections up to 1.5 TeV. The main issue in this measurement is the knowledge of the absolute luminosity which should reach a precision of 5%, an ambitious goal requiring theoretical improvements in the knowledge of the W and Z production cross sections.

The measurement of the forward-backward asymmetry $\mathrm{A_{FB}}$ allows the determination of the effective electroweak mixing angle $\sin^2\theta_{eff}^{lept}$. However, it requires the knowledge of the incoming quark and anti-quark direction, which in p-p colliders is difficult to determine and is affected by the uncertainty on parton density functions. Improving the LEP+SLD accuracy on $\sin^2\theta_{eff}^{lept}$ is therefore a very ambitious goal. Preliminary studies indicate that it might be possible to achieve it if the geometrical acceptance for electrons is extended up to $|\eta| < 4.9$ using the forward calorimeters.

1.3.2.3 Production of Vector Boson Pairs

At the lowest order vector boson pairs are produced in $q\bar{q}$ annihilation followed by triple gauge boson vertices. Triple Gauge Couplings (TGC) directly test the non-Abelian gauge symmetry of the SM. They are described by five parameters, which can be measured with fits to the total cross sections and shapes of distributions such as that of $p_T^{\gamma,Z}$ in Wγ and WZ events. Deviations from the SM values can provide evidence for new physics, *e.g.* the presence of new heavy particles decaying to WW and ZZ pairs (including heavy Higgs). Anomalous couplings are present in many extensions of the SM, including MSSM, Technicolour etc. Since the sensitivity to anomalous couplings is enhanced at high centre-of-mass energies, LHC is expected to increase significantly the precision on TGC parameters.

At high energy, the process of vector boson scattering becomes dominant. This process is particularly sensitive to the electroweak symmetry breaking mechanism and violates unitarity at a scale of ~ 1 TeV. In the SM this is solved introducing the Higgs boson; in the absence of the Higgs new physics must couple to this channel. Whatever the scenario will be, vector boson scattering will therefore probe the mechanism of electroweak symmetry breaking. It is thus important to measure the WW scattering cross section as a function of the invariant mass of the WW system up to a scale of ~ 1 TeV.

From the experimental point of view, the presence of two forward jets are a clear signature of these processes. Other selection criteria are similar to those used for heavy SM Higgs searches. Purely hadronic final states will not be accessible due to the high QCD background; on the other hand it will be useful to reconstruct the invariant mass of the final state boson-boson system also in the absence of a resonance, which is not possible in final states with more than one neutrino.

High integrated luminosities will be necessary for these studies, due to the small cross sections and branching ratios and the high background rates. In Chapter 6 an exploratory study is presented.

1.3.2.4 B-Physics and CP Violation

In the field of b-physics, LHC will benefit from a very large $b\bar{b}$ production cross section (see Fig. 1.1). The main interest is the study of the decays of neutral B mesons, and in particular of the CP violation in the $B_d^0 - \bar{B}_d^0$ and $B_s^0 - \bar{B}_s^0$ systems. B decays can be identified in leptonic final states, especially in the case of muons. However these leptons are usually soft and the identification is difficult due to the high backgrounds and pile-up. One LHC experiment, LHCb, is dedicated to b-physics, which will be studied also by ATLAS and CMS in the low-luminosity phase. At high luminosity, the luminosity in the LHCb collision point will be reduced by de-focusing the beams.

1.3.2.5 Diffraction

In hadron-hadron scattering a substantial fraction of the total cross section is due to diffractive [14] reactions. In elastic scattering both projectiles emerge intact in the final state, whereas single or double diffractive dissociation corresponds to one or both of them being scattered into a low-mass state; the latter has the same quantum numbers as the initial hadron and may be a resonance or continuum state. In all cases, the energy of the outgoing hadrons is approximately equal to that of the incoming beam particles, to within a few per cent. The two (groups of) final-state particles are well separated in phase space and in particular have a large gap in rapidity between them.

The production of the Higgs boson in diffractive pp collisions may be a clean channel to study the properties of a light Higgs boson or even discover it.

A fascinating link has emerged between diffraction and the physics of heavy-ion collisions through the concept of saturation [15], which offers a new window on QCD dynamics in the regime of high parton densities.

1.3.3 Higgs Search

The main processes which contribute to the Higgs production at LHC are shown in the diagrams in Fig. 1.3. The cross sections for these different processes as a function of m_H are shown in Fig. 1.4.

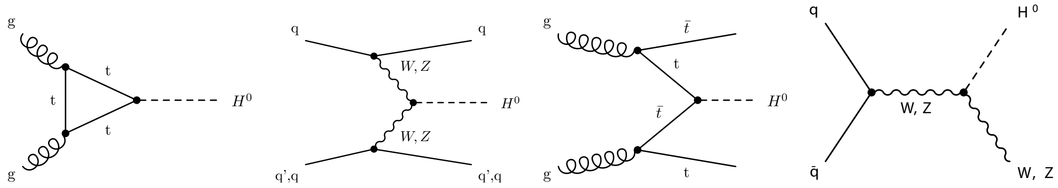

(a) (b) (c) (d)

Figure 1.3: *Higgs production mechanisms at tree level in proton-proton collisions: (a) Gluon-gluon fusion; (b) W and Z fusion; (c) $t\bar{t}$ associated production; (d) W and Z associated production.*

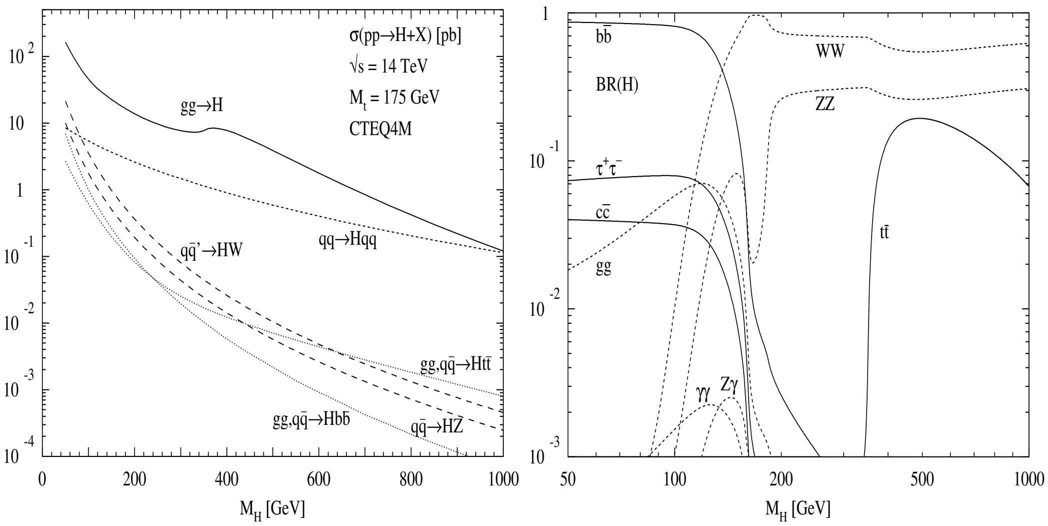

Figure 1.4: *Higgs production cross section (left) and branching ratios (right) as a function of the Higgs mass [16].*

Gluon fusion is the dominant process on the whole m_H spectrum and only at very high Higgs masses the vector boson fusion does become comparable. However, even if the WW scattering has on average a cross section about 5 to 10 times smaller than that of gluon-gluon fusion, this channel is extremely promising thanks to its clean experimental signature; the presence of two spectator jets provides a powerful tool to tag the signal events discriminating the backgrounds. The associated production channels $q_i\bar{q}_j \rightarrow WH$ or $q_i\bar{q}_j \rightarrow ZH$, where an off-shell boson is produced and radiates a Higgs, have very small cross sections, except for very low m_H. Also the production mechanism $gg, q_i\bar{q}_j \rightarrow t\bar{t}H$ has a cross section almost 100 times smaller than that of gluon-gluon fusion. However, also in this case a powerful signature is given by the additional bosons or jets in the final state.

Cross sections are typically of the order of few picobarns, which at the LHC design luminosity correspond to rates of about 10^{-2} Hz. However, not all final states will be experimentally accessible, and the branching ratios of the observable channels are usually small.

The branching ratios for several Higgs decay channels as a function of the Higgs mass are shown in Fig. 1.4. They can be interpreted on the basis of the Higgs couplings to fermions and gauge bosons:

$$g_{Hff} = \frac{m_f}{v} \tag{1.4}$$

$$g_{HWW} = \frac{2m_W^2}{v} \tag{1.5}$$

$$g_{HZZ} = \frac{m_Z^2}{v}. \tag{1.6}$$

The coupling is proportional to the fermion masses and to the square of the boson masses; basically three mass regions may be defined:

low Higgs masses (m_H < 130 GeV/c^2): the heaviest available fermion is the b quark, and $H \rightarrow b\bar{b}$ dominates. However, this decay channel could be difficult to observe at the LHC because of the huge QCD background (except maybe by exploiting associated $t\bar{t}H$ or WH production). In this mass region the most promising channel is $H \rightarrow \gamma\gamma$, which despite the very low branching ratio ($\sim 10^{-3}$) has a very clean signature. The signal should appear as a narrow peak over the continuum $(q\bar{q}, gg) \rightarrow \gamma\gamma$ background, but excellent photon energy and angular resolution are required as well as good π^0 rejection;

intermediate Higgs masses (130 GeV/c^2 < $m_H \lesssim 500 - 600$ GeV/c^2): the production of WW and ZZ pairs becomes possible; the branching ratio is high, but purely hadronic final states are again not accessible. $H \rightarrow 4\ell$ is the "gold-plated" channel for Higgs search; however it has very low branching ratio and suffers from the low Higgs production cross sections above $m_H \sim 600$ GeV/c^2. The channel $H \rightarrow WW$ has the disadvantage that experimentally accessible final states $(\ell\mu\ell\mu, \ell\nu jj)$ have at least one neutrino that escapes detection; however it will be a good discovery channel, especially for $m_H \approx 2m_W$ where the WW production is at threshold and the ZZ branching ratio drops to 20%;

very high Higgs masses (above 500 GeV/c^2): the cross section becomes low and semi-leptonic final states ($2\ell 2j, \ell\nu 2j$) have to be used. The Higgs width becomes also very broad, as shown in Fig. 1.5, so that the reconstruction of a mass peak becomes difficult.

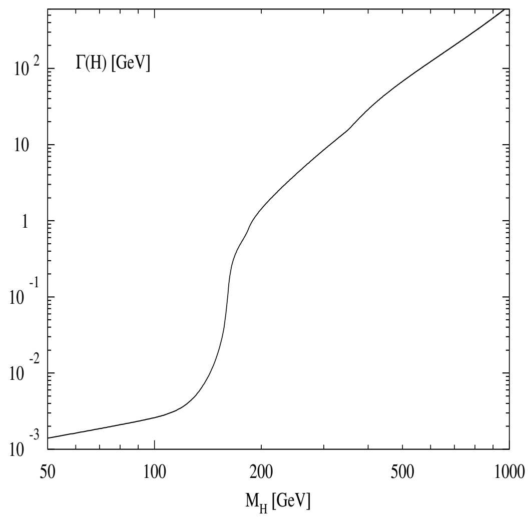

Figure 1.5: *Higgs width as a function of its mass [16].*

1.3.3.1 Higgs Mass Bounds

Theoretical bounds. The mass of the Higgs boson is not predicted by the SM; however arguments of self-consistency of the theory can be used to yield constraints on its value.

A lower limit [17, 18] on the Higgs mass m_H can be derived from the requirement of vacuum stability. The limit is a function of the top quark mass m_t and of the energy scale Λ where the model breaks down and new physics appears. The possible instability of the Higgs potential $V(\phi^\dagger\phi)$ is generated by quantum loop corrections to the classical expression of $V(\phi^\dagger\phi)$, where ϕ is the Higgs doublet. At large ϕ the derivative $V'(\phi^\dagger\phi)$ could become negative and the potential would become unbound from below. As demonstrated in [19, 20] the stability of the potential for $\phi \sim \Lambda \gg m_Z$ practically coincides with the requirement that the running coupling $\lambda(\mu)$ never becomes negative up to the break down scale Λ.

Similarly an upper bound on m_H (with mild dependence on m_t) can be obtained from the requirement that up to the scale Λ no Landau pole appears (*triviality*). In fact [21] considering the renormalisation group equation for λ in the simplified case when gauge and Yukawa couplings are neglected, then:

$$\Lambda < m_H \exp\left(\frac{4\pi^2 v^2}{3m_H^2}\right). \tag{1.7}$$

The relation (1.7) implies that for a given Higgs boson mass, there is a finite cutoff energy at which the description of the theory as a fundamental theory stops making sense.

The theoretical bounds on m_H as a function of Λ are shown in Fig. 1.6. For

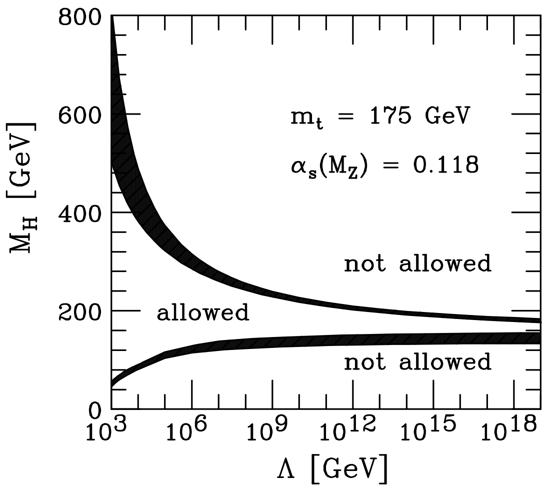

Figure 1.6: *Theoretical bounds on the Higgs mass as a function of the energy scale Λ up to which the Standard Model is valid [22].*

the SM to remain valid up to the Planck scale ($\Lambda = 10^{19}$ GeV), the Higgs mass must be in the range 130-190 GeV/c^2. Assuming the SM to be valid only up to $\Lambda \sim 1$ TeV, the Higgs mass can be up to 700 GeV/c^2. In any case, on the basis of these results, the guideline for the design of future colliders should be the search of the Higgs boson up to masses of the order of ≈ 1 TeV. If the Higgs particle is not found in this mass range then a more sophisticated explanation of the electroweak symmetry breaking mechanism is needed.

Experimental bounds. Experimental bounds on m_H are provided by measurements at LEP, SLC and Tevatron [23]. Direct searches [24] excluded the possibility of a Higgs boson with a mass below 114.4 GeV/c^2 at 95% confidence level. Indirect bounds can be obtained from precision electroweak measurements; observables like the top and $W^\pm$ masses and Z decay parameters are logarithmically sensitive to m_H through radiative corrections. These data can therefore be fitted taking the Higgs mass as a free parameter. The results of these procedure are summarised in Fig. 1.7. The plot shows the value of $\Delta\chi^2 = \chi^2 - \chi^2_{min}$ as a function of m_H. The solid curve is the result of the fit while the shaded band represents the uncertainty due to so far not calculated higher order corrections.

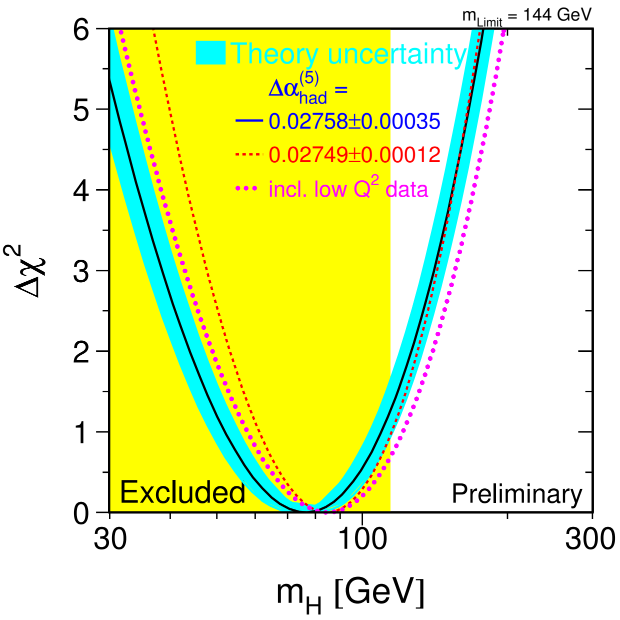

Figure 1.7: *$\Delta\chi^2$ of the fit of electroweak measurements of LEP, SLC and Tevatron as a function of the Higgs mass [23].*

The fit privileges low values of the Higgs mass and an upper limit of 144 GeV/c^2 can be set at 95% confidence level. This limit increases to 182 GeV/c^2 when including the LEP-2 direct search limit [23].

The Electroweak data can be also used to determine the top quark and the W masses indirectly and the results can be compared to the direct measurements performed at Tevatron and LEP-2. This is illustrated in Fig. 1.8 which also shows the SM prediction for the Higgs mass between 114 and 1000 GeV/c^2. The indirect and direct measurements of m_W and m_t are in good agreement. Since the accuracy on the measurement of m_W is much higher than that on m_t to further significantly constraint m_H a more accurate measurement of m_t is mandatory; to have the same weight on the Higgs mass prediction the two uncertainties should be $\Delta m_W \sim 7 \cdot 10^{-3} \Delta m_t$.

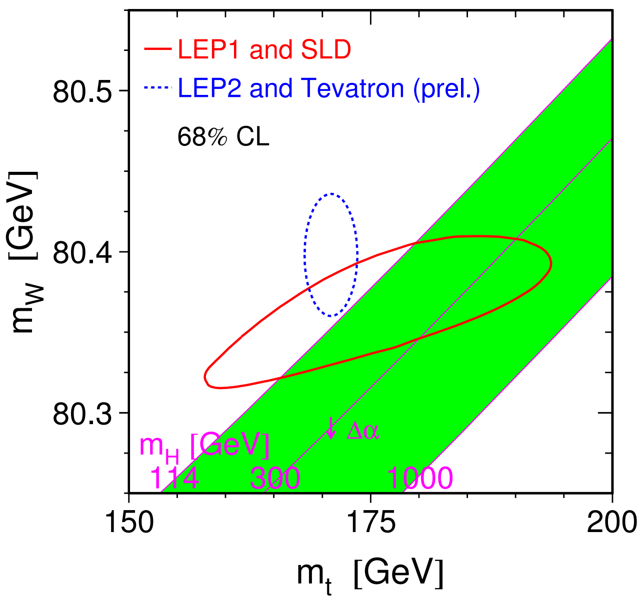

Figure 1.8: *Comparison of the indirect measurements of m_W and m_t (solid contour) and the direct measurements (dashed contour). In both cases the 68% CL contours are plotted. The Standard Model relationship for the masses as a function of the Higgs mass is also shown [23].*

1.3.3.2 Open Questions

The Higgs mass suffers from divergences caused by radiative corrections which are proportional to the energy cutoff; for the Standard Model to be valid up to very high energy scales, extremely precise cancellations should be present at all perturbation orders. Such cancellations are formally possible, but such precise tuning appears to be artificial; this represents the so called *naturalness problem.*

The Higgs mechanism has been criticised also on the basis of more aesthetic considerations: it is an ad hoc addition to the SM which introduces the only scalar particle of the theory. Moreover, there is no explanation to the fact that the particle masses would be significantly smaller than the energy scale up to which the theory remains valid (*hierarchy problem*). Finally, the number of free parameters (24) in the Standard Model appears too high for a fundamental theory.

Several solutions for these problems have been proposed [25, 26]. A model independent study with the aim to probe the electroweak symmetry breaking is shown in Chapter 6.

1.3.4 Beyond the Standard Model Physics

1.3.4.1 Supersymmetry

Supersymmetry [27] (SUSY) is a theory that introduces a new symmetry between bosons and fermions. SUSY predicts that each particle has a supersymmetric partner whose spin differs by one half. The naturalness problem is solved by the fact that the loop contributions from particles and their supersymmetric partners cancel. The simplest supersymmetric model, called the Minimal Supersymmetric Standard Model (MSSM), predicts the existence of two Higgs doublets, corresponding to five Higgs particles: two charged bosons, $H^{\pm}$, two scalar bosons, h and H, and one pseudo-scalar, A. At tree level, all masses and couplings depend on two parameters, chosen as the mass of the A boson, m_A, and the ratio of the vacuum expectation values of the two Higgs doublets, $\tan\beta$.

In most of the parameter space, charged Higgs bosons decay predominantly to $\tau\nu$. For the neutral Higgs bosons, the decays to vector bosons are suppressed, so that the golden channels described for the case of a SM Higgs will not be observable. The dominant decays modes are those to $b\bar{b}$ and $\tau^+\tau^-$ [16], but the former is hidden by the large background of b-jets. The observation of MSSM Higgs bosons will therefore rely on the identification the leptons coming from τ decays and of τ-jets.

Additionally, supersymmetric theories predict a rich phenomenology [28]. Supersymmetric particles should be accessible at LHC energies and have very spectacular signatures due to cascade decays with many leptons and jets in the final state and large missing energy. If supersymmetry exists, LHC experiments will certainly be able to observe and study it. However no evidence for supersymmetry has been observed so far and many limits on its parameters have been measured [29]. Moreover, even if it will be observed, SUSY will not cure the high number of SM parameters, as the SUSY models are based on more than 124 parameters.

1.3.4.2 Extra Dimensions

The existence of extra dimensions [30, Chapter 14] can lead to a characteristic energy scale of quantum gravity, M_D, which is the analogue of the Planck mass in a D-dimensional theory, and which could lie just beyond the electroweak scale. In terms of experimental signatures, three regimes can be distinguished [31]: i) Cis-Planckian, where $E \ll M_D$, leading to signals involving the emission of gravitons that escape into extra dimensions, e.g.

$pp \rightarrow$ jet+graviton $\rightarrow$ jet+E_T^{miss}, ii) Planckian, $E \approx M_D$, leading to model-dependent signatures. In string-theory motivated models there are Regge-like excitations that manifest themselves as Z-like resonances with $\sim$ TeV separations in mass, iii) Trans-Planckian, $E \gg M_D$, leading to anomalous high mass di-jet production and to mini black hole production with decays involving equal production of fundamental particles such as leptons, photons, neutrinos, W, Z, jets, etc. The resulting production and kinematic distributions could allow the determination of the Hawking temperature, the mass of the black holes, the number of extra dimensions.

1.3.4.3 Search for New Massive Vector Bosons

The detector requirements for high momenta can be determined by considering decays of high-mass objects such as $Z' \rightarrow e^+e^-$ and $\mu^+\mu^-$. The discovery of an object like a Z' [30] boson will, very likely, be limited by the statistical significance of the signal. Ways of distinguishing between different models involve the measurement of the natural width and the forward-backward asymmetry, both of which require sufficiently good momentum resolution at high p_T ($\Delta p_T/p_T < 0.1$ at $p_T \sim 1\text{TeV}/c$) to determine the sign of the leptons and a pseudorapidity coverage up to $\eta = 2.4$.

1.3.4.4 Heavy Ions

The recent results from RHIC indicate that very strongly interacting nuclear matter [32] is produced in high energy heavy-ion collisions. The most striking experimental signatures of the produced matter are the suppression of high p_T particles (jet quenching) and the strong elliptical flow approaching the hydrodynamic limit. The increase in collision energy from $\sqrt{s_{NN}} = 200$ GeV/c^2 at RHIC to 5500 GeV/c^2 at LHC will allow the extension of studies of jet quenching to much higher p_T and the identification of fully formed jets. The measurements of energy flow at LHC will stringently test the liquid-like behaviour of the hot nuclear matter. The increased energy will also allow studies of presently inaccessible hard probes like Υ and Z [30]. The studies of jet quenching, energy flow, and quarkonium production will require large-acceptance, high-resolution calorimeters and tracking devices, as well as a flexible trigger.

Chapter 2

The Compact Muon Solenoid

The Compact Muon Solenoid (CMS) [33] is a general-purpose experiment that will operate at the Large Hadron Collider.

The CMS design was driven by the requirements of a robust and redundant muon system, a precise electromagnetic calorimetry, and a high quality central tracking system. To achieve these goals a solenoidal magnetic field of 4 T was chosen. This chapter describes the general design of CMS with emphasis on the muon spectrometer.

2.1 Overall Design

The layout of CMS is illustrated in Fig. 2.1. The detector consists of a cylindrical barrel closed by two endcap disks. The overall length is 21.6 m, the diameter 14.6 m and the total weight about 12500 tons.

The CMS coordinate system is a right-handed frame where the x axis points to the centre of the LHC ring, the y axis points upward and the z axis is parallel to the beam.

The longitudinal view of one quarter of CMS and the transverse view of the barrel region are shown in Fig. 2.1 and Fig. 2.3 respectively. Components are indicated with standard two-letter codes (the second being `B` for barrel and `E` for endcap) which will be used in the following.

The iron return yoke (`YB`, `YE`) of the magnet hosts the muon spectrometer, composed by 4 stations of drift tube detectors (DT) in the barrel region (`MB`) and 4 stations of cathode strip chambers (CSC) in the endcaps (`ME`). Both the barrel and the endcaps are instrumented with resistive plate chambers (RPCs), which ensure redundancy and robustness at the muon trigger system. The overall pseudorapidity coverage of the muon system goes up to $|\eta| = 2.4$.

The core of the apparatus is the magnet (`CB`), a 13 m long super-conductive solenoid [34] cooled with liquid helium, which provides a 4 T magnetic field. The

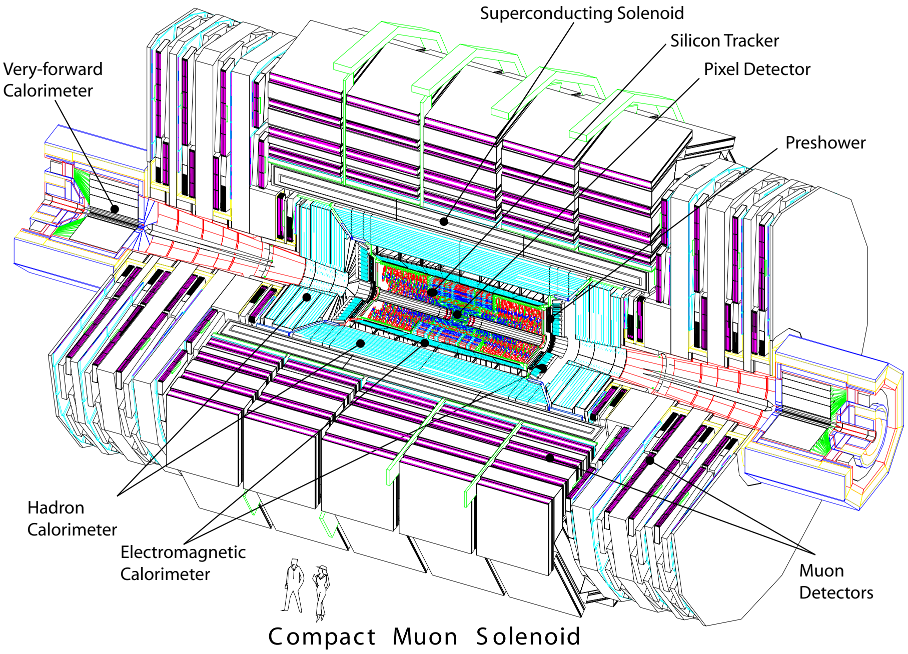

Figure 2.1: *The CMS detector.*

magnet coil has a diameter of 5.9 m and houses the hadronic and electromagnetic calorimeters and the tracker.

The hadronic calorimeter (HCAL) is a brass/scintillator sampling calorimeter. In the central part, the HCAL is complemented by a "tail-catcher" ensuring that hadronic showers are sampled with nearly 11 hadronic interaction lengths. The barrel and endcap parts (`HB`,`HE`) have the same $|\eta|$ coverage as the electromagnetic calorimeter, and are complemented by a very forward calorimeter (`HF`), which extends the coverage up to $|\eta| = 5.3$, enhancing the hermeticity of the detector and its ability to measure missing transverse energy.

Inside HCAL the electromagnetic calorimeter (ECAL) is installed. ECAL is a homogeneous calorimeter made of lead tungstate ($PbWO_4$) scintillating crystals. The scintillation light is detected by silicon avalanche photodiodes in the barrel region (`EB`) and vacuum phototriodes in the endcap region (`EE`). The pseudorapidity coverage extends up to $|\eta| = 3.0$. In the endcaps a lead/silicon pre-shower detector is installed to improve the resolution on electron and photon direction and help pion rejection.

The tracking detector is a cylinder of 5.8 m length and with a diameter of 2.6 m. Its design was driven by the requirement of a precise vertex reconstruction and a reliable b-tagging with very high track multiplicity. To achieve this goal very fine segmentation is crucial; CMS employs 10 layers of silicon

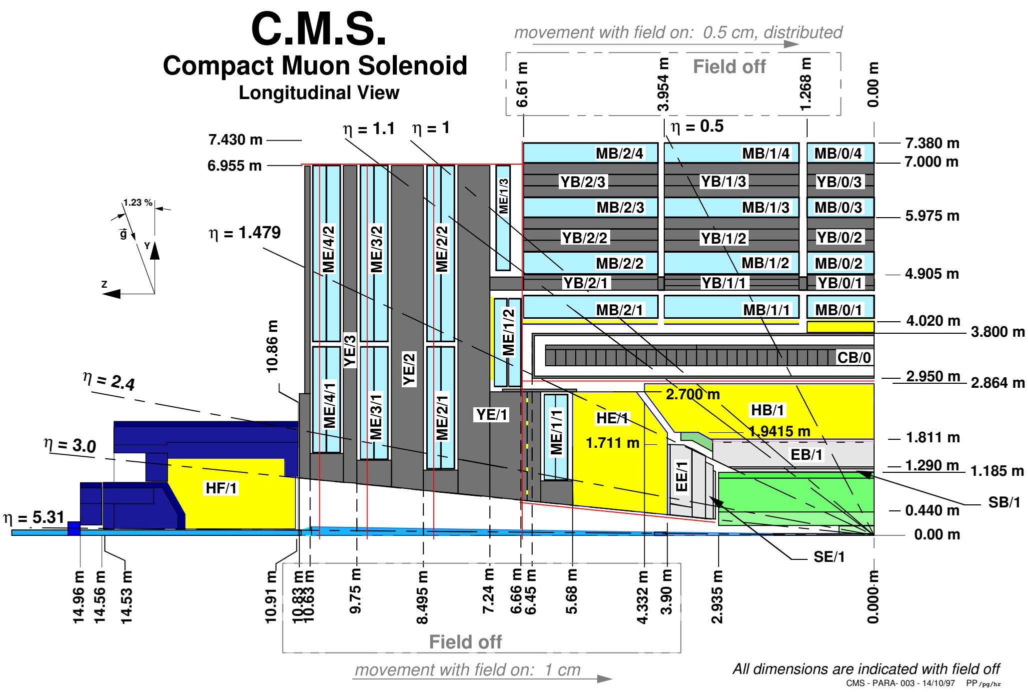

Figure 2.2: *Longitudinal view of one quarter of the CMS detector. The ME/4/2 station has been removed from the project as shown in Fig. 2.11.*

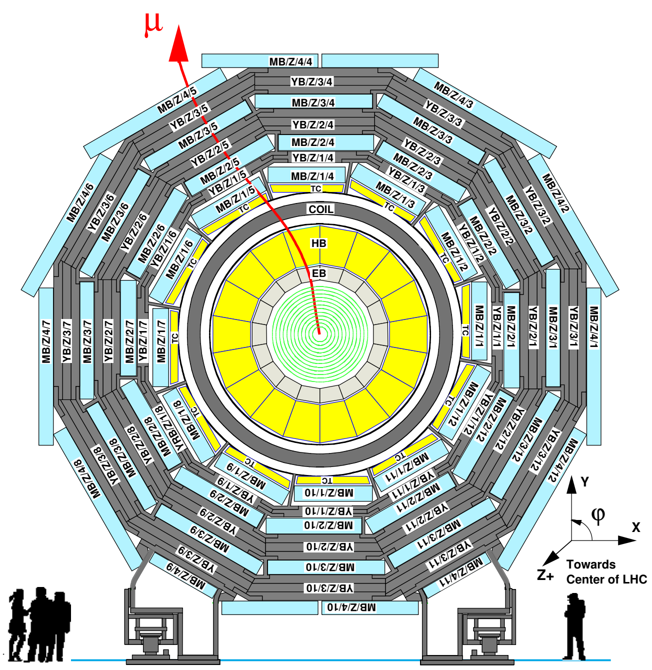

Figure 2.3: *Transverse view of the barrel region of the CMS detector. Barrel wheels are numbered Z = -2, -1, 0, 1, 2.*

microstrip detectors, which provide the required granularity and precision. In addition, 3 layers of silicon pixel detectors are placed close to the interaction region in order to improve the measurement of the impact parameter of charged-particle tracks, as well as the position of primary and secondary vertices. The tracking device allows charged-particle tracks reconstruction with at least 12 measurement points and a coverage of $|\eta| < 2.5$.

2.2 The Inner Tracking System

The inner tracker [35, 36] is designed to reconstruct high-p_T charged-particle tracks in the region $|\eta| < 2.5$ with high efficiency and good momentum resolution, to measure their impact parameter and to reconstruct secondary vertices. To achieve this goal several layers of silicon detectors are employed. By considering the charged particle flux at various radii at high luminosity three regions can be distinguished:

- Closest to the interaction vertex where the particle flux is the highest ($\approx 10^7$/s at $r \approx 10$ cm), pixel detectors are placed. The size of a pixel is $\sim 100 \times 150 \mu\text{m}^2$, giving an occupancy of about 10^{-4} per pixel per bunch crossing.

- In the intermediate region ($20 < r < 55$ cm), the particle flux is low enough to enable use of silicon microstrip detectors with a minimum cell size of 10 cm $\times 80$ μm, leading to an occupancy of $\sim$ 2–3% per bunch crossing.

- In the outermost region ($r > 55$ cm) of the inner tracker, the particle flux has dropped sufficiently to allow use of larger-pitch silicon microstrips with a maximum cell size of 25 cm $\times$ 180 μm, whilst keeping the occupancy to $\sim$ 1%.

Even in heavy-ion (Pb-Pb) running, the occupancy is expected to be at the level of 1% in the pixel detectors and less than 20% in the outer silicon strip detectors, permitting track reconstruction in the high density environment.

The performance of the tracker is illustrated in Fig. 2.4, which shows the transverse momentum and impact parameter resolutions in the r-ϕ and r-z planes for single muons with p_T of 1, 10 and 100 GeV/c, as a function of pseudorapidity. The resolution on the p_T measurement remains below 2% up to $|\eta| = 1.6$.

2.2.1 The Pixel Detector

The detector consists of 4.4 millions of n-type silicon pixels with a size of 100 μm $\times$ 150 μm on a n-type silicon substrate. The sensors are read-out

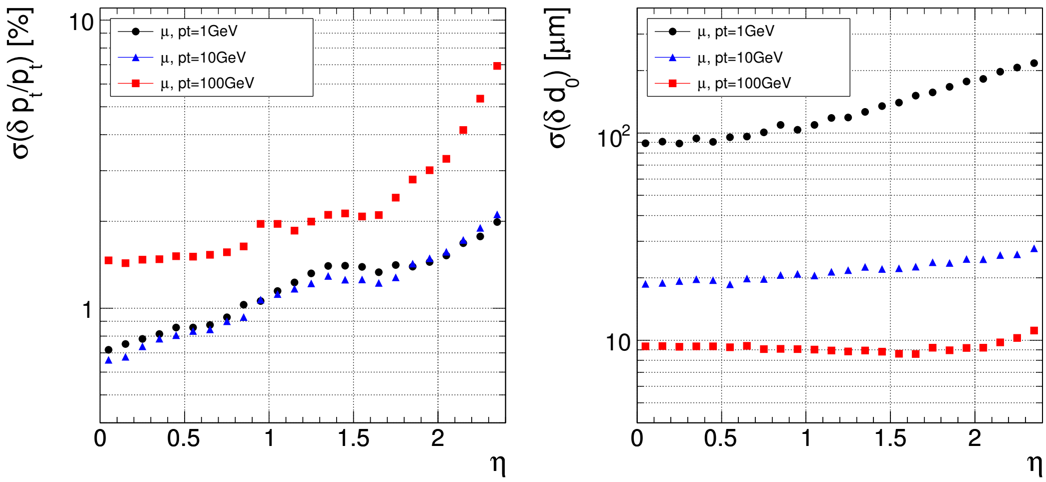

Figure 2.4: *Tracker tracks resolution on the transverse momentum (left) and the transverse impact parameter (right) as a function of pseudorapidity, for single muons with transverse momentum of 1, 10 and 100 GeV/c [37].*

analogically and a spatial resolution of $\sim 10\ \mu$m for the r-ϕ coordinate and of $\sim 20\ \mu$m for the r-z measurement is achieved interpolating the charge induced in nearby pixels, helped by the large Lorentz drift angle in the magnetic field. The charge sharing is enhanced in the endcaps, where the electric and magnetic fields are parallel, by tilting the detectors by 20°.

The sensors are organised in three barrel layers at mean radii of 4.4 cm, 7.3 cm and 10.2 cm, extending for a total length of 53 cm. In the endcaps two disks are placed at $|z| = 34.5$ cm and 46.5 cm extending in radius from 6 to 15 cm. The layout of the pixel detector is shown in Fig. 2.5. The pixel detector is designed to provide at least two hits for tracks originating within $2\sigma_Z$ [1] from the nominal interaction point up to about $|\eta| < 2.2$. Moreover, stand-alone track reconstruction, which requires three hits per track, is also possible with good efficiency.

The three-dimensional resolution of the pixels will play a key role in the identification of b and τ-jets allowing the accurate measurement of the impact parameter and the reconstruction of primary and secondary vertices.

The short distance from the interaction point imposes special requirements on radiation hardness and will probably require the substitution of the pixel detector during the lifetime of the experiment.

[1] Longitudinal size of the luminosity region of the LHC beam: $\sigma_Z \sim 5$ cm.

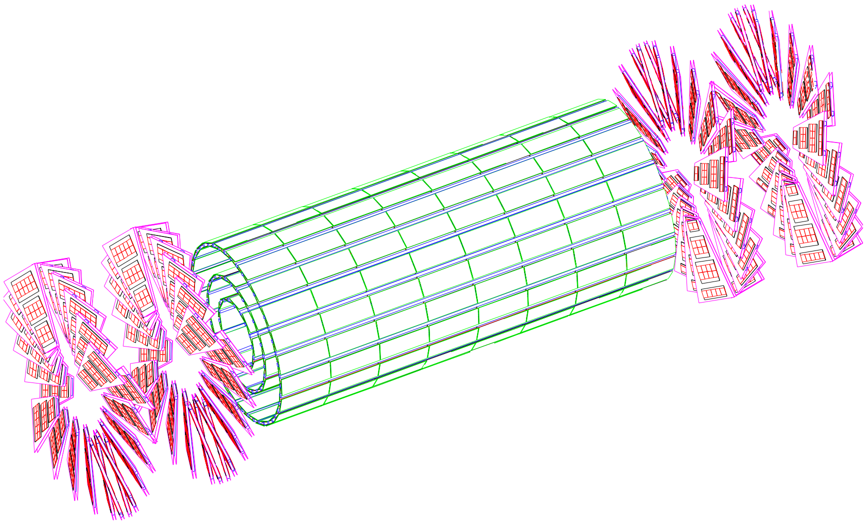

Figure 2.5: *Three-dimensional view of the full pixel detector.*

2.2.2 The Silicon Microstrip Detector

In addition to the pixel detectors, the tracker is composed of 10 layers of silicon microstrip detectors, whose layout is shown in Fig. 2.6. The barrel region is divided into two parts: the TIB (Tracker Inner Barrel) and the TOB (Tracker Outer Barrel). The TIB is composed by four layers of n-type silicon sensors with a thickness of 320 μm and strip pitches varying from 80 to 120 μm. The first two layers are made with double-sided ("stereo") modules, composed by two detectors mounted back-to-back with the strips tilted by 100 mrad. This kind of sensors provides a measurement in both r-ϕ and r-z coordinates with a single point resolution between 23-34 μm and 230 μm respectively. The TOB is made of six layers. In this region the radiation levels are smaller and thicker silicon sensors (500 μm) can be used to maintain a good S/N ratio for longer strip length and wider pitch. The strip pitch varies from 120 to 180 μm. Also the first two layers of the TOB provide a "stereo" measurement with a single-point resolution which varies from 35 to 52 μm in the r-ϕ direction and 530 μm in z.

The endcaps are divided into the TID (Tracker Inner Disks) and TEC (Tracker End Cap). The three disks of the TID fill the gap between the TIB and the TEC while the TEC comprises nine disks that extend into the region 120 cm $< |z| <$ 280 cm. Both parts are composed of wedge shaped modules arranged in rings, centred on the beam line, and have strips that point towards the beam line.

The entire silicon strip detector consists of about 15400 modules, which

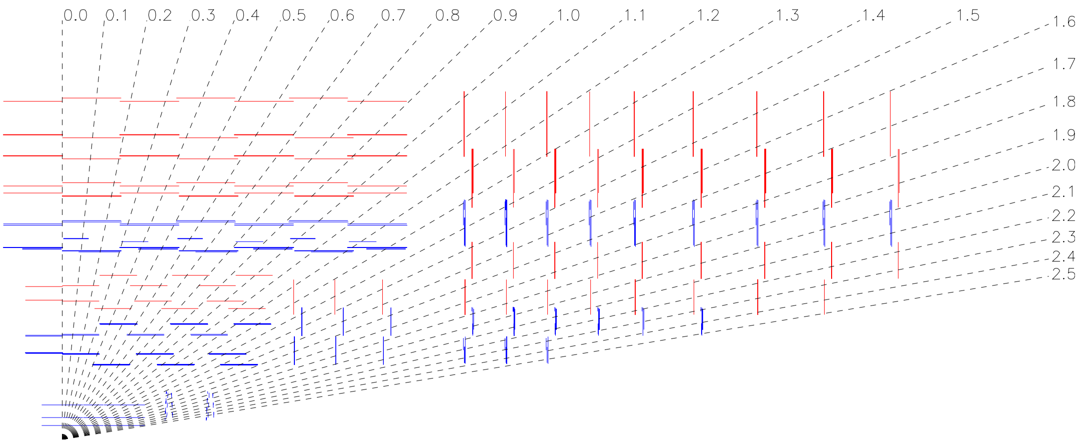

Figure 2.6: *Longitudinal view of one quarter of the silicon tracker, including the pixel detector. Different colours are used for single-sided (red), double-sided and pixel (blue) modules.*

will be mounted on carbon-fibre structures and housed inside a temperature controlled outer support tube. To enhance the radiation hardness of the system, the full detector will operate at a temperature of about $-20°C$.

Table 2.1: *Detector types in the silicon tracker*

part	No. detectors	thickness (μm)	mean pitch (μm)
TIB	2724	320	81/118
TOB	5208	500	81/183
TID	816	320	97/128/143
TEC	2512	320	96/126/128/143
TEC(2)	3888	500	143/158/183

2.3 The Calorimeters

2.3.1 The Electromagnetic Calorimeter

The goal of the electromagnetic calorimeter (ECAL) [38] is the accurate measurement of the energy and position of electrons and photons. The physics process that imposes the strictest requirements on its performance is the low mass Higgs decay into two photons: the goal is a 1% $\gamma\gamma$ invariant mass resolution. The natural choice to achieve this task is a homogeneous calorimeter;

ECAL is composed of 75848 finely segmented lead tungstate ($PbWO_4$) crystals. Lead tungstate is a fast, radiation-hard scintillator characterised by a small Molière radius (21.9 mm) and a short radiation length (8.9 mm), that allows good shower containment in the limited space available for the detector. Moreover, these crystals are characterised by a very short scintillation-decay time that allows the electronics to collect about 80% of the light within 25 ns.

The length of the crystals is 230 mm in the barrel and 220 mm in the endcaps, corresponding to 25.8 and 24.7 radiation lengths respectively. Crystals are trapezoidal, with a square front face of 22×22 mm^2 ($\Delta\eta \times \Delta\phi = 0.0175 \times 0.0175$) in the barrel and 28.6×28.6 mm^2 in the endcaps, matching the Molière radius.

A pre-shower detector is installed in front of the endcaps, consisting of two lead radiators and two planes of silicon strip detectors, with a total radiation length of 3 X_0. It allows rejection of photon pairs from π^0 decays and improve the estimation of the direction of photons, to improve the measurement of the two-photon invariant mass.

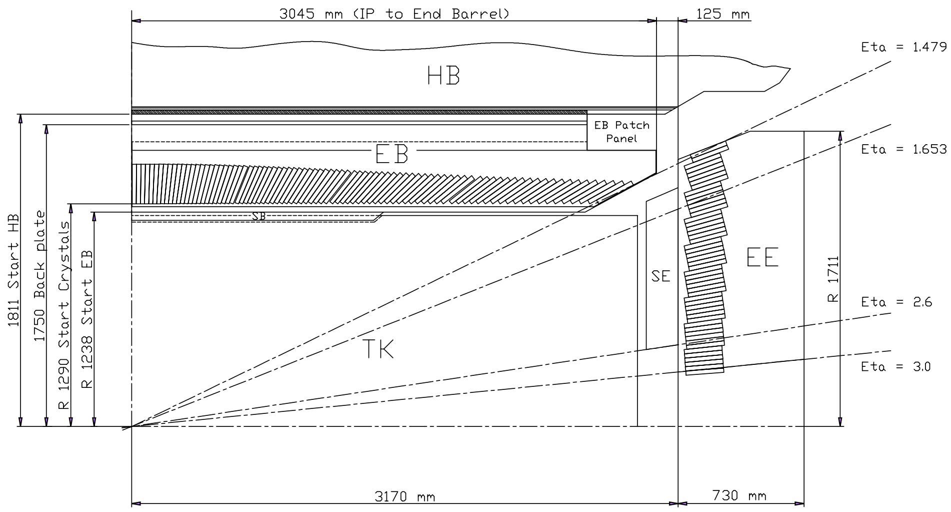

Figure 2.7: *Longitudinal view of one quarter of the ECAL. The barrel pre-shower (SB) has not been mounted.*

The geometric coverage of the calorimeter extends up to $|\eta| = 3.0$, as shown in Fig. 2.7. The crystals are arranged in a η-ϕ grid in the barrel and a x-y grid in the endcaps and they almost pointing to the interaction point: the axes are tilted at 3° in the barrel and at $2° - 5°$ in the endcaps with respect to the line from the nominal vertex position.

The relatively low light yield of the crystals ($\sim$ 80 γ/MeV) requires photodetectors with intrinsic high gain that can operate in a magnetic field. Silicon avalanche photodiodes (APDs) and vacuum phototriodes (VPTs) are used to collect the scintillation light in the barrel and in the endcaps respectively.

The energy (E) resolution of a calorimeter is usually parameterised as

$$\left(\frac{\sigma}{E}\right)^2 = \left(\frac{a}{\sqrt{E}}\right)^2 + \left(\frac{b}{E}\right)^2 + c^2 \tag{2.1}$$

where a is the stochastic term and it includes the effects of fluctuations in the number of photo-electrons as well as in the shower containment, b is the noise from the electronics and pile-up and c is a constant term related to the calibration of the calorimeter. The values of the three constants measured on test beams are reported in Table 2.2. The different contributions as a function of the energy are shown in Fig. 2.8.

Table 2.2: *Contributions to the energy resolution of ECAL.*

Contribution	Barrel ($\eta = 0$)	Endcap ($\eta = 2$)
Stochastic term	2.7%	5.7%
Constant term	0.55%	0.55%
Noise (low luminosity)	0.155 GeV	0.205 GeV
Noise (high luminosity)	0.210 GeV	0.245 GeV

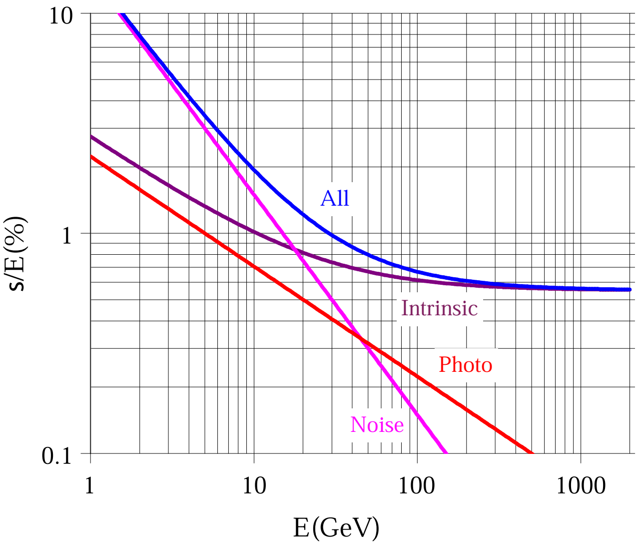

Figure 2.8: *Different contributions to the energy resolution of the ECAL [38]. The curve labelled "intrinsic" includes the shower containment and a constant term of 0.55%.*

2.3.2 The Hadron Calorimeter

The goal of the hadron calorimeter (HCAL) [39] is to measure the direction and energy of jets, the total transverse energy and the imbalance in the transverse energy (missing E_T). High hermeticity is required for this purpose. For this reason, the barrel and endcap parts installed inside the magnet are complemented by a very forward calorimeter which is placed outside the magnet return yokes, with a total coverage of $|\eta| < 5.3$. The overall HCAL is assembled with essentially no un-instrumented cracks or dead areas; the gap between the barrel and the endcap HCAL, through which the services of the ECAL and the inner tracker pass, is inclined at 53° and points away from the centre of the detector.

The barrel and endcap HCAL cover the region $|\eta| < 3.0$. They are sampling calorimeters, whose active elements are plastic scintillators interleaved with brass absorber plates and read out by wavelength-shifting fibres. The first layer is read out separately, while all others are read out together. The absorber material has been chosen for its short interaction length, and its non-magnetic property.

Both barrel and endcap are read-out in towers with a size of $\Delta\eta \times \Delta\phi = 0.087 \times 0.087$. In the barrel, full shower containment is not possible within the magnet volume, and an additional "tail catcher" is placed outside the magnet. It is referred as hadron outer (HO) detector and consists of an additional layer of scintillators.

The projective depth in terms of nuclear absorption length goes from 5.15 λ_0 at $\eta = 0$ to 9.1 λ_0 at $\eta = 1.3$, and is 10.5 λ_0 in the endcap (see Fig. 2.9).

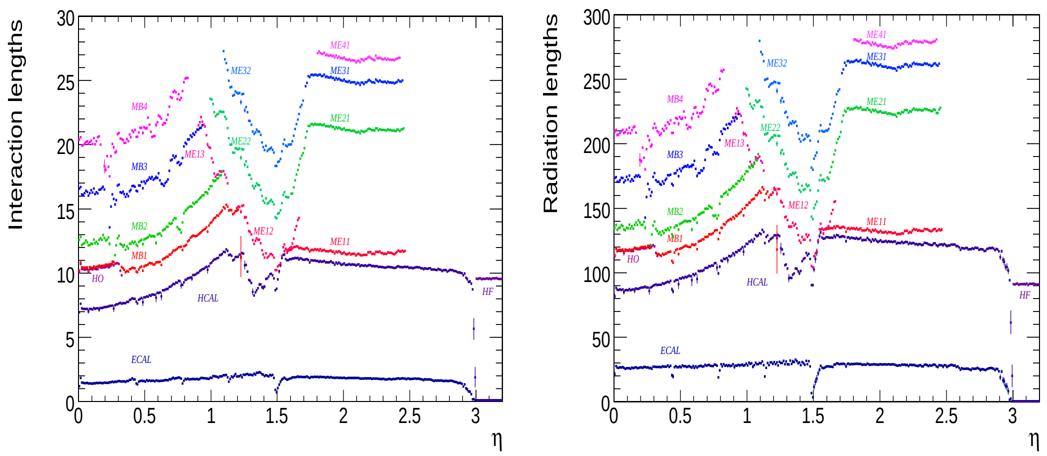

(a) (b)

Figure 2.9: *Interaction (a) and radiation (b) length as a function of pseudorapidity.*

The very forward calorimeter is placed outside the magnet yoke, 11 m from the interaction point. The active elements are quartz fibres parallel to the beam, inserted in steel absorber plates. The signal originated from the quartz fibres is Cerenkov light.

The expected energy resolution is $\sigma/E \sim 65\%\sqrt{E} \oplus 5\%$ in the barrel; $\sigma/E \sim 85\%\sqrt{E} \oplus 5\%$ in the endcaps and $\sigma/E \sim 100\%\sqrt{E} \oplus 5\%$ (E in GeV) in the very forward calorimeter.

2.4 The Magnet

The physics programme described in Chapter 1 imposes strict requirement on the momentum resolution of the charged particle. The required accuracy is of about 1% for particles with $p = 100\mathrm{GeV}/c$. Moreover the unambiguous charge-assignment for muons with a momentum of $\sim 1\mathrm{TeV}/c$ requires a momentum resolution of $\Delta p/p \approx 10\%$ at $p = 1\mathrm{TeV}/c$. In order to achieve this performance the CMS collaboration chose a super-conducting solenoid with a high nominal field value.

The parameters of the magnet are given in Table 2.3, while in Fig. 2.10 the magnetic field layout is shown.

Table 2.3: *Parameters of the CMS super-conducting solenoid.*

Parameter	Value
Field	4 T
Field in the yoke	2 T
Inner Bore	5.9 m
Length	12.9 m
Number of Turns	2168
Current	19.5 kA
Stored energy	2.7 GJ
Hoop stress	64 atm

2.5 The Muon System

High-p_T muons will provide a clear signature for many physics processes. For this reason, the muon spectrometer must provide a robust trigger and an accurate measurement of the muon momentum and charge, also without the contribution of the tracker.

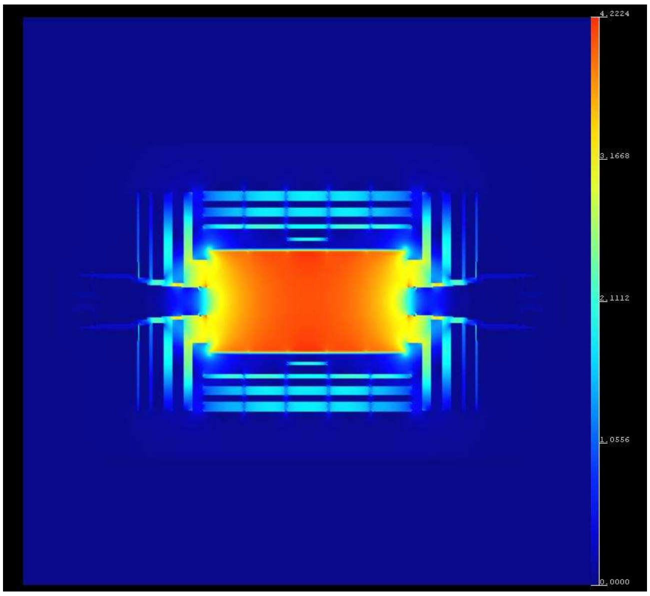

Figure 2.10: *Magnetic field layout.*

The muon system, shown in Fig. 2.11, is embedded in the iron return yoke of the magnet, which shields the detectors from charged particles other than muons.

The muon system consists of three independent subsystems. In the barrel ($|\eta| < 1.2$), where the track occupancy and the residual magnetic field are low, drift tube detectors (DT) are installed. In the endcaps ($0.8 < |\eta| < 2.4$), cathode strip chambers (CSC) are located, as detectors in this region have to cope with high particle rates and large residual magnetic field between the plates of the yoke. Redundancy is obtained with a system of resistive plate chambers (RPC), that are installed in both the barrel and the endcaps. RPCs have limited spatial resolution, but fast response and excellent time resolution, providing unambiguous bunch crossing identification. They are also used to complement DTs and CSCs in the measurement of the p_T. The RPC system covers the region $|\eta| < 2.1$.

The magnetic field inside the iron of the yoke bends the tracks in the transverse plane thus allowing the measurement of their p_T. The high field is fundamental for the momentum resolution of the spectrometer but it also sets the environment in which the detector operates. The innermost endcap CSCs, the ME1/1 chambers, are exposed to the full field which, in this region, is almost entirely axial and uniform. In the following CSC stations the field is no longer axial and uniform, however, the small drift space allows these detectors to limit the degradation of the chamber resolution (see Fig. 2.10).

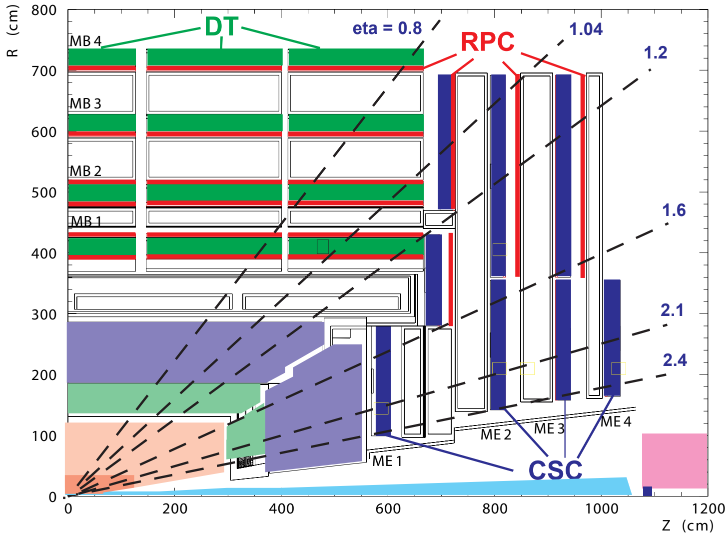

Figure 2.11: *Longitudinal view of one quarter of the muon system.*

In the barrel region most of the flux is contained within the iron plates of the yoke where the axial component of the field reaches $\sim$ 1.8 T. The space where the DT chambers are placed should ideally be field-free. However in the iron gaps and at the end of the coil the residual magnetic field is far from being negligible. The axial and the radial components are shown in Fig. 2.12 for the various barrel DT stations. There are spatially limited regions where the field in the radial direction reaches 0.8 T.

The robustness of the spectrometer is also guaranteed by the different sensitivity of DT, RPC and CSC to the background. The main sources of background particles in the LHC environment will be represented by secondary muons produced in pion and kaon decays, from punch-through hadrons and from low energy electrons originating after slow neutron capture by nuclei with subsequent photon emission. This neutron induced background will be the responsible of the major contribution to the occupancy level in the muon detectors. The total background rate at high pseudorapidity reaches up to 1 kHz/cm^2 in the innermost part of the ME1/1 station. In the barrel the fluences are much lower being everywhere less than 10 Hz/cm^2. As described in the following sections, CSC and DT chambers, in contrast with RPC detectors, are characterised by a layer layout which helps in reducing the effect of background hits: the request of correlation between consecutive layers is particularly effective against background hits affecting only a single layer.

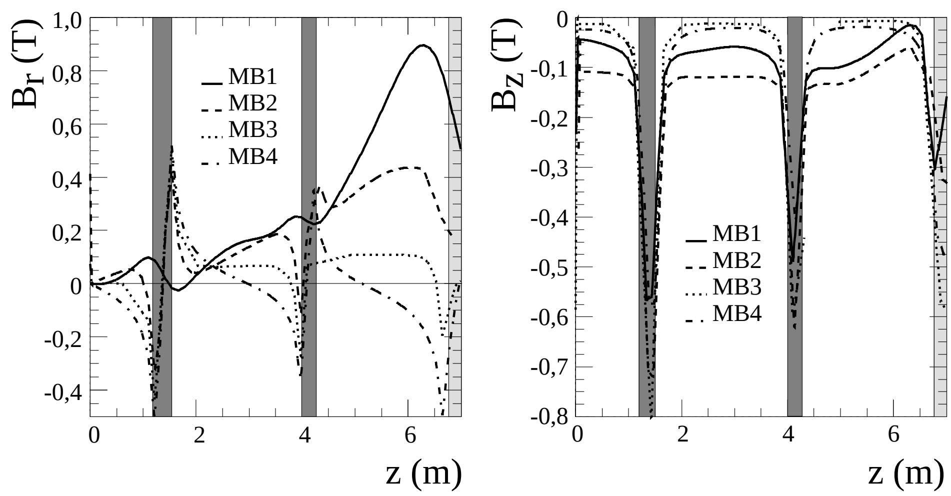

Figure 2.12: *Magnetic field components radial (B_r) and axial (B_z) with respect to the beam line in the different barrel stations as a function of the distance from the CMS centre in the axial direction (along the z-axis). The shaded areas are the gaps between the detector rings.*

2.5.1 The Drift Tube Chambers

Muon detectors in the barrel do not operate in particularly demanding conditions, since the occupancy in this region is low and the magnetic field is well contained in the iron plates of the return yoke. For this reason, drift tubes were chosen.

The chamber segmentation follows that of the iron yoke, consisting in five wheels along the z axis, each one divided into 12 azimuthal sectors. The wheels are numbered from -2 to +2, sorted according to global CMS z axis, with wheel 0 situated in the central region around $\eta = 0$.

Within all wheels, chambers are arranged in four *stations* at different radii, named MB1, MB2, MB3 and MB4 as shown in Fig. 2.11. The first and the fourth station are mounted on the inner and outer face of the yoke; the remaining two are installed in slots within the iron plates.

Each station consists of 12 chambers, one per sector, except for MB4 where 14 chambers are present. Sector numbering increases anti-clockwise when looking the detector from the positive z axis, starting from sector number 1 which contains the vertical chambers matching the positive x axis in the CMS global reference frame. The additional two chambers in MB4 are numbered 13 and 14 according to the scheme shown in Fig. 2.13.

The basic detector element is a drift tube cell, whose section is shown in Fig. 2.14. Cells have a size of 42×13 mm^2. A layer of cells is obtained by two parallel aluminium planes and by “I” shaped aluminium beams which define

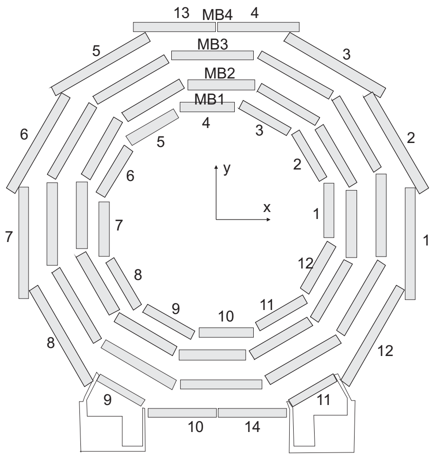

Figure 2.13: *Numbering of stations and sectors.*

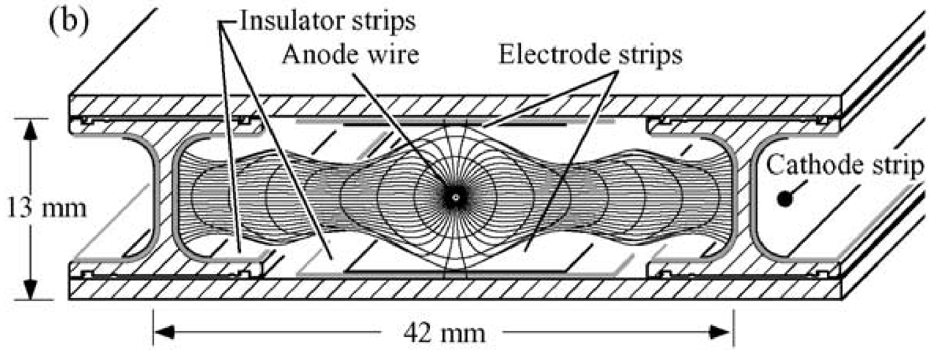

Figure 2.14: *Section of a drift tube cell.*

the boundary of the cells and serve as cathodes. I-beams are insulated from the planes by a 0.5 mm thick plastic profile. The anode is a 50 μm stainless steel wire placed in the centre of the cell. The distance of the track from the wire is measured by the drift time of electrons produced by ionisation. To improve the distance-time linearity, additional field shaping is obtained with two positively-biased insulated strips, glued on the the planes in correspondence to the wire. Typical voltages are +3600 V, +1800 V and -1200 V for the wires, the strips and the cathodes, respectively. The gas is a 85%/15% mixture of Ar/CO_2, which provides good quenching properties and a saturated drift velocity, of about 5.4 cm/μs. The maximum drift time is therefore $\sim$ 390 ns, *i.e.* 15 bunch crossings. A single cell has an efficiency of about 99.8% and a resolution of $\sim$ 180 μm.

Four staggered layers of parallel cells form a *superlayer*, which provides the measurement of a two-dimensional segment solving the left-right ambiguity of a single layer by means of pattern recognition. Also, the information of a superlayer can be used by the trigger to identify the bunch crossing originating a segment with no need of external input, using a generalisation of the mean-timer technique [40].

A chamber is composed by two superlayers measuring the r-ϕ coordinates, with the wires parallel to the beam line, and an orthogonal superlayer measuring the r-z coordinates. The latter is not present in the outermost station (MB4). The wire length varies, depending on the superlayer type and on the station, from about 2 m to 3 m. The superlayers are glued on the two sides of an honeycomb spacer which ensures a $\sim$ 15 cm long lever arm as well as the required stiffness to the structure. A cross-sectional view of a chamber is shown in Fig. 2.15.

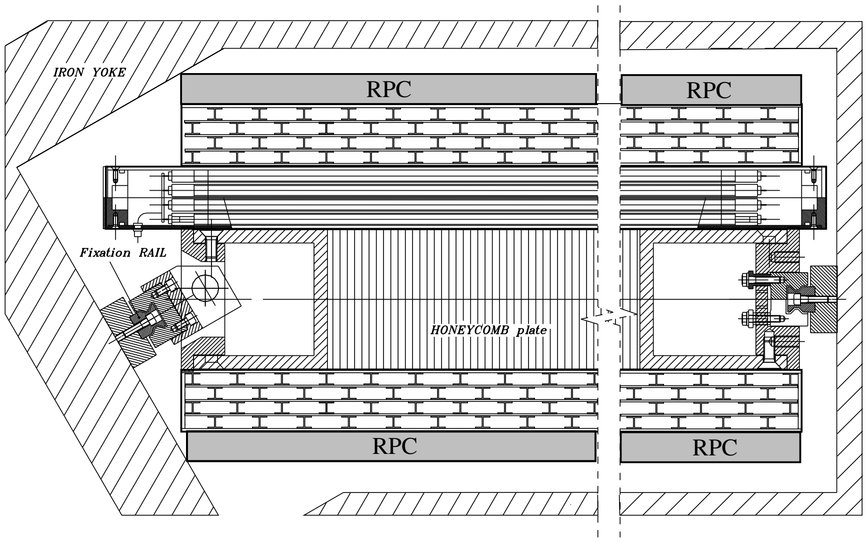

Figure 2.15: *Schematic view of a MB1/MB2 DT chamber. The two resistive plate chambers of the muon station are also shown.*

2.5.1.1 Labelling and Reference Frame

The convention on local reference frames used in the CMS simulation and reconstruction software is shown in Fig. 2.16.

Superlayers are numbered from 1 (innermost r-ϕ) to 3 (outermost r-ϕ). Number 2 is thus always the r-z superlayer, when present.

Layers are numbered from 1 (innermost) to 4 (outermost). Each layer has a local reference frame with the origin in its centre, the x axis along the measured coordinate and the y axis along the wires, pointing towards the front-end (FE)

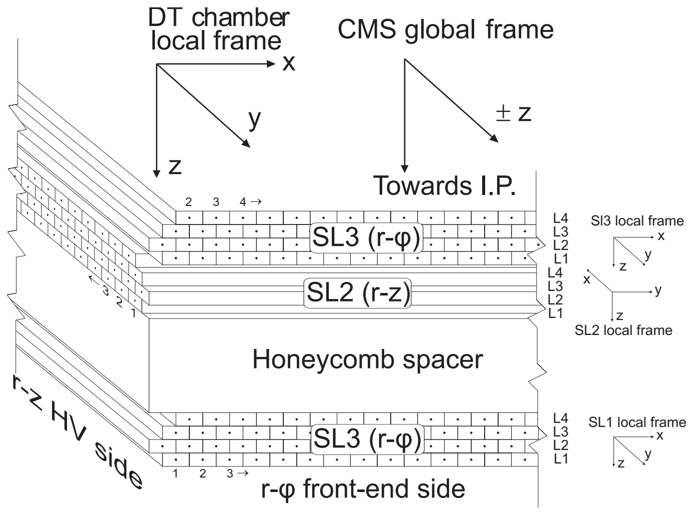

Figure 2.16: *Schematic view of a DT chamber, showing the conventions on superlayer, layer and wire numbering and the orientation of reference frames.*

electronics. Cells are numbered increasingly along local x and have a local reference frame parallel to the layer one, but centred on the wire position.

Superlayers have a local reference frame oriented in the same way as for their layers, but with the origin in the superlayer centre.

The chamber reference frame has the origin in the chamber centre and is oriented as the r-ϕ superlayer reference frames, i.e. with the x axis along the coordinate measured by the r-ϕ superlayers and the y axis along the coordinate measured by the r-z superlayer, pointing towards the r-ϕ front-end electronics.

With this choice of reference frames, the z axis of all mentioned local reference frames points towards the interaction region.

It should be noted that chambers are installed in CMS with the front-end of r-ϕ superlayers in the side farther from the interaction point (i.e. with the chamber y axis pointing outwards). This compensates, in r-ϕ superlayers, the different time of flight of particles at different η with the propagation time along the wires. The chamber local reference frames are oriented accordingly: in positive wheels (+1, +2) the chamber y axes are oriented along the global CMS z axis, while in negative wheels the x axis points towards the opposite direction. In wheel 0, chambers are oriented alternatively in the two ways in the different sectors.

2.5.2 The Cathode Strip Chambers

Cathode strip chambers are multi-wire proportional chambers with good spatial and time resolution, that can operate at high occupancy levels and in the presence of a large inhomogeneous magnetic field. For this reason they were adopted in the endcap region.

CSC chambers are arranged in four disks (*stations*) placed between the iron disks of the yoke (cf. Fig. 2.11). The innermost station consists of three concentric rings, the first (ME1/1) being closer to the interaction point than the other two. The other stations are composed by two disks only. The rings are formed by 18 or 36 trapezoidal chambers, which, with the exception of the outermost ring of ME1, are staggered with a small overlap in ϕ.

Chambers are composed of six layers, each consisting of an array of anode wires between two cathode planes (see Fig. 2.17). The gap is 9.5 mm thick and

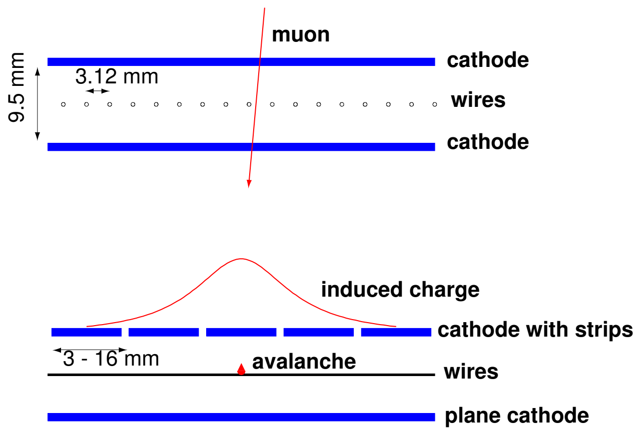

Figure 2.17: *Orthogonal sections of one CSC layer.*

is filled with a 30%/50%/20% mixture of Ar/CO_2/CF_4. One of the two cathode planes is segmented into strips orthogonal to the wires. The avalanche produced in the gap by a crossing charged particle induces a charge in several adjacent strips, an interpolation of the signals gives a precise spatial measurement.

Strips are radial and measure the ϕ coordinate. The orthogonal coordinate (r) is measured by the wires which, to reduce the number of channels, are read out in groups of 5 to 16. The resolution is of the order of $\sim$ 0.5 cm, to be compared with $\sim$ 150 μm of the strip measurement.

The first disk of ME/1 has to operate in difficult conditions, as it is exposed to a high magnetic field and particle rate. A slightly different design is adopted for chambers in this disk, with wires tilted by 25° to compensate for the Lorentz drift in the magnetic field. The gap is reduced to 6 mm and the number of strips is doubled above $|\eta| = 2.0$.

Although the single layer precision on the time measurement has a spread exceeding 25 ns, a sophisticate algorithm, using the second or third earlier hit in a pattern of six, can give more than 99% efficiency in finding the correct bunch crossing.

2.5.3 The Resistive Plate Chambers

The resistive plate chamber system is complementary to the DT and CSC systems, and adds robustness and redundancy to the muon trigger. Resistive plate chambers provide limited spatial resolution, but excellent time resolution, of the order of few nanoseconds.

In the barrel the RPC chambers follow the segmentation of DT chambers. A total of six layers of RPCs are present; the first four are attached to each side of the MB1 and MB2 DT chambers, as shown in Fig. 2.15. The other two are attached to the inner surface of MB3 and MB4. In the endcaps the chambers are trapezoidal; four layers are present.

The resistive plate chambers used in CMS are composed of four bakelite planes forming two coupled gaps, as shown in Fig. 2.18. The gaps are filled with a mixture of 90% $C_2H_2F_4$ (freon) and 5% i-C_4 H_{10} (ISO-butane). The

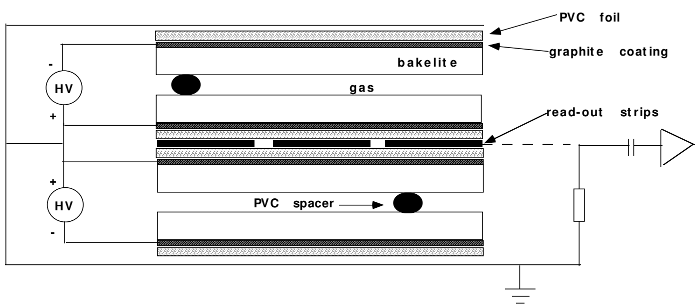

Figure 2.18: *Schema of a double-gap resistive plate chamber.*

planes are externally coated by graphite electrodes, the two innermost ones set to +9.5 kV. Insulated aluminium strips are placed in the middle, to collect the signal induced by crossing particles. This two-gap design is adopted to increase the charge induced on the strips.

RPCs will operate in "avalanche" mode rather than in the more common "streamer" mode, thus allowing the detectors to sustain higher rates. This mode is obtained with a lower electric field, thus the gas multiplication is reduced and an improved electronic amplification is required.

Other concerns come from the noise rate due to discharges caused by irregularities in the bakelite surfaces. These effects can be suppressed by treating the surfaces with line-seed oil.

In the barrel, the strips are parallel to the beam line, with a length of 80 or 120 cm and their pitch varies from 2.1 cm in the inner MB1 plane to 4.1 cm in the MB4 planes. In the endcaps, strips are radial with a length of 25 to 80 cm and have a pitch ranging from 0.7 cm in the most forward chambers to roughly 3 cm. This segmentation is dictated by the radial geometry and by the expected neutral background hit rates. The coordinate orthogonal to the strips is estimated as the centre of the cluster of fired adjacent strips. No measurement is available in the second coordinate, apart from the constraint coming from the strip length.

2.6 The Trigger

At the LHC nominal luminosity, the total event rate is of the order of 10^9 Hz; however, the rate for interesting events is very small, as shown in Fig. 2.19. A large fraction of the corresponding selection has to be performed on-line, since the raw event size is of the order of 1 MB, storing and processing the resulting amount of data would be prohibitively difficult and expensive. The goal of the trigger system is to perform this online selection, reducing the event rate to the order of 100 Hz, that is enough to accommodate the signal channels of interest. This task is difficult not only due to the high rejection factors it requires ($\sim 10^7$), but also because the output rate is saturated already by processes like $Z \to \ell\ell$ and $W \to \ell\nu$, where high-p_T leptons are produced. The trigger must therefore be able to select events on the basis of their physics, and online selection algorithms must have a level of sophistication comparable to that of off-line reconstruction.

Moreover, the time available to perform this selection is limited. Bunch crossings will occur at a rate of 40 MHz, so that a decision must be taken every 25 ns. This time is too small even to read out all raw data from the detector. The accept/reject decision will be taken in several steps (levels) of increasing refinement, where each one takes a decision using only part of the available data. In this way, higher trigger levels have to process fewer events and have more time available; they can go into finer details and use more refined algorithms.

Due to the strict timing constraints, the first step of the CMS trigger, the Level-1 trigger, is implemented on dedicated programmable hardware. The Level-1 has access to the data from the calorimeters and the muon detectors with coarse granularity; on the basis of this limited information it has to reduce the input rate up to a level acceptable for the Data Acquisition system (DAQ). At startup, the DAQ system will be able to handle an event rate of up to 50 kHz, which will be increased to 100 kHz when the full LHC design luminosity

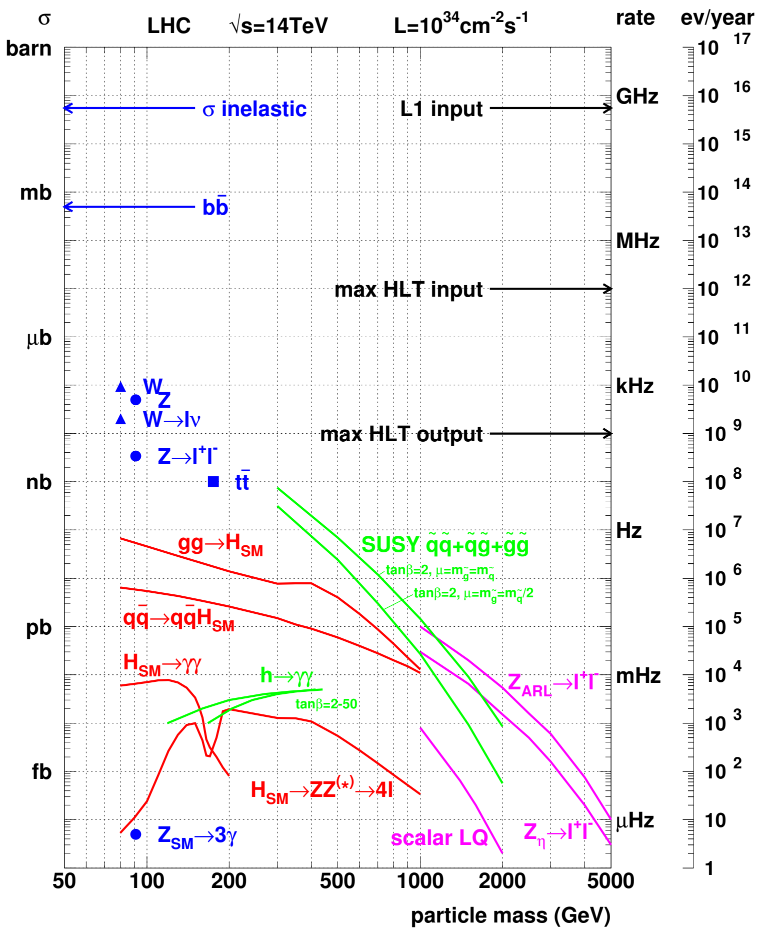

Figure 2.19: *Cross section and event rates at $10^{34} cm^{-2} s^{-1}$ as a function of the mass of produced objects.*

is reached. Only one third of this bandwidth is allocated, the rest being used as safety margin accounting for all uncertainties in the simulation of the basic physics processes. The allocation of this bandwidth among different triggers is discussed in Section 2.6.1.4.

The selected events are passed to the High Level Trigger (HLT), which will be completely implemented on software running on a farm of commercial processors. This allows full flexibility and optimisation of the algorithms. The HLT is further subdivided into logical levels (Level-2, Level-3), although this classification is somewhat arbitrary. The implementation and performance of the muon HLT algorithms is described in Section 5.5.

The following sections briefly describe the design of the Level-1 trigger, with particular focus on the muon trigger. A more detailed discussion can be found elsewhere [41].

2.6.1 The L1 Trigger

The Level-1 trigger is implemented on custom-built programmable hardware. It runs dead-time free and has to take an accept/reject decision for each bunch crossing, i.e. every 25 ns. This is achieved with a synchronous pipelined structure of processing elements, each taking less than 25 ns to complete. At every bunch crossing, each processing element passes its results to the next element and receives a new event to analyse. During this process, the complete detector data are stored in pipeline memories, whose depth is technically limited to 128 bunch crossings. The Level-1 decision is therefore taken after a fixed time of 3.2 μs. This time must include also the transmission time between the detector and the counting room (a cable path of up to 90 m each way) and, in the case of Drift Tube detectors, the electron drift times (up to 400 ns). The time available for calculations can therefore be as low as 1 μs.

The Level-1 trigger system is organised into three major subsystems: the Calorimeter Trigger, the Muon Trigger, and the Global Trigger. The Muon Trigger is further subdivided into three independent subsystems one for each of the three different muon detector systems, DTs, CSCs and RPCs. The results of these three systems are combined by the Global Muon Trigger. A schematic

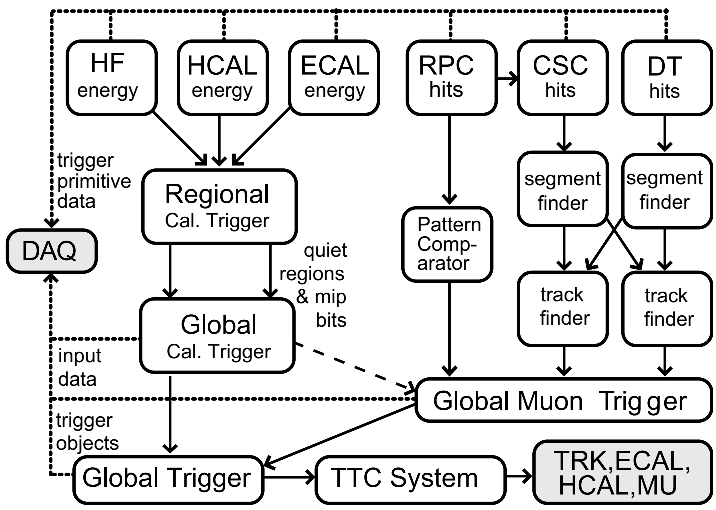

Figure 2.20: *Structure of the Level-1 trigger system.*

view of the components of the Level-1 trigger system and of their relationships is shown in Fig. 2.20.

The Calorimeter and Muon Triggers do not reject or accept events by themselves. They identify "trigger objects" of different types: isolated and non-isolated electrons/photons; forward, central and τ-jets; and muons. The four best candidates of each type are selected and sent to the Global Trigger, together with the measurement of their position, transverse energy or momentum and a quality word. The Global Trigger also receives the total and missing transverse energy measurement from the Calorimeter Trigger.

The Global Trigger selects the events according to programmable trigger conditions, that can include requirements on the presence of several different objects with energies or momenta above predefined thresholds. Topological conditions and correlations between objects can be required as well. Up of 128 of these conditions can be tested in parallel, and each can be pre-scaled to accept only a fraction of selected events.

The Level-1 Calorimeter and Muon Triggers are shortly described in the following. A more detailed discussion is outside the scope of this work, and the interested reader is referred to more specific publications [41].

2.6.1.1 The Level-1 Calorimeter Trigger

The calorimeter trigger identifies five types of objects: isolated electrons/photons, non-isolated electrons/photons, central jets, forward jets and tau jets. The measurement of the transverse energy and position of the four most energetic objects of each type is sent to the Global Trigger, together with a measurement of the total and missing transverse energy. In addition, the calorimeter trigger provides the Muon Trigger information about the activity in all calorimeter regions, to determine if the energy deposit is compatible with the passage of a muon (MIP bit) and if it is below a programmable threshold (Quiet bit).

For trigger purposes, the calorimeters are subdivided in towers with a size of $\Delta\phi \times \Delta\eta = 0.087 \times 0.087$ up to $\eta \sim 2$. At higher pseudorapidity values $\Delta\eta$ increases up to 0.35. Trigger towers match the granularity of HCAL up to $\eta > 1.74$; above that value, physical HCAL towers have twice the ϕ dimension of the trigger tower. In the barrel ECAL, each tower corresponds to 5×5 crystals, while the ECAL endcap crystals are arranged in a $x - y$ geometry, and a variable number of crystals is grouped, matching as much as possible the HCAL trigger tower boundaries. Towers are defined also in the very forward calorimeter, with a size of $\Delta\phi \times \Delta\eta = 0.348 \times 0.5$.

The trigger towers are organised in calorimeter regions, each formed by 4×4 trigger towers, with a size of about $\Delta\phi \times \Delta\eta = 0.35 \times 0.35$. Very forward calorimeter towers constitute a region by themselves, due to their size.

The data of each ECAL and HCAL trigger tower is first processed by the Trigger Primitive Generator, which is integrated in the calorimeter readout electronics. It provides bunch crossing identification based on a peak-finder algorithm, and for each tower calculates the so-called trigger primitives, *i.e.* the sum of the transverse energy and a fine grain bit. The ECAL fine grain bit provides information on the lateral extension of the electromagnetic shower, and is used in the rejection of backgrounds by the electron trigger. The HCAL fine grain bit is used to denote the compatibility of the deposit with the passage of a minimum ionising particle, and is set if the HCAL energy before conversion to the transverse scale is within a programmable range, of the order of [1.5, 2.5] GeV.

The trigger primitives are used by the different calorimeter trigger algorithms described in the following.

Photon and electron trigger. At Level-1, it is not possible to distinguish electrons and photons, which are treated together. Electron/photon candidates are found with a sliding window algorithm on 3×3 towers. Identification is based on the presence of a large energy deposition in one or two adjacent trigger towers. Requirements on the lateral and longitudinal profile of the shower are also set using the ECAL fine grain bit and the ratio of ECAL and HCAL energy deposits, respectively. A candidate is labelled isolated on the basis of the energy deposits and ECAL fine grain bits in the eight towers around the centre of the 3×3 window.

In each calorimeter region, the highest-E_T isolated and non-isolated candidates are found. The Global Calorimeter Trigger sends the four most energetic ones of each type to the Global Trigger.

Jets and τ-jets. The jet trigger uses the sum of the ECAL and HCAL transverse energies in calorimeter regions. Candidates are found with a sliding window algorithm on 3×3 regions, requiring the deposit in the central one to be higher than the deposits in the other eight.

Additionally, τ-jets are identified by their narrow profile. A jet candidate is identified as τ-jet if each of the nine regions of the window contains no more than two towers above a programmable threshold.

Jets are searched for separately in the central region ($|\eta| < 3$) and in the forward region ($3 < |\eta| < 5$), while τ jets are only identified in the central one. The Global Calorimeter Trigger sends the four most energetic candidates of each type to the Global Trigger, together with the number of jets above a programmable threshold.

Total and missing transverse energy. The total energy is obtained by summing the transverse energy of all ECAL and HCAL calorimeter regions. The missing transverse energy is determined from the sum of the E_x and E_y components of the deposit in each region, obtained from the E_T deposits using the coordinates of the centre of the region. The total and the missing energy (absolute value and ϕ direction) are then sent to the Global Trigger.

Quiet and MIP bits. For each calorimeter region a "Quiet" bit is defined if the transverse energy deposit in ECAL plus HCAL is below a programmable threshold. The MIP (Minimum Ionising Particle) bit is set if the quiet bit is set and if the HCAL fine grain bit is set in at least one of the 16 HCAL towers of the region. These two bits can be used by the Global Muon Trigger to select muons.

2.6.1.2 The Level-1 Muon Trigger

The Muon Trigger has the task to identify muons, reconstruct their position and transverse momentum and to provide bunch crossing assignment with high purity and efficiency. It is described in detail in [41]. The most relevant change from what described therein is that the trigger electronics will not be installed in the forward CSC station ME1/1a, thus limiting the Level-1 trigger acceptance to $|\eta| < 2.1$ (see below).

All three detector systems described in Section 2.5 contribute to the muon trigger, which benefits from the complementary characteristics of these systems: the good spatial resolution of drift tubes and cathode strip chambers and the excellent time resolution of resistive plate chambers. The redundancy of the muon system allows a robust trigger with high efficiency and good background rejection. The wire chamber systems and the RPC system are complementary in performance and also in the backgrounds and inefficiencies they are sensitive to. The complementarity can also be used for cross-checks and to improve the understanding of the performance of each system.

The internal structure of the Muon Trigger is shown in Fig. 2.21. In the case of DTs and CSCs, the information of each chamber is first processed independently by a Local Trigger step, where track segments are reconstructed. Segments of the different stations are matched by the DT and CSC Regional Track Finders, which reconstruct muon tracks and estimate their p_T. The candidates found are then delivered to the Global Muon Trigger, with a word to indicate their quality. In the overlap region, DT and CSC segments are used by both Track Finders to allow for reconstruction of full tracks in each of the two subsystems.

In the case of RPCs, the hits are collected by a Pattern Comparator Trigger (PACT), which looks for predefined patterns. The PACT provides an estimate of the p_T of the muon and its position, as well as a word to indicate its quality.

Each subsystem reconstructs up to four muon candidates. These are sent to the Global Muon Trigger that matches them and looks for the MIP and Quiet bits in the corresponding calorimeter regions. Finally, the four muons with highest p_T are sent to the Global Trigger. The track reconstruction in the different subsystems is shortly described in the following.

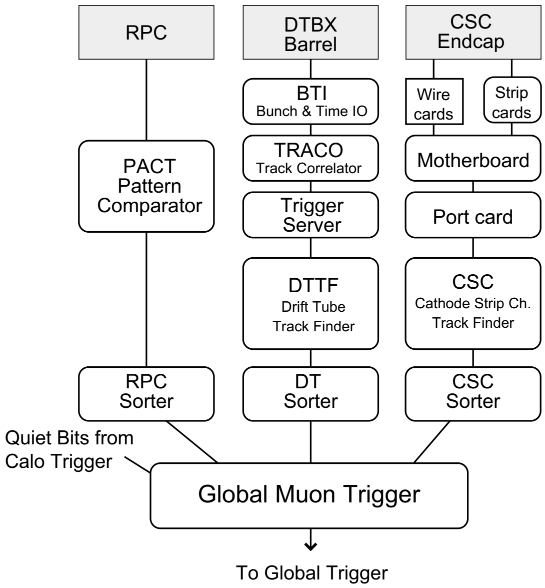

Figure 2.21: *Schematic structure of the muon trigger system.*

The DT Trigger. The DT trigger [42] front-end is called Bunch and Track Identifier (BTI). It is directly connected to the read-out electronics, and performs a straight segment fit within a superlayer using at least three hits out of the four layers of drift cells. The fit is done with a generalisation of the mean-timer technique [40], which also returns the unknown bunch crossing originating the segment. In r-z superlayers, only segments pointing to the interaction point are selected. The segments reconstructed in the two r-ϕ superlayers in each chamber are matched by the Track Correlator (TRACO), that improves the angular resolution thanks to the bigger lever arm. The Trigger Server (TS) selects, among all segment pairs in a chamber, the two corresponding to the highest p_T, and forwards them to the Drift Tube Track Finder (DTTF).

The DTTF matches the segments reconstructed in the four stations into a single muon track candidate, assigning the track parameters p_T, η, ϕ and a quality word. This device is based on pre-computed, memory-resident Look-Up Tables (LUT), which are used to extrapolate the segments between stations and to group matching segments. The track parameters are estimated with other LUTs on the basis of the the ϕ direction of the segments in the two innermost stations.

Finally, the candidates are sorted, and the four highest p_T muon candidates are delivered to the Global Muon Trigger.

The CSC Trigger. As for the barrel, the first trigger step in the endcaps is the local reconstruction. The CSC Local Trigger reconstructs segments independently using the strips and the wires of the six layers of each chamber. Cathode strips are used to reconstruct the ϕ coordinate and measure the transverse momentum of the track. First, the strips are digitised with half strip resolution, using a simple interpolation based on a comparator that analyses the charge in three adjacent strips. The hits in the six layers are then searched for patterns compatible with high-p_T tracks.

Anode wires are used to reconstruct the η coordinate and to provide a precise bunch crossing assignment. Wires are read out in groups of 5 to 16, to reduce the number of channels. Hit patterns compatible with a track coming from the nominal interaction point are searched for with a coincidence technique. A coincidence of two hits in different layers is needed to assign the bunch crossing, while the reconstruction of a segment requires four hits out of the six CSC planes.

Finally, the time coincidence of anode and cathode segments is required to construct three-dimensional segments. They are sent to the CSC Track Finder, which links the segments of the various stations to form a muon candidate and assigns p_T, η, ϕ and a quality word, using LUTs as in the case of the DTs.

The CSC system covers the region up to $|\eta| = 2.4$. However, the trigger electronics will not be installed in the region above $|\eta| = 2.1$ in the chamber ME1/1, effectively limiting the muon trigger geometrical acceptance to $|\eta| < 2.1$.

The RPC Trigger. No local reconstruction step is present in the RPC trigger [41], since the measurements in each chamber are simple points. The hits are collected by the Pattern Comparator Trigger (PACT), which looks for hits correlated in space and time in the four RPC stations. Hits are matched with pre-defined patterns in a large look-up table to provide identification and estimate of the p_T. The patterns allow identification of muons with at least three hits on four stations. In the case of the barrel, where six stations are present, the search is done independently for low-p_T muons in the first four layers (in MB1 and MB2) and for high-p_T ones using one layer in each station.

A ghost suppression algorithm is applied to reduce the effect of accidental coincidences due to background hits. The four highest p_T candidates in the barrel and endcaps are then separately sent to the Global Muon Trigger.

The Global Muon Trigger. The task of the Global Muon Trigger (GMT) is to match the muon candidates from the different subsystems and combine their parameters in an optimal way. The matching is done by comparing the spatial coordinates of the segment (ϕ, η), and can be tuned to achieve the optimal balance between efficiency and background suppression. High efficiency can be obtained accepting candidates even if they are found by only one subsystem. Maximum background rejection can be obtained requiring all candidates to be reconstructed by both subsystems. The price is a lower efficiency. More refined criteria can be used; in the current implementation, candidates are accepted if they are reconstructed by two systems, otherwise they are selected on the basis of their quality word. Low-quality candidates from problematic η regions are discarded [43]. If two candidates are matched, the parameters of the track are chosen according to a programmable logic.

The GMT also assigns each candidate the MIP and Quiet bit of the corresponding calorimeter region (cf. Section 2.6.1.1). These bits can optionally be used to confirm the muon candidate and require that it is isolated.

2.6.1.3 Performance of the Level-1 Muon Trigger Selection

The simplest possible Level-1 muon trigger selection is based on a threshold on the p_T of GMT tracks. The Level-1 p_T scale is defined at 90% efficiency, that is the scale where, for each given threshold, the efficiency for muons with a p_T equal to the threshold is 90% of the plateau efficiency. In other words, the p_T value reported by the trigger is such that there is only a 10% probability for the true value to be actually higher.

The resolution of the reciprocal of the transverse momentum, $1/p_T$, is shown in Fig. 2.22. The distributions are shifted with respect to zero due to the 90% scale definition. The resolution is about 17% in the barrel, 20% in the

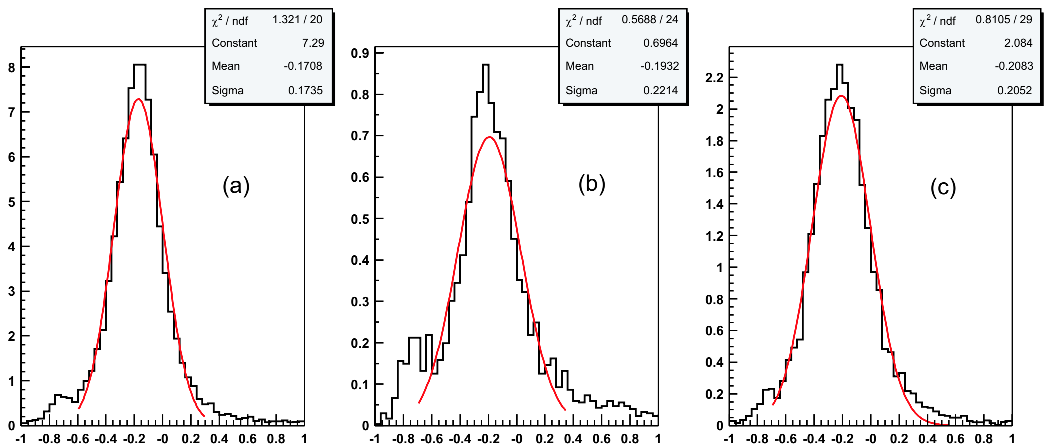

Figure 2.22: *Level-1 resolution on $1/p_T$ obtained with a sample of W decays at high luminosity for (a) the barrel region ($|\eta| < 0.8$); (b) the overlap region ($0.8 < |\eta| < 1.2$); (c) the endcap region ($1.2 < |\eta| < 2.1$) [44].*

endcaps and 22% in the overlap region. Non-Gaussian tails are present and, together with the limited resolution, are responsible for the "feed-through" of low p_T muons that are reconstructed at high momenta, thus passing typical trigger thresholds. This effect is important since the muon rate increases steeply for low p_T values, so that the contribution of feed-through muons to the Level-1 trigger rate is dominant even for high thresholds. This effect is visible in Fig. 2.23, where the spectrum of the generated p_T of muons passing a threshold of 14 GeV/c at low luminosity, and of 25 GeV/c at high luminosity, is shown.

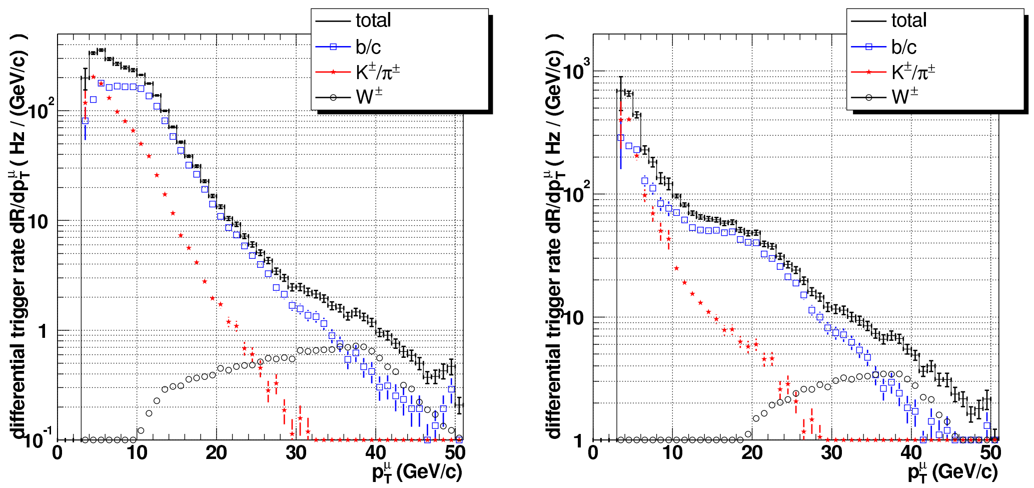

Figure 2.23: *Event rates as a function of the generated p_T for a Level-1 threshold of 14 GeV/c^2 at low luminosity (left) and of 25 GeV/c^2 at high luminosity (right). The separate contributions of b/c, K/π and W decays are shown [43].*

This feed-through effect can be reduced only by improving the p_T resolution. This is the task of the Muon High Level triggers. The event rate corresponding to the selection of one or two muons at each trigger level (single- and di-muon selection) is discussed in Section 5.5.3.

2.6.1.4 The Level-1 Trigger Table

The Level-1 trigger allows definition of complex trigger algorithms based on the presence of several, different objects and on topological conditions and correlations. However, whenever possible, "inclusive" criteria should be used, to avoid biasing the sample of selected events. The simplest triggers are in general those based on the presence of one object with an E_T or p_T above a predefined threshold (single-object triggers) and those based on the presence of two objects of the same type (di-object triggers) with either symmetric or asymmetric thresholds. Other requirements are those for multiple objects of the same or different types ("mixed" and multiple-object triggers). In the case of special channels that are not efficiently selected by these simple criteria, very specific exclusive algorithms can be used. These cases are not discussed in the following.

The allocation of the Level-1 bandwidth to the different trigger streams is discussed in [44]. The choice of the Level-1 trigger thresholds is determined by the maximum event rate (bandwidth) that can be accepted by the DAQ system. The current estimate is that at startup the DAQ system will be able to handle an event rate of up to 50 kHz, which will be increased to 100 kHz when the full LHC design luminosity is reached. Only one third of this bandwidth is allocated, the rest being used as safety margin accounting for all uncertainties in the simulation of the basic physics processes, the CMS detector, and the beam conditions [44]. This bandwidth is then subdivided among the Level-1 objects described in the previous sections (muons, electrons and photons, tau jets, jets and combined channels) and for each of them between the single- and multiple-object streams.

The result is a set of thresholds called trigger table. The present Level-1 trigger tables at low and high luminosity are shown in Table 2.4 and Table 2.5, respectively.

Table 2.4: *L1 trigger table at low luminosity [44].*

Trigger	Threshold (GeV or GeV/c)	Rate (kHz)	Cumulative Rate (kHz)
Inclusive isolated electron/photon	29	3.3	3.3
Di-electrons/di-photons	17	1.3	4.3
Inclusive muon	14	2.7	7.0
Di-muons	3	0.9	7.9
Single tau-jet trigger	86	2.2	10.1
Two tau-jets	59	1.0	10.9
1-jet, 3-jets, 4-jets	177, 86, 70	3.0	12.5
Jet * ET miss	88 * 46	2.3	14.3
Electron * Jet	21 * 45	0.8	15.1
Minimum-bias (calibration)		0.9	16.0
Total			16.0

Table 2.5: *L1 trigger table at high luminosity [44].*

Trigger	Threshold (GeV or GeV/c)	Rate (kHz)	Cumulative Rate (kHz)
Inclusive isolated electron/photon	34	6.5	6.5
Di-electrons/di-photons	19	3.3	9.4
Inclusive muon	20	6.2	15.6
Di-muons	5	1.7	17.3
Single tau-jet trigger	101	5.3	22.6
Two tau-jets	67	3.6	25.0
1-jet, 3-jets, 4-jets	250, 110, 95	3.0	26.7
Jet * ET miss	113 * 70	4.5	30.4
Electron * Jet	25 * 52	1.3	31.7
Muon * Jet	15 * 40	0.8	32.5
Minimum-bias (calibration)		1.0	33.5
Total			33.5

Chapter 3

Simulation of the DT Response

Many interesting LHC processes result in a final state containing muons with high transverse momenta. A reliable reconstruction of such events requires a deep understanding of their signature in the apparatus. For this reason an accurate simulation of the response of all CMS sub-detectors is needed. This Chapter presents the procedure developed for the simulation of the Drift Tubes [1].

The output of the simulation should be as close as possible to the real detector response. In the case of the DT detectors the output is a TDC measurement, containing the drift time information. The working principle of a Drift Tube cell is presented in Section 3.1.

The first step of the simulation of the DT response is the propagation of the simulated particles through the detector (described in Section 3.2), accounting for the interaction with material (multiple scattering, energy loss and production of secondary particles) and the bending of the track due to the magnetic field. This step is carried on using the GEANT4 [45] program, which takes into account the geometry and material of the detector and simulates the physics processes that occur as particles cross each volume. During this phase, the information about the passage of a track through the sensitive volume of the chamber is recorded in the "simulated hits"[1].

The information contained in the hits is then fed to a parametrisation of the cell response (described in Section 3.3) to simulate its behaviour. This last step, described in Section 3.4, is the so called *digitisation* and consists in the computation of the drift time of the electrons produced by ionisation of the crossing particle and of any additional delays. The output is stored in the so-called "digis".

[1] The information contained in a simulated hit is: the ID [29] of the particle which generated the hit; the process which generated the particle; the entry and exit points of the simulated particle crossing the gas volume; the position defined as the mid-point of the hit track; the time-of-flight from the interaction point to the hit position; the momentum, calculated at the entry point, of the track that produced the hit and the energy loss in the volume.

A comparison of the DT simulation with respect to the data taken at the October 2004 test beam is presented in Section 3.5.

3.1 Working Principle of Drift Tube Cells

The CMS drift chambers rely on the detection of the ionisation electrons produced in the Ar/CO_2 gas mixture by a particle crossing the cell. The drift time of electrons in the electrostatic field is measured and used to determine the spatial coordinates of the ionising event.

The cell design is shown in Fig. 2.14. A minimum ionising particle produces on average about 100 electrons in the cell volume. The electrons drift in the electrostatic field generated by the central anode wire, maintained at a positive potential, and the cathode strips glued on the I-beam profile, which have negative potential. The electric field is shaped in order to have a linear space-time relationship over the entire volume; this is achieved with the positively-biased strips glued at the centre of the aluminium planes delimiting the cell volume.

The ionisation electrons are eventually collected by the anode wire where a strong local electric field, increasing as $1/r$, accelerates them enough to produce secondary ionisation and hence an avalanche. A gain of about 10^5 is achieved. The CO_2 gas acts as a quencher: thanks to its large photo-absorption cross section it absorbs the majority of the photons produced during the avalanche development, keeping the avalanche region limited.

The induced signal on the anode is amplified and discriminated against a configurable threshold by the front-end electronics and it is sent to the read-out electronics for the TDC measurement.

Electrons produced at a time t_0 by the incoming particle migrate towards the anode with velocity v_d and reach the anode at the time t_1. The distance of the track with respect to the anode wire is therefore given by:

$$x = \int_{t_0}^{t_1} v_d \cdot dt; \tag{3.1}$$

which, considering a constant drift velocity, becomes:

$$x = (t_1 - t_0)v_d. \tag{3.2}$$

The CMS DTs do not need any external device to determine the time pedestal (t_0). In the trigger the on-chamber electronics (Section 2.6.1.2) uses the measurements in three consecutive staggered layers to recognise aligned hits and determine the bunch crossing in which the muon was produced. An extension of the meantimer technique [40], without the knowledge of the t_0 offset, is used. In the reconstruction, the fine calibration of the time pedestal is extracted directly by the measurement distribution with the procedure described in [46].

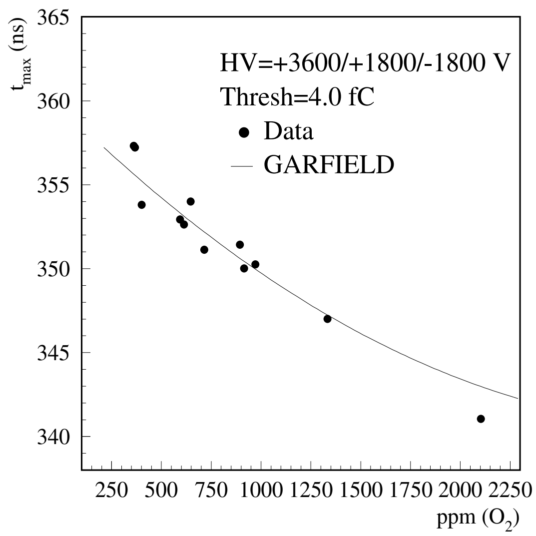

Figure 3.1: *Maximum drift time versus oxygen concentration [47].*

The major factors which can influence the drift velocity are:

- the strength and direction of the electric field and the gas pressure. To limit the dependence from these factors, the working point is chosen to have a E/p value corresponding to a saturated drift velocity: in the gas mixture used for the CMS DTs the drift velocity saturates for fields of about 1.9 kV/cm. The cell is therefore designed to avoid regions of field lower than this value;

- the gas composition and temperature. The pressure, temperature and purity of the mixture are continuously monitored. In particular the oxygen concentration (cf. Fig. 3.1) is always kept below 500 ppm;

- the presence of external factors like magnetic stray fields. The presence of a magnetic field modifies the drift properties of an electrons swarm. The Lorentz force applied to each of the moving charges transforms the trajectory into a curved path. In case of a homogeneous magnetic field along the wire, the main consequence is a lower effective drift velocity, as the movement of the swarm happens along a trajectory different from the electric field line, as shown in Fig. 3.2.

The spatial resolution of a drift chamber is limited by the diffusion of the ionisation electrons during the drift, the fluctuations of the the primary ionisation processes and by the knowledge of the space-time relationship. The cell resolution of the CMS DT chambers is about 180 μm.

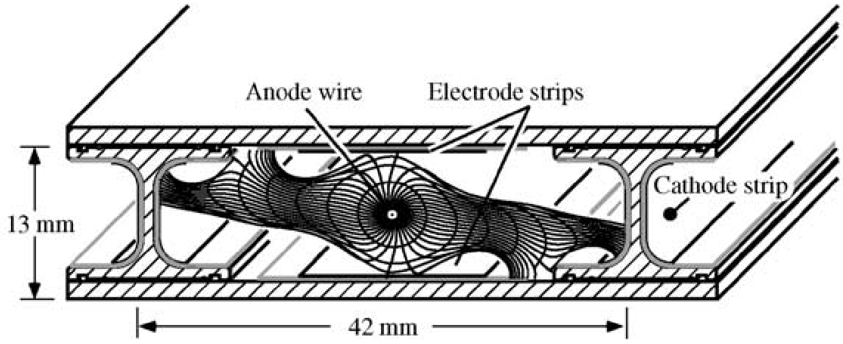

Figure 3.2: *Simulation of the effect produced on the drift lines by a 0.5 T magnetic field parallel to the wire.*

3.2 Particles Interaction with Detector Material

The interaction of crossing particles with the detector material, in the DTs as in all CMS sub-detectors, is simulated with GEANT4. This software uses a detailed description of the geometry and material of the apparatus to propagate particles through the detector. The tracking is performed in steps and, at each step, GEANT employs Monte Carlo techniques to simulate interaction processes and compute the effects on the simulated track. In this way the effect of the multiple scattering, the energy loss in the material and the bending due to the magnetic field are simulated at each step. In particular the energy loss is simulated continuously up to a configurable threshold (expressed in path length [45]) and, above it, by the explicit production of secondary particles like delta-rays and shower activities.

In the following the relevant processes involved in the simulation of the DT chamber response are analysed. For this purpose a sample of 20000 muons of both charges, with a flat momentum distribution between 10 GeV/c and 100 GeV/c was generated. The muons were required to be within the acceptance of the DT subsystem ($|\eta| < 1.2$).

The composition of the hits simulated by GEANT in the DTs is summarised in Fig. 3.3 which shows the number of hits per particle type for the various simulated processes. Only 56% of the hits is originated by a primary muon crossing the detector. The rest mainly comes from electrons, which contribute for the 39.7%, while the positrons represent only 4.2% of the total. There is also a very small contribution from hadronic hits (about 0.004%) which is not reported in the plot.

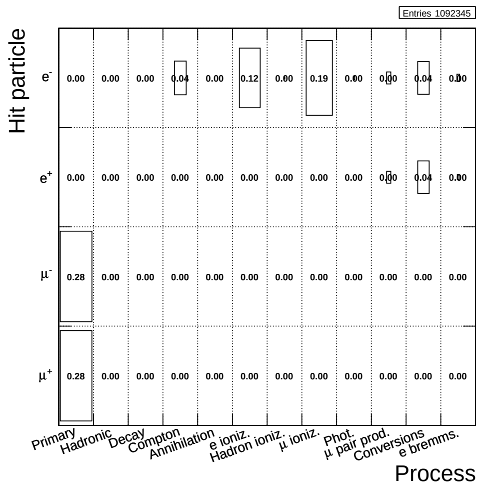

Figure 3.3: *Relative weight of the different particles and processes for the* GEANT *hits in the DT gas volume for a simulated sample of 20000 muons with* p_T *between 10 and 100 GeV/c.*

The large number of electron hits is mainly produced by the primary ionisation due to muons crossing the chamber material (48.4% of the electron hits), but also the secondary ionisation, produced by electrons, plays an important role, contributing to 30.6% of the e^- hits. Most of the positrons are originated by conversion processes in the aluminium.

The population of delta-rays can be ideally divided into two classes: electrons produced in the gas volume and electrons produced in the aluminium. The plots in Fig. 3.4 show the momentum (left plot) and the path (right plot) of the hits generated by the two families. The electrons produced in the gas present a softer momentum spectrum with respect to those produced in the aluminium and, as a consequence, their path in the gas volume is much shorter. Most of them stop in the sensitive volume. Only 6.0% of those electrons travels more than 200 μm, *i.e.* about the cell resolution, along the drift lines of the cell. On the contrary 88.7% of the electrons produced in the aluminium plates crosses the whole cell.

3.3 Modeling of the Drift Cell Response

Although the shaping of the drift field in the DT cell was designed to maintain a linear relationship between drift-time and distance, residual non-linear effects are present, especially in the region closest to the anode. For this reason a precise modeling of the cell response can not be obtained using a constant drift velocity. Moreover, the spatial distribution of the electrons produced by

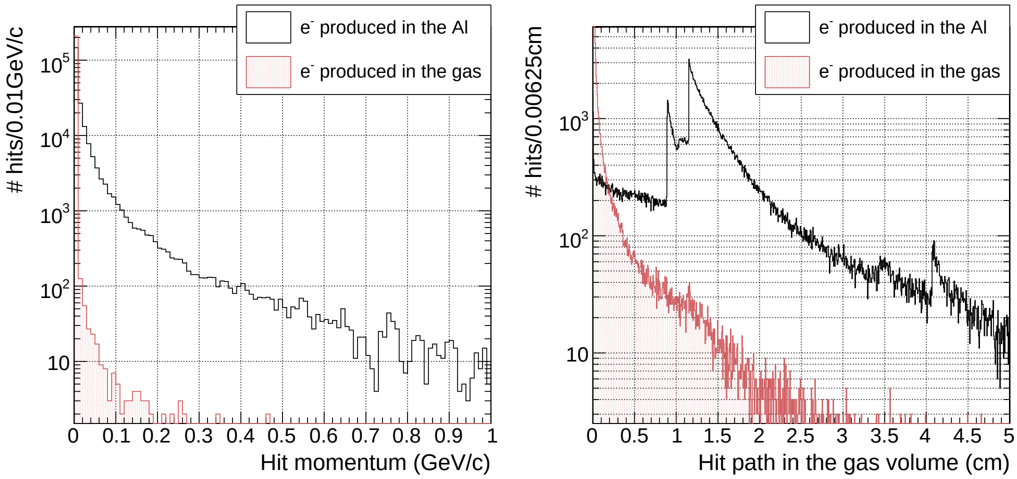

Figure 3.4: *Momentum (left) and path in the gas volume (right) for electron hits produced in the gas and in the aluminium. The peaks in the path of the* e^- *produced in the aluminium are due to particles transversing the cell vertically (peak at* $\sim$ *1.2 cm and* $\sim$ *0.9 cm, the latter in correspondence of the I-beam profiles) and horizontally (peak at* $\sim$ *4.2).*

ionisation depends on the track parameters, like the impact angle, which have direct impact on the measured time. The cell parametrisation must take into account these aspects and the effect of the residual magnetic field in the gas volume, which can modify the drift paths of electrons.

The parametrisation described in the two following sections has been integrated in the framework of the official simulation of the DT detector in order to simulate the response of the drift tube cell (Section 3.4).

3.3.1 Simulation and Parametrisation of the Cell Response

GEANT can not simulate the electric field, therefore to model the cell response as a function of the relevant parameters, a simulation using GARFIELD [48] and HEED [49] was performed. The result is a model which can be used in the CMS Drift Tube simulation [50].

GARFIELD is a software for detailed simulation of gas detectors. Given the description of the cell geometry, the configuration of the electrostatic field and the magnetic field in the gas volume it can simulate the response of the cell to ionising particles. The electrons produced in the gas are followed along their path towards the anode wire taking into account diffusion, avalanche development and signal induction.

The transverse cross section of the cell (cf. Section 2.5.1) was introduced describing the geometry of the I-beams and the plates with the strips and the cathodes voltages set to 1800 V and -1200 V respectively, while the anode wire was defined with a voltage of 3600 V.

The properties of the 85% Ar / 15% CO_2 gas mixture were simulated using HEED. This software can compute the energy loss by ionisation, of the particles which pass through the gas volume, the number of primary and secondary generated electrons, the diffusion coefficients and the cluster size. The ejection of electrons from atoms due to the passage of a charged particle is also considered in the simulation. When the energy of these electrons is large enough to cause further ionisation (giving rise to delta-rays) the simulation of the ionisation process is carried on, otherwise the electrons are simply drifted through the gas[2]. HEED considers the emission of Auger electrons and fluorescence photons from the excited atoms. The simulation also takes into account the external parameters which can influence the drift properties of the gas, namely the pressure, the temperature and the magnetic field.

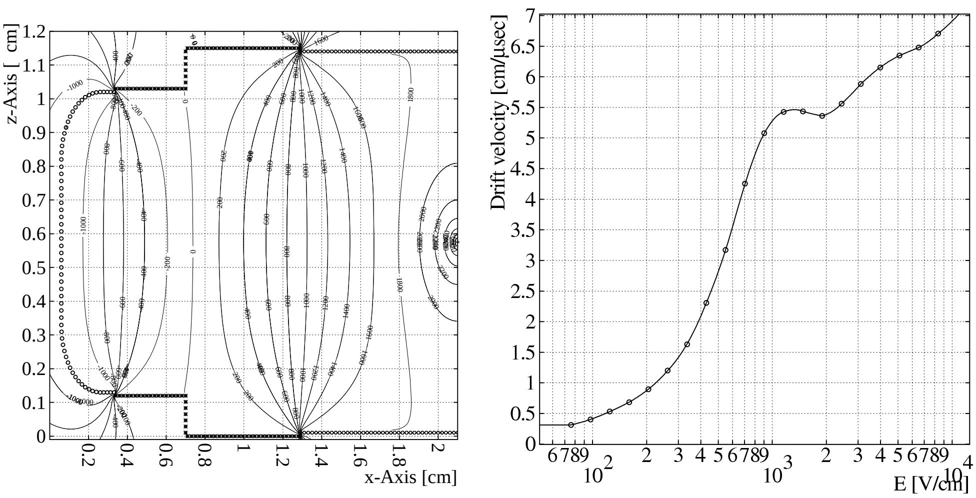

Figure 3.5: *Equipotential lines in the semi-cell (left) and drift velocity of electrons as a function of the electric field (right) computed by* GARFIELD *for the 85% Ar / 15% CO_2 gas mixture at a temperature of 293 K and a pressure of 1 atm [50].*

Figure 3.5 shows the electric potential within the cell volume. The predicted drift velocity is also shown for different values of the electric field. At the nominal field, which is around 1.9 kV/cm, the drift velocity is stable and

[2] In order to avoid double counting, the delta-rays generated in the gas volume by the GEANT simulation are ignored in the digitisation procedure as the parametrisation based on the GARFIELD simulation already accounts statistically for their production (cf. Section 3.3.2).

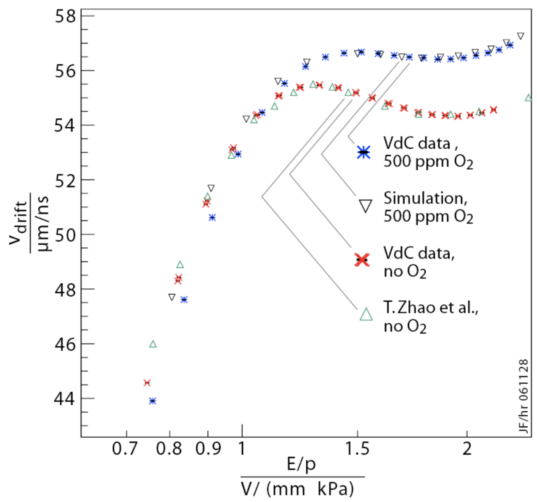

Figure 3.6: *Measured and calculated drift velocities as functions of electric field and gas pressure for a pure gas mixture 85% Ar / 15% CO_2 and for a gas mixture with air impurities corresponding to 500 ppm O_2. The measurements were obtained with the VdC, a dedicated reference drift chamber that is used for drift-velocity monitoring during CMS running. For comparison, results of measurements [53] for a pure gas mixture, and a simulation for a mixture with impurities are also shown.*

saturates around 54 μm/ns (Fig. 3.6), in agreement with experimental measurements [51, 52].

In order to build the parametrisation of the cell, muons of 100 GeV/c were used. The cell (Fig. 3.7) was divided along the x coordinate in regions of 0.2 mm length and for each of them 500 muons were simulated. The arrival time of the drift electrons depends on the magnetic field along the wire (B_{wire}), the magnetic field perpendicular to the cell (B_{norm}) and the impact angle of the muon (α). The simulation was repeated for 275 combinations of the values of these variables (Table 3.1).

GARFIELD can simulate the signal induced on the wire, otherwise a simplified approach consists considering the arrival time of the n^{th} drift electron on the wire. This approximation was adopted and, after a comparison with the experimental data, the time corresponding to the arrival time of the 5^{th} electron was chosen [50].

The peak value of the arrival time distributions as a function of the position along the cell (*e.g.* Fig. 3.8) was used to estimate the average drift velocity in each configuration. These time distributions are asymmetric and their width is due to diffusion, non-linearities and delta-rays emission. In order to take into account this asymmetry, the distibutions were fitted with two half gaussians.

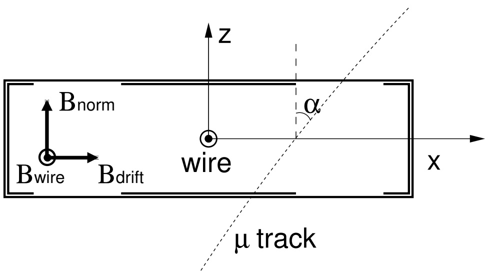

Figure 3.7: *Schematic view of the cell section illustrating the coordinate system and definition of the components of the magnetic field used by the* GARFIELD *parametrisation.*

Table 3.1: *Values of the B field components parallel and perpendicular to the wire and of the impact angle used in the* GARFIELD *simulation [50].*

B_{norm} (T)	B_{wire} (T)	α (degrees)
0	0	0
0.1	0.05	±5
0.2	0.1	±10
0.35	0.2	±15
0.75	0.4	±30
		±45

The fitted values of the maximum and of both the widths were recorded for each step.

A linear fit of these values was performed in the central part of the cell (from 2.5 mm to 19 mm from the wire), which is less influenced by non-linearities originated by the magnetic field. Once the parameters of the linear fit were calculated, the deviations from a linear space-time relationship were estimated using:

$$\Delta t = t_{sim}(x) - \left(\frac{x}{v_d} + b\right) \tag{3.3}$$

where v_d and b are the parameters of the linear fit and t_{sim} is the peak value of the arrival time distribution. An example of the non-linearities obtained for different values of the impact angle and of the two components of the magnetic field is shown in Fig. 3.9. The deviation affects mainly the regions close to the anode wire and the cathode and is directly related to the track angle. The field parallel to the wire has an important impact on the non-linearity while the effect of B_{norm} is almost negligible.

For each configuration of angle and magnetic field, a polynomial fit was per-

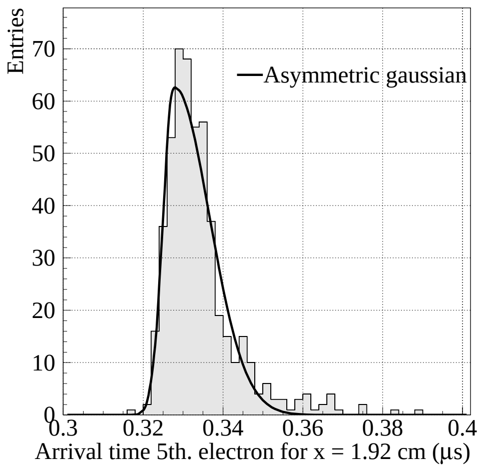

Figure 3.8: *Arrival time distribution of the* 5^{th} *electron on the wire, for 500 muons crossing the cell at an angle of 30 degrees, at a distance of 1.92 cm from the wire and in a magnetic field* $B_{wire} = 0.4$ *T. The distribution is fitted with a double Gaussian [50].*

formed to the distribution of deviations from linearity. The fit was done for the values $\Delta t(x)$, the widths at both sides of the peak, called $\sigma_p(x)$ (towards greater drift times) and $\sigma_m(x)$ (towards lower times), and for the inverse function $x(t)$, which provides linearity deviations on the position corresponding to a given drift time.

The complete set of functions was then used to implement a parametrisation which models the drift-time distributions analogous to the one in Fig. 3.8, thus allowing to produce them statistically for each simulated track. Given the position of the hit along the cell (defined on the cell mid plane), the impact angle of the track α, and the two components of the magnetic field B_{wire} and B_{norm}, this function performs a multidimensional linear interpolation returning the estimated average drift-time and the two widths. An example of the output of the parametrisation function is given in Fig. 3.10, where the drift time and the two widths are reported for several values of the position within the cell, impact angle and magnetic field.

The plots in Fig. 3.11 show the drift-time distributions obtained for various values of the input parameters, simulating tracks uniformly distributed along the cell. This distribution, usually referred as “time box” for the particular shape, reflects both the effect of the cell non linearities in the deviation from a flat behaviour, and the effect of the average drift velocity which determines the width. The peak at small times is due to the field close to the anode, where the drift of electrons is far from being linear.

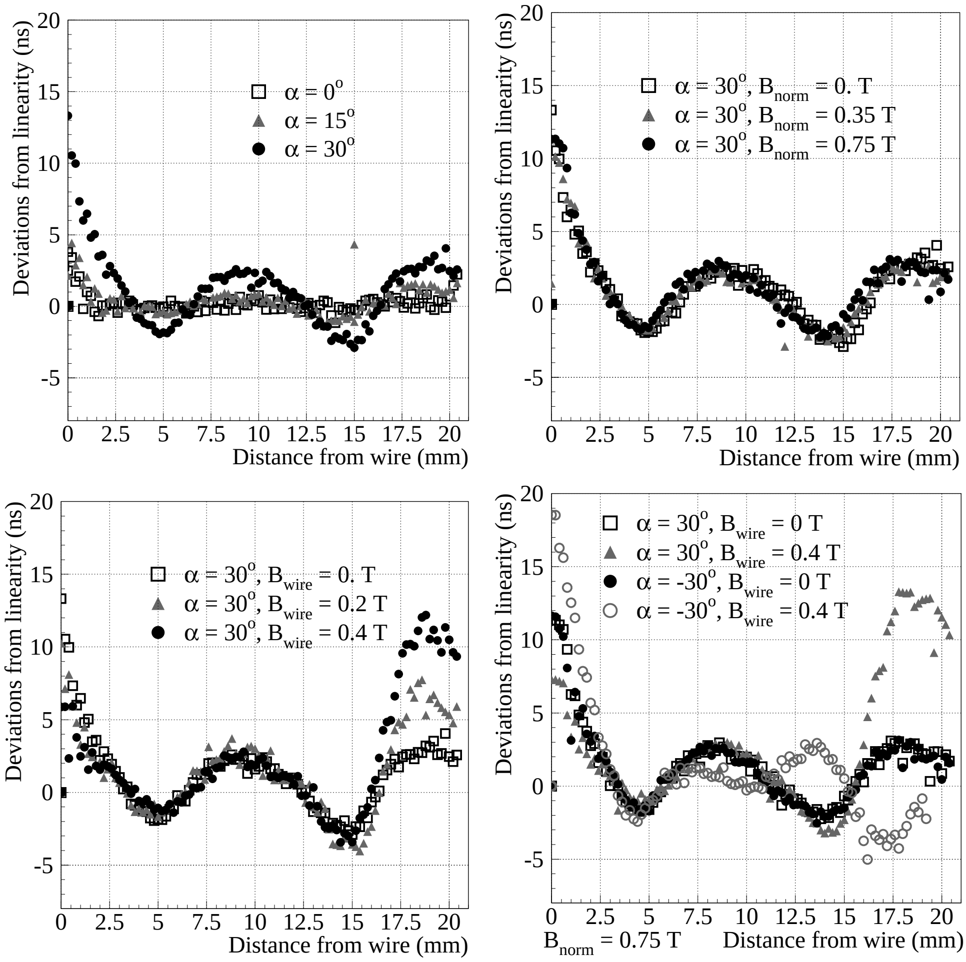

Figure 3.9: *Local deviations from the linearity of the time-space relation for different angles with no magnetic field (upper, left), different B_{norm} and B_{wire} values at 30° (upper right and lower left) and comparison among positive and negative angles for different B_{wire} values (lower, right). The asymmetry between positive and negative angles is clearly observed in the presence of B_{wire} [50].*

3.3.2 Treatment of Secondaries and Hits not Handled by the Parametrisation

The GARFIELD simulation was performed only for particles crossing the whole cell or one corner, *i.e.* entering and exiting from two adjacent surfaces. For this reason not all the GEANT particles traversing the cell can be treated by the parametrisation: tracks which cross the cell with a different topology can not be handled. In particular, the parametrisation does not handle the response of secondary particles produced in the aluminium which stop in the gas, while the

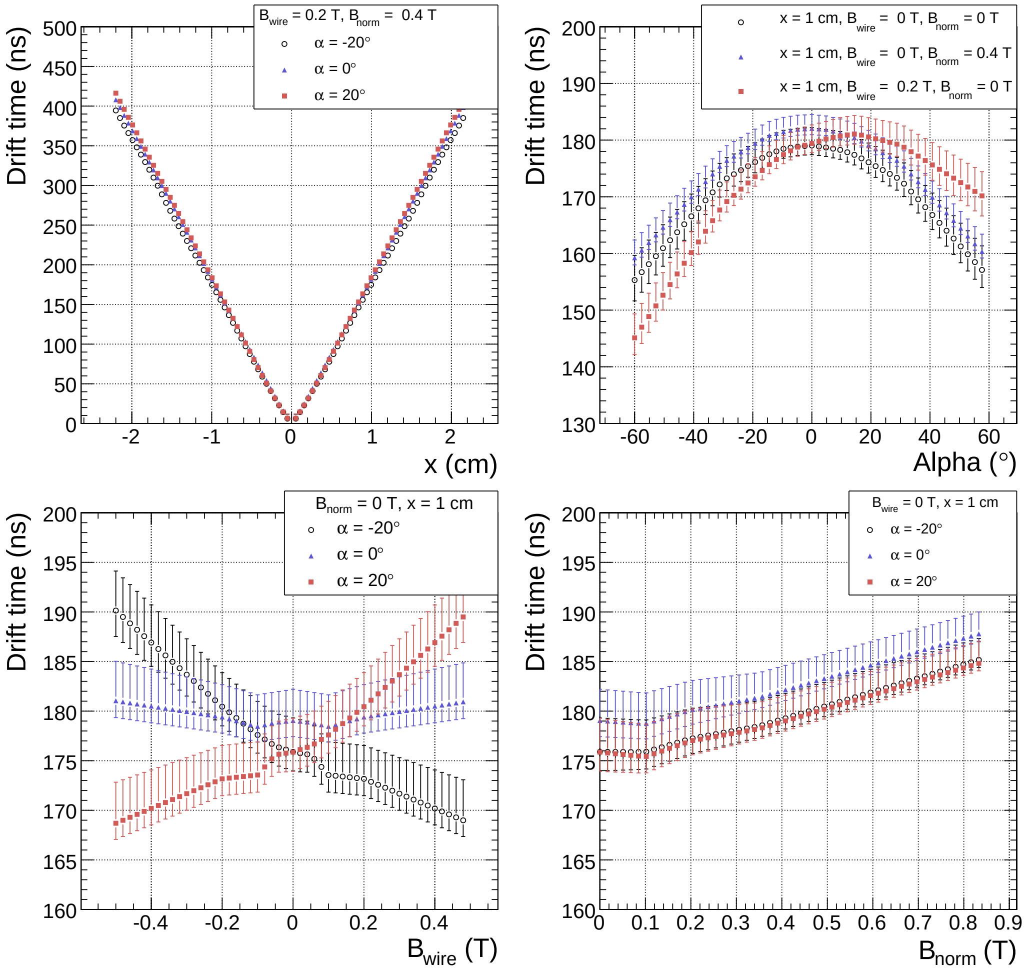

Figure 3.10: *Response of the parametrisation function for several values of the input parameters. The drift time is plotted as a function of the distance from the wire (left, top), of the impact angle (right, top) and of the two components of the magnetic field* B_{wire} *(left, bottom) and* B_{norm} *(right, bottom). The error bars associated to each point correspond to the two widths* σ_p *and* σ_m *of the drift-time distribution.*

energetic secondaries crossing the whole cell (e.g. e^+e^- from pair production and delta-rays) are treated the same way as muons.

The soft delta-rays produced in the sensitive volume are accounted for in the parametrisation, as they were generated by GARFIELD and their effect is already statistically included in the parametrisation. Therefore, the soft delta-rays have to be studied as a third separate set of secondaries.

Table 3.2 reports the relative composition of these three families of hits classified by the particle which generated the hit.

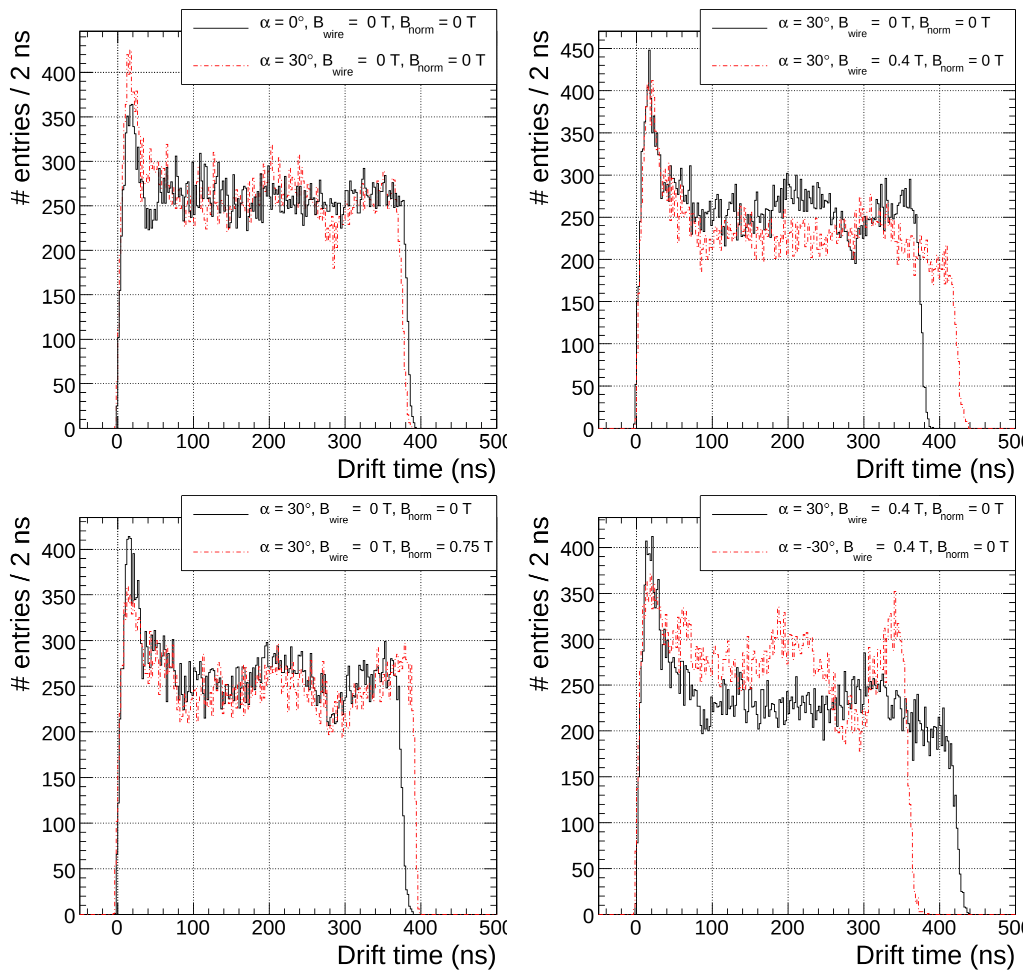

Figure 3.11: *Distributions of the drift-times obtained with the* GARFIELD *parametrisation shooting muons uniformly along the cell with different values of the impact angle and of the magnetic field.*

Secondaries produced in the gas. The effect of this kind of secondaries is already accounted in the GARFIELD simulation which explicitly generates and propagates these particles within the gas volume. As a consequence they directly contribute to the width of the arrival time distributions of the drift electrons considered in the parametrisation.

The processes involved in the production of these soft secondaries, which represent 19% of the total number of the GEANT hits, are shown in the left plot of Fig. 3.12. Almost 99% of those hits is produced by electrons generated in primary and secondary ionisation.

The path and the momentum distribution of these soft delta-rays have already been discussed in Section 3.2. Most of them, around 89%, travel less

Table 3.2: *Fraction of* GEANT *hits which can be handled by the parametrisation, soft electrons produced in the gas and therefore already considered statistically in the* GARFIELD *simulation and other hits which can not be treated by the parametrisation. The relative contribution of the electron, positron and muon hits is also reported.*

	Parametrised	Soft delt-rays	Not parametrised
e^-	16.19%	19.12%	4.36%
e^+	3.72%	0.02%	0.49%
μ	53.97%	–	2.14%
Sub-total	73.87%	19.14%	6.99%

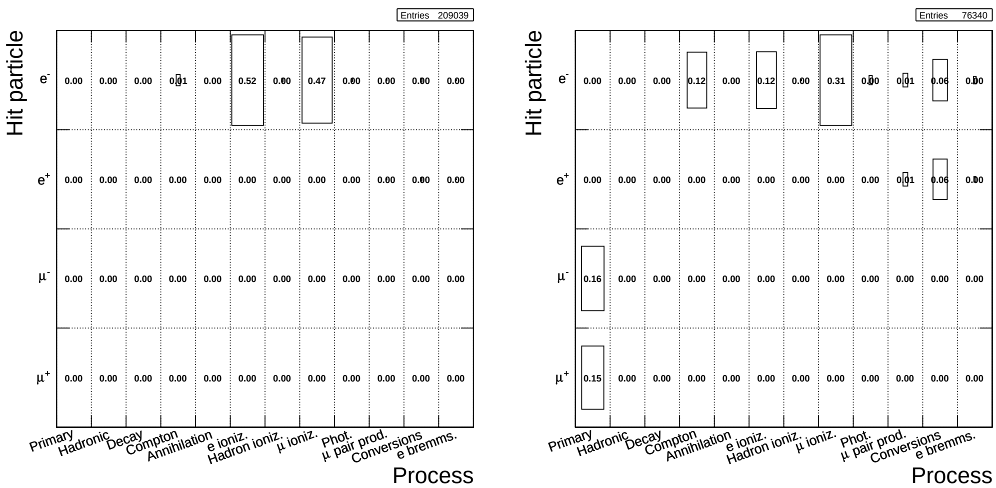

Figure 3.12: *Particle type versus generation process for the soft delta-rays produced in the gas (left) and the hits which can not be handled by the parametrisation (right).*

than 200 μm (see Fig. 3.4) which is a distance comparable with the resolution of the DT cell, therefore accounting for them only statistically does not affect the cell simulation. The distribution of their position along the measurement direction is shown in Fig. 3.13. As it depends only by the gas volume, the effect of this kind of secondaries is to smear the drift time of the primary electrons, accordingly to the parametrisation assumption.

Hits not treated by the parametrisation. The particles which cross the cell with a topology which was not simulated by GARFIELD can not be treated by the parametrisation and are discarded. This is the case of:

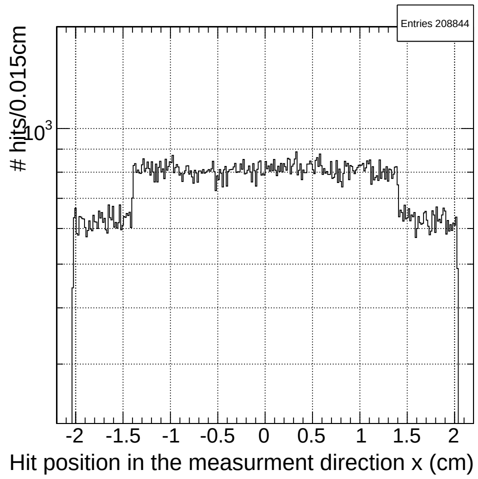

Figure 3.13: *Position within the cell, along the measurement direction, of the electron hits produced in the gas. The steps at the two sides of the cell correspond to the smallest gas volume available because of the I-beam profile.*

- secondary particles produced in the aluminium which do not have enough energy to cross the whole gas layer;
- particles which, due to the bending induced by the magnetic field, enter and exit the gas volume from the same surface;
- particles crossing the cell transversally from I-beam to I-beam;
- particles crossing the cell with a large impact angle, such that their position extrapolated to the mid plane of the cell is outside the cell volume;
- particles which enter or exit the gas volume from the surfaces delimiting the tube length.

Considering a reference sample of muons with transverse momentum between 10 and 100 GeV/c, the hits which can not be digitised account for almost 7% of the total population. Their composition and the relative importance of the various processes are shown in the right plot of Fig. 3.12.

The electrons represent 62.4% of the discarded hits; most of them are delta-rays while the other relevant processes are the Compton scattering and the conversion in the aluminium plates (these three production processes account respectively for 68.8%, 18.8% and 10.4% of the e^- hits). The plots in Fig. 3.14 show the momentum and path length distributions for these components of the discarded electron hits.

A consistent fraction of the discarded electron hits (around 43%) can not be treated because the electron crosses the cell with a large angle, such that its

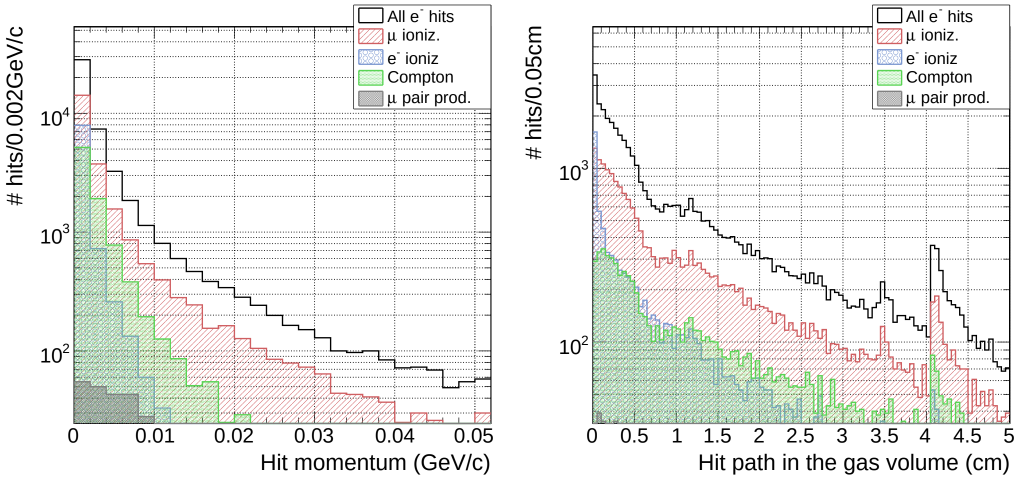

Figure 3.14: *Momentum and path length in the gas volume of the electron hits not handled by the parametrisation.*

extrapolated position on the wire plane falls outside the gas. The distribution of this kind of hits along the cell and their path in the gas volume are shown in Fig. 3.15. Most of these electrons cross only one corner of the cell describing

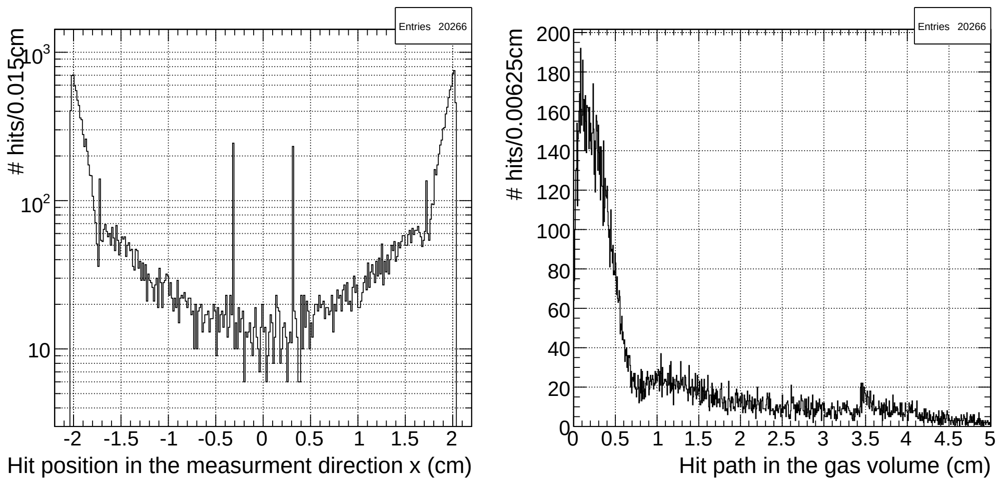

Figure 3.15: *Position along the cell and path length in the gas volume of electron hits which cross the cell volume with a large impact angle. They are discarded during the digitisation since their position extrapolated on the wire plane falls outside the gas volume.*

a short trajectory in the sensitive volume. The peak structure in the x coordinate of their position is related to particular geometry configurations for tracks crossing the whole cell almost horizontally.

Almost 38% of the electron hits is discarded because of the particular topology due to the bending generated by the magnetic field: the entry and exit points of these particles are on the same side of the cell. The spectrum of momentum of these electrons is plotted, together with their path in the gas volume, in Fig. 3.16. The distribution of the x coordinate of their position in

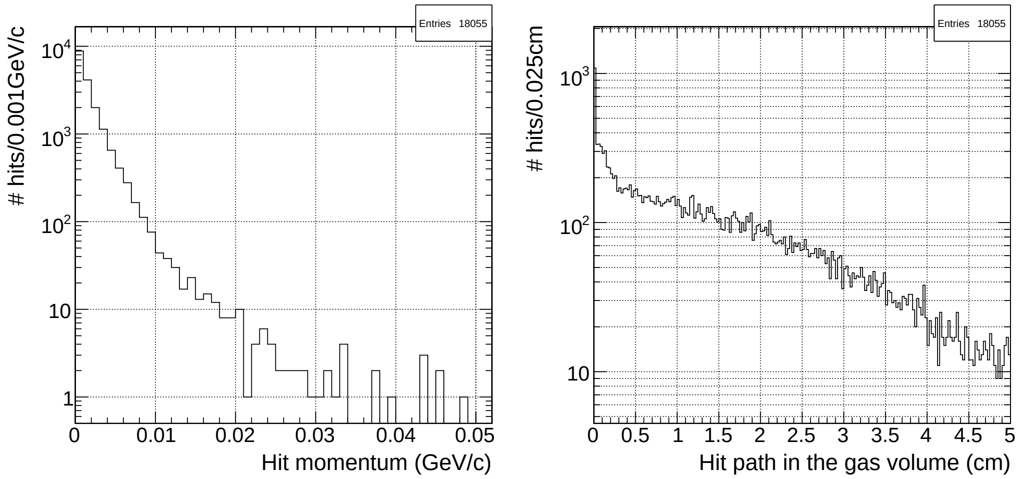

Figure 3.16: *Momentum and path length in the gas volume of the electron hits which, due to the bending by the magnetic field, enter and exit the gas volume on the same side of the cell.*

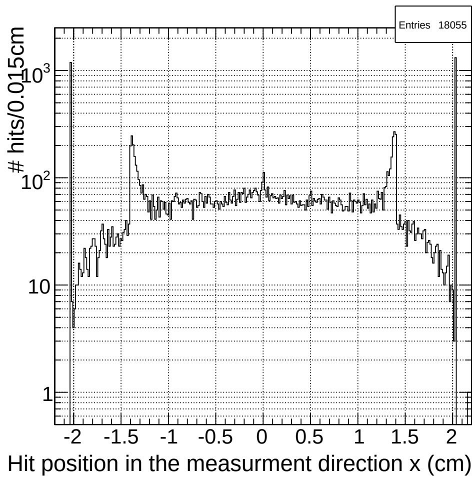

Figure 3.17: *Position within the cell, along the measurement direction, of the electron hits which enter and exit the cell volume thorough the same surface due to the bending.*

the gas volume is shown in Fig. 3.17. The peaks at $|x| \sim 1.4$ cm are due to electrons which enter and exit in correspondence of the I-beam feet, which is located 6 mm before the end of the cell.

The electrons which are discarded because they stop their trajectories within the gas volume are 15% of the discarded hits. They are homogeneously distributed along the cell, as shown in Fig. 3.18, where their position and path are plotted.

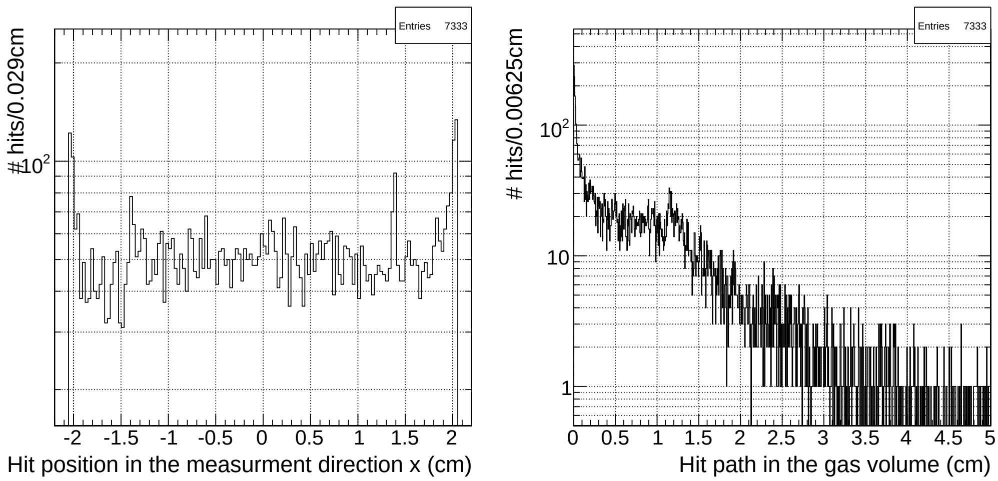

Figure 3.18: *Position along the cell and path in the gas volume of the electron hits which stop in the gas volume*

Finally, the remaining fraction of electrons, around 4%, has enough energy to cross the whole cell volume from I-beam to I-beam and they are responsible for the tail above 4.2 cm in the hit path distributions visible in the right plots of Figures 3.4 and 3.14.

The plot on the right in Fig. 3.12 shows that an important contribution to the hits which cannot be parametrised comes from muons. Those hits represent 30.7% of the hits discarded during the digitisation and 3.8% of the muon hits totally produced. Most of them, almost 80%, can not be parametrised because they cross only one corner of the cell with a distance from the wire which is estimated to be bigger than 2.1 cm. However, they normally cross the I-beam giving a hit, and therefore a digi, in the adjacent cell. Other muon hits are lost because they enter the gas volume from one of the surfaces delimiting the tube length. In this case it is not possible to digitise them because the parametrisation does not consider the effect of the impact angle along this coordinate.

Not all of the hits which account for the 7% of hits not treated by the parametrisation are expected to actually produce a signal. Some of them might not be detected as their path in the gas volume is too short. Also, part of the hits, due to the bending, enter and exit the cell from the same surface and cross particular regions of the gas volume where the charge collection is not efficient. Finally, even if a signal is produced it may fall in the TDC dead time, masked either by the muon hit or by other secondary particles. In conclusion, the effect of these hits on the number of digis is expected to be smaller than 7%.

3.4 Digitisation of the Drift Tubes

The digitisation process starts from the information contained in the GEANT hits and consists in the computation of a time that simulates a real TDC measurement. This involves the estimation of the drift time of the electrons produced by ionisation and the computation of the delays which contribute to the measurement, namely the time-of-flight of the muon (from the interaction point to the cell), the propagation time of the signal along the wire and the time pedestal (electronic and trigger offsets). At the end a time expressed with the precision of the TDC (1 TDC count=25/32 ns) is delivered.

The parametrisation described in the previous section has been integrated in the framework of the official simulation of the DT detector. The parametrisation is implemented as a function of the form:

$$t_{drift}^{peak}, \sigma_p, \sigma_m = f(d, \alpha, B_{\text{wire}}, B_{\text{norm}}). \tag{3.4}$$

The distance d is defined as the distance of the hit from the wire on the plane parallel to the layer and containing the anode. The hit position provided by GEANT, corresponding to the mid point of the hit track in the cell, can be used to estimate the distance only if its z component is close to wire plane, otherwise d is computed extrapolating the direction identified by the entry and exit points. In case of very inclined tracks, if the extrapolated distance is bigger than 2.1 cm, *i.e.* if the extrapolation falls outside the cell, the hit is discarded. Note that the particle trajectories are approximated to a straight line not considering the bending due to the magnetic field.

As far as the impact angle is concerned, the parametrisation was built considering only the two dimensional section of the cell, therefore only the projection of the track in the (x,z) plane (Fig. 3.7) is considered. As a consequence in the simulation the angle is defined as:

$$\alpha = \arctan \frac{\Delta x}{\Delta z} \tag{3.5}$$

where Δx and Δz are the two components of the hit direction in the superlayer reference frame.

The three plots in Fig. 3.19 show the distributions of the impact angle α and of the magnetic field components B_{wire} and B_{norm} for all the GEANT hits

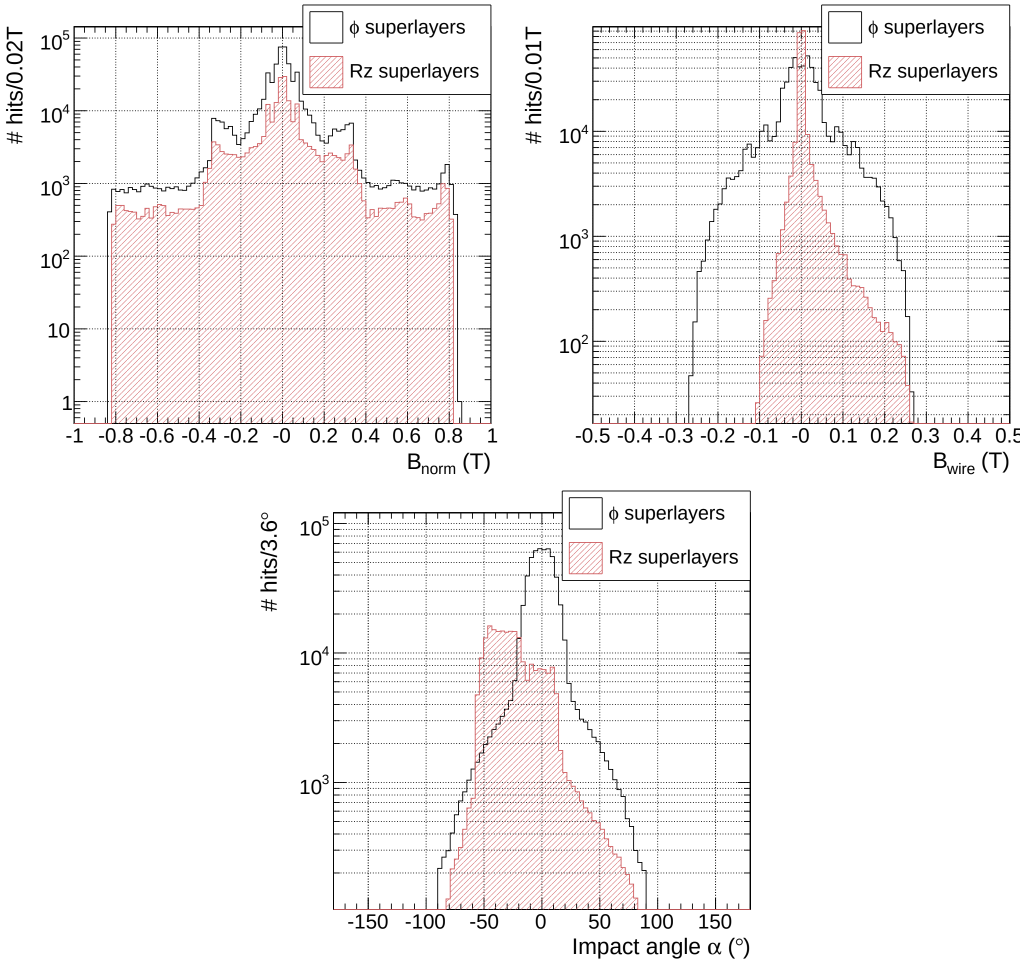

Figure 3.19: *Distribution of the input parameters* B_{norm} *(left),* B_{wire} *(right) and* α *(bottom) for the hits handled by the cell parametrisation.*

treated by the parametrisation inserted in the CMS geometry. The sample used is the same described in Section 3.2.

The impact angle of muons with transverse momentum between 10 GeV/c and 100 GeV/c in r-ϕ superlayers is well contained between $-20°$ and $20°$ while, in the r-z superlayers of the most forward chambers, it can also reach $50°$. However, in all superlayer types long tails, due to secondaries travelling almost parallel to the drift lines, are present.

The residual magnetic field in the gas volume ranges from -0.27 T to 0.28 T for the component parallel to the wires and from almost from -0.8 T to 0.8 T for the component orthogonal to the anode. The asymmetry in the distributions of α and B_{wire} for the r-z superlayers is due to the choice of the chamber reference frames with respect to the CMS one (cf. Section 2.5.1.1).

The range of the input parameters is much wider than the one used in the GARFIELD simulation. Therefore for $\alpha > 45°$, $B_{\text{wire}} > 0.4$ T and $B_{\text{norm}} > 0.75$ T the parametrisation functions are extrapolated.

To take into account the statistical nature of the drift-time distribution, the t_{drift}^{peak} is smeared according to a asymmetric Gaussian distribution defined by the two widths σ_p and σ_m defined in Section 3.3.1. The result of the smearing is the drift-time (t_{drift}) assigned to the hit. Additional time delays, described in next section, are then added to the t_{drift} to form the time information contained in a DT digi.

If several hits are present in the same cell, the drift times are computed independently, but separate digis are created only if the difference between the two times, comprensive of the delays, is larger than a configurable dead time (the default value is 150 ns), thus simulating the behaviour of the readout electronics. In case a second hit is within the dead time, only the first hit is recorded.

3.4.1 Additional Time Contributions

A DT measurement consists in a TDC time which also contains contributions other than the drift time of the electrons in the cell. The delays and offsets which directly contribute to the measurement are:

- propagation time of the signal along the anode wire;
- time-of-flight of the muon from the interaction point to the cell;
- delays due to the cable length and to the read-out time of the electronics;
- latency due to the Level-1 trigger.

These offsets must be estimated during the reconstruction through appropriate calibration and synchronisation procedures. The jitter in the drift-time deriving from the uncertainties of this procedure directly contributes to the DT resolution.

In order to emulate these contributions in the simulation the time contained in a digi is built as follows:

$$t_{digi} = t_{drift} + t_{prop} + TOF_{GEANT} + t_{offset} - TOF_{light} \tag{3.6}$$

The propagation time of the signal along the sense wire (t_{prop}) depends on the distance of the crossing particle from the front-end electronics. The propagation velocity, in the simulation, is assumed to be 0.244 m/ns. This value was directly measured using a chamber prototype tested on a muon beam [54].

The contribution of the time-of-flight (TOF_{GEANT}) of the muon from the collision vertex is directly computed by GEANT. A delay, multiple of 25 ns, is also added for hits coming from muons generated in a different bunch crossing than the signal one. These hits represent the so called "out-of-time pile-up".

A time pedestal t_{offset}, which represents the delays due to cables, phases, and readout, is also added. In the real data taking this offset can be different for each channel and it is measured using "test pulses" sent to the front-end electronics. In the simulation there is no need for a different offset for each channel and the default value is 500 ns for all the cells.

The important reason to introduce these delays in the simulation is the jitter remaining after the calibration and not their absolute value. In the analysis of simulated data is convenient to have all the time boxes for the different chambers aligned to the same time. This is obtained subtracting the time-of-flight of an infinite-momentum particle travelling from the nominal interaction point to the centre of the chamber. This is the TOF_{light} term in eq. 3.6 and it is re-absorbed by the calibration procedure during the reconstruction. This assumption, although it has no impact on the simulated resolution, simplifies the handling of the inter-chamber synchronisation in the whole simulation chain and the emulation of the Level-1 trigger.

The simulation is such that the digi time (*i.e.* t_{digi}) is not affected by the bunch crossing assignment performed by the Level-1 emulator. In fact in *p*-*p* collisions the BX assignment is known to be correct in more than 99% of the cases. On the contrary, this assumption of the simulation must be carefully considered when the simulation code is used to study the response of the DT apparatus to cosmic rays. Since cosmic muons are uniformly distributed in time, the Level-1 bunch cross assignment may be different to the one assumed for the *p*-*p* collisions.

3.5 Comparison of the Simulation with Test Beam Data

In October 2004 two Drift Tube chambers were tested on a 40 MHz bunched muon beam at the SpS facility at CERN. The validation of the cell simulation described in the previous sections requires the test of two aspects of the cell response:

- comparison of the average space-time relationship in the cell. The parametrisation must model the average drift velocity and the effect of the non-linearities for different track configurations;

- comparison of the intrinsic cell resolution. The parametrisation must statistically reproduce the effect of the spread of the drift times.

In the following, a comparison of the drift properties of the simulated and real cell is presented, underlining the dependence of the drift-time distribution on the track angle.

An important test of the performance and accuracy of the cell simulation is the comparison of the drift-time distributions.

The plot in Fig. 3.20(a) shows the drift-time distribution for real and simulated data collected with a 100 GeV muon beam. In order to avoid any bias due to the different hit multiplicity, only the first hit of each cell is considered in the plots.

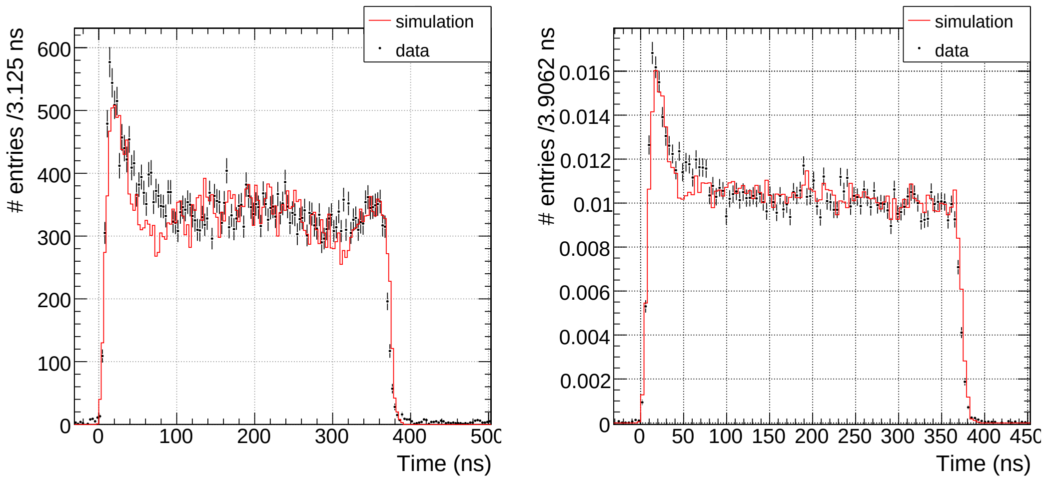

(a) (b)

Figure 3.20: *Drift time distributions for simulation and data collected in one r-ϕ superlayer exposed to 100 GeV/c muon beam orthogonal to the chamber (MB3 type). In (a) no normalisation is applied, while (b) refers to one uniformly illuminated cell and the distributions are normalised to the number of entries between 0 and 400 ns.*

The agreement on the number of entries is satisfactory, although small differences in the shape of the distribution are present. This difference can be explained taking into account the different beam profile in the real data taking and in the simulation: for non uniformly illuminated cells the shape of the time box is distorted. In order to account for this effect, only the digis in one uniformly illuminated cell of each layer in a superlayer r-ϕ have been considered. The resulting plot is shown in Fig. 3.20(b). In this case, the number of hits in the cell was different for simulation and reality, therefore the distributions have been normalised to the number of entries between 0 and 400 ns. These time boxes show very good agreement between data and simulation apart from a small excess of hits under the peak at small times, corresponding to the region close to the anode wire. In both cases the bulk of the distribution is smooth and the trailing edge drops sharply, as expected for a cell with saturated drift velocity.

In order to test the response of the parametrisation at different angles, the same selection of uniformly illuminated cells was applied to data taken with different rotation angles of the chamber with respect to the 150 GeV muon beam axis. The resulting plots are shown in Fig. 3.21 for impact angles of 0°, 10°, 20° and 30°. In all cases the agreement is satisfactory. The non-linearities occurring at large impact angles are well reproduced by the parametrisation.

3.6 Conclusions

The output of the simulation should be as close as possible to the real detector response to deeply understand the behaviour of the apparatus. The DT cell simulation is based on a parametrisation of the cell response obtained with a GARFIELD simulation; the drift time is parametrised as a function of the distance of the simulated hits from the wire, the incidence angle of the muon, and the magnetic field parallel and orthogonal to the wire. The simulation of the DT cell can take into account the effect of non-linearities in the drift time of the electrons. This time is smeared according to a double-half-Gaussian distribution, where the two sigmas are also parametrised.

Hits from energetic delta rays and any other secondaries crossing the whole cell are handled the same way as muons. Delta rays produced in the gas are ignored, since they are already included (statistically) in the parametrisation. Soft electrons stopping in the gas or entering and exiting on the same face of the cell cannot be handled by the parametrisation and are ignored. The effect of this approximation is negligible.

The simulation of the DT cells have been tested comparing its output with the real data collected during the October 2004 test beam: the properties of the cell are accurately reproduced and the agreement with real data is satisfactory.

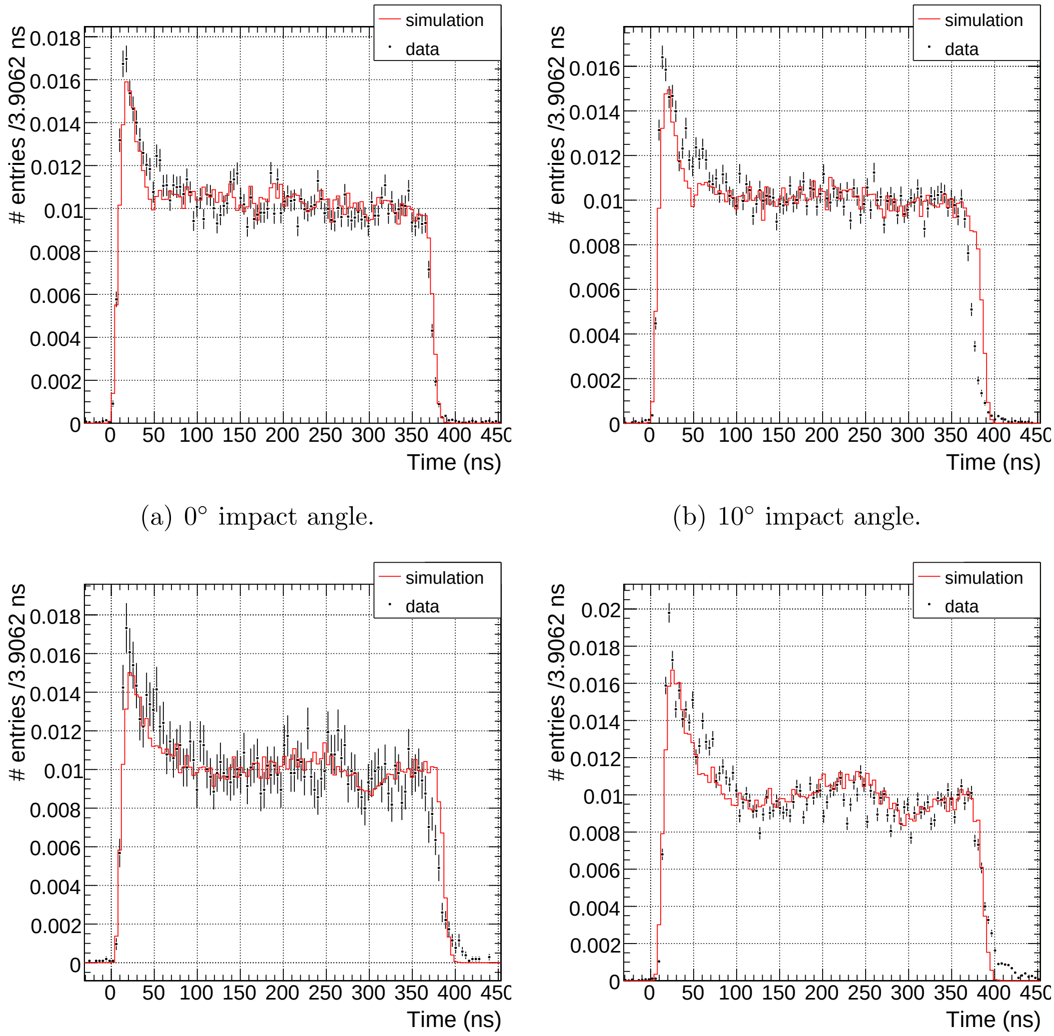

(a) 0° impact angle.
(b) 10° impact angle.
(c) 20° impact angle.
(d) 30° impact angle.

Figure 3.21: *Drift-time distributions for data and simulation for different impact angles of the 150 GeV muon beam with respect to the normal to the chamber: 0° (a), 10° (b), 20° (c) and 30° (d). The plots refer to the uniformly illuminated cell of each layer of* r-ϕ *superlayer in MB3 chamber. The distributions are normalised to the number of entries between 0 and 400 ns.*

Chapter 4

Local Reconstruction in Muon Detectors

The muon reconstruction starts at the level of the individual chamber. The results are track segments in the Drift Tubes and in the Cathode Strip Chambers, and 3D points in the Resistive Plate Chambers. Despite being different, all of them represent a measurement and therefore they are generally referred as *reconstructed hits* and implemented with the same interface. This feature is crucial for the next step of the muon reconstruction (Chapter 5).

In this chapter the local reconstruction of the DT is explained in detail, while for CSC and RPC only a brief description is given.

4.1 Local Reconstruction in the CSC

Each CSC plane measures a point in two dimensions. One coordinate is measured by the wires, which are read out in bunches. The other coordinate is measured by the strips, where the charge distribution of a cluster of three neighbouring strips is fitted to the so-called "Gatti function" to obtain a precise position measurement. The hits in a chamber are used to fit a three-dimensional straight line segment (made of up to six points). The direction resolution of the segment varies from 7 to 11 mrad in ϕ and from 50 to 120 mrad in θ for 50 GeV/c muons.

4.2 Local Reconstruction in the RPC

The hits produced by the RPCs are three-dimensional points. They are obtained by clustering the strips and calculating the centre of gravity of the area covered by the strips in the cluster (*i.e.* the width of the strips times their full length). Uncertainties are computed assuming in this area the hits distribute with uniform probability. In the simplest case of a rectangular area the errors on the position are equal to the length of each side divided by $\sqrt{12}$.

4.3 Local Reconstruction in the DT

The local reconstruction in the CMS drift tube detectors [2] is the reconstruction step where basic hits and track segments are built in a chamber starting from the output of the Data Acquisition System.

Local reconstruction begins with the reconstruction of mono-dimensional hits in the single drift cells. The only information contained in these hits is their distance from the anode, with an intrinsic left/right ambiguity and without any information about their position along the wire.

The cell hits are the starting point for the reconstruction of segments in the r-ϕ and r-z projections separately. These two-dimensional segments still do not provide any information about the coordinate along the sense wires, but they measure the track angle in the measurement plane (orthogonal to the wires).

Combining the two projections it is possible to reconstruct the direction and position of the muon crossing the chamber. The resulting three-dimensional segments are the input to the muon track fit in the muon spectrometer both in the off-line and in the High Level Trigger reconstruction. The performance of the local reconstruction must therefore meet the reliability and robustness requirements needed by such a task: provide good resolution on the track position and direction within a limited processing time, even in a high multiplicity environment.

In the following the steps leading to the reconstruction of three-dimensional segments within the chambers, starting from the TDC measurements, are described (Section 4.5 and 4.6). The performance of each step is also discussed, focusing mainly on resolution and efficiency.

The algorithms presented here have been implemented in the official reconstruction software of the CMS experiment.

4.4 Input to the DT Local Reconstruction

The input to the DT local reconstruction are TDC measurements stored in the so-called "digis". During the data taking the DT digis are created by decoding the raw output of the Data Acquisition (DAQ) system. In case of simulated samples the digis are created by the digitisation procedure described in Chapter 3. In both cases, the time measurement contained in a digi is a sum of different contributions:

- the drift time of the electrons produced by ionising particle;

- the delays due to the cable length and read-out electronics;
- the propagation time of the signal along the anode wire;
- the time-of-flight (TOF) of the muon from the interaction point to the cell;
- the latency of the Level-1 trigger.

A synchronisation procedure [46] must therefore be applied to the digis in order to extract the drift time, which is the relevant information for the hit reconstruction. The drift time is extracted from the TDC measured time subtracting the t_0^{wire} of each wire, the t_{trig}^{SL} measured by the calibration procedure for each superlayer, which may account for the average TOF and time of signal propagation along the wire, and a further hit by hit correction for the latter two effects:

$$t_{\text{drift}} = t_{\text{TDC}} - t_0^{\text{wire}} - t_{\text{trig}}^{SL} - \Delta TOF - \Delta t_{\text{prop}} \tag{4.1}$$

The jitter in the drift time deriving from the synchronisation procedure directly contributes to the DT resolution.

However, in the study of the hit reconstruction algorithms it is useful to decouple the performance of the algorithm itself from the resolution degradation introduced by the jitter on the estimated synchronisation constants. For this reason, during the reconstruction of simulated data, it is possible to use the *true* time offsets, which have been set during the digitisation procedure (cf. Section 3.4.1), in place of the measured t_0 and t_{trig} pedestals estimated with the calibration procedure. This is the case for the results presented in Section 4.5.3 and Section 4.6.1. The corresponding hit resolution is determined by the intrinsic cell resolution and by the precision on the corrections for TOF and t_{prop}, but is not affected by uncertainties deriving from the calibration of the t_0 and t_{trig} pedestals.

In order to discard noise and pile-up signals, the reconstruction is performed only for drift times falling in a user-defined time window. Normally, the times are required to be within -3 and 415 ns, after t_0 and t_{trig} subtraction. All other digis are discarded as they do not belong to the signal event which passed the trigger.

4.4.1 Determination of the Time Pedestals

The extraction of the drift time from the TDC measurement is performed in several consecutive steps.

- *Inter-channel synchronisation.*
  First, it is necessary to synchronise each wire with respect to the others of the same chamber, as for each wire the signal can have a different path length to reach the readout electronics. The constants (called t_0's) are measured for each wire by sending simultaneous "test-pulses" to the front-ends. This relative correction is usually between 1 and 8 ns.

- *Absolute offset determination.*
  Once the channels are synchronised, the absolute offset of the drift time distribution is computed. This offset, called t_{trig} because of its dependence on the trigger latency, allows extraction of the drift time from the TDC measurement. The t_{trig} is directly estimated from the distribution of the digi times using the procedure described in [46] and its value depends on the specific DAQ setup. The t_{trig} is usually of the order of few μs.

The determination of these two delays does not completely solve the problem of synchronisation of the digi times. Limited available data usually imposes computation of the t_{trig} by group of cells, *e.g.* by superlayer. In this case, the measured t_{trig} includes the *average* TOF of the muons (crossing the superlayer) and the *average* t_{prop} in the superlayer. Therefore, further corrections for these two effects can be computed as soon as the three-dimensional hit position is known, namely after the hits are associated into 3D track segments. Specifically, if the t_{trig} is computed for a uniformly illuminated full superlayer[1]:

- the 3D position obtained from the extrapolation of the segment to the hit plane, when available, is used to correct the average TOF, assumed to be that of a particle crossing the superlayer centre;

- the hit coordinate along the wire is used to correct the signal propagation time with respect to the middle of the wire, assuming a propagation velocity of 0.244 m/ns, as directly measured on test-beam data [54].

These corrections can be as high as $\approx$ 2 ns for the TOF and $\approx$ 6 ns for the signal propagation delay and they can be adapted or switched off in case of different running conditions. This is the case, for example, for cosmic data, where the previous definition of the TOF can not be applied, or for test-beam data, where the chamber is usually illuminated in a relatively small region. Particular care has been taken to provide enough flexibility for such cases.

[1] If the chamber is uniformly illuminated, which is the case for *p*-*p*-collisions, the average TOF is approximately equivalent to that of a muon crossing the superlayer centre, while the average signal propagation time is equivalent to the propagation time for a signal produced in the middle of the wire.

4.5 Reconstruction of the Hit Position within the DT Cell

Electrons produced at a time t_{ped} by the ionising particle migrate towards the anode with a velocity v_{drift} and reach the wire at a time t_{TDC}, which is the time measured by the TDC. The distance of the track with respect to the anode wire is given by

$$x = \int_{t_{ped}}^{t_{TDC}} v_{drift}\, dt. \tag{4.2}$$

The measurement of the track distance from the wire (x in the cell reference frame) requires understanding of this time-space relationship.

Two algorithms have been implemented. The first is based on the assumption of a constant drift velocity within the entire cell. In this case, the eq. 4.2 becomes

$$x = (t_{TDC} - t_{ped}) \cdot \overline{v}_{drift} = t_{drift} \cdot \overline{v}_{drift}, \tag{4.3}$$

where $\overline{v}_{drift}$ is the average drift velocity in the cell. However, the space-time relationship depends on the track impact angle and on the residual magnetic field in the cell. Therefore a second, more accurate, algorithm has been developed. This algorithm is based on a parameterisation of the cell response obtained with GARFIELD (Section 3.3). The parameterisation includes the dependence of the space-time relationship on the track impact angle, α, and on the stray magnetic field $\mathbf{B}$:

$$x = f(t_{drift}, \alpha, \mathbf{B}) \tag{4.4}$$

The two reconstruction algorithms are described in Section 4.5.1 and 4.5.2 respectively.

For both algorithms the information contained in the digi alone is not enough to compute the optimal hit position. For this reason an iterative procedure is adopted:

- *first step.* Reconstruction at the cell level: the left-right ambiguity is unsolved and the position of the hit along the wire is not yet determined;
- *second step.* The hits are used to build a segment within a superlayer. The left-right ambiguity for each hit is solved and the track impact angle is estimated. The position along the wires is still unknown, but the hit position can be refined using the information on the track impact angle;
- *third step.* The segments in r-ϕ and r-z projections are used to build a three-dimensional segment. The position of each hit along the wire is determined. This new information allows further refinement of the hit position.

At the second and third steps the segments are refitted after the hit positions have been recomputed. The information available at each step is used differently by the two reconstruction algorithms.

4.5.1 Reconstruction with Constant Drift Velocity

The good uniformity of the electric field within the cell allows reconstruction of the distance from the wire assuming a constant drift velocity over the entire cell.

The constant drift velocity algorithm does not account for local variations of the magnetic field in the tube nor for different impact angles of the tracks, but the calibration procedure of the drift velocity determines the average drift velocity which best fits the working conditions of a group of cells.

The drift velocity depends on many parameters, including the gas characteristics and the electrostatic configuration of the cell. The working conditions of the chambers are supposed to be continuously monitored and no significant differences between chambers in different places of the spectrometer are expected. The situation is different for the residual magnetic field in the cell and the incidence angle of the track, which vary substantially from chamber to chamber and also from superlayer to superlayer and affect the linearity of the time-to-distance relationship. For this reason, the reconstruction algorithm based on a constant drift velocity requires a calibration procedure that allows the average velocity to be calculated separately for different groups of cells.

To fulfil these requirements, a calibration algorithm based on the so-called *meantimer* [40] computation has been developed and the drift velocity can be estimated from data with appropriate calibration procedures [46].

This simple reconstruction algorithm gives satisfactory results especially for tracks with small impact angles and in regions with low residual magnetic field, because in these cases the cell non-linearities are less important. For this algorithm, the three-steps reconstruction procedure described in Section 4.5 is only used to refine the synchronisation constants.

4.5.2 Reconstruction Using the Cell Parametrisation

The optimal resolution on the hit position can be achieved taking into account the non-linearities of the space-time relationship. This has been done with an algorithm based on a parametrisation obtained from a GARFIELD simulation [50], complementary to that described in Section 3.3.

Referring to the cell reference frame described in Section 2.5.1.1, the space-time relationship has been parametrised as a function of:

- the track angle (α) calculated with respect to the z-axis;

- the value of the magnetic field parallel to the y-axis calculated at the hit position (B_{wire});
- the value of the magnetic field parallel to the z-axis calculated at the hit position (B_{norm}).

As described in Section 3.3, the output of the GARFIELD simulation is a function of the form:

$$f : x \longmapsto t_{drift}, \sigma_m, \sigma_p, \tag{4.5}$$

Therefore the inverse function gives the distance of tracks from the anode that would give a drift electron arrival time distribution *peaked* at the given time t_{drift}. This distance can be called $x^{t_{\text{mode}}}$, as it is the distance corresponding to a drift time distribution with the mode equal to t_{drift}:

$$x^{t_{\text{mode}}} = f(t_{\text{drift}}, \alpha, B_{\text{wire}}, B_{\text{norm}}). \tag{4.6}$$

The parametrisation also provides the variances (σ_m,σ_p) which correspond to t_{drift}, converted to distances using the average drift velocity:

$$\sigma_p^x, \sigma_n^x = f(t_{\text{drift}}, \alpha, B_{\text{wire}}, B_{\text{norm}}). \tag{4.7}$$

Actually, $x^{t_{\text{mode}}}$ is not the relevant quantity for reconstruction, which, instead, requires the knowledge of the *average* distance from the wire that leads to a given t_{drift}. This quantity it is approximately equal to the distance $x^{t_{\text{mean}}}$ corresponding to a drift time distribution with the *mean* equal to t_{drift}. In the case of an ideal distribution composed of two half Gaussians, as considered by the parametrisation, $x^{t_{\text{mean}}}$ is related to $x^{t_{\text{mode}}}$, σ_p^x and σ_n^x by:

$$x^{t_{\text{mean}}} = x^{t_{\text{mode}}} - (\sigma_p^x - \sigma_n^x)\sqrt{\frac{2}{\pi}}. \tag{4.8}$$

Note that this is an approximation of the actual value. A more correct result would be obtained by a dedicated GARFIELD parametrisation of the mean of the distribution of distances from the wire that result in a certain drift time. Such a parametrisation is currently not available. The effect of this approximation is expected to be small in all the regions of the cell where the width of the distribution is slowly varying along the cell axis. This is normally the case, except for the vicinity of the anode wire.

The resulting parametrisation has been implemented in the framework of the official CMS reconstruction code as a function of the form:

$$x_{\text{drift}} = f(t_{\text{drift}}, \alpha, B_{\text{wire}}, B_{\text{norm}}). \tag{4.9}$$

Since α, B_{wire} and B_{norm} are not known at the level of the individual hit, they are introduced during iterative procedure described in Section 4.5. In the first step the input parameters are estimated approximately: B_{wire} is taken at the middle of the wire and the track angle is determined assuming a straight line connecting the nominal interaction point to the mid point of the wire. In case the hit belongs to the r-ϕ superlayers, α is simply set to zero. In the second step the angle of the segment is used to update the hit position. In the third step the knowledge of the hit position along the wire is used to better evaluate the magnetic field components and x_{drift} is computed again. The knowledge of the three-dimensional position of the hit also allows fine-tuning of the synchronisation (cf. Section 4.4).

The two variances, σ_r and σ_l, are not related to the actual error to be assigned to the measurement, as they represent the width of the drift electron arrival time distributions translated into a distance. The actual errors assigned to the reconstructed hits have been estimated from the residual distributions obtained comparing the distances from the wire of reconstructed and simulated GEANT hits. Gaussian fits of the residuals have been performed and the corresponding variance recorded separately for the r-ϕ and r-z superlayers and for each reconstruction step. In the case of r-z superlayers, different errors are assigned in different wheels, as track impact angles are larger for the external wheels. The values of the errors are reported in Table 4.1. It should be noted that no dependence of the error on the hit position within the cell is taken into account.

Table 4.1: *Errors (in μm) assigned to the hit position, reconstructed using the time-to-distance parametrisation, for different reconstruction steps and superlayer types.*

	r-ϕ	r-z		
		Wheel 0	Wheel ± 1	Wheel ± 2
Step 1	237	250	271	308
Step 2	231	250	271	305
Step 3	207	196	210	228

4.5.3 Performance of the Hit Reconstruction

In this section the algorithmic performance of the hit reconstruction is shown using simulated data. The reconstruction is performed using the GARFIELD parametrisation and the t_{trig} offsets set during the digitisation procedure, as discussed in Section 4.4.

The simulated sample used for this study consists of 10^5 single muons generated with flat p_T spectrum in the 10–100GeV/c range and with $|\eta| < 1.3$.

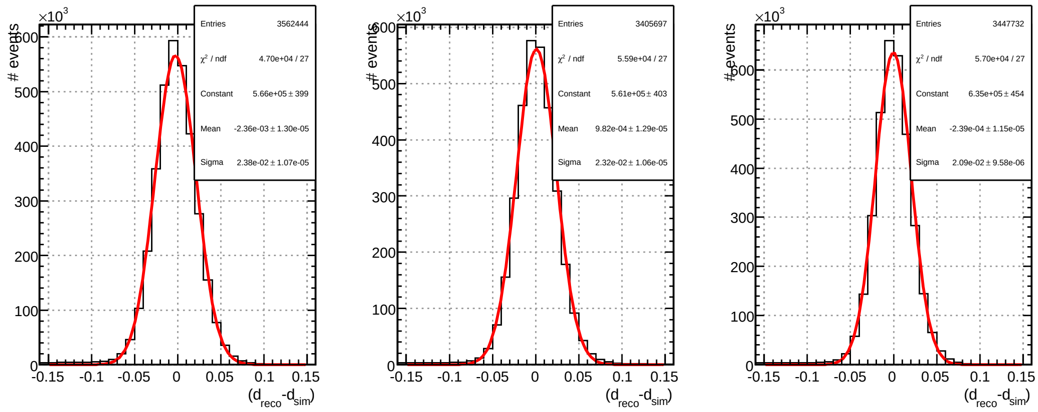

Figure 4.1: *Residuals (in cm) between the reconstructed and the simulated hit distances from the wire, in r-ϕ superlayers. The three plots refer to the first (left) second (centre) and third (right) reconstruction step of the time-to-distance parametrisation.*

The plots in Fig. 4.1 show the resolution on the (unsigned) distance from the wire for hits reconstructed in r-ϕ superlayers. The distributions have been fitted with a Gaussian function; the mean values and variances are reported in Table 4.2, together with the corresponding values for the r-z superlayers.

Table 4.2: *Residuals between the reconstructed and the simulated hit distances from the wire, in r-ϕ and r-z superlayers. The mean value and the variance of the Gaussian fit are reported (both in μm) for the three reconstruction steps performed with the time-to-distance parametrisation algorithm.*

	r-ϕ		r-z					
			Wheel 0		Wheel ± 1		Wheel ± 2	
	mean	σ	mean	σ	mean	σ	mean	σ
Step 1	-23.6 ± 0.1	238	6 ± 0.5	265	6 ± 0.4	281	-7 ± 0.5	314
Step 2	9.8 ± 0.1	232	7 ± 0.5	264	7 ± 0.4	281	-4 ± 0.5	315
Step 3	-2.4 ± 0.1	210	-2.7 ± 0.4	204	-1.6 ± 0.5	219	-7 ± 0.4	231

In the r-z superlayers the width of the residuals increases moving towards the outermost wheels. This is due to the impact angle of muons, which increases with pseudorapidity, enhancing the effect of the non-linearities in the cell. This effect is less important at the second and third reconstruction steps where the knowledge of the segment angle is used as input of the parametrisation. The final resolution is about 200 μm in all chambers. The plots in Fig. 4.2 show the resolution on the hit position as a function of the impact angle after each of the three reconstruction steps. Already at the second step the knowledge of the impact angle allows a better estimation of the actual position of the hit. The correction for this systematic effect improves the resolution at every angle.

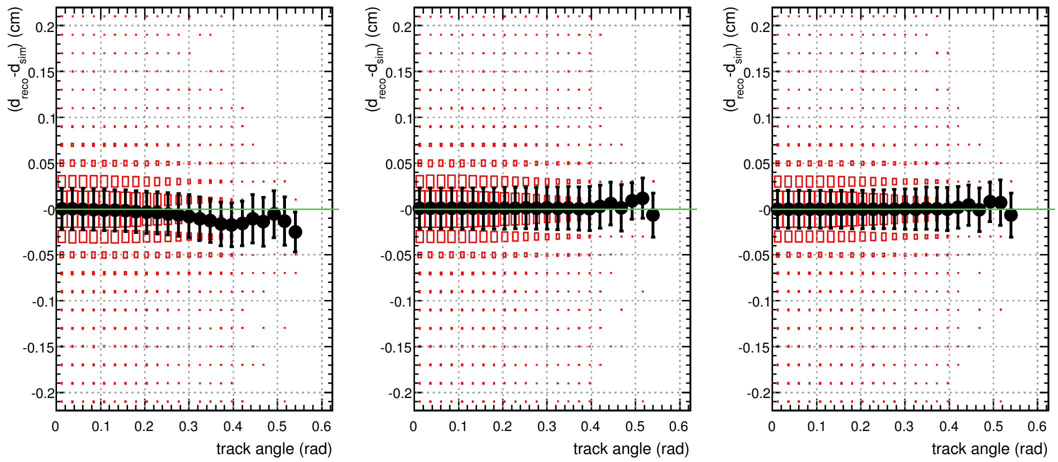

Figure 4.2: *Residuals on the hit position, in r-ϕ superlayers, as a function of the impact angle on the DT cell after the three steps of the hit reconstruction.*

The plots in Fig. 4.3 show the dependence of the resolution on the hit position on the distance from the superlayer front-end. The systematic error, due to the incomplete correction of the time of signal propagation along the wire, is visible as a slope of the mean value of the residual. The reconstruction at the third step fully compensates for this effect.

The error assignment on the reconstructed position plays an important role in the segment reconstruction because the pattern recognition is based on a χ^2 quality selection. The plots in Fig. 4.4 and 4.5 show the pull[2] distributions of the distance from the wire for the three reconstruction steps in the r-ϕ and r-z superlayers. The parameters of the Gaussian fits of these distributions are reported in Table 4.3.

Figure 4.6 shows that, although the assigned errors are constant in the whole cell, the widths of the pulls are very close to unit. The only critical region is around the wire where the errors are under-estimated.

A comparison between the algorithm based on constant drift velocity (Section 4.5.1) and the time-to-distance parametrisation (Section 4.5.2) is illustrated in Fig. 4.7. The plots show the residuals between the reconstructed and simu-

[2] The pull of a variable a is defined as:

$$\text{Pull} = \frac{a^{rec} - a^{gen}}{\sigma_a}.$$

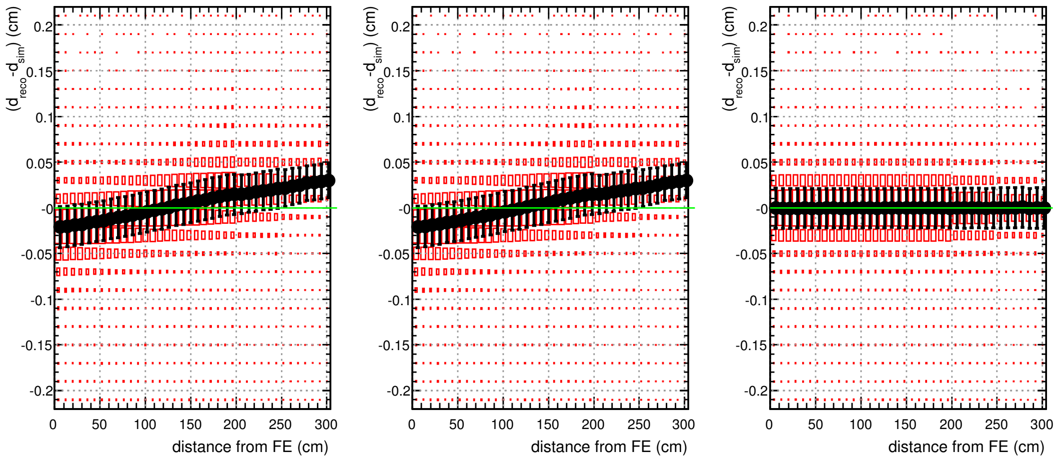

Figure 4.3: *Residuals on the hit position as a function of the hit distance from the front-end after the three steps of the hit reconstruction, for r-z superlayers.*

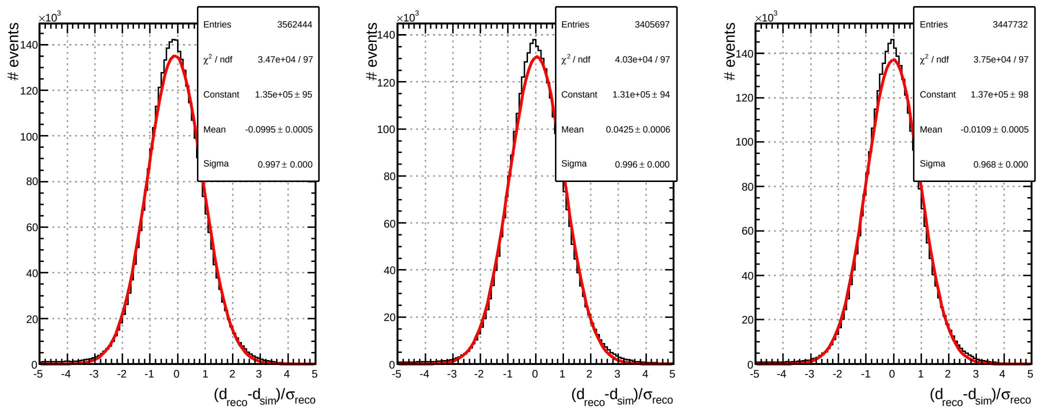

Figure 4.4: *Pulls for the reconstructed distance from the wire. The 3 plots refer to the first (left) second (centre) and third (right) reconstruction step of the drift time parametrisation in r-ϕ superlayers (all wheels).*

lated distance from the wire as a function of the distance from the anode. The plot on the left shows the results obtained using the GARFIELD parametrisation while the one on the right shows the performance of the constant drift velocity algorithm. The plots refer to the worst situation: the first reconstruction step in r-z superlayers of wheels +2 and -2, where the large impact angle and the non-negligible magnetic field enhance the effect of the non-linearities in the space-time relationship. The effect of cell non-linearities are well visible in case of the constant drift velocity algorithm. Using the parametrisation the effect

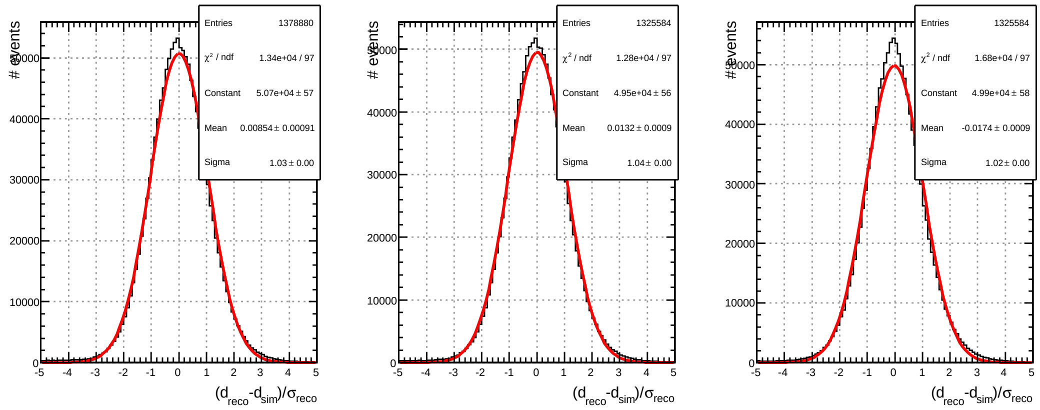

Figure 4.5: *Same as for Fig. 4.4, for superlayers r-z (all wheels).*

Table 4.3: *Pulls of the reconstructed distance from the wire. The sigmas of the Gaussian fit are reported for the three reconstruction steps with the drift time parametrisation in* r-ϕ *and, for each wheel,* r-z *superlayers.*

	r-ϕ	r-z		
		Wheel 0	Wheel ±1	Wheel ±2
Step 1	0.997	1.053	1.030	1.015
Step 2	0.996	1.050	1.031	1.027
Step 3	0.968	1.031	1.031	1.004

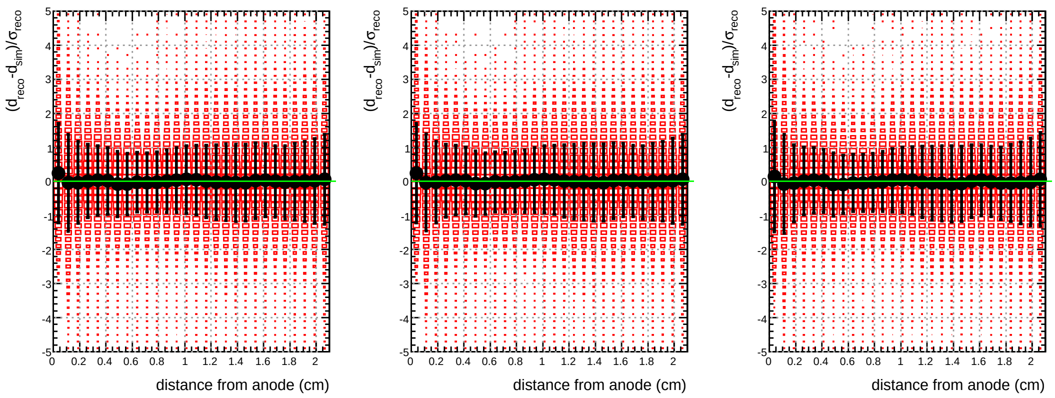

Figure 4.6: *Pulls of the reconstructed distance from the wire as a function of the distance of the hit from the anode. The 3 plots refer to the first (left) second (centre) and third (right) reconstruction step of the drift time parametrisation in superlayers* r-z.

of the non-linearities is well contained below 100 μm also in the problematic region, *i.e.* close to the anode. A completely different response is shown in the plot on the right where the average value of the residuals can vary of more than 150 μm moving a few millimetres away from the wire.

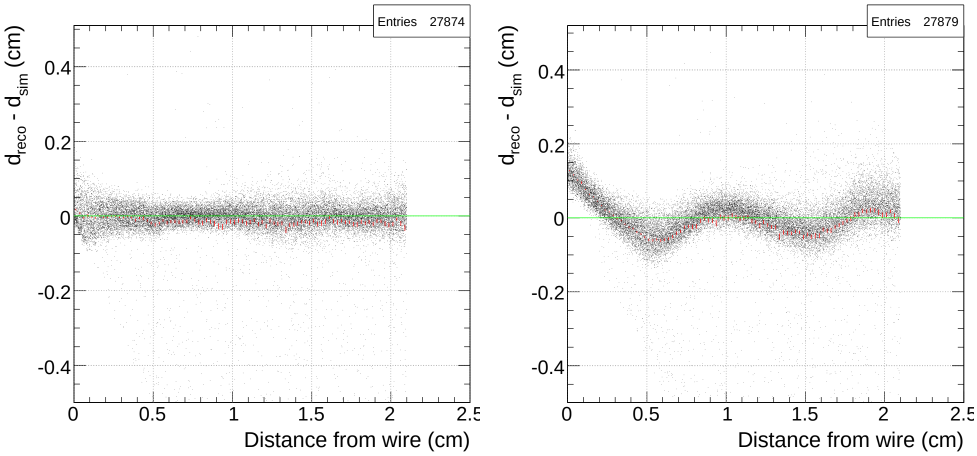

Figure 4.7: *Residuals between the reconstructed and simulated distance from the wire as a function of the simulated one. The plots refer to hits reconstructed using the time-to-distance parametrisation (left) and the constant drift velocity (right) in r-z superlayers of wheels ± 2.*

4.6 Segment Reconstruction in DT Chamber

The purpose of the segment building procedure is twofold: solve the left-right ambiguity of the mono-dimensional hits and provide track stubs, thus helping the pattern recognition during the muon track reconstruction (Chapter 5). Moreover the segment reconstruction provides a precise determination of the track impact angle and of the hit position along the wire, which can be used to refine the computation of the drift distance (cf. Section 4.5).

The segment reconstruction acts in each chamber on the r-ϕ and r-z projections independently. At the end of the procedure the two projections are combined and three-dimensional segments are built. The algorithm performs in each projection the pattern recognition and a linear fit of the hits. A linear fitting model, given the hit resolution and the small height of a chamber, is a correct approximation. The reconstruction is performed in three steps:

- segment candidates are built from sets of aligned hits, built with a combinatorial algorithm;

- the best segments among those sharing hits are selected, removing conflicts and suppressing ghosts;

- the positions of the hits in the segment are updated using the information from the segment (cf. Section 4.5) and the segments are re-fitted.

Building segment candidates. The selection begins identifying pairs of hits in different layers, starting from the most separated layers.

A pair of hits is kept if the angle of the proto-segment is compatible with a track pointing to the nominal interaction point, within a configurable tolerance. The tolerance is usually set to 0.1 rad in the r-z projection and 1.0 rad in r-ϕ plane (as this is the projection interested by the track bending). These constraints can be switched off in the reconstruction of cosmic muons. As each hit has a left-right ambiguity, both hypotheses are considered if they fulfil the above condition.

For each pair, additional compatible hits are searched for in all layers. The x-coordinate (layer reference frame) of the intersection between the proto-segment and the layer is taken as a reference position. The hits are tested checking if the left or the right hypotheses have a distance from the intercept smaller than 10 times the error on their position, as estimated by the hit building algorithm. It is possible that both the left and right hypotheses are compatible with the segment. In this case, both candidates are retained and the ambiguity is solved later. Also, a muon can cross the I-beam separating two cells generating a signal in both. In this case, both hits are considered for that layer, in order to avoid any bias.

Once the pattern recognition is completed each collection of hits is fitted using the positions and the errors assigned to the hits. For each pair of hits only the segment candidate with the highest number of hits and the smallest χ^2 is retained; all the others are rejected. Finally, a loose quality criterion is applied, requiring the number of hits ≥ 3 and the χ^2/d.o.f. < 20 for all the candidates.

This algorithm is applied directly to each r-z superlayer. It can also be applied to the individual r-ϕ superlayers (the resulting segments are useful for detailed studies of the chamber performance), however for track-fitting purposes it is more convenient to build the r-ϕ projection using the hits from both the r-ϕ superlayers in the chamber.

In case of showering, the occupancy in the chamber can be very high and an increasing of the combinatorics can deteriorate the performance of the pattern recognition. For this reason the procedure described above is not attempted if the number of hits in a given projection is larger than a programmable number (default is 50). A complementary algorithm to treat such cases is under study.

Segment selection. The pattern recognition described above produces a set of segment candidates. A consistency check is performed in order to test whether two candidates use the same hits but with different left-right hypotheses. In that case, the conflicting hit is removed from the worst of the two segments, where the quality is defined by the number of hits and the χ^2 of the segment.

There is also the possibility to retain all candidates, without removing the conflicting hits, thus leaving the selection of the best segments to the muon track fit algorithm.

Specific incidence angles can result in particular hit patterns. Two segment candidates can share all their hits but with different left-right hypotheses for each hits. The two candidates have in this case the same quality. In p-p collisions, the choice is implicit in the request of compatibility with the nominal interaction point described previously. When this requirement is removed, as for the reconstruction of cosmic muons, two options are available: either retaining both candidates, thus leaving the muon track fit algorithm to select the best segments, or choosing the candidate with the smallest angle (in the r-z view) among the two.

After the removal of the conflicting hits, the segments are allowed to share non-conflicting hits up to a configurable number (default is two). If more than two are present, the worst segment candidate is rejected. If two segments share hits, they are required to have a minimum number of unshared hits, in order to further reduce the number of short ghost segments. The minimum number of unshared hits is configurable as well and the default is two.

The position of the hits in the remaining segment candidates are updated ("second step" mentioned in Section 4.5.2), taking into account the incidence angle as reconstructed by the segment. The segment linear fit is recomputed using the updated hits.

Matching of the two projections. Up to this point, the r-ϕ and r-z projections are handled independently. As the two projections are orthogonal, a segment in one projection cannot be used to validate or invalidate a segment in the other: all combinations of segments from the two projections are kept.

The additional knowledge of the position along the wire is used to update the hit position in the cells ("third step" described Section 4.5.2) before performing the final fit of the segment. The result is a segment inside a chamber suitable for use in the track reconstruction (Chapter 5).

4.6.1 Performance of the Segment Reconstruction

4.6.1.1 Angle and Position Residual of the Segments

Residuals on position and angle of two-dimensional segments in a single superlayer are shown in Fig. 4.8 and 4.9 for r-ϕ and r-z projections, respectively. The position resolutions are about 115 μm and 140 μm in the two cases. The worse resolution on the r-z projection is mainly due to the higher impact angle of the muon in these superlayers. The resolution on the angle is about 8 mrad for both projections.

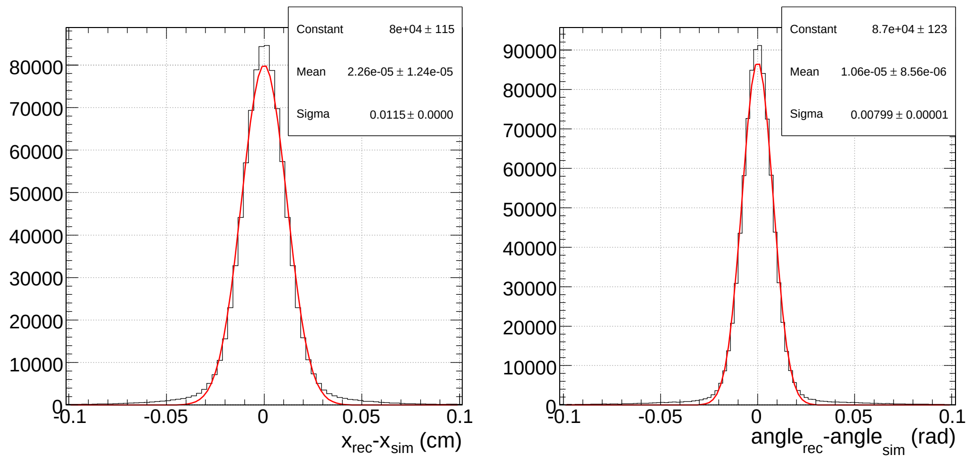

Figure 4.8: *Residuals on the position (left) and angle (right) measured by two-dimensional segments in individual r-ϕ superlayers.*

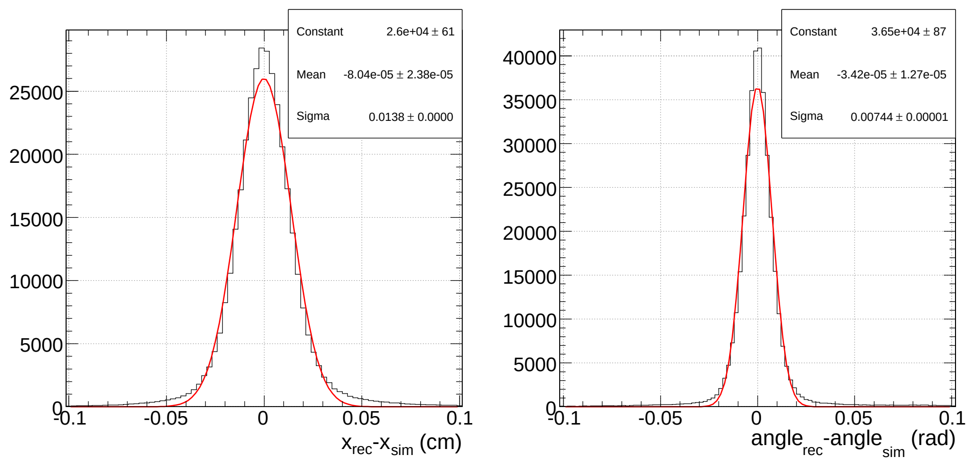

Figure 4.9: *Residuals on the position (left) and angle (right) measured by two-dimensional segments in r-z superlayers.*

The three-dimensional segments are the input for the track fit. Figure 4.10 shows the residuals on the bending coordinate x and on the non-bending coordinate y, which are the positions measured by the r-ϕ and r-z superlayers respectively (cf. Section 2.5.1.1). The resolution improvement with respect to Fig. 4.8 is due, in the case of x, to the fact that the two r-ϕ superlayers are now used together, doubling the number of measurements planes and increasing the lever arm from ~ 4 cm to ~ 16 cm. Also, for both projections the single hit resolution is better due to the additional knowledge of the position of the hit along the wire. In the bending plane, the resolution on the single hit position

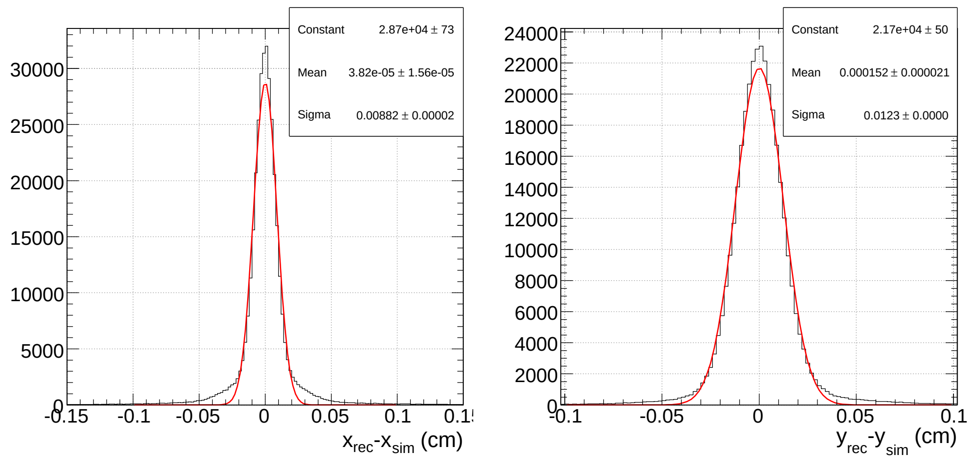

Figure 4.10: *Residuals on the position of three-dimensional segments. Left: residual on x (bending coordinate), given at the middle plane of the two r-ϕ superlayers. Right: residual on y (non-bending coordinate) given at the middle plane of the r-z superlayer.*

is of about 240 μm (see Section 4.5.3). After the segment reconstruction it is possible to achieve a precision of about 70 μm.

The resolution on the non-bending coordinate is of about 120 μm. It should be noted that the most accurate determination of a segment coordinate is obtained at a plane corresponding to the centre of gravity of the hits, weighted by their errors. This corresponds approximately to the middle plane of the chamber in the case of the r-ϕ projection, and the middle plane of the r-z superlayer for the r-z projection. These two planes do not coincide, as can be observed in Fig. 2.16. However, it is often convenient to report the position of the segment as a single three-dimensional point, and in this case both coordinates have to be reported on the same plane. The middle plane of the chamber is chosen, in order to favour the bending coordinate, while the non-bending coordinate has to be extrapolated from the position measured on the middle plane of the r-z superlayer. Therefore in the reported 3D position of the segment, the residual on the y coordinate is degraded to about 530 μm (although the full error matrix, including the correlations terms between positions and angles, is available).

The resolution on the direction of the reconstructed segments is shown in Fig. 4.11. An angular resolution of about 0.7 mrad is achieved in the r-ϕ projection, thanks to the presence of two superlayers and thus a long lever arm. On the other projection (r-z), the resolution is about 6 mrad.

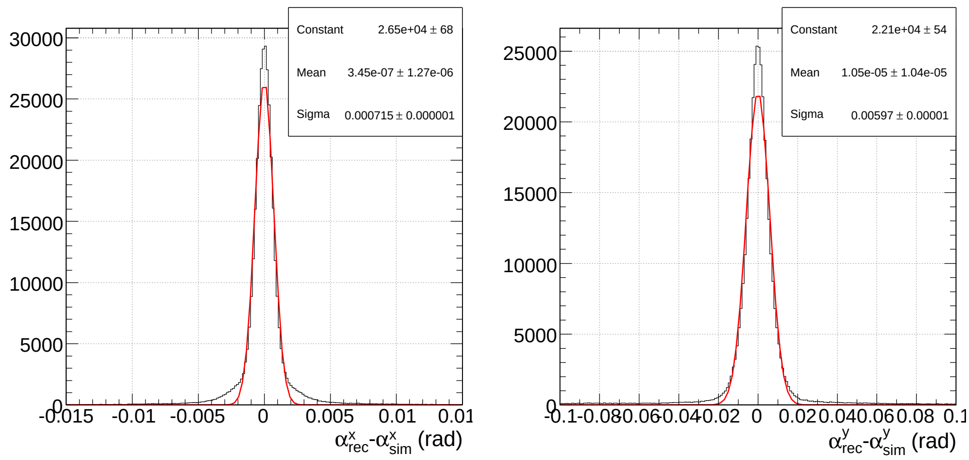

Figure 4.11: *Residuals on the angles measured by three-dimensional segments in the r-ϕ (left) and r-z (right) projections.*

In Fig. 4.12, the pulls for the three-dimensional segments are shown. The pulls are well centred at zero and with a σ close to unit. Figure 4.13 shows how the pull on the angle measured in the r-z superlayer does not show a dependence on η.

4.7 Conclusions

The algorithms for the local reconstruction in the DT system have been discussed.

Concerning the resolution, the GARFIELD parametrisation used in the reconstruction of the cell hits allows achieving better results with respect to the constant drift velocity algorithm, especially in the most critical regions, thanks to the modelling of the cell non-linearities. This has been also tested on test-beam data [55].

However, the reconstruction algorithm based on the parametrisation of the cell behaviour is intrinsically more complex than the one using a constant drift velocity. The very simple algorithm with constant drift velocity can be used with the first data; afterwords, when stable operation of the DT cell will be

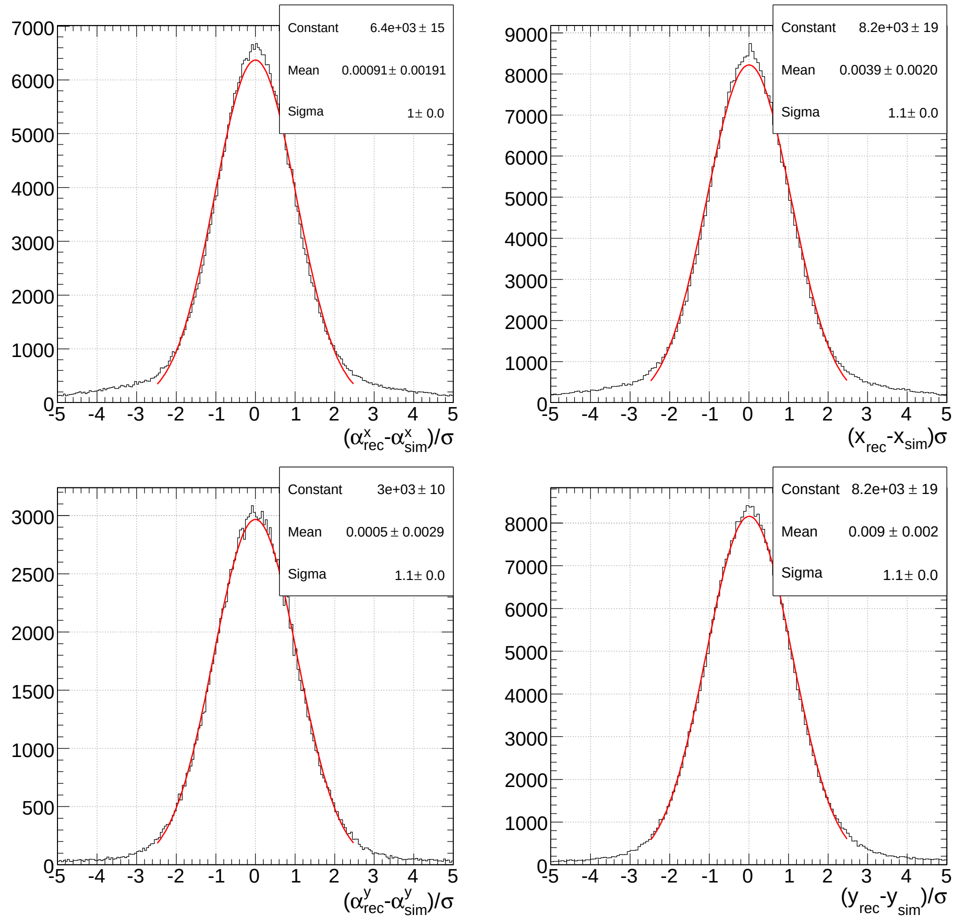

Figure 4.12: *Pulls on the parameters measured by three-dimensional segments. Top line: pulls for angle (left) and position (right) in the r-ϕ projection. Bottom line: pulls for the r-z projection, given at the middle plane of the r-z superlayer (see text).*

achieved, the usage of the parametrisation will be advisable in order to obtain the best resolution.

Although the local reconstruction procedure has been designed for *p*-*p* events, since October 2005 the reconstruction has been extensively used also for cosmic muons acquired during the chamber commissioning and the *Magnet Test Cosmic Challenge* [4], both in the off-line analysis of the data, for the certification of the chamber functionality, and in the on-line monitoring.

The tests of the reconstruction on real data have been a useful benchmark for the reconstruction chain and suggested many improvements in the algorithms. This experience led to a design capable to guarantee to the end user the flexibility needed to treat data acquired in different running conditions: cosmics,

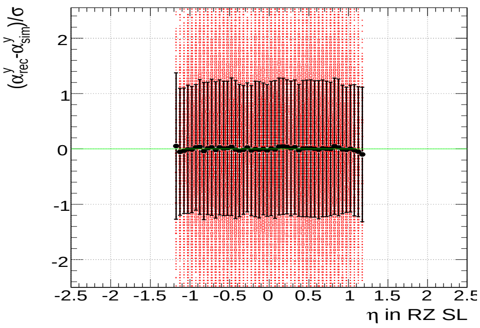

Figure 4.13: *Pull on the angle in the r-z projection vs η . The black dots show the mean and the bars the sigma of Gaussian fits on each η slice.*

test-beam and (for the time being simulated) *p*-*p* data.

Chapter 5

Muon Reconstruction

In a hadron collider leptons provide a clear signature for many of the most interesting physics processes, therefore a precise and fast reconstruction of the leptons is mandatory. In this context the muons play a key role as their parameters can be measured with great precision and, at least at high p_T, they can be identified unambiguously.

The tracks within the muon system are built using the Kalman filter technique, combining the information coming from each muon sub-detector (Chapter 4). This step is the so called *Stand-Alone Muon Reconstruction* (Section 5.1) and it is also the basis of the Level-2 of the muon trigger. The last step is the propagation of the muon tracks to the silicon tracker. The information of the muon spectrometer and the tracker system are combined (*Global Muon Reconstruction*), giving the final muon track used also by the third level of the muon trigger. The reconstruction of the muons is completed by matching the muon track with the energy deposits in the calorimeters.

5.1 Track Reconstruction in the Muon Spectrometer Alone

Based on the Kalman filter technique (cf. Appendix A), track reconstruction starts with the estimation of the seed state from track segments in the off-line reconstruction (Section 5.1.1) and from the trajectory parameters estimated by the Level-1 of trigger in the on-line (Section 5.5.1). The track is then extended using an iterative algorithm which updates the trajectory parameters at each step and, in order to reduce the possible bias from the seed, a pre-filter can be applied before the final filter (Section 5.1.2). Once the hits are fitted and the fake trajectories removed, the remaining tracks are extrapolated to the point of closest approach to the beam line. In order to improve the p_T resolution a beam-spot constraint is applied.

The track reconstruction handles the DT, CSC and RPC reconstructed segment/hits and it can be configured in such a way to exclude the measurements from one or more muon subsystems. The independence to the subsystem from which the measurements come is achieved thanks to a generic interface also shared with the inner tracking system. This allows the *tracker* and the *muon* code to use the same tracking tools (such as the Kalman filter) and the same track parametrisation.

5.1.1 Seed Generator

The algorithm is based on the DT and CSC segments (Chapter 4).

A pattern of segments in the stations is searched for, using a rough geometrical criteria. Once a pattern of segments has been found (it may also consist of just one segment), the p_T of the seed candidate is estimated using parametrisations of the form:

$$p_T = A - \frac{B}{\Delta\phi} \tag{5.1}$$

For DT seed candidates with segments in MB1 or MB2, $\Delta\phi$ is the bending angle of the segment with respect to the vertex direction. This part of the algorithm assumes the muon has been produced at the interaction point. If segments from both MB1 and MB2 exist, the weighted mean of the estimated p_T's is taken. If the seed candidate only has segments in MB3 and MB4, the difference in bending angle between the segments in the two stations is used to calculate p_T.

In the CSC and overlap region, the seed candidates are built with a pair of segments in either the first and second stations or the first and third stations. $\Delta\phi$ is the difference in ϕ position between the two segments. Otherwise, the direction of the highest quality segment is used.

Although this algorithm is currently used only for the off-line seeding, it can also be used as a very fast muon reconstruction, which can be used in the High Level Trigger chain as an intermediate step between L1 and L2.

5.1.2 Pattern Recognition and Track Reconstruction

In the standard configuration the seed trajectory state parameters are propagated to the innermost compatible muon detector layer (the technique to find the compatible layers is described in Section 5.1.2.1) and a pre-filter is applied in the inside-out direction. Its main purpose is to refine the seed state before the true filter. The final filter in the outside-in direction is then applied and the trajectory built. The algorithm is flexible enough to perform the reconstruction starting from the outermost layer instead of the innermost. The pre-filter step can optionally be skipped, hence increasing the speed of the reconstruction which could be important for the High Level Trigger. However, the standard reconstruction can already meet the strict HLT speed requirement (Section 5.5).

The pre-filter and filter are based on the same iterative algorithm used in two different configurations. In both cases it can be subdivided into different sub-steps: search of the next compatible layer (cf. Section 5.1.2.1) and propagation of the track parameters to it, best measurement finding and possibly update of the trajectory parameters with the information from the measurement. The process stops when the outermost (for the pre-filter) or the innermost (for the filter) compatible layer of muon detectors is reached.

At each step the track parameters are propagated from one layer of muon detectors to the next. A suitable propagator must precisely take into account material effects like multiple scattering and energy losses due to ionisation and bremsstrahlung in the muon chambers and in the return yoke. In order to reduce the processing time, the propagator must be fast. The trajectory is extrapolated in sequential steps using helix parametrisations. The required precision is obtained by using smaller steps in regions with larger magnetic field inhomogeneities. Multiple scattering and energy losses in each step are estimated from fast parametrisations, avoiding time-consuming accesses to the detailed material and geometry descriptions. The resulting propagated state contains these effects in its parameters and errors.

The best measurement is searched for on a χ^2 basis. The χ^2 compatibility is examined at the segment level, estimating the incremental χ^2 given by the inclusion in the fit of the track segment. In case no matching hits (or segments) are found, the search continues in the next station.

For the update of the trajectory parameters the pre-filter and the filter follow two different approaches. As the pre-filter should give only a first estimate of the track parameters, it uses the segment for the fit. The parameters are almost always updated as the χ^2 cut imposed at this stage is loose (of the order of one hundred). The final filter instead uses the hits composing the segment with a tighter χ^2 cut (of the order of 25) which can reject individual hits. This results in a more refined trajectory state. The RPC measurements are not aggregated in segments, so that for them the only distinction between the pre-filter and the filter is the χ^2 cut.

The mechanism for updating the trajectory parameters can be seen as a combination of the predicted trajectory state and the hit in a weighted mean, as the weights attributed to the measurement and to the predicted trajectory state depend on the respective uncertainties. A more detailed explanation is given in Appendix A.

In order to finally accept a trajectory as a muon track, at least two measurements, one of which must be of the DT or CSC type, must be present in the fit. This allows rejection of fake DT/CSC segments due to combinatorics. Moreover the inclusion of the RPC measurements can improve the reconstruction of low momentum muons and those muons which escaped through the inter-space between the wheels (and the DT sectors), leaving hits in only one DT/CSC station. In Fig. 5.1 the effect of the inclusion of the RPC measurements in the track fitting is shown.

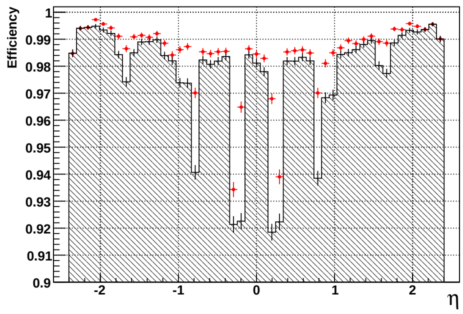

(a) Efficiency as a function of pseudorapidity.

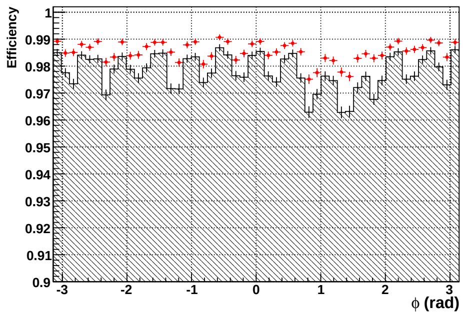

(b) Efficiency as a function of ϕ.

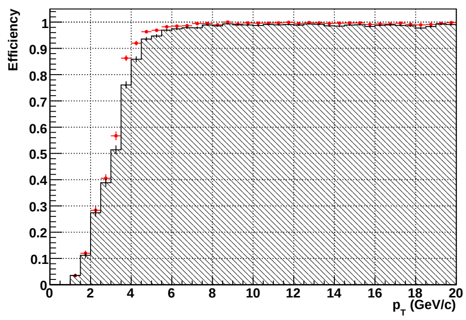

(c) Efficiency as a function of p_T.

Figure 5.1: *Efficiency of the reconstruction in the muon spectrometer as a function of η, ϕ and p_T, with (red cross) and without (dashed area) the inclusion of RPC in the tack reconstruction.*

After the fake track suppression the parameters are extrapolated to the point of closest approach to the beam line. In order to improve the momentum resolution a constraint to the nominal interaction point (IP) is imposed. The matrix error of the IP is diagonal and its values are: (15 μm 15 μm 5.3 cm).

The performance of the stand-alone muon reconstruction is reported in Section 5.4.

5.1.2.1 Navigation in the Muon Detector

The track fitting method described in the previous sections does not require the full set of reconstructed hits to be available before the fit. Instead, at each step the track parameters are used to identify the detectors that most probably contain the next hit to be included in the trajectory.

The algorithmic problem of finding the next detector crossed by one trajectory, given its parameters at a given point, is called *navigation*. The efficiency and speed of this operation are fundamental: the navigation is one of the most time consuming parts of the track fit, and a fast implementation is necessary to allow track reconstruction within the timing constraints of the trigger.

The possibility of an optimised implementation derives from the fact that the tracking detectors in CMS are arranged in layers with a defined distance from the detector centre, so that a track coming from the interaction point always crosses them in a defined sequence. Moreover, individual detectors within the layers are arranged in a (quasi-) periodic way, and can be organised in substructures with a simple geometrical shape, like disks or rods.

The problem of navigation is therefore solved by organising the detectors in a hierarchical structure. Each element in the hierarchy is described geometrically in terms of an elementary surface that approximates the surface of its constituents (detectors or groups of detectors). The element can be queried to find which detectors are compatible with a given trajectory; in this case, the trajectory is extrapolated to the surface of the element and compatible constituents are selected taking into account the uncertainty on the extrapolated track position. Selected constituents are queried in the same way, so that the hierarchy is traversed vertically, up to the level of individual detectors. As a result, the reconstructed hits are returned together with the trajectory state extrapolated to the corresponding detector surface. Both the reconstructed hits and the state are directly used for the Kalman filter update step described in the previous section. This procedure minimises the number of track extrapolations, especially in the case of extrapolations between stations in the muon system where the trajectory crosses the iron return yoke. These constitute the time-consuming part of the navigation.

The CMS software provides a framework and a set of base classes for the implementation of these hierarchies. Such classes are shared by all tracking detectors, to allow a consistent behaviour. Navigation in each detector system is implemented by specialising these classes, *i.e.* grouping the detectors in the optimal way and defining the rules to determine how the search is performed within each hierarchy level. The case of the muon system is described in the following.

The first level of the hierarchy is a full layer of detectors; in the barrel muon system it consists of a cylinder, corresponding to either one DT or one RPC station. In the endcap, layers are flat vertical disks corresponding to either one CSC or one RPC station, except for the first station (ME1), which is split into two layers at different positions in z (cf. Fig. 2.1). Layers are sorted by their distance from the detector centre (*i.e.* by radius in the barrel and by z in the endcaps). This is the order in which they are traversed by a trajectory coming from the interaction point, so that, at each fitting step, reconstructed hits are looked for in the next layer in the list (provided that the track direction with its error is within the layer's η boundaries.)

Inside layers, detectors are organised in groups with a common surface. Since an extrapolation to each detector surface is needed to test the compatibility with a track, the most efficient organisation is obtained when individual detectors with a common surface are grouped together. The organisation is different for the barrel and the endcaps.

Muon barrel layers. From the mechanical point of view, the muon barrel is composed of five wheels of 12 or 14 chambers each. However, as discussed above, it is preferable to have chambers with the same flat surface grouped together. For this reason, barrel muon layers are constituted of rods, each consisting of five chambers. There are 12 rods in each layer, except for MB4, where there are 14. Chambers in a rod lie on the same plane, are contiguous in z and are all at the same r and ϕ coordinates. Rods in a layer are quasi-periodic in ϕ and, in some cases, slightly overlap in this coordinate.

When a layer is queried for the reconstructed hits compatible with a given track, a first extrapolation is done to the cylinder representing the layer's surface. The extrapolated position in ϕ is used to determine the closest rod, which is selected. If the extrapolated error, scaled by an adjustable factor, extends beyond the rod's border in ϕ, the neighbouring rods are selected as well. Then, selected rods are individually queried for compatible chambers. A short extrapolation is made from the layer's cylinder to the rod plane, and one or more chambers are selected according to the z position of the extrapolated track and its uncertainty.

Muon endcap layers. Endcap layers are organised in rings of chambers. All chambers in one ring are located at the same r and are periodic in ϕ. In all endcap layers, with the exception of ME1/3 CSCs, the chambers in a ring are staggered in z. In this case, the ring's nominal surface is a flat disk placed between the two planes of chambers.

When the layer is queried for the measurements compatible with a track, a first extrapolation is made to the plane representing the layer's surface. The radius of the extrapolated position is used to determine the closest disk, which is selected. If the extrapolated error, scaled by an adjustable factor, extends beyond the disk's border in r, the neighbouring disks are selected as well. Then, selected disks are individually queried for compatible chambers. This is done using the ϕ coordinate and the uncertainty of the previously extrapolated state. In the case of staggered chambers in a disk, one more short extrapolation from the ring's central surface to the surface of each chamber is needed to obtain the state on the detector surface as required by the track fitting procedure.

5.2 Track Reconstruction with the Full CMS Detector

5.2.1 Track Reconstruction in the Tracker

As in the muon system, the reconstruction process starts with the seed finding, but while in the muon system the trajectory is built during the pattern recognition, in the tracker the pattern recognition and the final fit are performed separately.

Two different algorithms have been implemented. The first [37] uses two or three consecutive hits, in the pixel and/or in the strip detector, to find the seeds. Based on the Kalman filter technique, the algorithm uses an iterative process to pass from one layer to the next and to perform the pattern recognition. The principle is very similar to that used in the muon spectrometer alone (Section 5.1.2).

The second algorithm, called *road search*, uses only the silicon strip detector to find the seeds: it takes one hit in the inner layer and one in the outer and considers the possible paths which can connect the two initial hits. The pattern recognition is performed collecting the measurements around the paths.

Both the algorithms end with a final fit of the collected hits, followed by the suppression of fake tracks.

In the following only the Kalman filter based approach is considered, because it is the default choice for matching with the tracks in the muon system.

5.2.2 Track Matching: the Global Muon Track

The track in the muon spectrometer is used to define a region of interest (ROI) in the tracker. The determination of the ROI is based on the stand-alone muon with the assumption that the muon originates from the interaction point. The definition of the region of interest has a strong impact on the reconstruction efficiency, fake rate, and CPU reconstruction time.

The ROI can be used according to two strategies: first, track matching with previously reconstructed tracker tracks; and second, prompt reconstruction and matching of the tracker tracks with the track in the muon spectrometer.

The latter approach has been designed for the High Level Trigger because it allows regional track reconstruction, but it can also be used in the off-line reconstruction. Inside the region of interest candidates for the muon trajectory (regional seeds) are built from pair or triplet of hits reconstructed on different tracker layers. It is possible to use all combinations of compatible pixel and double-sided silicon strip layers in order to achieve high efficiency. In addition, a relaxed beam-spot constraint is applied to track candidates above a given transverse momentum threshold to obtain initial trajectory parameters. Starting from the regional seeds, the standard tracker track-reconstruction algorithms described in Section 5.2.1 are used to reconstruct tracks inside the selected region of interest.

In both ROI strategies, the track matching is performed by propagating the muon and the tracker tracks onto the same plane and looking for the best χ^2 value from the comparison of track parameters. In the case of very poor χ^2 comparison which results in no matches, the matching is subsequently attempted by comparing the track separation in $\eta - \phi$ space and then Cartesian space. If there is a suitable match between tracker track and stand-alone muon track, then the hits from the tracker and the stand-alone muon track are combined in one collection and a final fit is performed over all hits. After the final global fit is made for all stand-alone track matches in the event, fake tracks are suppressed. The reconstruction of the muons ends with the matching of the global muon track and the energy deposits in the calorimeters.

5.3 Muon Identification

Standard muon track reconstruction (Sections 5.1 and 5.2) starts from the muon system and combines stand-alone muon tracks with tracks reconstructed in the inner tracker. This approach naturally identifies the muon tracks in the detector. However, a large fraction of muons with transverse momentum below 6-7 GeV/c (cf. Fig. 5.11) does not leave enough hits in the muon spectrometer to be reconstructed as stand-alone muons. Moreover, some muons can escape in the gap between the wheels (Fig. 2.11). A complementary approach, which starts from the tracker tracks, has therefore been designed [37] to identify off-line these muons and hence improve the muon reconstruction efficiency.

The algorithm for the muon identification of the tracker tracks extrapolates each reconstructed silicon track outward to its most probable location within each detector of interest (ECAL, HCAL, HO, muon system). After collecting the associated signals from each detector, the algorithm determines compatibility variables corresponding to how well the observed signals fit with the hypothesis that the silicon track is produced by a muon. The compatibility variable allows different physics analyses to make different cuts on the minimum value required to identify muons, which however should be carefully tuned in order to balance the purity and efficiency of the muon identification.

The algorithm which associates the potential muon track with the energy deposits is general enough to accept as input not only the tracker tracks, but also the global and the stand-alone muon tracks. In particular this is done at the last stage of the standard muon reconstruction, in which the energy deposits in the calorimeters are associated with the global track and the muon compatibility variable is built.

The muon identification efficiency improves by combining the different approaches, *i.e.* identifying a muon using the global, the stand-alone and the tracker tracks.

5.4 Muon Reconstruction Performance

In this section the performance of the muon reconstruction algorithms described in Section 5.1 and 5.2 is discussed. The performance of the reconstruction in the inner tracker alone is also discussed, as the tracker tracks are fundamental for the global muon reconstruction.

The muon reconstruction performance has been tested using samples of single muons generated with different values of p_T and flat distributions in η and ϕ (Table 5.1). In Chapter 7 the performance in presence of more than one muon and with non-flat distributions of their parameters is also shown.

Table 5.1: *Samples used for the study of the muon reconstruction performance ($|\eta| \leq 2.4$ and $|\phi| \leq \pi$).*

Transverse Momentum (GeV/c)	Number of events (for each muon charge)
5	50000
10	50000
50	50000
100	50000
200	50000
500	50000
1000	50000
2000	35000
3000	20000
5000	10000
1-200 (flat)	200000

The most important observables to be taken into account, in order to monitor the track reconstruction quality, are the efficiencies, the resolutions and pulls of the track parameters.

Another aspect to be considered is a possible dependence on the reconstruction to the muon charge. In Appendix B it is shown that there is no such asymmetry. For this reason in the following no distinction is made between the two charges (the two type of samples have been considered together).

Finally, in order to associate the simulated muon with the reconstructed track, a matching using a $\Delta R = \sqrt{(\Delta\phi)^2 + (\Delta\eta)^2}$ cone criterion has been used.

5.4.1 Efficiencies

Two different types of efficiency are evaluated: the total efficiency normalised to the number of simulated tracks and the algorithmic efficiency, which can be defined as the efficiency with respect to one (or more) previous reconstruction step. For the reconstruction in the muon spectrometer alone the effect of the system acceptance on the total reconstruction efficiency is also of particular interest.

For the different parts of the muon track reconstruction the efficiencies can be factorised as follow:

$$\begin{aligned}
\varepsilon_{seed} &= \varepsilon_{seed-algo} \times \varepsilon_{\mu-acceptance}, \\
\varepsilon_{sa} &= \varepsilon_{seed} \times \varepsilon_{sa-algo}, \\
\varepsilon_{glb} &= \varepsilon_{sa} \times \varepsilon_{tk} \times \varepsilon_{matching},
\end{aligned} \tag{5.2}$$

where $\varepsilon_{\mu-acceptance}$ accounts for the muon system geometry acceptance, the inefficiency due to the energy loss in the material before the muon chamber stations and the bending in the magnetic field.

In Fig. 5.2 the total efficiency for the muon seeding step (ε_{seed}) and for the stand-alone reconstruction (ε_{sa}) is shown. In Fig. 5.3 the algorithmic efficiency of the pattern recognition in the muon system ($\varepsilon_{sa-algo} = \varepsilon_{sa,seed} = \varepsilon_{sa}/\varepsilon_{seed}$) is shown. These figures and Table 5.2 show that the stand-alone muon reconstruction efficiency is determined by the seed, as $\varepsilon_{sa,seed}$ is close to 100%. The small inefficiency is due to incorrectly estimated parameters at the seeding stage, which may lead to a failure in the pattern recognition. This assumption can be verified by looking at the resolution and pulls of the seed parameters shown in Sections 5.4.2 and 5.4.3.

The loss in efficiency at $|\eta| \sim 0.3$ is due to a geometrical effect, since in that region there is a discontinuity between the central wheel and its neighbours (Fig. 2.3). The dips in the $0.8 < |\eta| < 1.2$ region are due to failures in the seed-finding algorithm which may be recovered although that region is known to be problematic as there DT and CSC segments are used together to estimate the

Table 5.2: *Integrated efficiencies for the stand-alone muon reconstruction.*

p_T sample (GeV/c)	ε_{sa} (%)	ε_{seed} (%)	$\varepsilon_{sa,seed}$ (%)
5	96.96 ± 0.06	97.51 ± 0.05	99.43 ± 0.02
10	99.43 ± 0.02	99.57 ± 0.02	99.865 ± 0.012
50	99.53 ± 0.02	99.61 ± 0.02	99.919 ± 0.009
100	99.51 ± 0.02	99.62 ± 0.02	99.891 ± 0.011
200	99.49 ± 0.02	99.60 ± 0.02	99.896 ± 0.010
500	99.34 ± 0.03	99.51 ± 0.02	99.829 ± 0.013
1000	99.11 ± 0.03	99.38 ± 0.03	99.731 ± 0.017

seed state. The overall integrated efficiency, for momenta above 10 GeV/c, is more than 99%. For low momenta the efficiency decreases because a significant fraction of muons looses energy in the material before the muon stations or because of the bending in the magnetic field.

A possible way to decouple the algorithmic efficiency from the muon system acceptance is to select only a special set of the simulated tracks. In particular it is possible to select only those simulated tracks that leave more than a given number of simulated hits in the detector and study the corresponding reconstruction efficiency. With this set it is possible to evaluate the efficiency to find a seed or a track as a function of the minimum required number of *true* hits in the detector. In Fig. 5.4 this efficiency is shown both for the seed, $\varepsilon_{seed}(n^{min}_{simhits})$, and for the whole stand-alone muon reconstruction, $\varepsilon_{sa}(n^{min}_{simhits})$. As a sanity check $\varepsilon_{sa,seed}(n^{min}_{simhits})$ is also evaluated. The efficiencies corresponding to the point at the x-axis origin are equal to the values reported in Table 5.2 because making no requirement on the number of simulated hits means no restriction on the simulated tracks. Similarly the n^{th} point means: only simulated track with *n or more* associated simulated hits in the muon spectrometer are selected and used to calculate the efficiency.

The curves show the expected trend (they are monotonically increasing, except for the TeV-muons). Two regions can be identified: from 0 to about 9 and from about 9 to the plateau. The first interval is defined by the minimum number of reconstructed hits required to have a segment in CSC and DT stations, in addition to a RPC measurement. Requiring at least 9 simulated hits is equivalent to request at least two segments in the muon system. The curves asymptotically reach a maximum, which is the efficiency for a high quality muon in the spectrometer. Notice the behaviour of the TeV-muons: the pattern recognition efficiency (Fig. 5.4) decreases above 24 hits. This is due to the high probability that a TeV-muon emits a photon during the energy loss

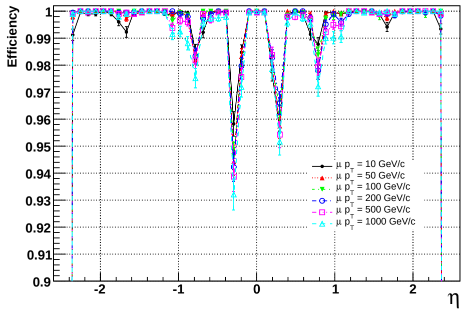

(a) ε_{seed} vs η

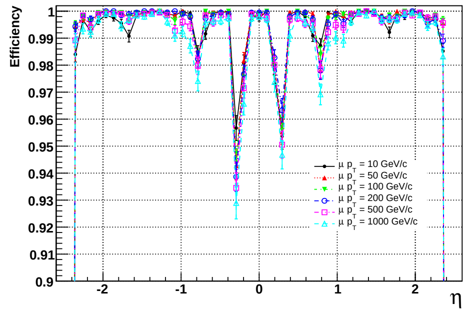

(b) ε_{sa} vs η

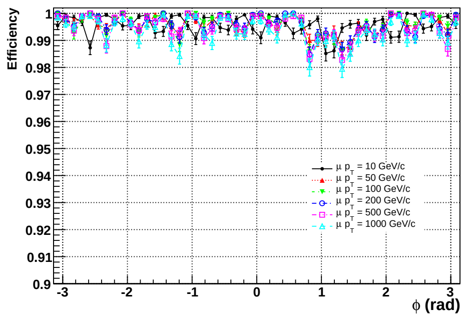

(c) ε_{seed} vs ϕ

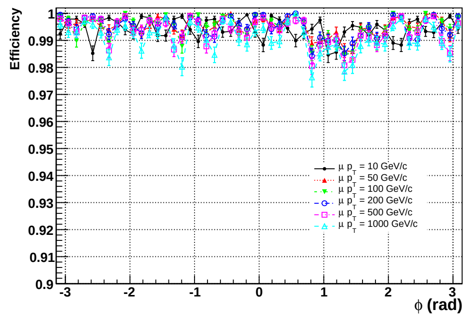

(d) ε_{sa} vs ϕ

Figure 5.2: *Efficiency of the reconstruction in the muon spectrometer as a function of η and ϕ, for different p_T samples.*

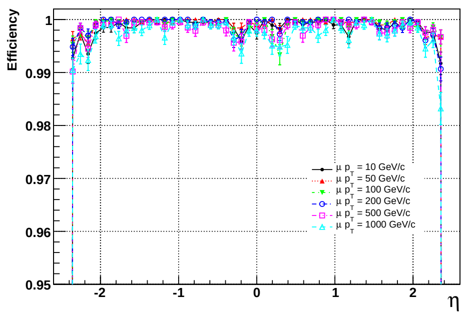

(a) $\varepsilon_{sa,seed}$ vs η

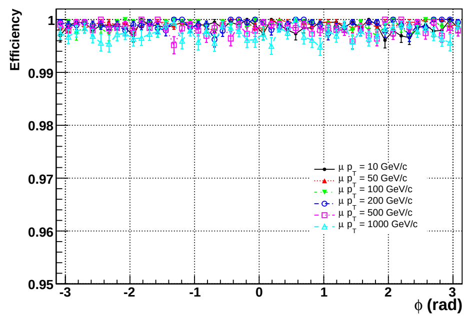

(b) $\varepsilon_{sa,seed}$ vs ϕ

Figure 5.3: *Algorithmic efficiency of the stand-alone muon reconstruction.*

process, leading to an electromagnetic shower in the spectrometer. Many segments are generated and the probability of building fake segments (or segments with incorrect parameters) increases considerably, reducing the algorithmic ef-

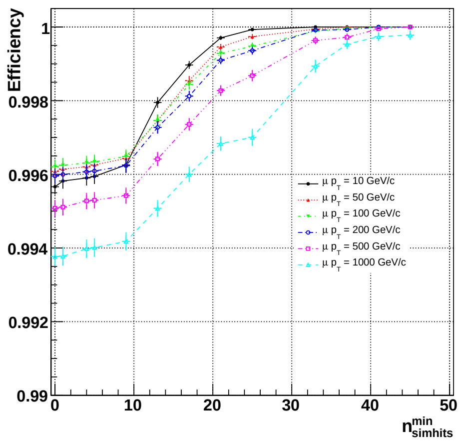

(a) ε_{seed} vs $n^{min}_{simhits}$.

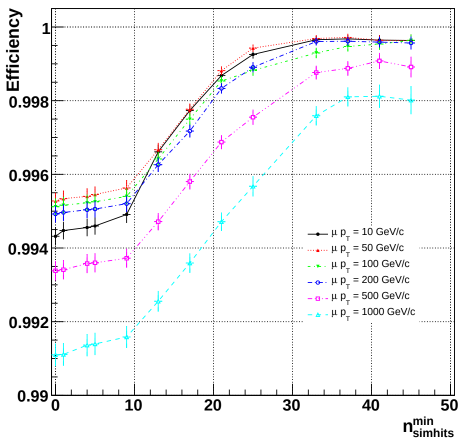

(b) ε_{sa} vs $n^{min}_{simhits}$.

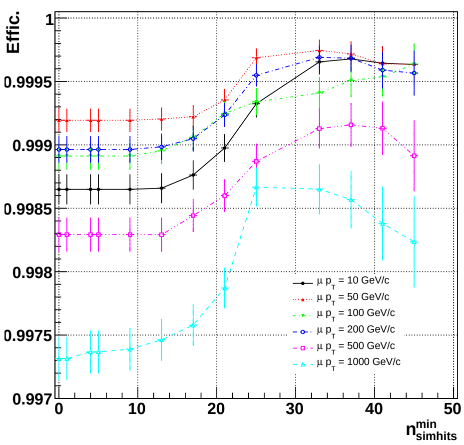

(c) $\varepsilon_{sa,seed}$ vs $n^{min}_{simhits}$.

Figure 5.4: *Efficiency as a function of the minimum required number of simulated hits in the muon spectrometer.*

ficiency of the pattern recognition. Therefore for TeV-muons the requirement on the *minimum* number of simulated hits is no longer a useful parameter for establishing the quality of the track, and $\varepsilon(n_{simhits})$ should be evaluated instead.

The value at the plateau gives the efficiency divided by the acceptance and the loss in efficiency due to the muon spectrometer acceptance is the difference between the value at the plateau and the value at the origin. This shows that the loss in efficiency in the muon track reconstruction is due to the acceptance.

It is interesting to note that modifying the requirement, *i.e.* changing it from the simulated hits to the reconstructed hits, it is possible to estimate, using real data and a tag and probe method, the algorithmic efficiency and the effect of acceptance on the stand-alone muon reconstruction.

The inner tracker is less affected by multiple scattering and energy loss than the muon system. Moreover the magnetic field in the tracker volume is homogeneous and almost constant. In Fig. 5.5 the efficiency as a function of pseudorapidity and ϕ, for different p_T samples, is shown. The integrated efficiency is almost constant for all p_T values (Table 5.3 and Fig. 5.11) and its value is above 99.5%. The dip at $\eta \simeq 0$ is due to the tracker geometry. The tracker is made of two half-barrels joined together, and the junction surface is at $\eta = 0$.

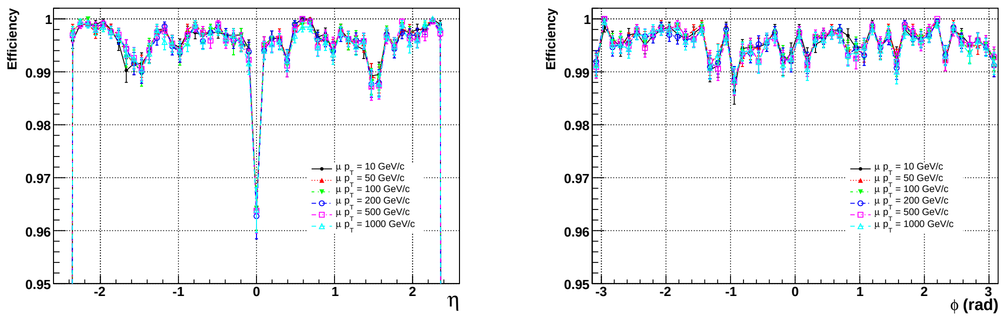

(a) ε_{tk} vs η

(b) ε_{tk} vs ϕ

Figure 5.5: *Efficiency of the reconstruction in the inner tracker system alone as a function of η and ϕ, for different p_T samples.*

For the global muon reconstruction it is important to evaluate four types of efficiency: ε_{glb} (Fig. 5.6), $\varepsilon_{glb,sa} = \varepsilon_{glb}/\varepsilon_{sa}$ (Fig. 5.7), $\varepsilon_{glb,tk} = \varepsilon_{glb}/\varepsilon_{tk}$ (Fig. 5.8) and $\varepsilon_{matching} = \varepsilon_{glb}/(\varepsilon_{sa} \times \varepsilon_{tk})$ (Fig. 5.9).

From the analysis of the efficiency spectra, the structure in Fig. 5.6 can be classified as follow:

- $\eta \simeq 0$: junction surface between the two tracker barrels;
- $|\eta| \simeq 0.3$: inter-space between the DT central wheel and its neighbours;

Table 5.3: *Integrated efficiency for the tracker tracks reconstruction.*

p_T sample (GeV/c)	ε_{tk} (%)
5	99.56 ± 0.02
10	99.56 ± 0.02
50	99.57 ± 0.02
100	99.55 ± 0.02
200	99.54 ± 0.02
500	99.54 ± 0.02
1000	99.51 ± 0.02

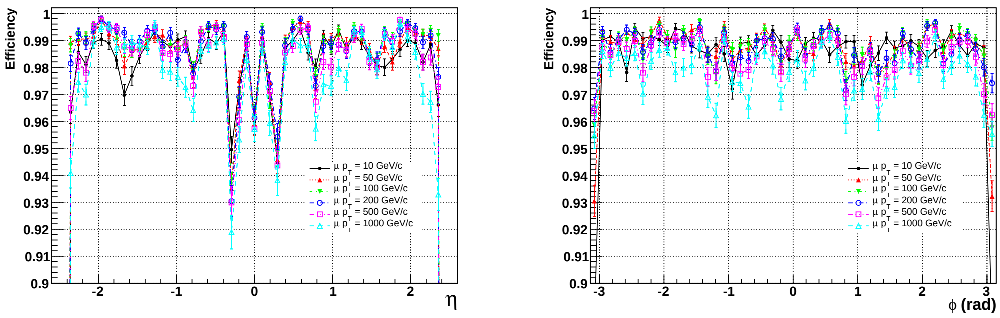

(a) ε_{glb} vs η (b) ε_{glb} vs ϕ

Figure 5.6: *Efficiency of the global muon reconstruction as a function of η and ϕ, for different p_T samples.*

- $0.8 < |\eta| < 1.2$: problematic region for seed estimation (DT and CSC overlap);
- $|\eta| \simeq 1.8$: problematic region for tracker track reconstruction (transition from TID to TID/TEC subsystem);
- $\phi \simeq 1.2$: barrel inactive region (chimney), because of instrumentation services;
- periodic structure in *phi*: loss in efficiency in the stand-alone muon reconstruction due to muons which escape in the space between two adjacent sectors (Fig. 2.3) or chambers in CSCs (although all chambers overlap in ϕ, except those in ME1/3). See also the effect on the parameter resolutions in Fig. 5.19.

The $\varepsilon_{matching}$ is above 99% over all the p_T spectra down to 5 GeV/c, for which is

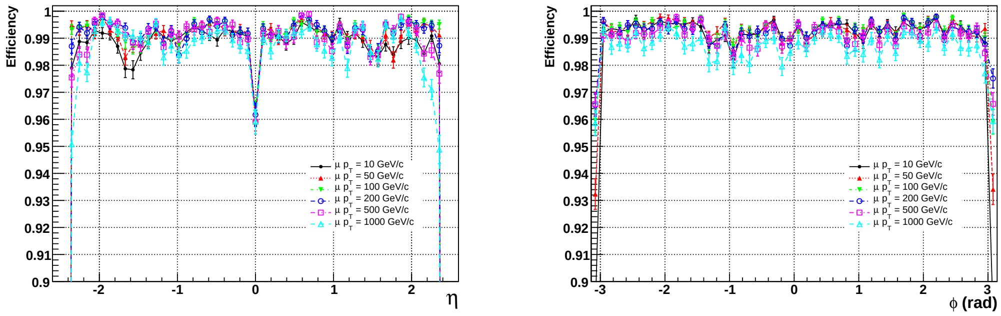

(a) $\varepsilon_{glb,sta}$ vs η (b) $\varepsilon_{glb,sta}$ vs ϕ

Figure 5.7: *Efficiency of the muon reconstruction normalised to the stand-alone muon tracks reconstruction, as a function of η and ϕ, for different p_T samples.*

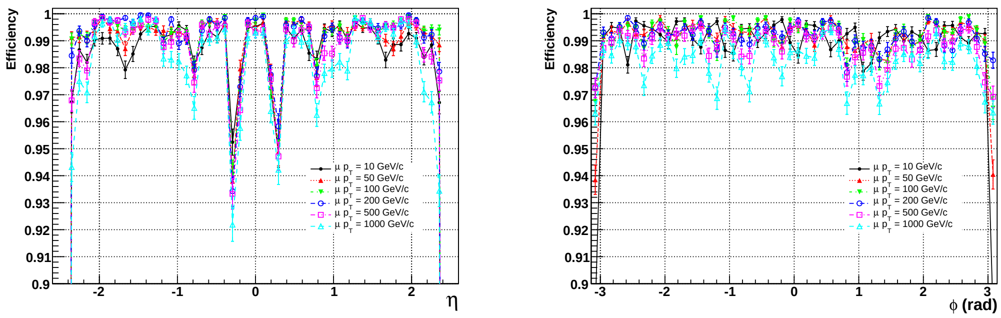

(a) $\varepsilon_{glb,tk}$ vs η (b) $\varepsilon_{glb,tk}$ vs ϕ

Figure 5.8: *Efficiency of the muon reconstruction normalised to the tracker track reconstruction, as a function of η and ϕ, for different p_T samples.*

around 91%. This is due to muon seed parameters which are poorly estimated; this directly affects the stand-alone muon reconstruction and the subsequent matching with the tracker tracks. This can be cured by tuning the seed parameters for low p_T muons. $\varepsilon_{glb,sta}$ shows that the stand-alone muon efficiency dominates the final muon reconstruction efficiency. The integrated efficiencies of the global muon reconstruction, for different p_T bin samples, are shown in Table 5.4.

The Fig. 5.10 shows a direct comparison of the reconstruction efficiencies: ε_{seed}, ε_{sa}, ε_{tk} and ε_{glb}, as a function of p_T, η and ϕ. The plots have been made using the flat p_T sample described in Table 5.1. The values are almost the same for $p_T \geq 10$ GeV/c. The structure visible in the efficiency as a function of ϕ, for the seed, stand-alone and global reconstruction, is due to the ϕ-acceptance of

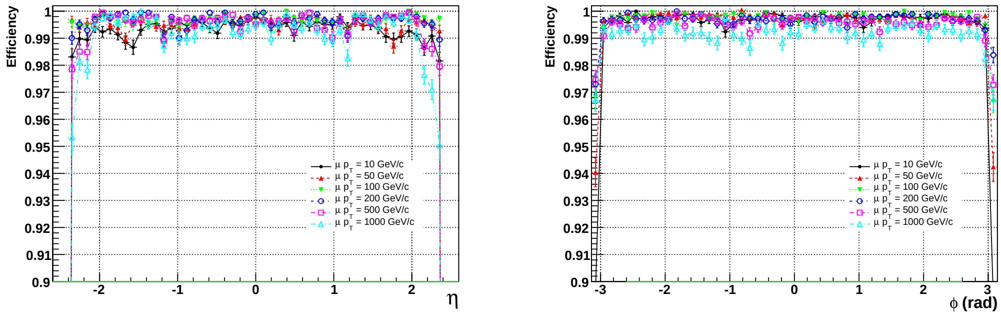

(a) $\varepsilon_{matching}$ vs η

(b) $\varepsilon_{matching}$ vs ϕ

Figure 5.9: *Matching efficiency between muon and tracker tracks, as a function of η and ϕ, for different p_T samples.*

Table 5.4: *Integrated efficiencies for the global muon reconstruction.*

p_T sample (GeV/c)	ε_{glb} (%)	$\varepsilon_{glb,sa}$ (%)	$\varepsilon_{glb,tk}$ (%)	$\varepsilon_{matching}$ (%)
5	87.78 ± 0.11	90.54 ± 0.10	88.17 ± 0.11	90.94 ± 0.09
10	98.31 ± 0.04	98.88 ± 0.03	98.75 ± 0.04	99.31 ± 0.03
50	98.65 ± 0.04	99.11 ± 0.03	99.07 ± 0.03	99.54 ± 0.02
100	98.72 ± 0.04	99.21 ± 0.03	99.17 ± 0.03	99.65 ± 0.02
200	98.68 ± 0.04	99.19 ± 0.03	99.14 ± 0.03	99.65 ± 0.02
500	98.37 ± 0.04	99.03 ± 0.03	99.83 ± 0.03	99.49 ± 0.02
1000	97.77 ± 0.05	98.65 ± 0.04	98.35 ± 0.04	99.13 ± 0.03

the muon system, as discussed in Section 5.4.2.

The efficiency as a function of the muon transverse momentum (Fig. 5.11) is of particular interest. The muon reconstruction efficiency increases up to a plateau which is approximately constant from 8 GeV/c to 1 TeV/c (starting from $p_T = 5$ GeV/c more than 50% of muons is reconstructed). At TeV momenta the muon reconstruction efficiency decreases, even if very slowly, due to an increased bremsstrahlung probability.

For the track reconstruction in the tracker the efficiency is stable already above 1 GeV/c, but it does not take into account the muon identification efficiency, which is naturally included in the track reconstruction with the muon spectrometer. The high reconstruction efficiency in the tracker together with the muon spectrometer ensure a robust muon identification system.

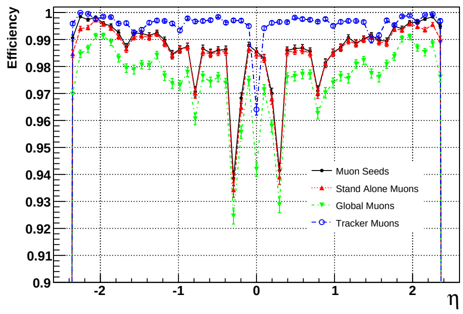

(a) ε_{seed}, ε_{sa}, ε_{tk} and ε_{glb} vs η

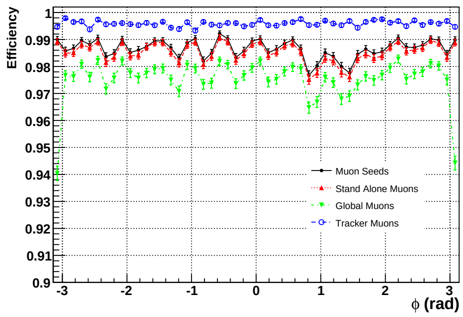

(b) ε_{seed}, ε_{sa}, ε_{tk} and ε_{glb} vs ϕ

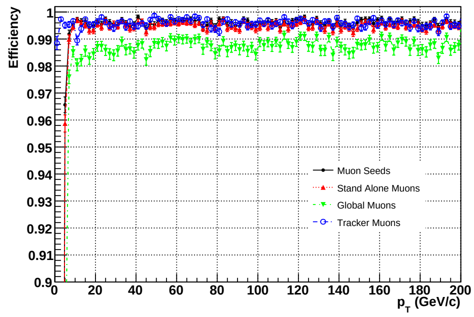

(c) ε_{seed}, ε_{sa}, ε_{tk} and ε_{glb} vs p_T

Figure 5.10: *Efficiencies of the different muon reconstruction steps as a function of η, ϕ and p_T.*

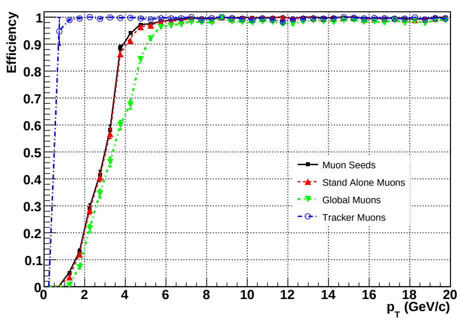

(a) 1-20 GeV/c region.

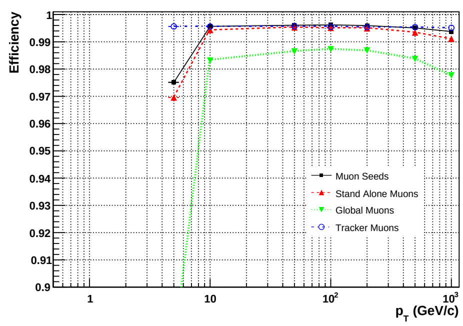

(b) 5-1000 GeV/c region.

Figure 5.11: *Efficiencies of the different muon reconstruction steps as a function of p_T.*

5.4.2 Resolutions and Residuals

To describe a track, the following information is used: a reference position on the track (**v**), the momentum at this given reference point on track, a 5D curvilinear covariance matrix resulting from the track fit, the charge, the χ^2, the number of degrees of freedom and a summary of the information on the collected hits. For tracks reconstructed in the tracker, the reference position is the point of closest approach to the centre of CMS. This may not be the case for muons originated by decays of long-lived particles, although for the samples used in the present analysis this is the case. The parameters associated with the 5D curvilinear covariance matrix are: q/p, λ, ϕ, d_{xy}, d_{sz}. These are defined as:

- $q/|\mathbf{p}|$ = signed inverse of momentum expressed in $(GeV/c)^{-1}$;
- λ = complement to $\pi/2$ of the polar angle at the given point;
- ϕ = azimuthal angle at the given point;
- $d_{xy} = -v_x \sin\phi + v_y \cos\phi$, expressed in cm. Geometrically, d_{xy} is the signed distance in the (x,y) plane between the point (0,0) and the straight line passing through (v_x,v_y) with azimuthal angle ϕ. It coincides with the impact parameter with respect to (0,0,0) only if the reference point is close to (0,0,0). In other parametrisations it is also called d_0 ($d_0 = -d_{xy}$).
- $d_{sz} = v_z \cos\lambda - (v_x \cos\phi + v_y \sin\phi)\sin\lambda$ expressed in cm. The d_{sz} parameter is the signed distance in the (s,z) plane between the point ($s = 0$,$z = 0$) and the the straight line passing through **v** with angles (ϕ,λ). The s-axis is defined by the projection of the straight line onto the (x,y) plane. The convention is to assign the s coordinate for (v_x,v_y) as the value $v_x \cos\phi + v_y \sin\phi$. This value is zero when (v_x,v_y) is the point of minimum transverse distance to (0,0). A more intuitive parameter, which represents the track position along the beam axis, is $d_z = d_{sz}/\cos\lambda$.

Note that d_{xy} and d_z provide sensible estimates of the distance from the true particle trajectory to the IP only in two cases:

1. when **v** already corresponds to the point of minimum transverse distance to the IP or it is close to it (so that the differences between considering the exact trajectory or a straight line are negligible).
2. When the track has very high momentum.

There are two more parameters of particular interest for the physics analysis: the pseudorapidity and q/p_T. Since η and λ are closely related, only the former is studied here. For the same reason q/p_T is chosen instead of q/p. Moreover q/p_T is more suitable than p_T because it distributes normally around the true value. This because q/p_T is, locally, directly proportional to the curvature in the bending plane, which is what is actually measured by the tracking system. The resolution on this parameter is defined as the Gaussian width of:

$$\frac{\delta(\frac{q}{p_T})}{\frac{q}{p_T}} = \frac{q^{\text{rec}}/p_{\text{T}}^{\text{rec}} - q^{\text{sim}}/p_{\text{T}}^{\text{sim}}}{q^{\text{sim}}/p_{\text{T}}^{\text{sim}}}, \tag{5.3}$$

where q is the charge and $p_{\text{T}}^{\text{sim}}$ and $p_{\text{T}}^{\text{rec}}$ are the simulated and reconstructed transverse momenta, respectively. In the following the resolution is indicated as $R(\frac{q}{p_T})$. Summarising, in this section the following quantities are studied: the resolution on q/p_T and the residuals of ϕ, η, d_{xy} and d_z, where the residual for a variable a is defined as the Gaussian width of:

$$\delta a = a^{rec} - a^{gen}.$$

In the following the residual is indicated as $R(a)$.

The q/p_T resolution as function of η and ϕ, for the seed and the stand-alone muon reconstruction is shown in Fig. 5.12. The resolution for the stand-alone muon reconstruction ranges from 8% in the barrel, for the 10 GeV/c p_T sample, to 40% at 2.4 for the TeV-muons, matching the design performance of the muon system [47]. The peak in the spectra corresponds to the problematic regions already discussed in the analysis of the efficiencies. The resolution degrades as the pseudorapidity increases. This is due to the more complex environment in which the endcaps are embedded: the integral of the magnetic field decreases, the magnetic field presents large inhomogeneities and it is no longer solenoidal. As an example, for muons with a momentum of 100 GeV/c the sagitta measured at $|\eta| \sim 2.4$ is five times smaller than the sagitta measured at $|\eta| \sim 1.6$. The q/p_T resolution as a function of ϕ reflects the periodic structure of the CMS apparatus (Fig. 5.19), moreover it shows the improvement obtained passing from a parametrised estimation (the seed) to a true fit.

It is also interesting to evaluate the effect of the constraint at the vertex on the q/p_T resolution. In Table 5.5 the $R(q/p_T)$ values before and after the constraint at the vertex are reported. To better appreciate the improvement, the table has been divided in three pseudorapidity regions: barrel ($|\eta| < 0.8$), overlap ($0.8 < |\eta| < 1.2$) and end-caps ($1.2 < |\eta| \leq 2.4$). The $R(q/p_T)$ distribution before the constraint at the IP is shown in Fig. 5.13. An improvement is visible for all p_T values. In particular the high p_T muons gain a factor of two in the $R(q/p_T)$ resolution.

The $R(q/p_T)$ distributions for the track reconstruction in the tracker and for the global muon reconstruction are shown in Fig. 5.14. The two curves do

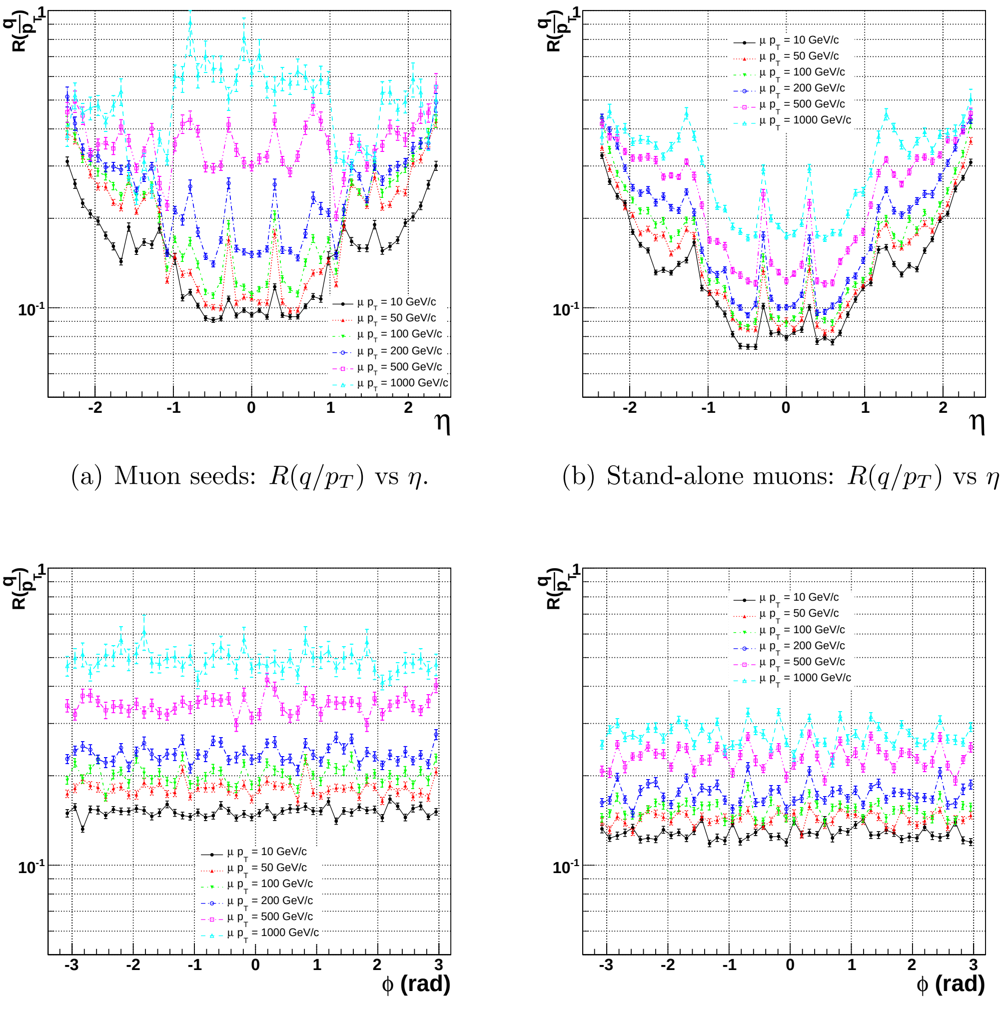

(a) Muon seeds: $R(q/p_T)$ vs η.

(b) Stand-alone muons: $R(q/p_T)$ vs η.

(c) Muon seeds: $R(q/p_T)$ vs ϕ.

(d) Stand-alone muons: $R(q/p_T)$ vs ϕ.

Figure 5.12: *Resolution on q/p_T in the muon spectrometer as a function of η and ϕ, for different p_T samples.*

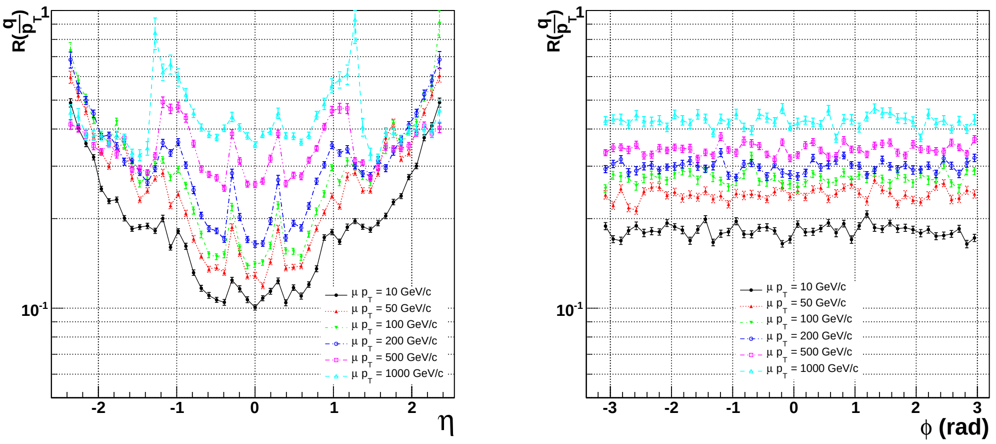

(a) Stand-alone muons: $R(q/p_T)$ vs η. (b) Stand-alone muons: $R(q/p_T)$ vs ϕ.

Figure 5.13: *Resolution on q/p_T before the constraint at the vertex as a function of η and ϕ, for different p_T samples. Cf. Fig. 5.12.*

not differ much for low-p_T; the main differences are at high η. The benefits to include, in the trajectory, the hits reconstructed in the muon chambers become evident for momenta greater than 200 GeV/c (Fig. 5.15). The main reason of

Table 5.5: *Resolution on q/p_T before and after the constraint at vertex, divided by pseudorapidity regions.*

p_T (GeV/c)	$R(q/p_T)$ (%) Before/after the vertex constraint		
	Barrel	Overlap	End-caps
5	9.63±0.06 / 6.80±0.04	12.21±0.09 / 10.25±0.08	19.76±0.09 / 16.17±0.08
10	11.51±0.06 / 8.36±0.04	17.38±0.13 / 11.97±0.09	23.21±0.12 / 17.55±0.08
50	14.52±0.08 / 9.26±0.05	21.68±0.18 / 12.67±0.10	30.1±0.2 / 19.79±0.09
100	16.14±0.09 / 9.74±0.05	24.9±0.2 / 13.75±0.11	32.9±0.3 / 21.24±0.11
200	18.83±0.11 / 10.82±0.06	29.7±0.4 / 15.11±0.13	32.6±0.3 / 24.29±0.14
500	26.2±0.2 / 13.63±0.08	40.3±1.0 / 19.30±0.18	32.9±0.3 / 30.8±0.3
1000	49.2±1.2 / 18.64±0.11	95.2±1.7 / 24.6±0.3	39.4±0.7 / 38.5±0.6

this behaviour is related to the formula[1]:

$$\frac{\delta p_T}{p_T} = \frac{0.0136}{\beta BL}\sqrt{\frac{x}{X_0}}\sqrt{\frac{4A_N}{N}} \oplus \frac{\sigma \cdot p_T}{0.3BL^2}\sqrt{4A_N}, \tag{5.4}$$

where $\beta = v/c$, x/X_0 is the thickness of the scattering medium in radiation lengths, B is the magnetic field value, L the length of the tracking system, N the number of measurements, σ their individual errors and

$$A_N = \frac{180N^3}{(N-1)(N+1)(N+2)(N+3)}. \tag{5.5}$$

The first term represents the contribute of multiple scattering and it is constant with respect to p_T. This term is dominant in the stand-alone muon reconstruction particularly in the barrel and it has the effect to maintain the resolution almost constant up to 100 GeV/c. Above this value, the second term starts to become important. In the tracker the multiple scattering is lower than in the muon system and the dominant term is the one directly related to measurement precision. As the p_T increases, the measurement term becomes more and more important, but can be balanced by a a longer path length in the magnetic field (*i.e.* a larger L): this is accomplished using the tracker and the muon system together. The combination of the information from the tracker and the muon chamber ensures the best p_T estimation both at low and high momenta.

In Table 5.6 a summary of the values of $R(q/p_T)$, in the barrel, overlap and endcap regions is reported for the global muon reconstruction and for the tracker track reconstruction.

Table 5.6: *Resolution on q/p_T divided by pseudorapidity regions for the different muon reconstruction steps.*

p_T (GeV/c)	$R(q/p_T)$ (%) Tracker/Global		
	Barrel	Overlap	End-caps
5	$0.814 \pm 4 \cdot 10^{-3}$ / $0.857 \pm 5 \cdot 10^{-3}$	$1.275 \pm 8 \cdot 10^{-3}$ / $1.385 \pm 1.2 \cdot 10^{-2}$	$1.607 \pm 6 \cdot 10^{-3}$ / $1.611 \pm 7 \cdot 10^{-3}$
10	$0.838 \pm 4 \cdot 10^{-3}$ / $0.838 \pm 4 \cdot 10^{-3}$	$1.307 \pm 9 \cdot 10^{-3}$ / $1.410 \pm 1.1 \cdot 10^{-2}$	$1.681 \pm 7 \cdot 10^{-3}$ / $1.672 \pm 7 \cdot 10^{-3}$
50	$1.059 \pm 5 \cdot 10^{-3}$ / $1.051 \pm 5 \cdot 10^{-3}$	$1.594 \pm 1.1 \cdot 10^{-2}$ / $1.584 \pm 1.1 \cdot 10^{-2}$	$2.203 \pm 1.0 \cdot 10^{-2}$ / $2.177 \pm 1.0 \cdot 10^{-2}$
100	$1.459 \pm 7 \cdot 10^{-3}$ / $1.431 \pm 7 \cdot 10^{-3}$	$2.029 \pm 1.3 \cdot 10^{-2}$ / $1.962 \pm 1.3 \cdot 10^{-2}$	$2.976 \pm 1.5 \cdot 10^{-2}$ / $2.899 \pm 1.5 \cdot 10^{-2}$
200	$2.405 \pm 1.1 \cdot 10^{-2}$ / $2.263 \pm 1.1 \cdot 10^{-2}$	3.20 ± 0.02 / 2.89 ± 0.02	4.76 ± 0.03 / 4.42 ± 0.02
500	5.66 ± 0.03 / 4.07 ± 0.02	7.01 ± 0.05 / 4.71 ± 0.03	10.61 ± 0.06 / 8.13 ± 0.05
1000	11.20 ± 0.05 / 5.14 ± 0.03	13.60 ± 0.10 / 5.93 ± 0.04	19.71 ± 0.11 / 11.60 ± 0.08

The value of $R(q/p_T)$ is obtained by fitting the central part of the distribution. Also, the charge identification probability has been evaluated for the

[1] eq. 5.4 is not directly used in the CMS track reconstruction because it neglects the magnetic field inhomogeneities, in particular in the muon system, and the very complex geometry. Nevertheless the general features extracted from it are also valid for the real CMS tracking system.

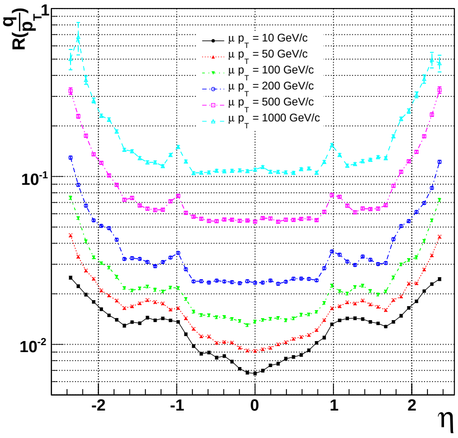

(a) Tracker tracks: $R(q/p_T)$ vs η.

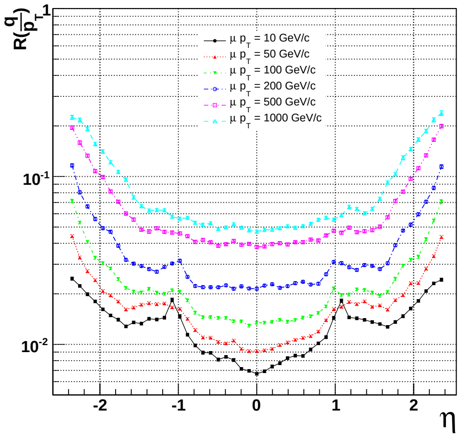

(b) Global muons: $R(q/p_T)$ vs η.

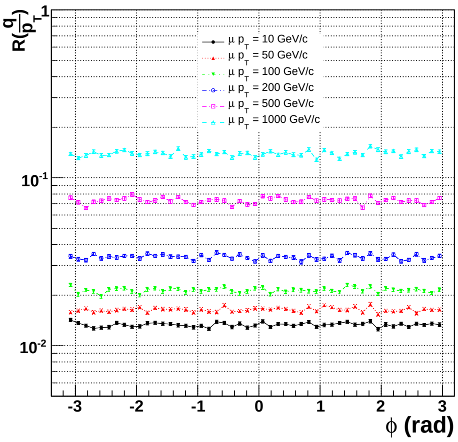

(c) Tracker tracks: $R(q/p_T)$ vs ϕ.

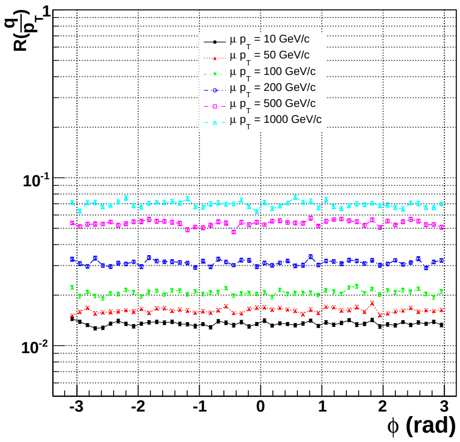

(d) Global muons: $R(q/p_T)$ vs ϕ.

Figure 5.14: *Resolution on q/p_T with the tracker alone and with the full CMS tracking system as a function of η and ϕ, for different p_T samples.*

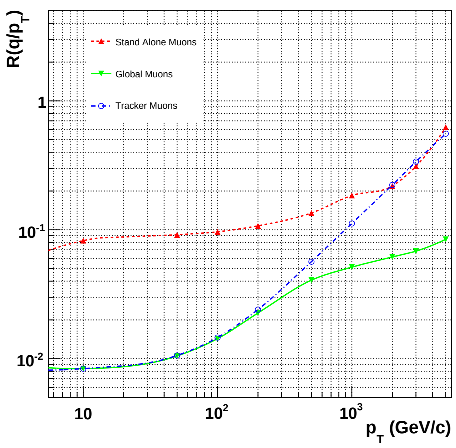

(a) Barrel.

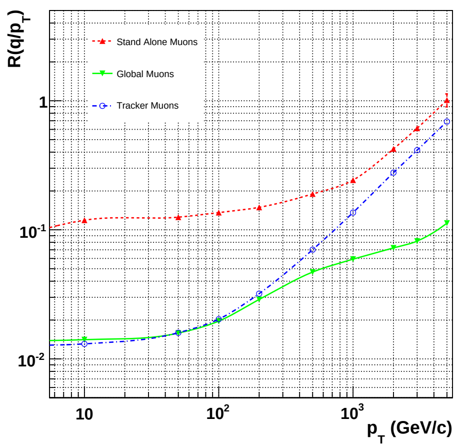

(b) Overlap.

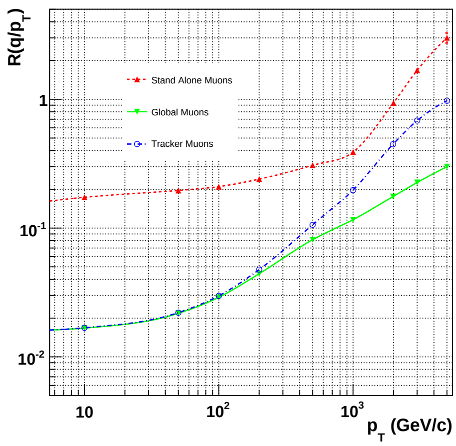

(c) End-caps.

Figure 5.15: *Resolution on q/p_T with the tracker alone, with the muon spectrometer alone and with the full CMS tracking system, as a function of p_T.*

different stages of the reconstruction. In Fig. 5.16 and 5.17 the probability to assign the correct charge is shown as a function of η and ϕ.

The correct charge assignment probability in the muon spectrometer is above 75% for TeV-muons and reaches 99% for lower p_T muons. With the full tracking system the probability stays above 98%, even for TeV-muons. It is interesting to note that, contrary to the momentum estimation, the track reconstruction in the tracker alone has a higher probability to assign the correct sign of the charge than the full tracking system. This derives from the more complex assumptions

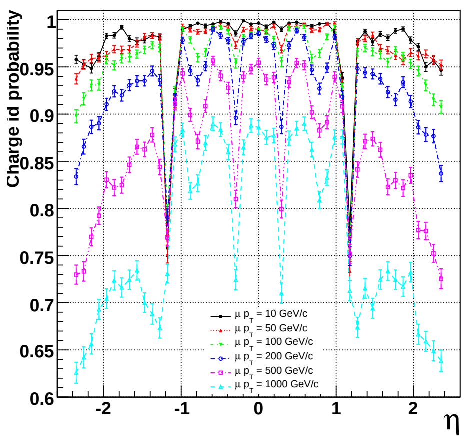

(a) Muon seeds: charge id vs η.

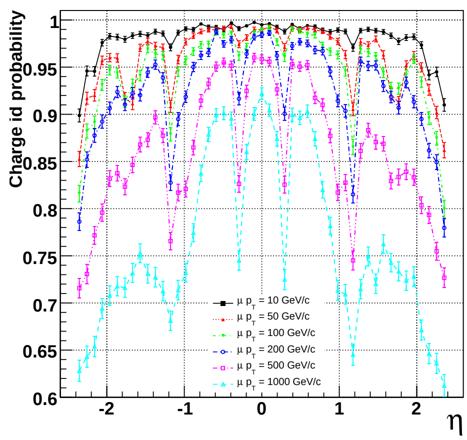

(b) Stand-alone muons: charge id vs η

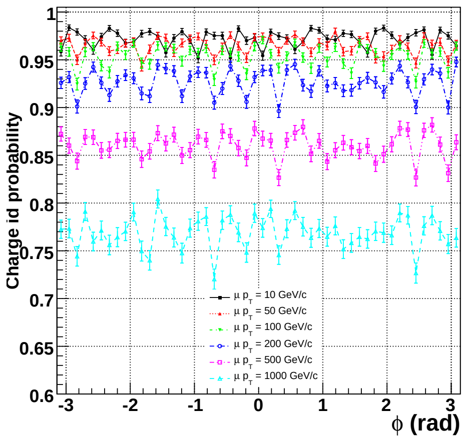

(c) Muon seeds: charge id vs ϕ

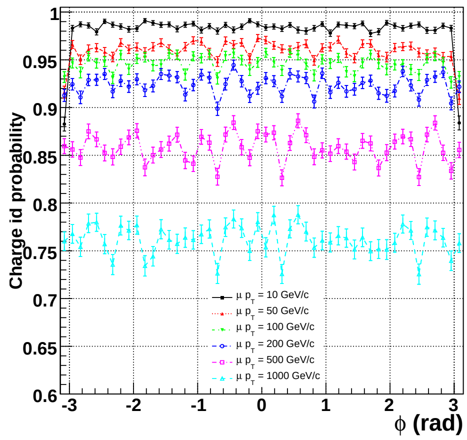

(d) Stand-alone muons: charge id vs ϕ

Figure 5.16: *Correct charge assignment probability in the muon spectrometer alone as a function of η and ϕ, for different p_T samples.*

used during the fit of the measurements collected in the whole tracking system. A better assignment can be achieved by either reviewing the assumption made at the fit level or by more heavily weighting the tracker track charge.

The q/p_T resolution is directly connected to the residual of the ϕ parameter, because the curvature measured in the $r-\phi$ plane determines the q/p_T value. Almost all what has been said for $R(q/p_T)$ is also applicable to the ϕ residual. The structure in the $R(q/p_T(\phi))$ present in the stand-alone muon reconstruction is even more evident in the ϕ residual as a function of ϕ (Fig. 5.19). In the barrel the peaks correspond to the discontinuity between sectors (Fig. 2.3). In

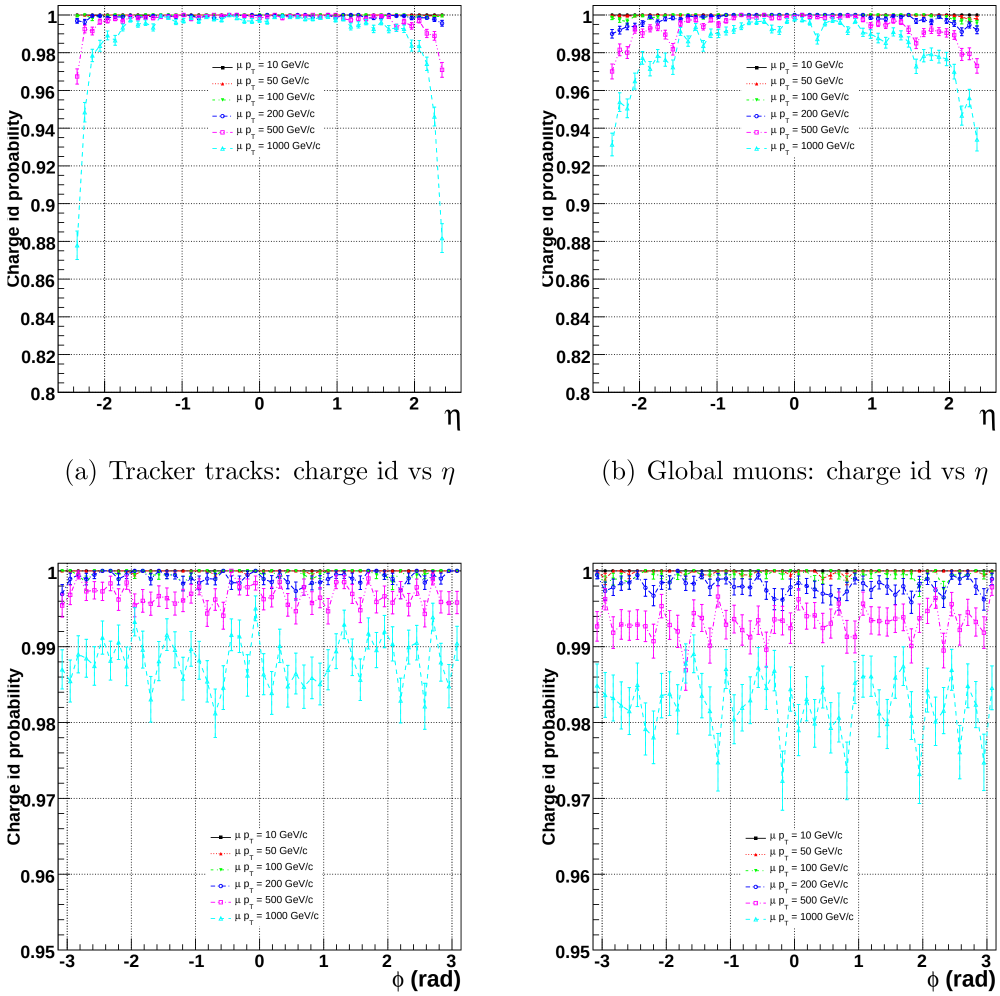

(a) Tracker tracks: charge id vs η

(b) Global muons: charge id vs η

(c) Tracker tracks: charge id vs ϕ

(d) Global muons: charge id vs ϕ

Figure 5.17: *Correct charge assignment probability with the tracker alone and with the full tracking system as a function of η and ϕ, for different p_T samples.*

the endcap the structure is due to the geometrical configuration of the CSC stations.

The distribution of the ϕ residual as a function of p_T, for the tracker tracks, the seed, the stand-alone and the global muon reconstruction is shown in Fig. 5.20. The residuals for the global muon and the tracker track reconstruction overlay each other.

$R(\phi)$ is proportional to $1/p_T$, which means it is proportional to r_T, the curvature in the bending plane, as expected. The improvement passing from the stand-alone muon tracks to the global tracks leads to a gain of a factor 40

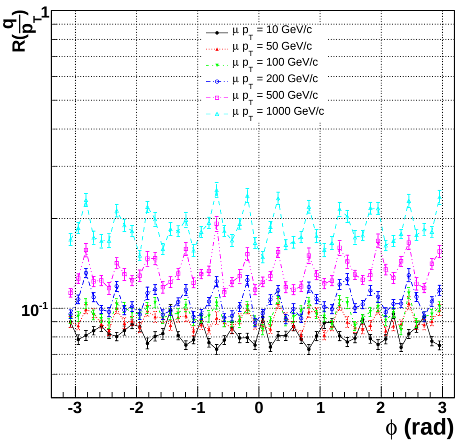

(a) $R(q/p_T)$ vs ϕ in the barrel.

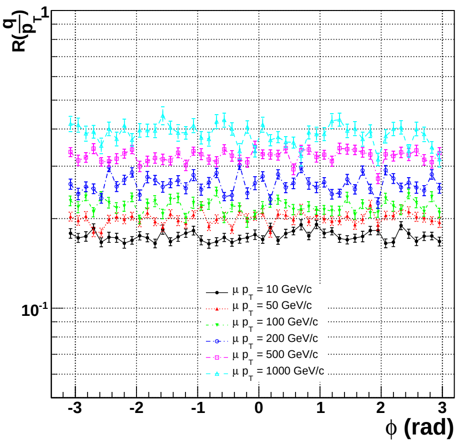

(b) $R(q/p_T)$ vs ϕ in the endcaps.

Figure 5.18: *Resolution on q/p_T in the muon spectrometer, divided by pseudorapidity regions.*

on the ϕ residual.

The other parameter which defines the direction of the muons is the pseudorapidity (Fig. 5.21). Also $R(\eta)$ is proportional to $1/p_T$, because a set of positions is what is really measured in the detector. The gain in the η residual passing from the stand-alone reconstruction to the reconstruction with the whole CMS tracking system is a factor of 10. Note also the better resolution around $\eta = 0$ of the global reconstruction with respect to the tracker alone. Although small, it shows the interplay of the two terms in eq. 5.4.

The other two parameters to be evaluated are d_{xy} and d_z. In Fig. 5.22 there quantities are shown only for the global reconstruction; for the tracker they distribute identically. The resolution (expressed in μm) on the transverse impact parameter is about three times more accurate than the one on the longitudinal parameter. For both parameters, a better accuracy is obtained as the muon transverse momentum increases.

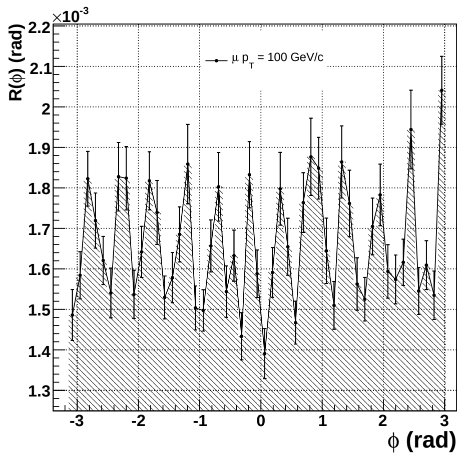

(a) p_T=100 GeV/c in the barrel.

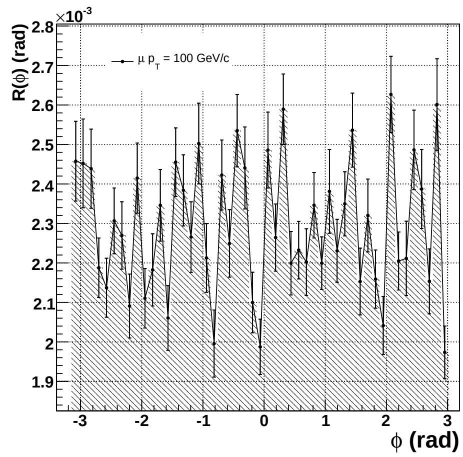

(b) p_T=100 GeV/c in the endcaps.

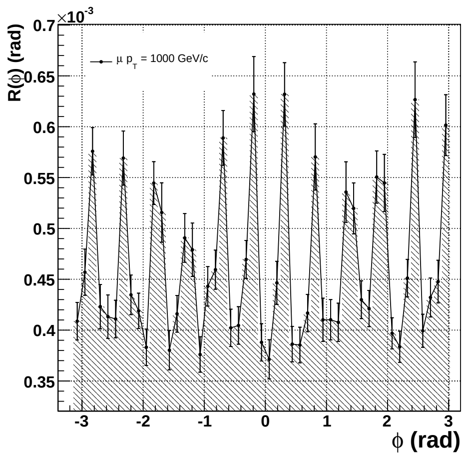

(c) p_T=1000 GeV/c in the barrel.

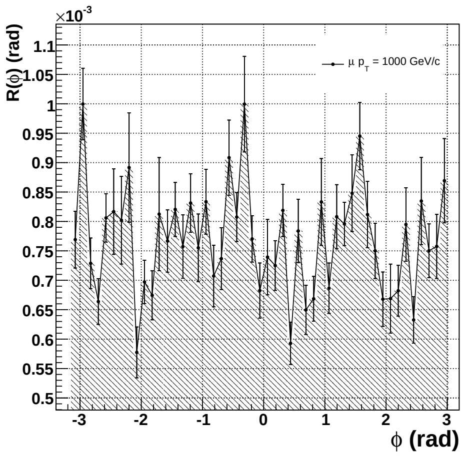

(d) p_T=1000 GeV/c in the endcaps.

Figure 5.19: *ϕ residual as a function of ϕ for the stand-alone muon reconstruction.*

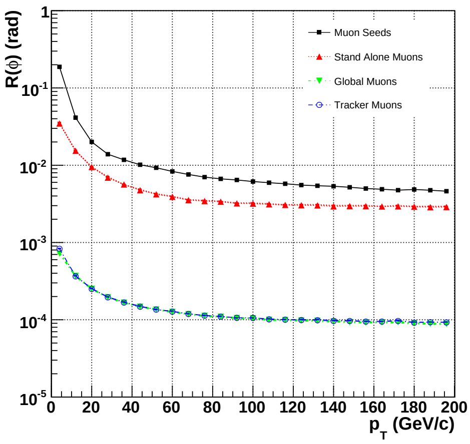

Figure 5.20: *ϕ residual for the different reconstruction steps, evaluated using the $(1 \div 200)$ GeV/c p_T sample.*

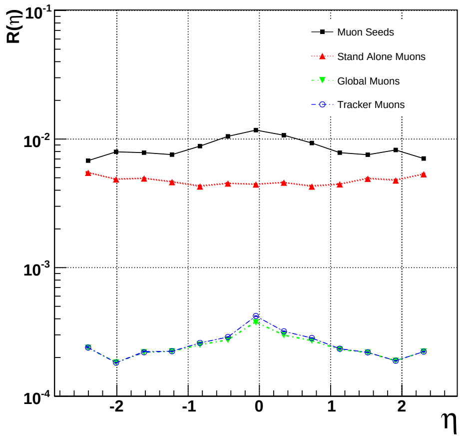

(a) R(η) vs η.

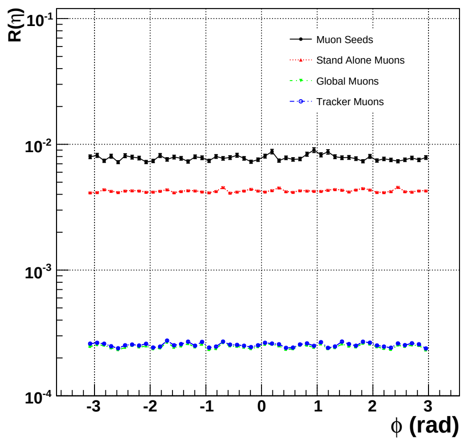

(b) R(η) vs ϕ.

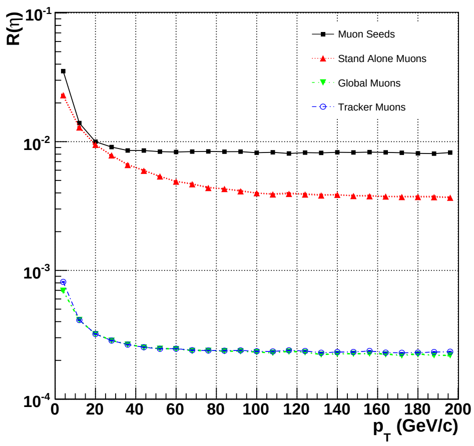

(c) R(η) vs p_T.

Figure 5.21: *η residual for the different reconstruction steps, evaluated using the $(1 \div 200)$ GeV/c p_T sample.*

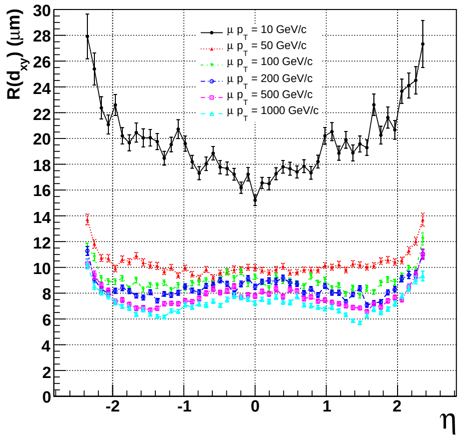

(a) R(d_{xy}) vs η.

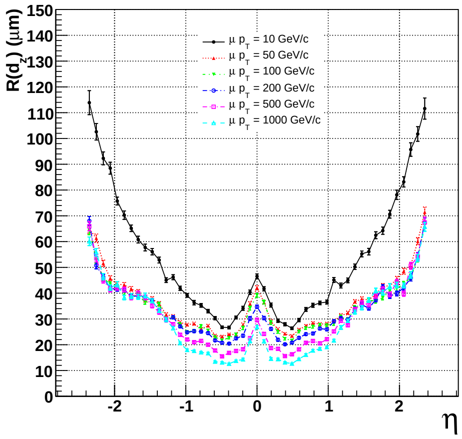

(b) R(d_z) vs η.

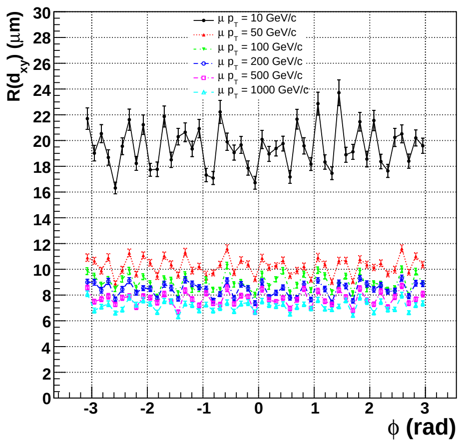

(c) R(d_{xy}) vs ϕ.

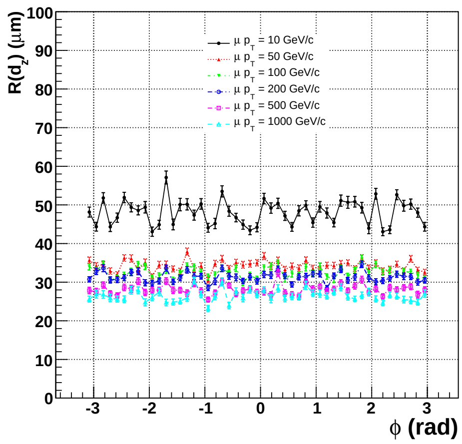

(d) R(d_z) vs η.

Figure 5.22: *Residuals of d_{xy} and d_z for global muons as a function of η and ϕ.*

5.4.3 Muon Reconstruction Parameter Pulls

In order to study the uncertainties assigned to the measured parameters, their pulls are studied in this section. The pull of a variable a is defined as:

$$\text{Pull} = \frac{a^{rec} - a^{gen}}{\sigma_a}.$$

For a normally distributed variable a the pulls are Gaussian with null mean value and unit variance. Deviation from unit indicates incorrectly estimated uncertainties. More precisely, if $\sigma_{pull} < 1$ the error is over-estimated, while $\sigma_{pull} > 1$ means the error is under-estimated.

The width of the q/p_T pull distributions (Fig. 5.23) shows a complex structure. The pulls of η (Fig. 5.24) are homogeneous within few eta regions, although the mean value is far from one. The correction in this case is easy, as it implies a set of re-scale factors. The seed algorithm does not compute the errors, instead they were assigned with a dedicated study of the muon seed parametrisation (Section 5.1.1). This study was performed on an old version of the CMS detector model. Further work is ongoing in order to update the assignment of seed uncertainties.

The stand-alone reconstruction computes the errors together with the parameters; they are better assigned than in the seeding step, although the pulls still do not show unit variance. The pull width of the q/p_T parameter (Fig. 5.23) is of about 1.4 and indicates that the errors are under-estimated by about 30% of the true value. In the case of TeV-muons the assigned errors are, in average, about 40% of the true value. The uncertainties assigned to η produce pull widths much closer to unit (Fig. 5.24), but the spectra in η show they are under-estimated in the barrel by 20% and the end-caps by 10%, in average. In the overlap region the errors are well estimated. For 10 GeV/c muons the pull width is equal to one over all the η range.

The pull distributions (Fig. 5.25 and 5.26) for the global and the tracker track reconstruction are better, although they show similar features. The q/p_T pull variances show that the errors are under-estimated, on average by about 15%. The uncertainties assigned to η distribute with a similar pattern as the one shown for the stand-alone muon reconstruction, but with smaller deviations from unit. The η errors are, in mean, under-estimated by about 10%. The uncertainties on the impact parameters are well estimated (Fig. 5.27).

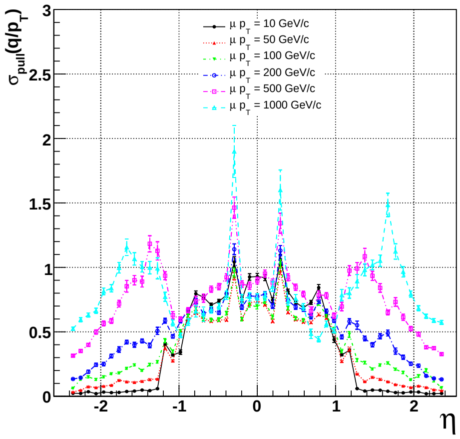

(a) Muon seeds.

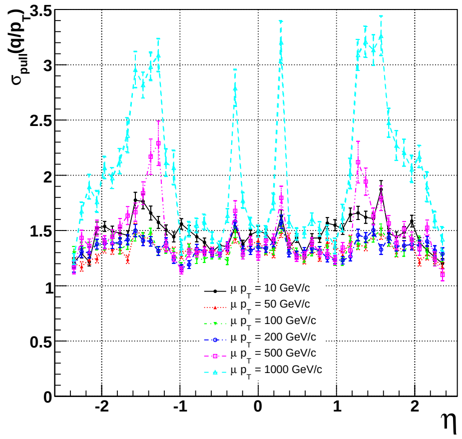

(b) Stand-alone muons.

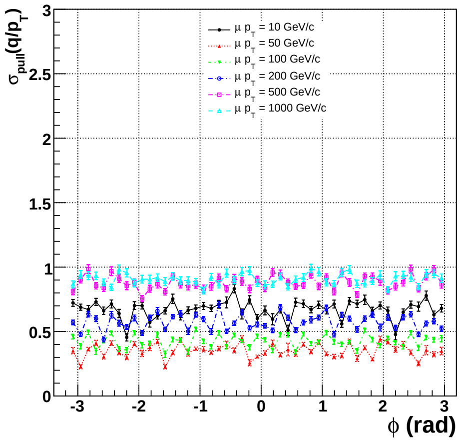

(c) Muon seeds.

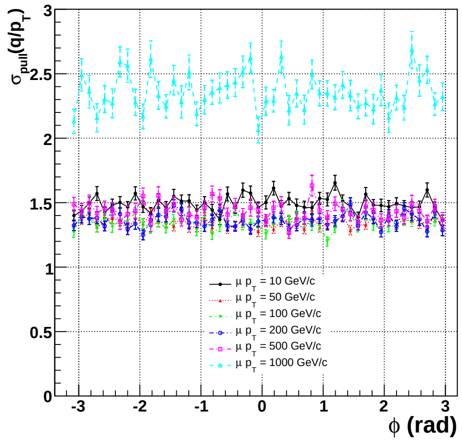

(d) Stand-alone muons.

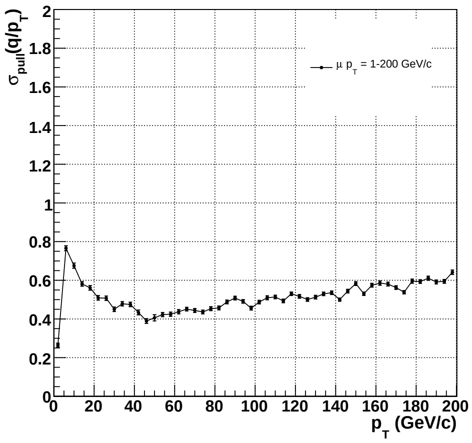

(e) Muon seeds.

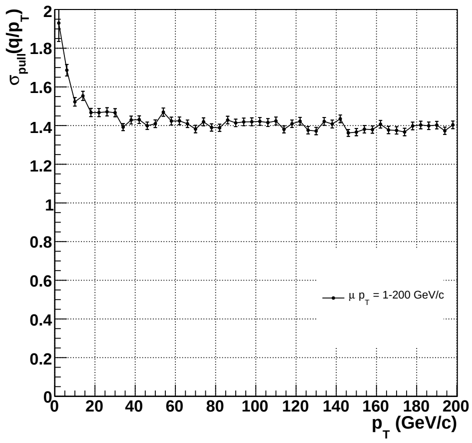

(f) Stand-alone muons.

Figure 5.23: *Pull of q/p_T in the muon spectrometer as a function of η and ϕ, for different p_T samples.*

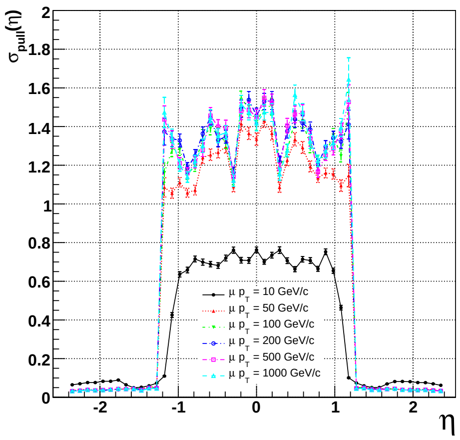

(a) Muon seeds.

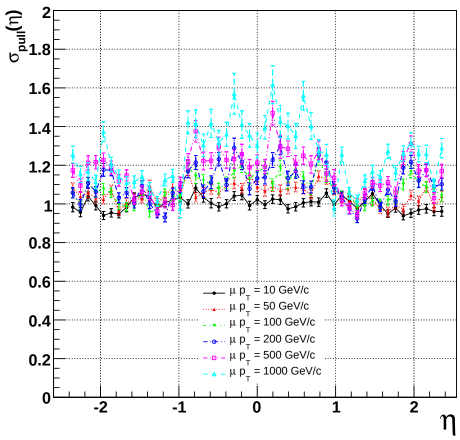

(b) Stand-alone muons.

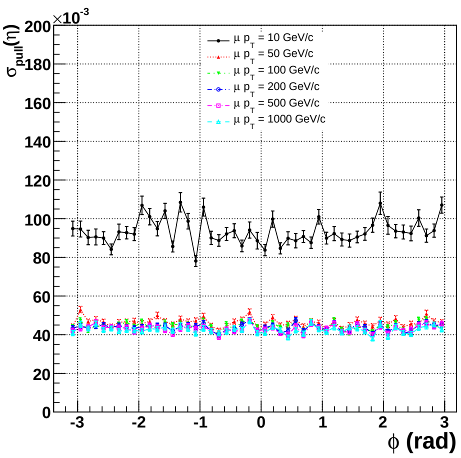

(c) Muon seeds.

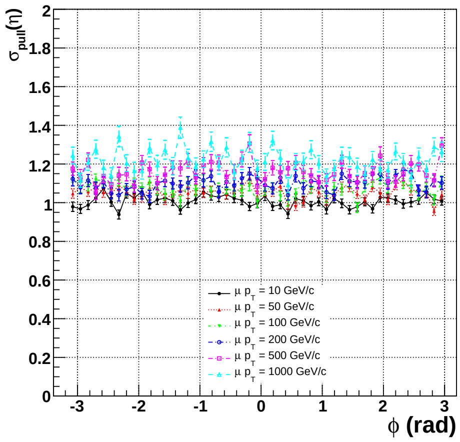

(d) Stand-alone muons.

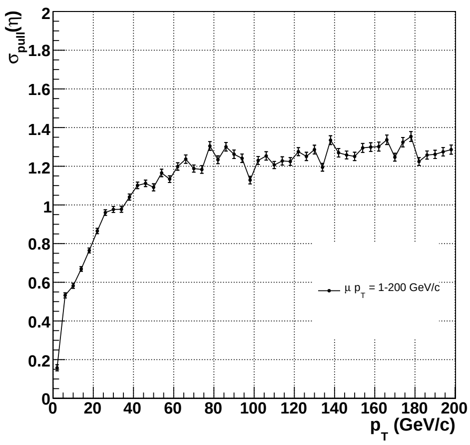

(e) Muon seeds.

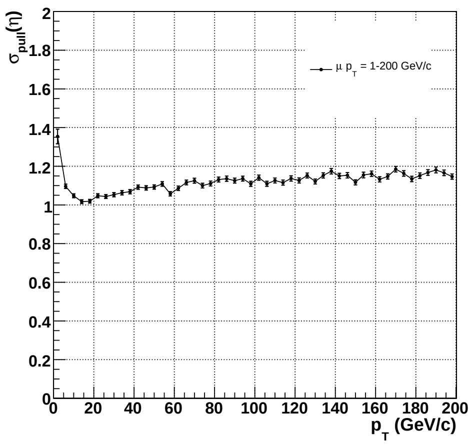

(f) Stand-alone muons.

Figure 5.24: *Pull of η in the muon spectrometer as a function of η and ϕ, for different p_T samples.*

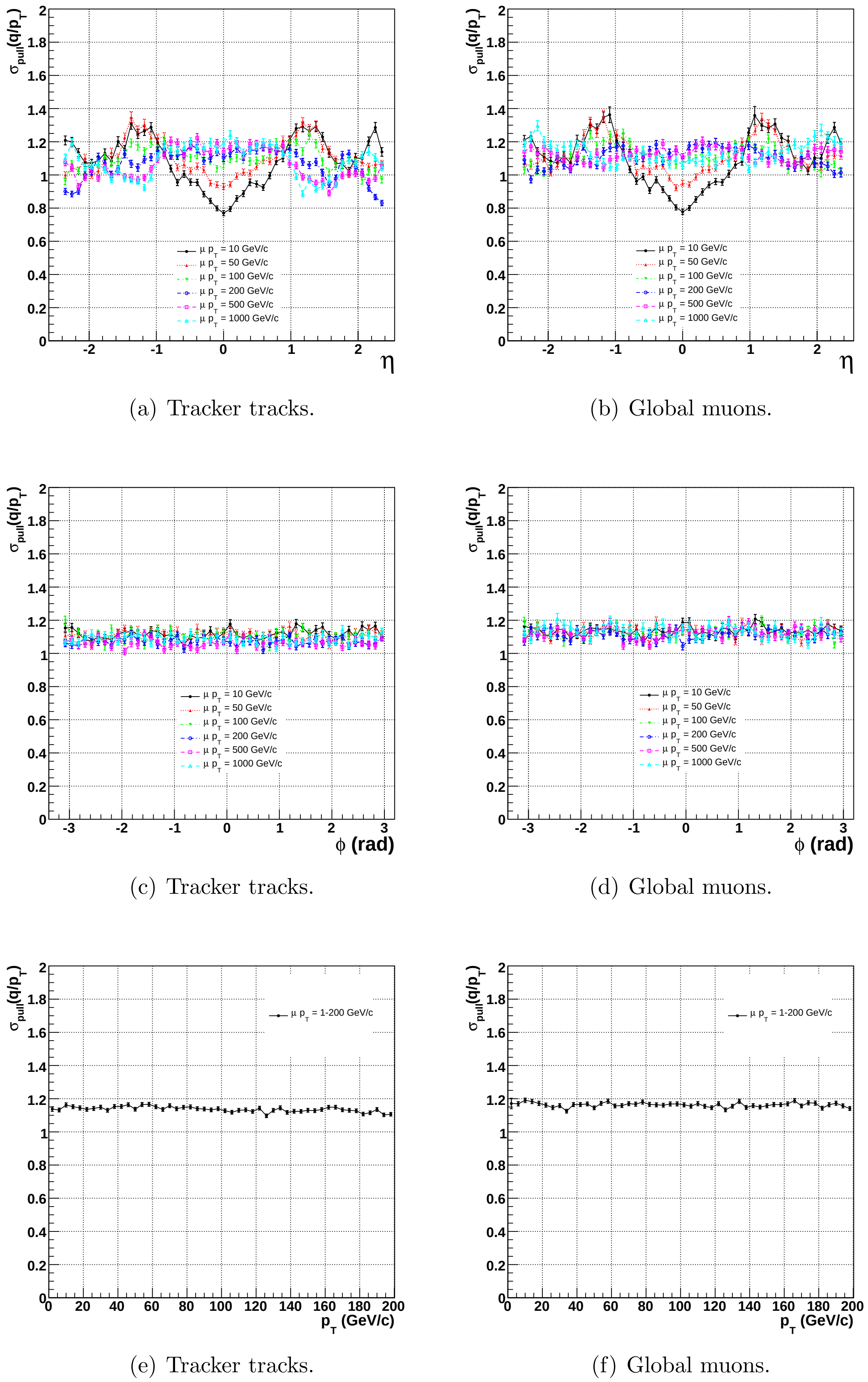

(a) Tracker tracks. (b) Global muons.

(c) Tracker tracks. (d) Global muons.

(e) Tracker tracks. (f) Global muons.

Figure 5.25: *Pull of q/p_T with the tracker alone and with the full CMS tracking system as a function of η and ϕ, for different p_T samples.*

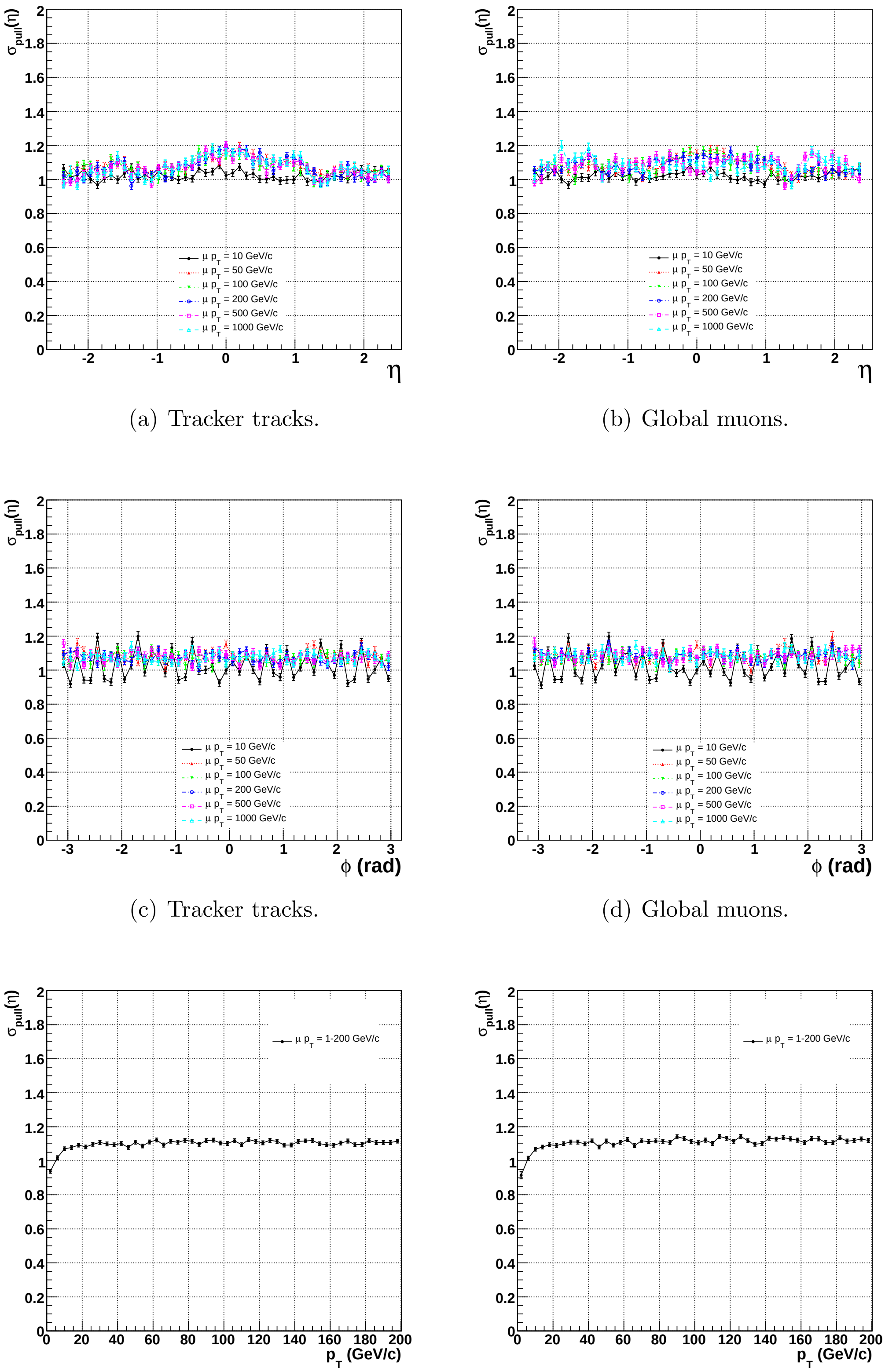

(a) Tracker tracks. (b) Global muons.

(c) Tracker tracks. (d) Global muons.

(e) Tracker tracks. (f) Global muons.

Figure 5.26: *Pull of η with the tracker alone and with the full CMS tracking system as a function of η and ϕ, for different p_T samples.*

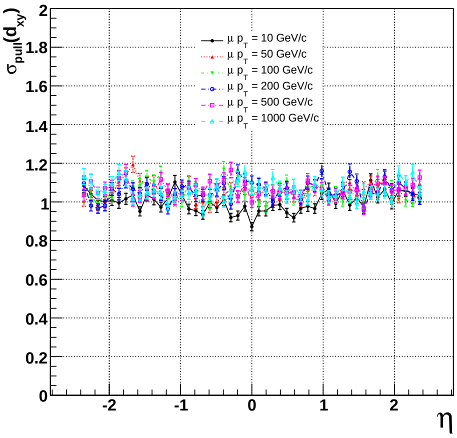

(a) $\sigma_{pull}(d_{xy})$ vs η.

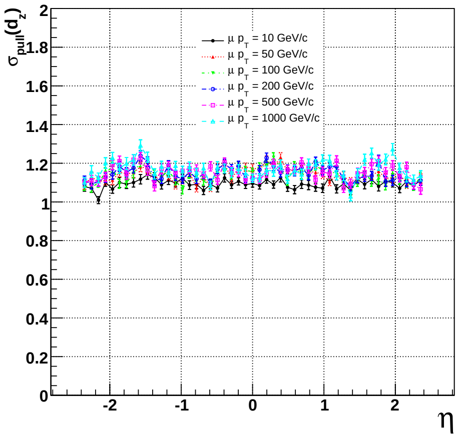

(b) $\sigma_{pull}(d_z)$ vs η.

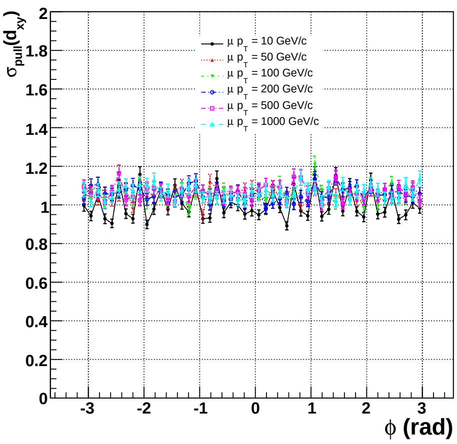

(c) $\sigma_{pull}(d_{xy})$ vs ϕ.

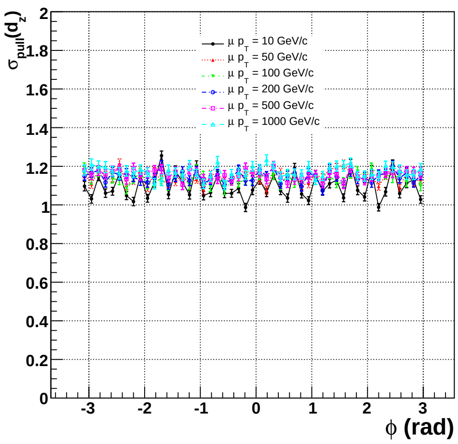

(d) $\sigma_{pull}(d_z)$ vs ϕ.

Figure 5.27: *Pull of the impact parameters of the global muon tracks as a function of η and ϕ, for different p_T samples.*

5.5 High Level Trigger

Muons will be used to calibrate detectors, perform precision studies of the Standard Model and search for new physics. This section presents the HLT reconstruction strategy for muons and the estimated performance of the main muon triggers: single and double-muon with and without isolation criteria. Additional muon triggers, mostly intended for calibration purposes or for specific physics signatures are also included in the trigger table [56], although they are not discussed here.

5.5.1 Seed From Level-1

The Kalman filter method starts from the determination of a trajectory seed, that in general can be built from any measurement in the muon detector (cf. Section 5.1.1). However, for trigger purposes the reconstruction can take advantage of the fact that the Level-1 trigger provides muon candidates, which are suitable to be used as seeds. This *external seeding* allows significant time savings, in particular because it does not require searching for the tracks in the full muon detector. On the other hand, this limits the efficiency of the HLT, which cannot reconstruct muons not already selected by the Level-1.

The seeds are created using the parameters and uncertainties of Level-1 candidates, which are estimated at the second barrel or endcap station, and are fed to the stand-alone muon reconstruction algorithm.

At a luminosity of 10^{32} cm^{-2} s^{-1}, the Level-1 single-muon rate is about 1 kHz for p_T thresholds as low as 7 GeV/c while the di-muon rate is below 200 Hz at the threshold of 3 GeV/c. More detailed information on Level-1 rates as a function of p_T can be found elsewhere [56].

The efficiency of the Level-1 single-muon criteria on a $W \rightarrow \mu\nu$ sample, with muons generated in the fiducial volume $|\eta| < 2.4$ and with $p_T >$ 10 GeV/c, is 83%. The combined efficiency of single and double-muon criteria on a $Z \rightarrow \mu\mu$ sample in a similar fiducial volume is 99%.

5.5.2 The Muon High Level Trigger Chain

The first step of the HLT muon selection is referred to as "Level-2 reconstruction". The Level-2 reconstruction is based on the algorithm described in Section 5.1.2 which can be optionally tuned to be faster at the expense of precision. The pre-filter can be suppressed and only the outside-in fit performed, or the RPC measurements can be excluded, thus saving the time spent for RPC local reconstruction. Level-2 muons are required to exceed p_T threshold values that depend on the trigger path.

Muons passing the Level-2 selection are input to the Level-3 reconstruction step (cf. Section 5.2). The track parameters and uncertainties of the Level-2 muon constrained to the IP region define a rectangular $\eta - \phi$ region in the silicon tracker. Pairs or triplets of hits in the innermost layers of the tracker form trajectory seeds that are required to be compatible with the $\eta{-}\phi$ region and with primary vertex. Trajectories from these seeds are subsequently extended using Kalman filtering techniques. The best reconstructed trajectory, determined by a χ^2 test, is chosen. This trajectory is then optionally combined with the reconstructed hits from the original Level-2 muon track. The final selection step is applied to the precisely measured Level-3 muons.

Isolation is an optional step in HLT reconstruction. Isolation variables are defined as sums of transverse energies in the calorimeter towers (for Level-2) or of transverse momenta of charged-particle tracks (for Level-3) found in a cone around the direction of the muon[2].

In the Level-2 isolation variable the calorimeter deposits are calculated as a weighted sum of the energies deposited in the ECAL (weight of 1.5) and in the HCAL (weight of 1.0). The unpacking of the ECAL data is done within regions surrounding the Level-1 seeds. This regional ECAL unpacking approach is approximately a factor of four faster than the full sub-detector unpacking, without loss of signal efficiency.

In the Level-3 isolation variable only charged-particle tracks compatible with the vertex of the candidate muon are selected. This suppresses contributions from pile-up collisions, thus making the Level-3 isolation requirement less dependent on instantaneous luminosity than the Level-2 isolation.

In both Level-2 and Level-3 isolation algorithms the deposits associated with the candidate muon as well as from other muons in the event are excluded from the sum. The thresholds and cone sizes used are adjusted in different pseudo-rapidity ranges [57] in order to provide an optimal signal selection and background rejection. The event can be rejected if there are too few isolated muons, according to the criteria of each trigger path.

5.5.3 Performance

The study of the HLT performance [57] was designed to be as realistic as possible. It focused on conditions expected at the startup of the LHC, and thus all studies assumed an instantaneous luminosity of 10^{32} cm^{-2} s^{-1}. The CPU time measurements were performed on a *Core 2 5160 Xeon* processor running at 3.0 GHz, *i.e.* using a processor that is very close to the one that is likely to be used for the Event Filter Farm prior to data-taking.

[2]The size of the cone is defined in the $\eta - \phi$ space as $R = \sqrt{\Delta\eta^2 + \Delta\phi^2}$ around the direction of the muon at the collision point.

5.5.3.1 Special MC Samples for Muon HLT Paths

A large fraction of the Level-1 muon trigger rate is due to low-p_T muons which are mis-reconstructed above the nominal p_T threshold. Most of these muons come from pion and kaon decays. Although the probability of decays in the volume in front of the calorimeter is small, the number of hadrons is very high and therefore this process dominates the Level-1 rate in the low-p_T muon region.

In order to obtain an enriched sample of muons in this region, pion and kaon decays into muons are forced and an event weight is assigned according to the prescription described in [58]. Significant statistics over the full momentum range are obtained by generating samples of minimum bias events forced to contain a muon in three different p_T intervals: a) $p_T < 4$ GeV/c, b) $p_T > 4$ GeV/c and c) $p_T > 10$ GeV/c (the latter also with a cut of $\hat{p}_T > 10$ GeV/c on the hard process). The performance of the muon HLT code on the muon-enriched sample was compared with that on minimum bias samples. The trigger rates and average processing times estimated for the various muon HLT paths show good agreement among the two Monte-Carlo samples.

5.5.3.2 Trigger Rates

All HLT single-muon paths are seeded by Level-1 candidates passing single-muon criteria ($p_T > 7$ GeV/c). Similarly, only candidates passing the Level-1 double-muon criteria ($p_T > 3$ GeV/c) are considered in HLT double-muon paths.

Paths without isolation criteria, which are denoted as “relaxed paths”, are essential to maintain high efficiency for events with high-p_T muons, for which the application of isolation criteria is not necessary. The resulting p_T threshold for the relaxed single-muon trigger is 16 GeV/c, giving a HLT rate of $\lesssim 20$ Hz, as shown in Figure 5.28. For the relaxed double-muon trigger, the threshold of $p_T > 3$ GeV/c for both muons guarantees a trigger rate below 20 Hz (Figure 5.29). These low thresholds also allow detailed studies of the performance of HLT isolation algorithms on reference samples like $W \to \mu\nu$ and $Z \to \mu\mu$. Understanding this performance with the W and Z samples will be essential in designing selections for higher LHC luminosities.

The composition of the HLT muon selected samples is presented in Figures 5.30 and 5.31, for the case of relaxed paths. It can be seen that decays from bottom and charm quarks dominate the rate at any p_T threshold, and that the contribution from pion and kaon decays at the thresholds chosen (16 GeV/c for single-muon and 3 GeV/c for double muons) is almost negligible.

Isolation cuts allow lowering the p_T thresholds for physics analyses which require isolated muons in the final state. As shown in Fig. 5.32 a single isolated muon path with a threshold of $p_T > 11$ GeV/c can be sustained.

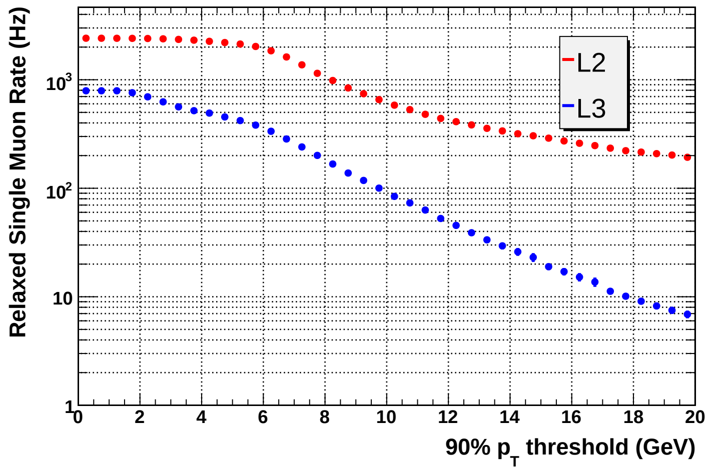

Figure 5.28: *HLT rates for the relaxed single-muon path – from the muon-enriched Monte Carlo sample. The rate for a p_T threshold of 16 GeV/c is $\lesssim 20$ Hz.*

5.5.3.3 Efficiency

The efficiency of the three trigger paths described above on $W \to \mu\nu$ and $Z \to \mu\mu$ events is shown in Table 5.7. HLT efficiencies are related to the total number of events passing the corresponding Level-1 criteria (single or di-muon Level-1 triggers, depending on the case). The overall (Level-1)$\times$(HLT) acceptance is calculated from the total number of generated events. Both samples have been generated with the following cuts on the muons in the final state: $|\eta| < 2.4$ and $p_T > 10$ GeV/c.

Table 5.7: *HLT efficiencies and overall acceptance of muon trigger paths on the benchmark processes $Z \to \mu\mu$ and $W \to \mu\nu$.*

Signal	HLT Single Relaxed muon eff.(%)	HLT Double muon eff.(%)	HLT Single Isolated muon eff.(%)	(Level-1)*HLT acceptance (%)
$Z \to \mu\mu$	98.6	91.2	95.8	98.1
$W \to \mu\nu$	86.9	-	81.4	76.7

5.5.3.4 CPU Performance

Table 5.8 shows a summary of the timing for each step of the isolated single-muon path. The most time-consuming part of the chain is the Level-2 reconstruction, as it involves the extrapolation of the track parameters through the steel yoke. In fact the propagation time accounts for about 65% of the total Level-2 time. Per input muon, the time spent at Level-3 is more than the one

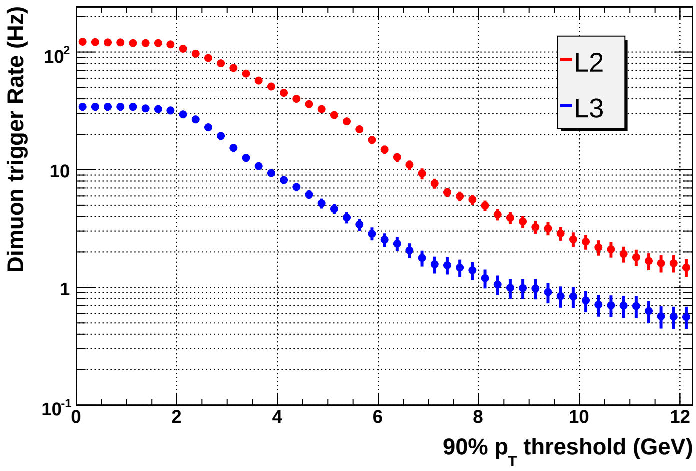

Figure 5.29: *HLT rates for the relaxed double-muon path as a function of p_T. QCD, Drell-Yan and additional prompt-J/Ψ contributions not included in standard QCD production have been taken into account. For $p_T > 3$ GeV/c a HLT rate of $\sim$ 15 Hz is obtained.*

spent at Level-2, but it is less critical as the input rate is a factor 10 lower, resulting in a more diluted average time. The maximum acceptable HLT processing time is about 40 ms per event.

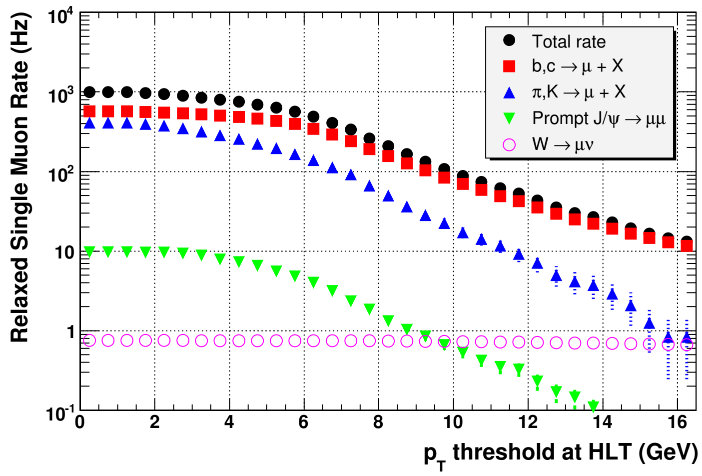

Figure 5.30: *HLT relaxed single-muon rate as a function of the p_T threshold for the reference Level-1 threshold of 7 GeV/c. The main components contributing to the rate are shown.*

Table 5.8: *Running and average processing times for different steps of the isolated single-muon HLT path for Level-1 accepted minimum bias events.*

HLT step	Running time (ms)	Averaged time (ms)	Fraction of all L1 events processed
MUON unpacking	3.0	3.0	0.1090
MUON local reconstruction	7.0	7.0	0.1090
Level-2 reconstruction	13.8	13.8	0.1090
ECAL unpacking	3.6	0.4	0.0135
HCAL unpacking	0.6	0.1	0.0135
ECAL local reconstruction	1.7	0.2	0.0135
HCAL local reconstruction	0.5	0.1	0.0135
Calo towers reconstruction	2.6	0.3	0.0135
Level-2 isolation	0.2	0.0	0.0135
Pixel unpacking	1.3	0.1	0.0101
SiStrip unpacking	0.2	0.0	0.0101
Pixel local reconstruction	5.5	0.5	0.0101
SiStrip local reconstruction	0.1	0.0	0.0101
Level-3 reconstruction	50.1	4.6	0.0101
Pixel Tracks	6.3	0.1	0.0012
Level-3 isolation	0.1	0.0	0.0012
Total		30.2	

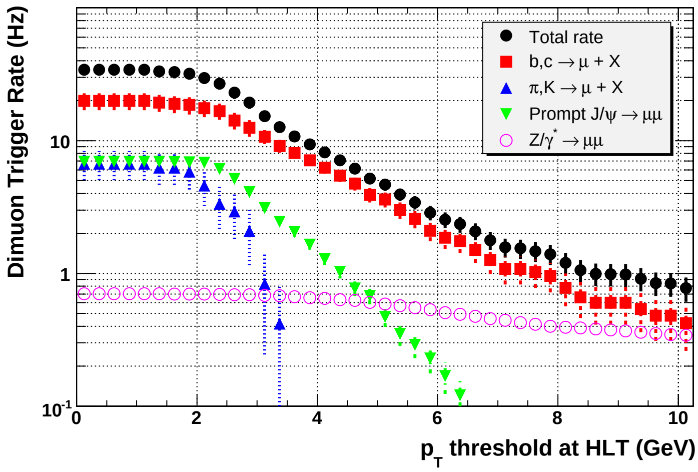

Figure 5.31: *HLT di-muon rate as a function of the p_T threshold for the reference Level-1 threshold of 3 GeV/c. The main components contributing to the rate are shown.*

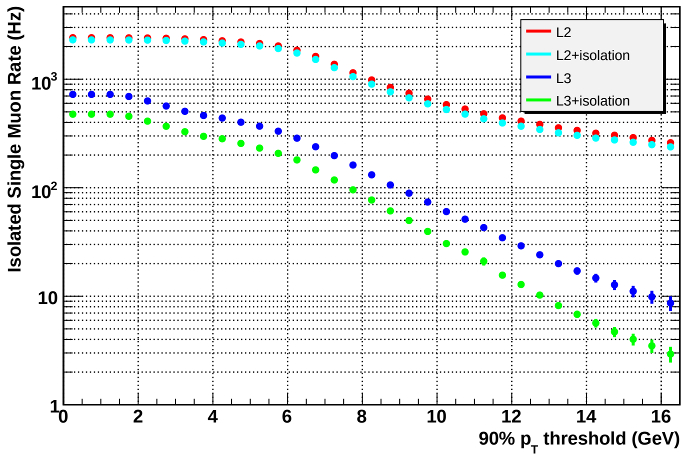

Figure 5.32: *HLT rates for the isolated single-muon path on the muon enriched sample. For $p_T > 11$ GeV/c a HLT rate of $\sim$ 20 Hz is expected.*

5.6 Conclusions

The muon reconstruction in CMS has satisfactory performance at each level of the chain and the design requirements [47] are satisfied. For the reconstruction in the muon spectrometer alone the efficiency is above 99% over a wide range of muon momenta and the resolution on the momentum ranges from 8% in the barrel, for muon with p_T=10 GeV/c, to 40% at $|\eta| = 2.4$ for the TeV-muons. The global muon reconstruction efficiency is about 98% and the momentum resolution, which benefits of the high tracker performance, ranges from 0.6% at $\eta \simeq 0$, for muons with p_T=10 GeV/c, to 25% at $|\eta| = 2.4$ for the TeV-muons.

The muon track reconstruction has been tested at the *Magnet Test Cosmic Challenge* [4] held during Summer 2006 and it has been shown to be able to reconstruct cosmic muons starting from the true detector information. This, together with the analysis of the reconstruction performance, confirms the muon reconstruction is ready for the data taking.

The timing studies of the muon HLT algorithms shows that the CPU time spent in the muon reconstruction and isolation algorithms is acceptable. In conclusion, the current prototype of the CMS HLT is a complete, fully functional system. However, this is not intended to be the final implementation. The flexibility of the HLT framework will allow trigger algorithms to evolve in parallel with those of the off-line reconstruction, to adapt to the experimental conditions of LHC and to respond to the physics demands of CMS.

Chapter 6

Vector Boson Scattering as a Probe of Electroweak Symmetry Breaking

An exploratory study of the $pp \rightarrow \mu^+\mu^- jjjj$ channel has been performed in order to assess the possibility of probing the symmetry breaking mechanism through the VV ($V = W^\pm, Z$) fusion process using the CMS detector. A model-independent analysis was carried out with no assumption on the mechanism restoring the unitarity of the scattering amplitude and without any degree of freedom beyond the Standard Model. In order to explore the sensitivity of the analysis method to an heavy Higgs resonance, a data set produced using a Higgs mass of 500 GeV/c^2 have been analysed. Moreover, in order to consider the VV fusion cross section in a region where no resonances are present, a sample in the no-Higgs scenario, that in the SM is equivalent to a very high Higgs mass, has been also studied.

6.1 Theoretical Aspects

Vector boson scattering is the key process to probe the nature of the electroweak symmetry breaking (EWSB) mechanism [59, 60, 61, 62, 63, 64].

In absence of the Higgs particle, the SM predicts that the scattering amplitude of longitudinally polarised vector bosons ($V_L V_L \rightarrow V_L V_L$) grows linearly with s and violates unitarity at 1–1.5 TeV. Violation of perturbative unitarity implies that the SM becomes a strongly interacting theory at high energy. Adopting one of the many schemes for turning perturbative scattering amplitudes into amplitudes which satisfy, by construction, the unitarity constraints [65, 66, 67], the presence of resonances in boson-boson fusion processes is expected. This mechanism is analogous to low energy QCD where unitarisation of the pion-pion scattering amplitude leads to the appearance of the ρ resonance. Alternatively, new physics phenomena must appear below the TeV scale. Several theories have been proposed and can be schematically classified in three categories:

- *Little Higgs.* In these models there is an expanded gauge symmetry at the TeV scale that contains the standard $SU(2) \times U(1)$. An approximate global symmetry prevents the Higgs boson from receiving quadratically divergent mass contributions at one loop. The Higgs boson is a pseudo-Goldstone boson resulting from spontaneous breaking of the approximate symmetry and it is therefore light. These models contain new heavy gauge bosons whose mass is of the order of the TeV.

- *Dynamical symmetry breaking.* EWSB arises in these theories from chiral symmetry breaking of a new strong interacting gauge sector. The role of the Higgs is played by a condensate of new heavy quarks (techniquarks). The oldest version of these theories, Technicolour, was proposed in 1976 as an alternative to the Higgs mechanism, to provide the mass of the to the weak gauge bosons. In 1979 Technicolour was enlarged into "Extended Technicolour" to allow quark and leptons to get their masses. These theories suffered by problems in preventing flavour changing neutral currents. Successive versions went under the name of Walking Technicolour (with different scales of chiral symmetry breaking).

- *Higgless models.* Models with extra dimensions can generate EWSB from boundary conditions on the brane of the extra dimensions. The Higgless models all contain a tower of Kaluza Klein particles with the quantum numbers of the SM gauge bosons. These particles take part in elastic scattering amplitudes and restore unitarity as the Higgs does in the SM.

On the other hand, if a massive Higgs boson exists, a resonance will be observed in the VV invariant mass spectrum in correspondence of the Higgs mass. In fact the VV fusion process represents the second most important contribution to Higgs production at LHC, while $H \to VV$ is the favourite Higgs decay channel beyond the $m_H > 2\,m_V$ kinematic threshold and it provides one of the clearest signatures for the Higgs detection [37].

Moreover, if the Higgs boson is present, its mass is strictly related with the nature of the interaction among the longitudinally polarised vector bosons: if the Higgs particle is relatively lighter than the vector bosons, then the vector boson are weakly coupled, whereas they are strongly coupled at high energy if the Higgs boson mass is larger. In particular, the absence of strong interactions in high energy boson-boson scattering could be an indication for a light Higgs boson, whose discovery will require several years of data taking [30]. However even if a Higgs particle is discovered, in this or other channels, it will be necessary to study in detail the boson-boson scattering in order to verify if the longitudinally polarised vector bosons are indeed weakly coupled.

At LHC the VV invariant mass region beyond the unitarity violation threshold can be explored by studying a wide set of processes [6]. These channels offers a clear experimental signature, because of the presence of high p_T leptons from the W or Z decay, together with the highest branching ratio among the final states which are possible to reconstruct in an hadronic environment. In this chapter the $pp \to \mu\mu jjjj$ process is presented.

6.2 Signal Definition and Simulation

In order to explore the EWSB through the analysis of the VV fusion process, a precise knowledge of the cross section $\sigma(pp \to VVjj)$ on the whole VV invariant mass spectrum is essential. The choice of the Monte Carlo program (MC) to be used for the signal generation is therefore a key aspect of this study.

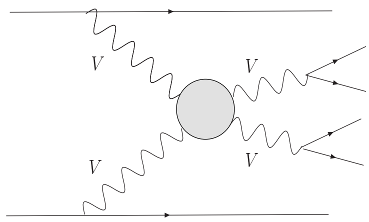

Figure 6.1: *The vector boson fusion process generic diagram.*

The generic diagram describing vector boson fusion processes is shown in Fig. 6.1. Once vector bosons are decayed, a six-fermion final state is produced. If the finite width of the EW bosons is properly taken into account and the vector bosons are allowed to be off-mass shell, then the full set of diagrams describing $qq \to 6$ fermions has to be considered in order to preserve the gauge invariance.

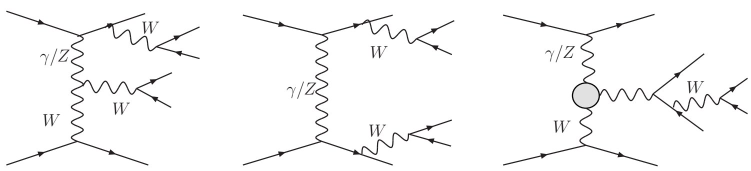

Figure 6.2: *Examples of non-scattering diagrams in $WWjj$ production. The two on the left must be included even when the final state bosons are on-shell.*

At the LHC there is no kinematic region where the scattering diagrams dominate. Therefore, the set of boson-boson scattering diagrams and the complementary set of diagrams (*e.g.* Fig. 6.2) at the same perturbative order and with the same initial and final state, which represent the irreducible background, cannot be computed and simulated separately. Moreover the gauge cancellations among the different diagrams can be huge [68]. For example, in the unitarity gauge, even in the simplified treatment of $qq \to qqVV$ processes in which the two bosons are taken to be strictly on mass shell, large cancellations occur: the cross section obtained from the boson-boson scattering diagrams alone is about two orders of magnitude larger than the result obtained from the complete set of diagrams. For other gauges, cancellations are smaller but always substantial. For a detailed discussion see ref. [69]

6.2.1 Six-Fermion Final State Processes

The $qq \to 6$ fermions process has been simulated with an exact leading order matrix element MC (PHANTOM [69]) at α^6_{EW} perturbative order. For the first time the thousands of reactions in the full set of processes $qq \to 4j2l$ and $qq \to 2j4l$ have been generated without resorting to the Equivalent Vector Boson Approximation or to a *production times decay* approximation.

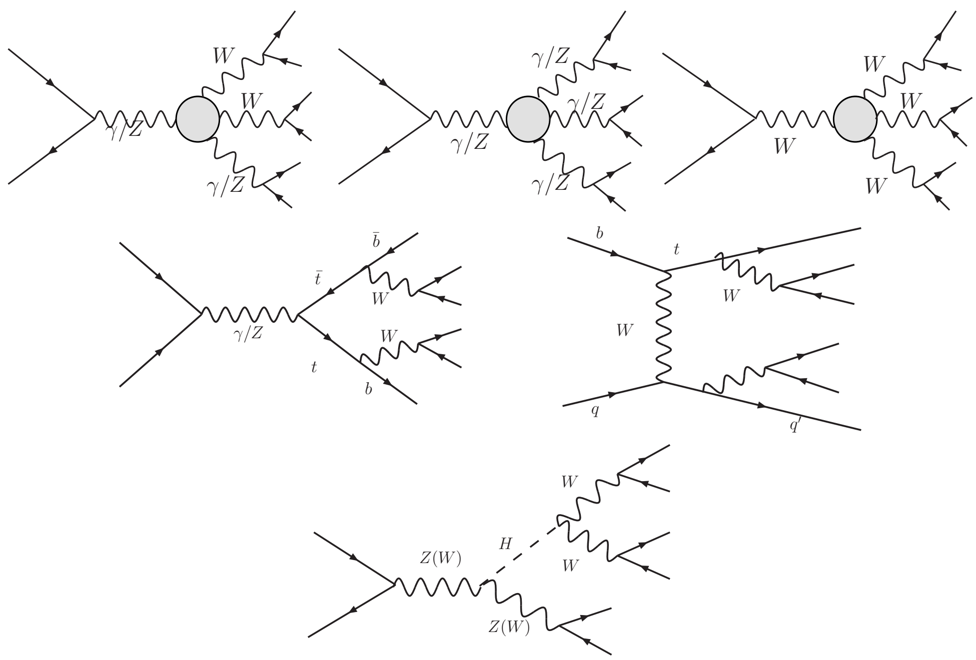

Figure 6.3: *Examples of non scattering diagrams which contribute to the full $qq \to 6f$ amplitude.*

In addition to boson-boson scattering diagrams, the amplitude includes diagrams in which a pair of V's are produced without undergoing scattering as well as diagrams which describe $t\bar{t}$ or single top production through purely electroweak interactions. Furthermore there are subprocesses with three outgoing vector bosons from Triple or Quartic Gauge Coupling vertexes and contributions from Higgs production via Higgstrahlung. “Non resonant” diagrams where only one pair of fermions in the final state come from a vector boson decay are also present. Some examples can be found in Fig. 6.2 and 6.3. For a detailed description of all these contributions see [70].

As already mentioned, these different sets of diagrams in general cannot be computed separately because they interfere among each other and are not individually gauge invariant. Moreover there are aspects which cannot be tackled without a full calculation of the six-fermion final state, like exact spin correlations among the decays of different heavy particles.

6.2.2 Kinematic Criteria for VV-Fusion Signal Definition at Parton Level

In order to investigate EWSB, the VV fusion process should be isolated from the others six-fermion final states (the irreducible background). In order to enhance the contribution of boson-boson scattering with respect to the irreducible background, kinematic cuts have been applied to the simulated events.

The main irreducible backgrounds to be subtracted at parton level are single top and $t\bar{t}$ EW productions. Thus events which have a b-quark and two other quarks of the right flavour combination to be produced in a W decay and with an invariant mass between 160 and 190 GeV/c^2 are rejected.

Both muons must come from a Z decay, so the invariant mass of the pair is required to be in the range $m_Z \pm 10$ GeV/c^2. Moreover an additional W or a Z decaying hadronically is expected to be present, therefore events are required to contain two quarks with the correct flavours to be produced in W or Z decay and with an invariant mass of $\pm$ 10 GeV/c^2 around the central value of the corresponding EW boson. If more than one combination of two quarks satisfy these requirements, the one closest to the corresponding central mass value is selected. This combination will in the following be assumed to originate from the decay of an EW vector boson.

Events with the production of three outgoing vector bosons have to be rejected: if the two remaining quarks have the right flavour to reconstruct a W or a Z boson and if their invariant mass is compatible within 10 GeV/c^2 with the corresponding boson mass then the event is rejected.

In order to comply with the acceptance of the CMS detector and with the CMS trigger requirements, the cuts shown in Table 6.1 have also been applied during the events simulation.

Table 6.1: *Standard acceptance cuts applied during the $qq \to qqq\mu\mu$ events generation.*

Quarks	Muons
E> 20 GeV	E> 20 GeV
$p_T > 10$ GeV/c	$p_T > 10$ GeV/c
$\lvert\eta\rvert < 6.5$	$\lvert\eta\rvert < 3$
$m_{qq} > 20$ GeV/c^2	–

In Table 6.2 are listed the signal and irreducible background cross sections corresponding to the described cuts, while in Fig. 6.4 the signal m_{VV} spectrum is shown.

Table 6.2: *Total* PHANTOM *cross sections and percentages for the signal and the irreducible background processes for each final state defined by kinematical cuts "a posteriori". The no-Higgs scenario corresponds to the case where no resonance is produced, equivalently to set the Higgs mass to infinity.*

	no-Higgs		m_H=500 GeV/c^2	
	σ (pb)	frac. (%)	σ (pb)	frac. (%)
total	0.0305	100	0.0350	100
signal	0.0125	41	0.0165	47
top	0.0137	45	0.0137	39
non resonant	0.0030	10	0.0035	10
three bosons	0.0012	4	0.0014	4

6.2.3 High Invariant Mass Region: No-Higgs Case

The cross section $\sigma(pp \to VVjj)$ and the polarisations of the VV pair depend sensitively on the presence or not of a light Higgs in the physical spectrum. As a consequence, the measurement of the cross section at large m_{VV} could provide information on the existence of the Higgs boson independently of its direct observation. In particular, the dominant contribution to the total VV-scattering cross section at m_{VV} larger than 1 TeV/c^2, in case of a light Higgs ($m_H <$ 500 GeV/c^2), comes from the transversally polarised VV production. In the no-Higgs case instead, at the LHC, the production cross section for longitudinal and transverse vector bosons is very similar for m_{VV} larger than 1 TeV/c^2. Thus,

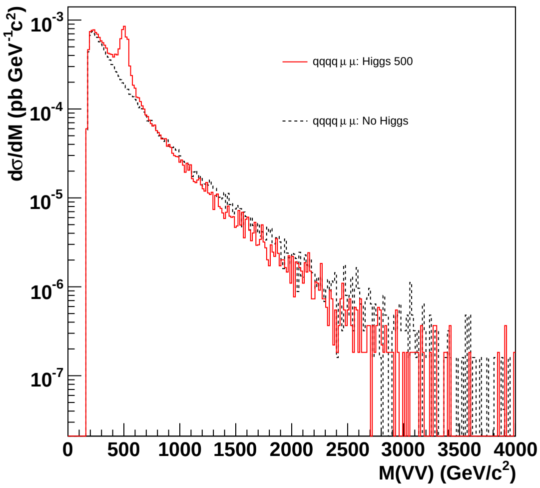

Figure 6.4: *m_{VV} spectrum after the cuts of signal definition with a Higgs mass of 500 GeV/c^2 and in the no-Higgs scenario.*

even if a light Higgs boson exists, the high VV invariant mass region should be studied in detail to verify if weak or strong interactions occur. Experimentally this is not easy, but kinematic cuts can enhance the difference between the Higgs and no-Higgs scenarios, as shown in Section 6.4.1. Studies have been done at parton level [70, 71]. A simple cut on the pseudorapidity of the bosons ($|\eta_V| < 2$) [71] has been used to enhance the difference between the Higgs and no-Higgs case as shown in Fig. 6.5. This cut is applied for the results presented in Section 6.4.1.

6.3 Selection Strategy

The channel $pp \to \mu\mu jjjj$ has been processed through the simulation of the CMS detector, then the reconstruction algorithms have been applied to all the simulated events. For this first exploratory study the official CMS fast simulation and reconstruction software (FAMOS [72]) has been used.

The main backgrounds for the different final states have been considered. They have been generated with the appropriate MC and then processed through FAMOS.

The low luminosity pile-up has been taken into account. Even if the physics channels of interest for this note will require high luminosity, the low luminosity scenario has been considered because FAMOS was tuned for this case only. Thus a total integrated luminosity of 60 fb^{-1} has been considered.

The reconstructed events have been analysed in order to separate the signal

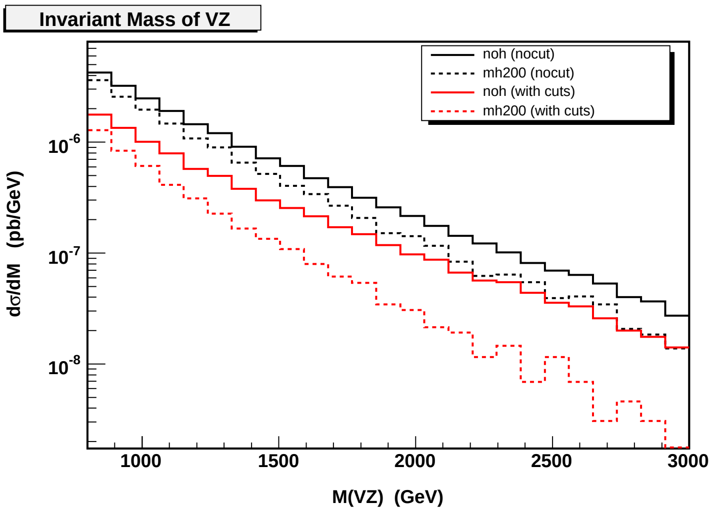

Figure 6.5: *Invariant mass distribution for* $m_{VZ} > 800\ GeV/c^2$*. The full line refers to the no-Higgs case, the dashed one to the* $m_H = 200\ GeV/c^2$*. The upper two curves are the results for the signal. For the two lower curve* $|\eta_{Z_{ll}}| < 2$ *and* $|\eta_{q_V}| < 2$ *(where* q_V *are quark from the boson decay.)*

from the backgrounds. The most important kinematic variable is the invariant mass of the two outgoing bosons since it corresponds to the energy scale of the Vector Boson Fusion process. The main goal of this study is the measurement of the signal cross section as a function of the centre of mass energy of the boson-boson system, in order to determine the scale at which the electroweak symmetry breaks.

6.3.1 Signal Topology

The particles in the final state arising from the decay of a W (or a Z) are expected to have quite high transverse momentum and to be mostly produced centrally in the detector, *i.e.* at low absolute value of pseudorapidity.

On the contrary, the two quarks that have radiated the vector bosons, the so called "spectator quarks", preferentially go in the forward/backward regions at high $|\eta|$ and they have very large energy and p_T. Thanks to their peculiar kinematic pattern, the presence of these two spectator quarks is essential to tag the VV fusion events as a six-fermion final state, therefore they are also called "tag quarks".

In Fig. 6.6 the kinematic configurations of the two quarks from the boson decay and of the two tag quarks are compared.

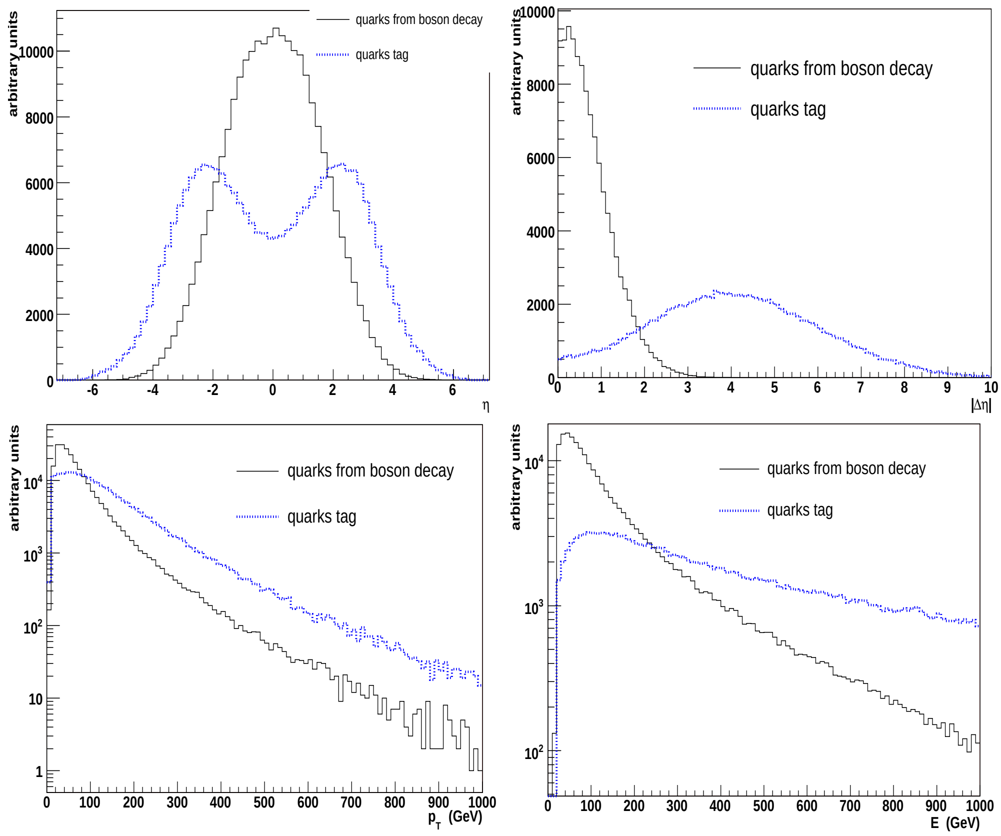

Figure 6.6: *Pseudorapidity, pseudorapidity difference, transverse momentum and energy of the two quarks from the boson decay and of the two tag quarks in the no-Higgs scenario.*

6.3.2 Main Backgrounds

The most problematic background for the vector boson fusion signal is the production of a single Z in association with n jets (n=2,3,4,5). Another potentially dangerous background with a huge cross section is the QCD production of $t\bar{t}$ pairs. Finally, the irreducible background must be considered, which has a cross section of the same order as the signal and a very similar kinematics. A list of all the considered background processes with the relative cross sections is shown in Table 6.4, while in Table 6.3 the cuts applied in the MC generation are reported. In the following the simulation and the partonic kinematic configuration of these background processes are briefly described.

The production of a single boson in association with n jets has been simulated with a matrix element MC ALPGEN [73]. The boson usually has larger absolute value of pseudorapidity and smaller transverse momentum with respect to the two outgoing bosons in the signal process. The additional jets have small energy and small transverse momentum and they have intermediate pseudorapidities between the tag quarks and the fermions from the boson decay in the signal process.

The production of two bosons in association with n jets has been simulated with ALPGEN. The kinematics of the bosons is very similar to the signal case, therefore the most effective strategy to reject this background is based on the very peculiar kinematics of the tag jets in the signal process. The additional jets in this background are softer than the tag jets. Moreover, they are usually in the central detector region and close to each other.

The $t\bar{t}$ and single top production via QCD processes ($q\bar{q} \to t\bar{t}$ and $gg \to t\bar{t}$) is another background with a very high cross section. Top quarks decay into a W boson and a b-quark with a branching ratio of almost 100% giving a final state similar to that produced in VV fusion events. However the outgoing b-quarks can be recognised through a b-tagging algorithm and they have a kinematic behaviour quite different from the signal tag quarks: the former are in fact more central and they have much less energy. The $t\bar{t}$ and single top production events have been produced with ALPGEN. The radiation of an additional jet has been considered too.

Finally the irreducible background must be considered as well; it is extracted from the PHANTOM sample by using the cuts listed in Table 6.1. It should be noted that the irreducible background is not completely independent of the Higgs boson presence (cf. Table 6.2): it contains the Higgsstrahlung process inside the category of three outgoing vector bosons. All the results shown in the following for the irreducible background refer to the no-Higgs case.

Table 6.3: *Summary of cuts applied in the MC backgrounds generation.*

MC Generator	min p_T(j) (GeV/c)	max η(j)
ALPGEN Z+nj	20	5
ALPGEN VZ+2j	20	6.5

6.3.3 Signal Reconstruction and Background Rejection

A strategy to reconstruct the signal final state has been developed by taking into account the signal topology described in Section 6.3.1. Moreover, a set of kinematic cuts has been applied in order to separate the signal events from all the processes considered as backgrounds and listed in Table 6.4.

The trigger for the vector boson fusion will be based on high transverse momentum charged leptons.

Table 6.4: *Summary of the cross sections and the number of used events.*

Process	σ (pb)	Generated ev.
$pp \to Z$+2 jets, $Z \to e, \mu, \tau$	230	73770
$pp \to Z$+3 jets, $Z \to e, \mu, \tau$	66	88100
$pp \to Z$+4 jets, $Z \to e, \mu, \tau$	17	207958
$pp \to Z$+5 jets, $Z \to e, \mu, \tau$	4.0	65347
$pp \to t\bar{t}(j)$ + 0 jets	190	572534
$pp \to t\bar{t}(j)$ + 1 jets	170	778369
$pp \to ZZ$+0 jets, Z inclusive, $Z \to e, \mu, \tau$	1.45	94906
$pp \to ZZ$+1 jets, Z inclusive, $Z \to e, \mu, \tau$	0.68	22000
$pp \to ZZ$+2 jets, Z inclusive, $Z \to e, \mu, \tau$	0.27	91501
$pp \to ZZ$+3 jets, Z inclusive, $Z \to e, \mu, \tau$	0.23	36886
$pp \to ZW$+0 jets, W inclusive, $Z \to e, \mu, \tau$	1.70	16500
$pp \to ZW$+1 jets, W inclusive, $Z \to e, \mu, \tau$	1.14	12000
$pp \to ZW$+2 jets, W inclusive, $Z \to e, \mu, \tau$	0.61	10000
$pp \to ZW$+3 jets, W inclusive, $Z \to e, \mu, \tau$	0.85	6983
Signal – $pp \to \mu\mu jjjj$		
No Higgs	0.0305	120760
$m_H = 500$ GeV/c^2	0.0350	137325

Unless explicitly indicated, the analysis used the following FAMOS algorithms:

- the jets are reconstructed with the Iterative Cone method with $\Delta R = 0.5$ and they are calibrated with the *GammaJet* [74] procedure. A cut of 0.5 GeVon the transverse energy in each tower is applied;

- the muons are selected with the *FamosGlobalMuonReconstructor* procedure, exploiting hits in the muon system as well as information from the tracker.

Muons and jets pre-selection. A very loose cut of 8 GeV/c has been applied to the transverse momentum of the muon: this reduces the combinatorics of possible pairs which can give $m_{\mu\mu} \sim m_Z$, without decreasing the $Z \to \mu^+\mu^-$ reconstruction.

In order to remove pile-up, only jets with $p_T > 30$ GeV/c have been considered. The event is required to have at least 4 jets with transverse momentum above this threshold.

$Z \to \mu^+\mu^-$ **reconstruction.** All possible muon pairs with opposite charges are built, then the p_z collinearity of the muons is requested:

$$p_z^+ \cdot p_z^- > -2000\ \text{GeV}^2. \tag{6.1}$$

If more than one pair is found, the one that gives the Z with the highest p_T is chosen.

To reduce the background, requirements on the invariant mass and the transverse momentum of the Z are imposed:

$$81 < m_Z < 101\ \text{GeV}/c^2; \tag{6.2}$$

$$p_T^Z > 100\ \text{GeV}/c. \tag{6.3}$$

The purity for the Z reconstruction is at the level of 99%, the efficiency is about 75% in the case of $m_H = 500\ \text{GeV}/c^2$ and at the level of 73% in the no-Higgs case (Table 6.5).

The mass resolution of the reconstructed Z is about 1.5%, as reported in the summary Table 6.6.

Tag jets reconstruction. The tag jets usually have large energy and are in the high pseudorapidity region, therefore a variable which takes into account both the aspects has been introduced: $T = m_{jj} \cdot \Delta\eta_{jj}$. The pair with the higher value of T is chosen as tag jets pair.

Once the pair has been recognised, requests on $\Delta\eta_{jj}$, invariant mass and energy are applied:

$$E_{j_i} > 100\ \text{GeV}, i = 1, 2; \tag{6.4}$$

$$m_{jj} > 500\ \text{GeV}/c^2; \tag{6.5}$$

$$|\eta_{j_1} - \eta_{j_2}| > 1.5. \tag{6.6}$$

The efficiency of the tag jets selection is 75% in both in the Higgs case and in the no-Higgs case as reported in Table 6.5.

$V \to jj$ **reconstruction.** As for the muons from the Z, the jets from the vector boson decay are requested to be collinear:

$$p_z^{j_1} \cdot p_z^{j_2} > -2000\ (\text{GeV}/c)^2. \tag{6.7}$$

If more than one pair survives, then the two pairs with the highest p_T are compared on the basis of their mass: the one which has the less difference with respect to m_V is chosen.

The mass resolution of the reconstructed boson is about 20% (Table 6.6).

The efficiency of the V reconstruction is about 76% in the case of $m_H = 500\text{GeV}/c^2$ and at the level of 75% in the no-Higgs case, as reported in Table 6.5.

A selection based on the invariant mass of the reconstructed vector boson is not useful in order to increase the final significance of the analysis therefore only a wide invariant mass window is applied:

$$50 < m_V < 180 \text{ GeV}/c^2. \tag{6.8}$$

Signal requirements. The reconstructed events are required to satisfy the following condition on the invariant mass of the $Z + V +$ tag jets system:

$$m_{ZVjj} > 1000 \text{ GeV}/c^2. \tag{6.9}$$

The final efficiency is at the order of 18% in the Higgs case and 14% in the no-Higgs case (Table 6.5). A resolution on the VZ system at the level of 9.5% is reached for the no-Higgs case and about 8.7% for $m_H = 500$ GeV/c^2, as reported in Table 6.6.

Despite its very large cross section the background $t\bar{t}$ is completely removed with the request of a Z with high p_T in the final state. The selections on the tag jets kinematics and on the total system mass are quite efficient in the rejection of the backgrounds with $VZ+n$ jets. The most critical background is $Z+n$ jets as it has a very large cross section; the low resolution on the reconstruction of the boson decaying into jets does not allow an optimal rejection of this background.

A summary of the signal reconstruction procedure and of the background rejection strategy is reported in Table 6.5, including the efficiencies of the cuts on the signal and on the different backgrounds.

Table 6.5: *Signal reconstruction cuts and backgrounds rejection efficiencies for different final states*

Cut	signal 500 GeV/c^2	signal no-Higgs	Z+nj	$\bar{t}t$	ZZ+nj	ZW+nj	irr. bg.
$Z \to \mu^+\mu^-$ rec.	75%	73%	20%	3%	19%	18%	70%
m_Z, p_T^Z	50%	44%	24%	0.8%	39%	45%	25%
tag jets selection							
E_j, m_{inv}, $\Delta\eta_{jj}$	75%	75%	30%	11%	32%	40%	45%
$Z \to jj$ rec.	75%	75%	28%	73%	28%	39%	67%
m_V	82%	80%	79%	90%	81%	79%	88%
Final state rec.	57%	56%	1.3%	1.2%	2%	4%	47%
m_{ZVjj}	79%	78%	33 %	8%	37%	47%	48%
After all cuts	18%	15%	0.08%	$1{\cdot}10^{-3}$	0.2%	0.6%	5%

6.4 Results

The main goal of this study is to investigate the feasibility of the measurement of the VV fusion cross section at CMS as a function of the process energy scale, *i.e.* the invariant mass of the boson-boson system.

The results presented in this work are preliminary and have to be considered only as a feasibility study. The resolution on the invariant mass of the hadronic boson decay $V \to jj$ will be improved in the future when more sophisticated jets algorithms will be available. This resolution does not allow an efficient background subtraction, since a lot of combinatorial will mimic an hadronic boson decay. Thus stronger cuts on other kinematical variables have to be imposed reducing the signal efficiency.

A quite good sensitivity to the heavy Higgs mass resonance is achieved and also in the no-Higgs scenario the VV invariant mass spectrum is enough well reconstructed. In fact a reasonable reconstruction efficiency for the region of high VV invariant mass is achieved, as shown in Fig. 6.7. The resolution on m_{VV} is of the order of 10% (Table 6.6).

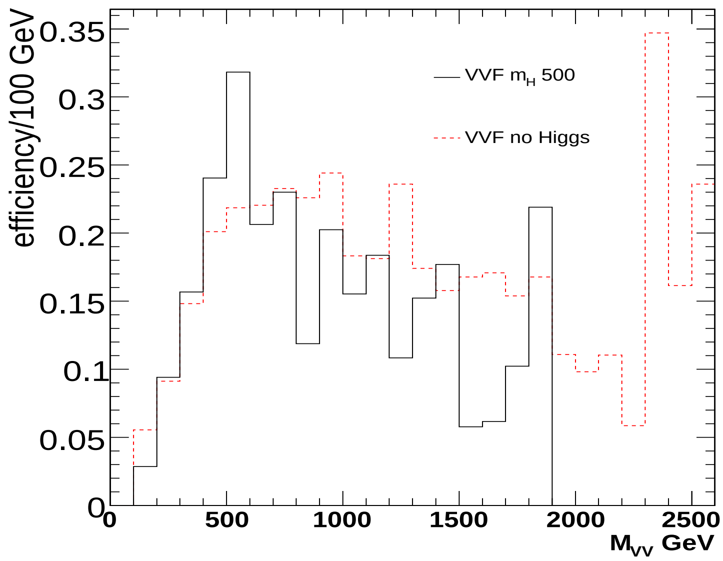

Figure 6.7: *Signal reconstruction efficiency as a function of the generated VV invariant mass.*

The signal-to-background ratio appears to be encouraging at high invariant mass: in Table 6.7 the number of signal and backgrounds events after 60 fb^{-1} of integrated luminosity is reported. The corresponding significance is computed using the program S_{cP} [75]. For the Higgs case only the Higgs boson

Table 6.6: *Resolution of the reconstructed invariant masses.*

State	Resolution (%)
$Z \to ll$	1.5
$W/Z \to jj$	20
$VV \to 4f$	9.5

peak is considered, while in the no-Higgs case the high invariant mass region is considered (m_{VV} >1 TeV/c^2)

Finally in Fig. 6.8 the number of events after 60 fb^{-1} of integrated luminosity is shown as a function of the reconstructed m_{VV}.

Since FAMOS could only deal with low luminosity pile-up, the results have been given for 60 fb^{-1}. With a higher luminosity a better signal to noise separation could be achieved, and for some of the channel a resonable number of signal events could be reached as well. Assuming no change in efficiency due to the higher pile-up, if the integrated luminosity would be 300 fb^{-1} a significance of 0.6 for the no-Higgs case, with m_{VV} > 1 TeV/c^2, and of 2.78 for the region around the peak for m_H =500 GeV/c^2 would be achieved. It has to be stressed that better efficiencies are expected whenever a better jet reconstruction and therefore a better resolution on $m_{V \to jj}$ will be achieved.

Table 6.7: *Number of signal and backgrounds events after the analysis cuts, with 60 fb^{-1} of integrated luminosity. No-Higgs case: events with $m_{VV} > 1\,TeV/c^2$; m_H = 500 GeV/c^2: events with $m_{VV} = m_H \pm \Gamma_H/c^2$, with $\Gamma_H = 100$ GeV).*

Sample	No-Higgs	m_H=500 GeV/c^2
signal	5	86
Z + n jets	205	3798
$\bar{t}t$	0	30
ZZ + n jets	10	125
ZW + n jets	139	781
irreducible backgrounds	1	20
backgrounds	355	4754
significance	0.38	1.24

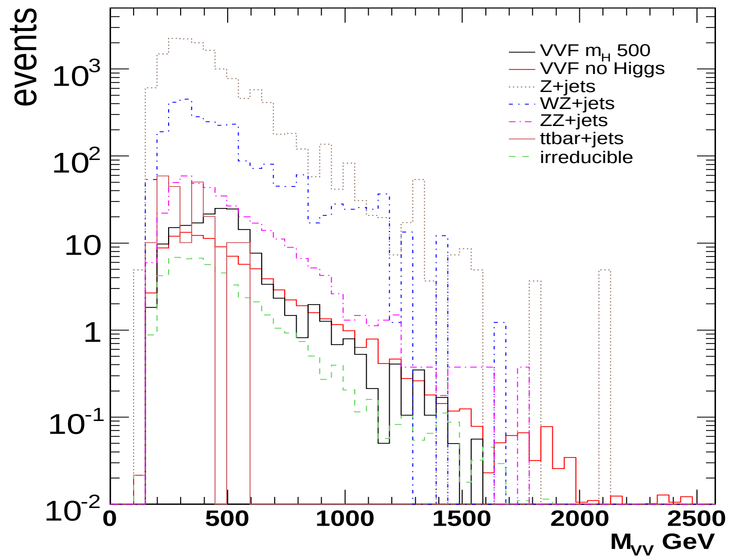

Figure 6.8: *Number of events after the analysis cuts with 60 fb^{-1} of integrated luminosity.*

6.4.1 High Invariant Mass Results

As discussed in Section 6.2.3 the region of high values of m_{VV} is sensitive to the presence or not of a Higgs particle. The results are summarized in Table 6.8 and Fig. 6.9.

Table 6.8: *Ratio between Higgs case and no-Higgs case signal events and number of background events with $m_{VV} > 1$ TeV after the analysis cuts for each final state with 60 fb^{-1} of integrated luminosity.*

$\left(\int_{1TeV}^{+\infty} NdM\right)_{noHiggs}$	$\left(\int_{1TeV}^{+\infty} NdM\right)_{m(H)500}$	$\frac{\left(\int_{1TeV}^{+\infty} NdM\right)_{noHiggs}}{\left(\int_{1TeV}^{+\infty} NdM\right)_{m(H)500}}$	$\left(\int_{1TeV}^{+\infty} NdM\right)_{backgr}$
5	2.7	1.85	355

6.5 Conclusions

An exploratory study of the VV-scattering process at CMS as probe of Electroweak Symmetry Breaking has been presented. If a Higgs boson exists the invariant mass spectrum of the two bosons in the final states will show a

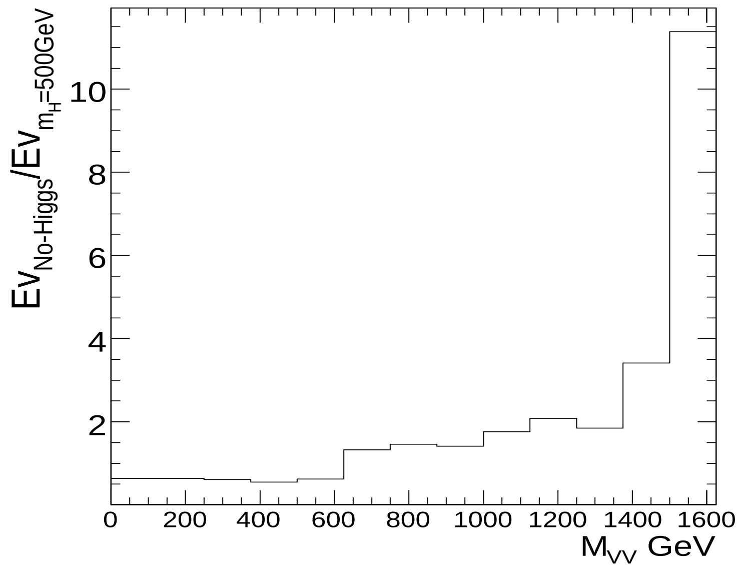

Figure 6.9: *The ratio of the signal events expected in 60 fb^{-1} after the analysis cuts in the no-Higgs case and in the Higgs case. The ratio is integrated from m_{VV} up to infinity and shown as a function of m_{VV}.*

peak at $m_{VV} = m_H$. If the Higgs boson will not exist the cross section for $m_{VV} > 1$ TeV/c^2will deviate from the Standard Model predictions.

The final state is characterized by the presence of six fermions. The two fermions which have emitted the two bosons have peculiar kinematic pattern and are essential to tag the event as VV fusion, allowing an efficient background subtraction. Among the various possibilities for the flavours of the four fermions from the boson decays, the case with a presence of two muons has been studied. A dedicated MC (PHANTOM [69]) has been used, to properly described the signal and the irreducible background. The results should improve in the near future when more sophisticated jet algorithms will be available. Due to the quite poor signal over background ratio, it is still difficult to say how long it will take to be able to relay only on the high m_{VV} region to understand the mechanism which breaks the symmetry, but high luminosity will surely be needed.

Chapter 7

Z Boson into $\mu\mu$

The aim of the present chapter is to show the impact of the muon reconstruction (Chapter 4 and 5) performance on the observables related to the $Z \to \mu\mu$ process, as a high quality reconstruction of the electroweak boson is fundamental for the analysis of the vector boson fusion channel (Chapter 6).

In order to perform this study a sample of $3.5 \cdot 10^5$ events containing a Z boson decaying into two muons has been generated, with pile-up corresponding to the start-up luminosity. Only muons with $|\eta| \leq 2.4$ and $p_T \geq 5$ GeV/c have been considered. The request on p_T is essential to remove the muons at high rapidity which come from in-flight hadron decays.

A brief description of the $Z \to \mu\mu$ HLT selection efficiency has been given in Section 5.5.3.3.

7.1 Muon Reconstruction Performance

As done in Chapter 5, some of the relevant quantities related to the muon reconstruction are studied in the following. In particular the properties of the stand-alone and global muon reconstruction are shown. The stand-alone muon reconstruction is evaluated before the matching with the inner tracking system.

First, distributions of reconstructed p_T, η and ϕ are compared to the simulated ones. Fig. 7.1 shows the transverse momentum distribution of the muons that come from the Z boson. Both the stand-alone and the global muon well match the simulated distribution, although the lower resolution of the muon spectrometer alone is visible. The angular distributions (Figures 7.2 and 7.3) show that the reconstructed and simulated quantities are in good agreement. The resolution on q/p_T has been evaluated as a function of p_T and η (Fig. 7.4 and 7.5). The distributions of the resolution on the other parameters are similar to the corresponding quantities studied in Section 5.4.2, therefore only the mean values are reported in Table 7.1.

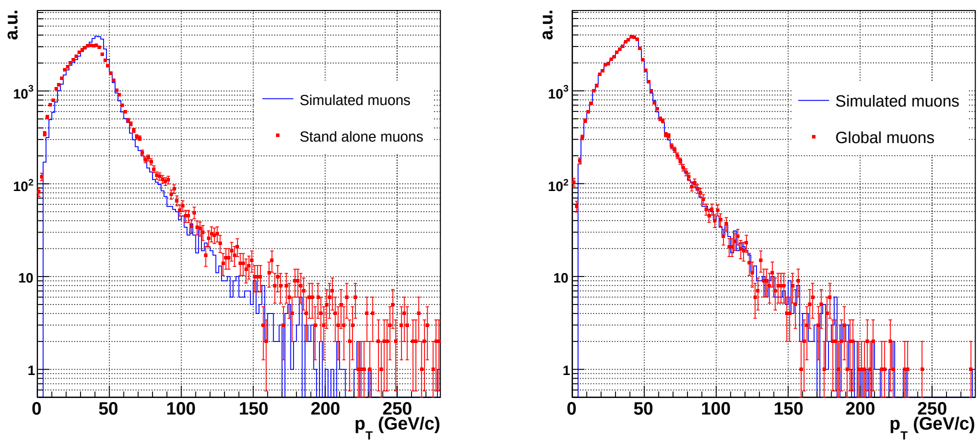

(a) Stand-alone muons. (b) Global muons.

Figure 7.1: *Transverse momentum distribution of the muons from the Z boson.*

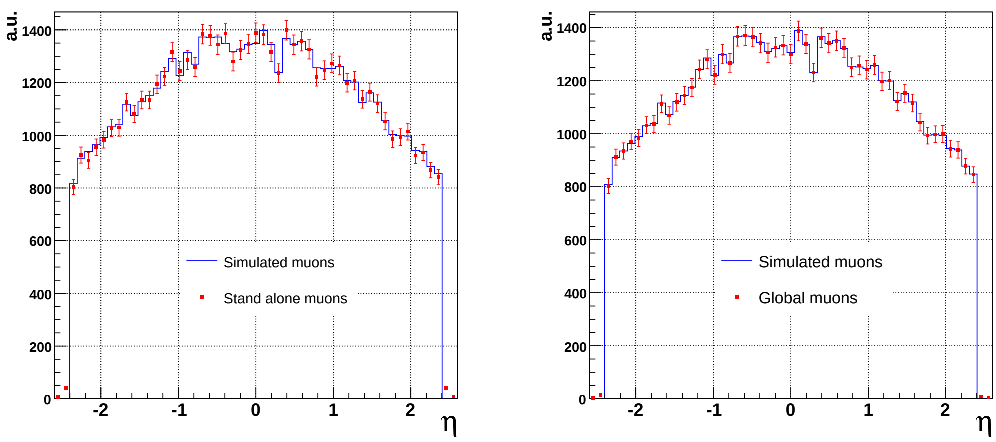

(a) Stand-alone muons. (b) Global muons.

Figure 7.2: *Pseudorapidity distribution of the muons from the Z boson.*

Other relevant parameter is the muon reconstruction efficiency as a function of η (Fig. 7.6), ϕ (Fig. 7.7) and p_T (Fig. 7.8). The results shown here are compatible with the ones obtained in Section 5.4.1, although the $Z \rightarrow \mu\mu$ sample contains more than one muon per event and in the tracker additional tracks from the underlying events are also present (Fig. 7.9). About 80% of the events contains more than 200 charged particles in the inner tracker.

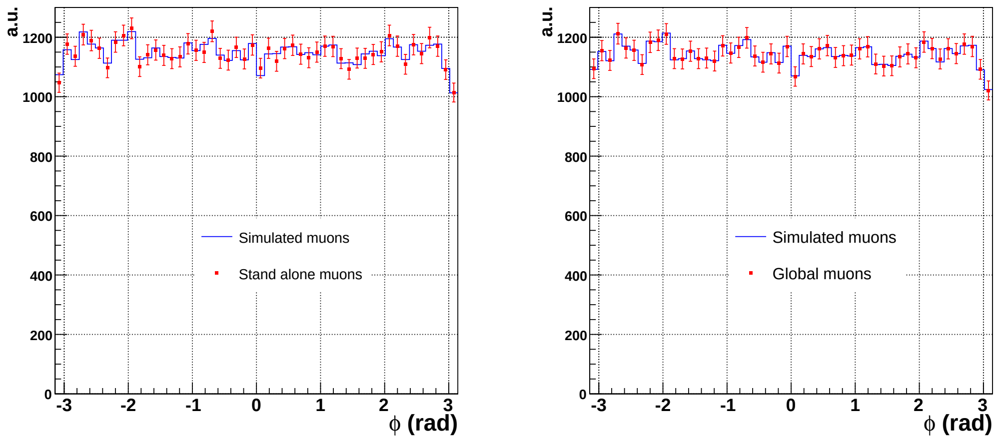

(a) Stand-alone muons. (b) Global muons.

Figure 7.3: *ϕ distribution of the muons from the Z boson.*

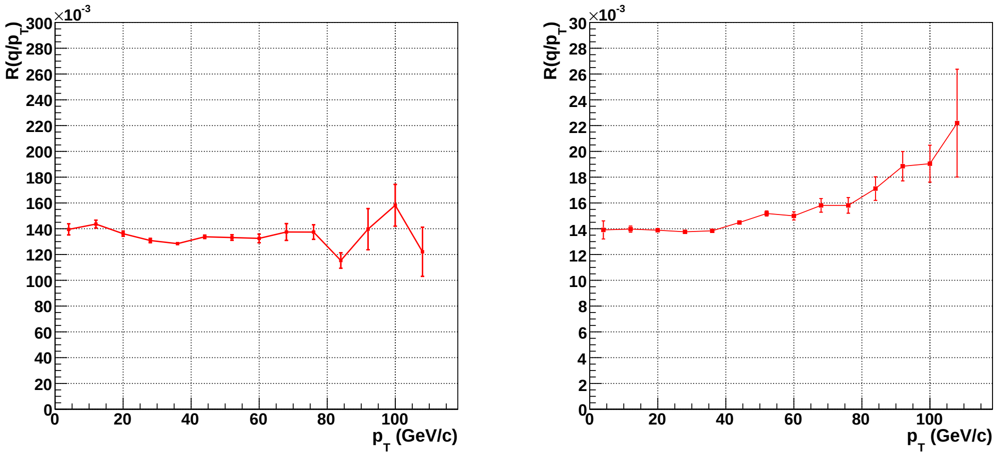

(a) Stand-alone muons. (b) Global muons.

Figure 7.4: *Resolution on the q/p_T parameter of the muons from the Z boson decay as a function of the muon transverse momentum.*

7.2 Z Reconstruction Performance

The Z boson identification is done using a combinatorial algorithm which matches muons of opposite charge. Since it is not intention of this analysis to perform a particular physics selection, no special requirement is applied to the muon pair. Only a loose cut on the di-muon invariant mass is imposed ($m_{\mu\mu} \leq 200$ GeV$/c^2$).

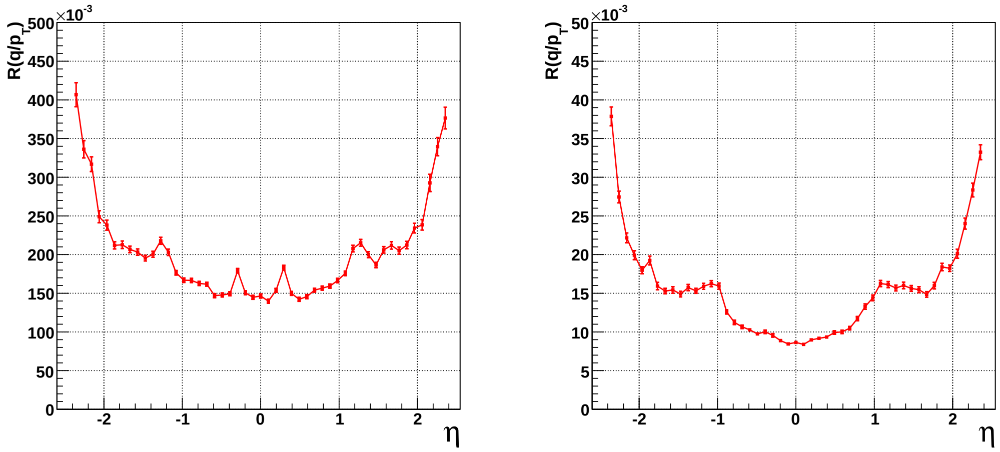

(a) Stand-alone muons. (b) Global muons.

Figure 7.5: *Resolution on the q/p_T parameter of the muons from the Z boson decay as a function of the muon pseudorapidity.*

Table 7.1: *Resolution on q/p_T, η, ϕ and on the impact parameters of the muons from the Z.*

Observable	Stand-alone muons	Global muons
q/p_T (%)	13.26 ± 0.07	1.557 ± 0.006
η	$(6.83 \pm 0.03)10^{-3}$	$(2.807 \pm 0.012)10^{-4}$
ϕ $(mrad)$	5.66 ± 0.03	$(1.622 \pm 0.007)10^{-1}$
d_{xy} (μm)	–	12.21 ± 0.06
d_z (μm)	–	31.91 ± 0.16

The efficiency of the Z reconstruction as a function of ϕ and p_T of the simulated Z is shown in Fig. 7.10. Since no selection cuts are applied, the efficiency of the Z identification shown here represents the limit that can be achieved in a physics analysis at CMS. The mean value of the efficiency is about 97%.

The efficiency as a function of η is shown in Fig. 7.11. The figure illustrates the effect of the mis-assignment of the charge in the muon spectrometer. Fig. 7.11(a) shows the efficiency obtained using the Monte Carlo truth information to select the pair of reconstructed muons, whereas in Fig. 7.11(b) the pairing is performed using only the estimated muon quantities. The curve related to the global muons does not significantly change, while for the stand-alone muons there are sensible differences: the plot in Fig. 7.11(a) confirms the

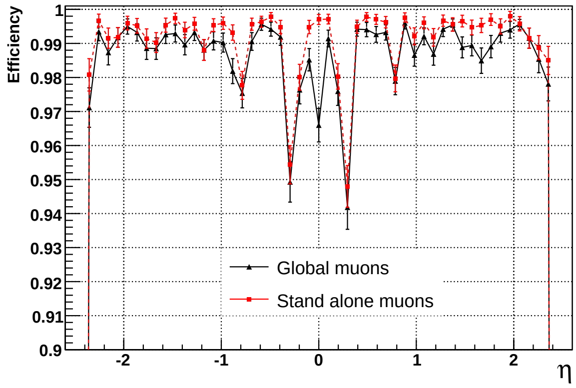

Figure 7.6: *Muon reconstruction efficiency as a function of the muon pseudo-rapidity.*

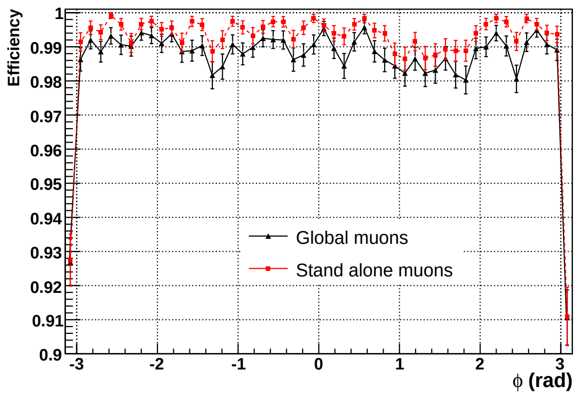

Figure 7.7: *Muon reconstruction efficiency as a function of ϕ.*

muons from the Z boson are reconstructed, but Fig. 7.11(b) shows that about 4% of the Z bosons is lost. This is due to incorrect muon charge assignment. Therefore, although the stand-alone muon reconstruction has a higher efficiency than the global, currently no selection based on the charge of the stand-alone muon pair should be applied. In the following, the quantities related to the Z boson, reconstructed using global muons unless otherwise specified, are studied in detail.

In Fig. 7.12 the reconstructed and the simulated Z bosons are compared on the basis of their 4-momenta. The reconstructed variables distribute accordingly to the simulated quantities. In Fig. 7.13 and 7.14 the resolution on the transverse momentum as a function of p_T and η of the simulated boson is shown. The mean value of $\delta(p_T)/p_T^{sim}$ indicates that the transverse momentum

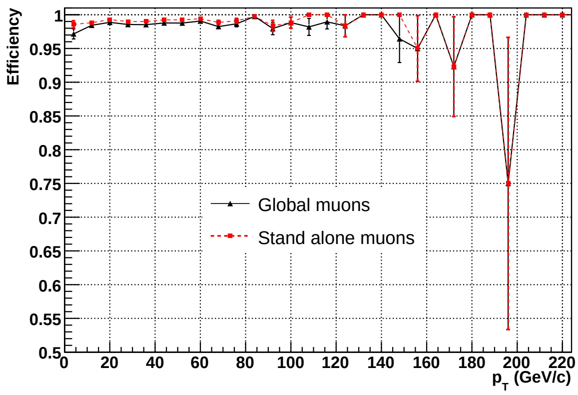

Figure 7.8: *Muon reconstruction efficiency as a function of the muon transverse momentum.*

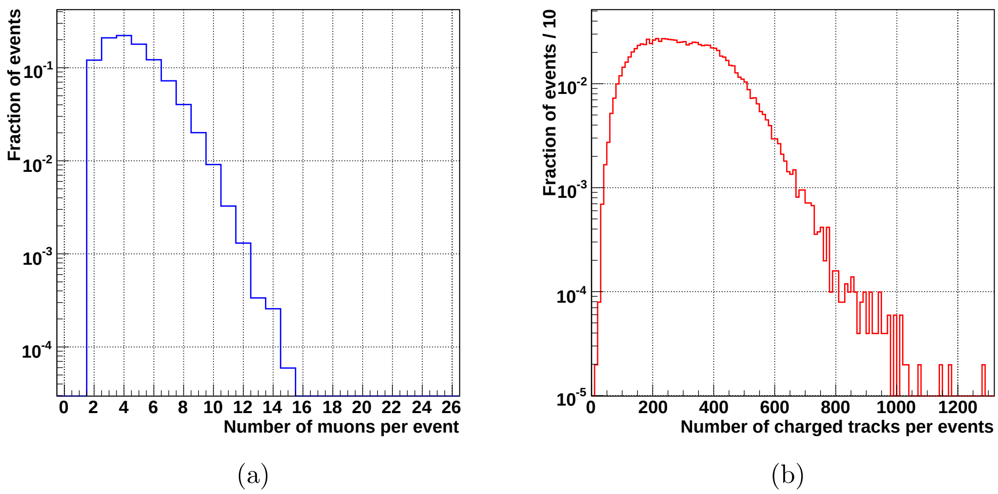

Figure 7.9: *Fraction of simulated muons (a) and of simulated charged particles (b) in the events.*

is slightly (about 0.2%) over-estimated, while the width shows the average value of the resolution is about 3.8%. In Fig. 7.15 the mean and the width of the residual on η are illustrated. Although the plot in Fig. 7.15(a) is not flat, the deviation from linearity is of the order of 10^{-3}. A summary of the average resolutions on the Z boson observables is reported in Table 7.2.

The most important observables for this sample are the mass (m_Z) and the width (Γ_Z) of the Z boson. To calculate them the di-muon invariant mass (Fig. 7.16) has been computed and the Z resonance interpolated with

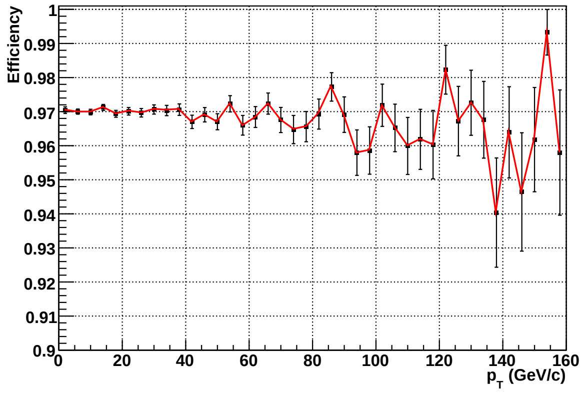

(a) ε_Z vs p_T.

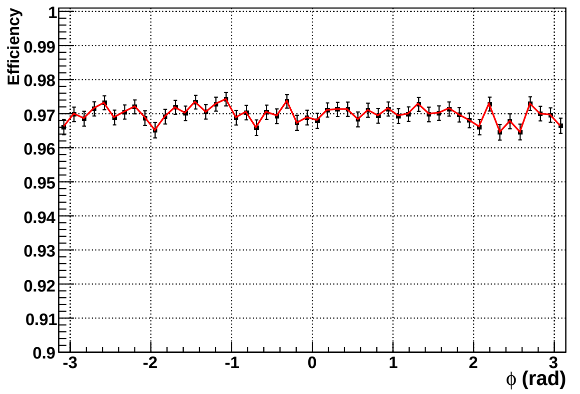

(b) ε_Z vs ϕ.

Figure 7.10: *Z boson reconstruction efficiency as a function of the transverse momentum and the ϕ angle calculated from the momentum of the simulated Z.*

Table 7.2: *Resolution on m_Z, p_T, η and ϕ of the Z.*

Observable	Resolution	
	Stand-alone muons	Global muons
m_Z (%)	7.6 ± 0.2	1.0566 ± 0.0018
p_T (%)	34.59 ± 0.13	3.814 ± 0.011
η	$(2.364 \pm 0.011) \cdot 10^{-1}$	$(2.611 \pm 0.010) \cdot 10^{-2}$
ϕ (rad)	$(2.352 \pm 0.011) \cdot 10^{-1}$	$(2.631 \pm 0.010) \cdot 10^{-2}$

a Lorentzian function. The half width at half maximum and the mean of the

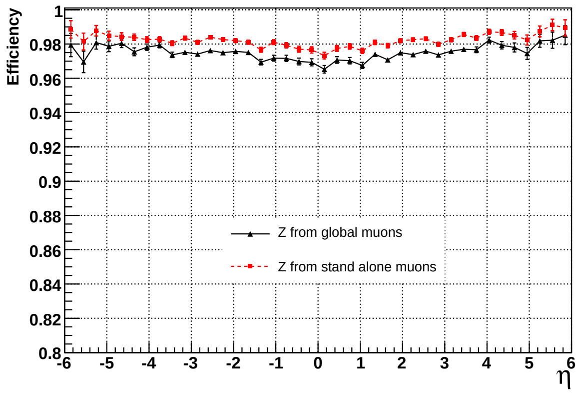

(a) Using simulation information to associate two muons.

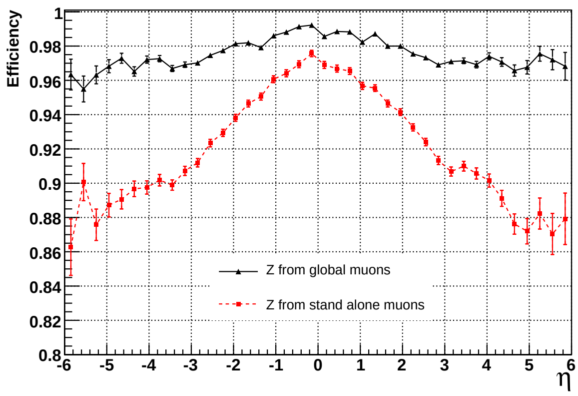

(b) Using reconstructed information to associate two muons.

Figure 7.11: *Z boson reconstruction efficiency, using the stand-alone and the global muon separately, as a function of the pseudorapidity calculated from the momentum of the simulated Z.*

fit have been taken as the width and the mass of the Z boson[1], respectively.

In Fig. 7.17, 7.18 and 7.19 m_Z and Γ_Z are shown as a function of the kinematic parameters (η_Z, ϕ_Z and p_T^Z) of the Z boson. Both the invariant mass and the width of the Z boson are stable around the mean value up to $p_T^Z = 140$ GeV/c. Also in the studied η range the deviations from the average value are small, although they are non-zero. The spectrum in ϕ is almost flat and has been used to compute m_Z and Γ_Z through a linear fit.

[1]The parameters m_Z and Γ_Z are not strictly the Z physical mass and width. They should be intended as phenomenological parameters as they are the convolution of the true values and the detector resolution.

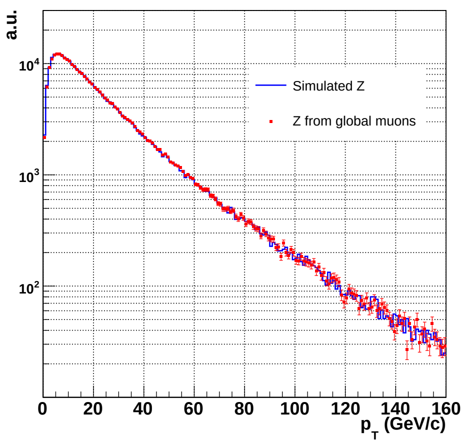

(a) Transverse momentum.

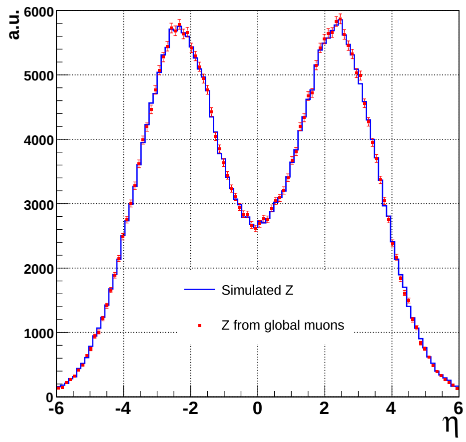

(b) Pseudorapidity.

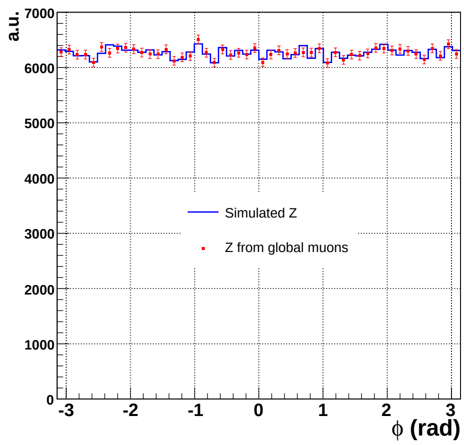

(c) Direction in $R - \phi$ plane.

Figure 7.12: *Distribution of the observables related to the Z boson reconstruction compared with the simulated Z.*

In Table 7.3 the values of m_Z and Γ_Z are reported for the boson reconstructed using the muon spectrometer alone and using the global tracking system.

The resolution on m_Z as a function of the kinematic variables of the Z boson is shown in Figures 7.20, 7.21 and 7.22. The distribution of the mean value of $\delta(m_Z)/m_Z^{sim}$ as a function of p_T shows a little bias in the m_Z computation. This shift towards greater mass estimation amounts to about 0.3% and is almost constant as a function of the transverse momentum of the boson. The mean value of the resolution on the invariant mass is about 1% (Table 7.2).

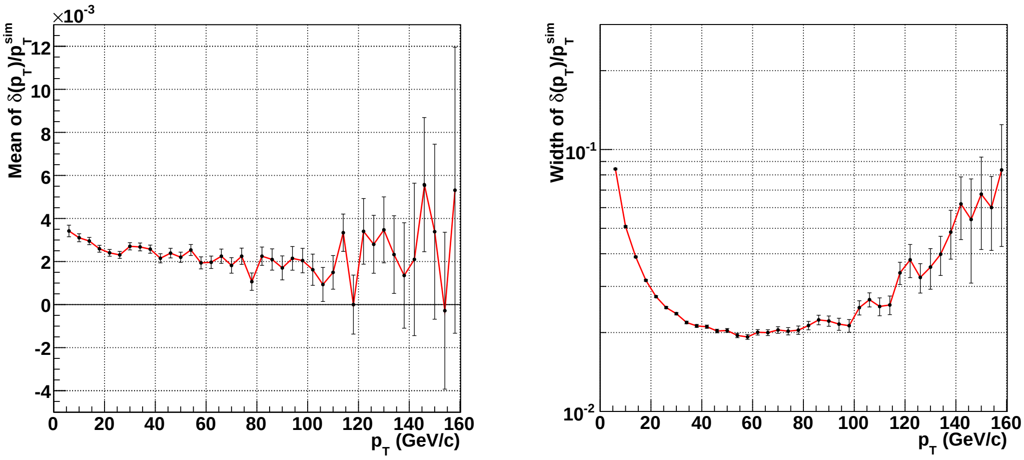

(a) Mean of $\delta(p_T)/p_T^{sim}$ vs p_T. (b) Width of $\delta(p_T)/p_T^{sim}$ vs p_T.

Figure 7.13: *Resolution on the transverse momentum of the reconstructed Z as a function of the transverse momentum of the simulated boson.*

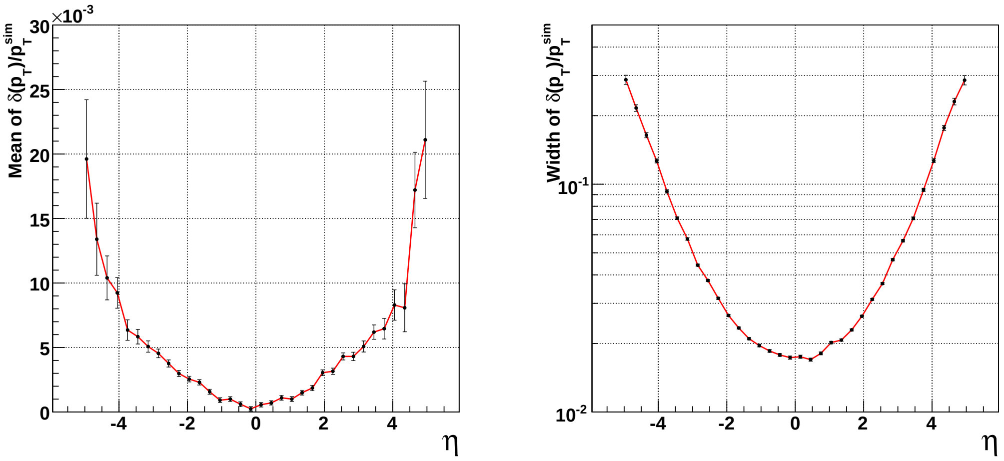

(a) Mean of $\delta(p_T)/p_T^{sim}$ vs η. (b) Width of $\delta(p_T)/p_T^{sim}$ vs η.

Figure 7.14: *Resolution on the transverse momentum of the reconstructed Z as a function of the pseudorapidity of the simulated boson.*

7.3 Conclusions

The muon reconstruction efficiency evaluated using the $Z \to \mu\mu$ sample is compatible with the results on single muons presented in Section 5.4 and the average value is above 98%. Also the resolutions are compatible with the values estimated in Section 5.4, in particular the mean value of q/p_T resolution is about

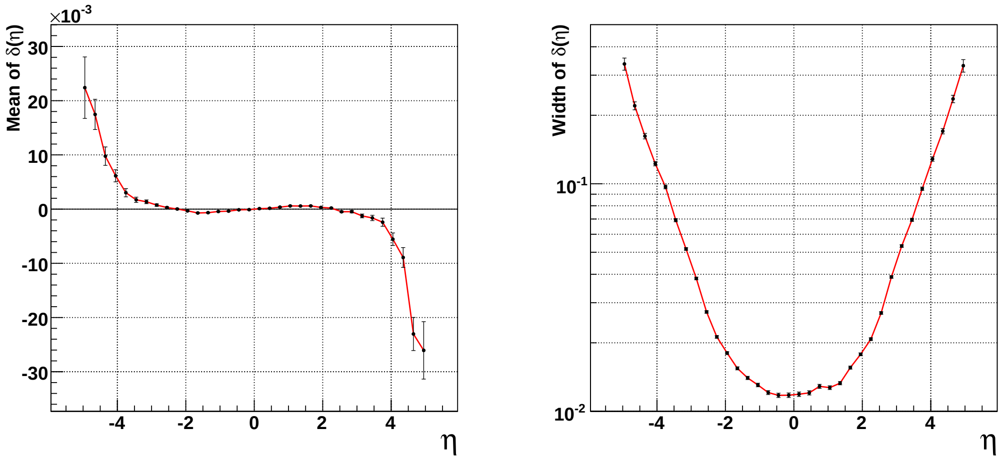

(a) Mean of $\delta(\eta)$ vs η. (b) Width of $\delta(\eta)$ vs η.

Figure 7.15: *Residual on the pseudorapidity of the reconstructed Z as a function of the pseudorapidity of the simulated boson.*

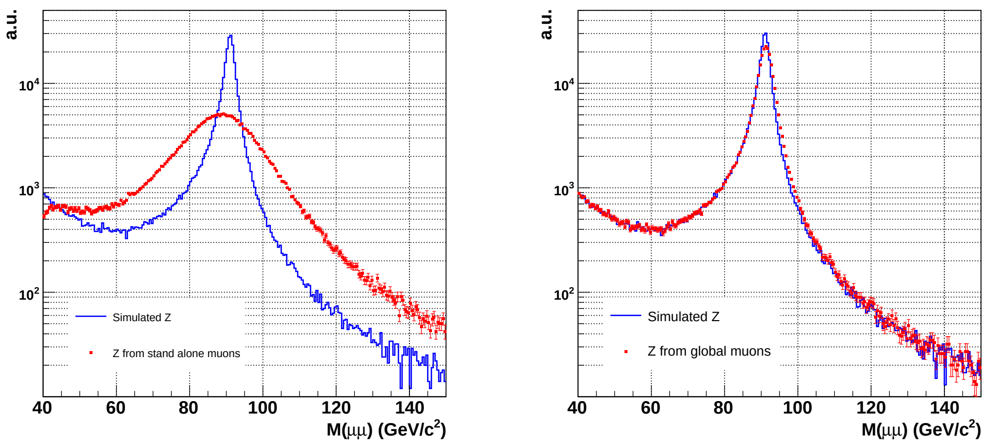

(a) Stand-alone muons. (b) Global muons.

Figure 7.16: *Invariant mass of the di-muon system calculated using the track reconstructed in the muon spectrometer alone (a) and the full tracking system (b) compared with the Monte Carlo information ((b)).*

1.6%.

The good muon reconstruction performance determines the quality of the resolution on the $Z \to \mu\mu$ boson observables. The results of this Chapter show the Z decaying into two muons can be reconstructed with high precision, thus

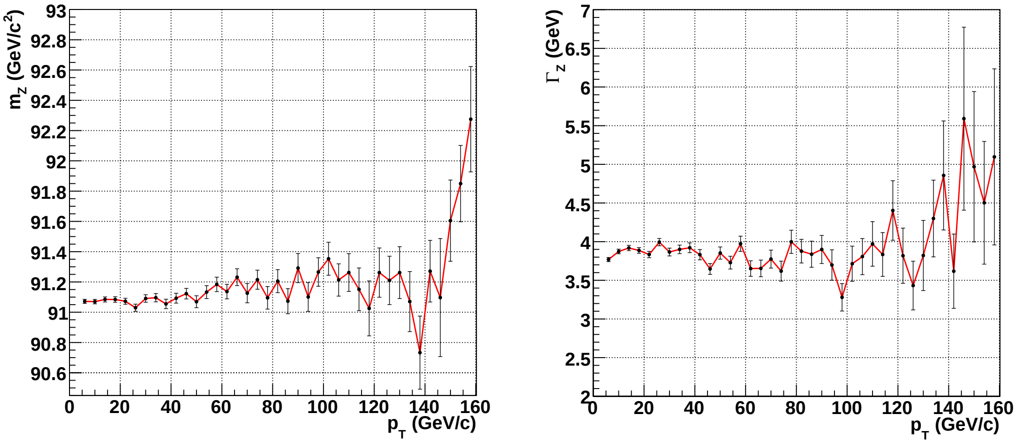

(a) m_Z vs p_T.

(b) Γ_Z vs p_T.

Figure 7.17: *Invariant mass and width of the reconstructed Z as a function of the transverse momentum of the simulated Z.*

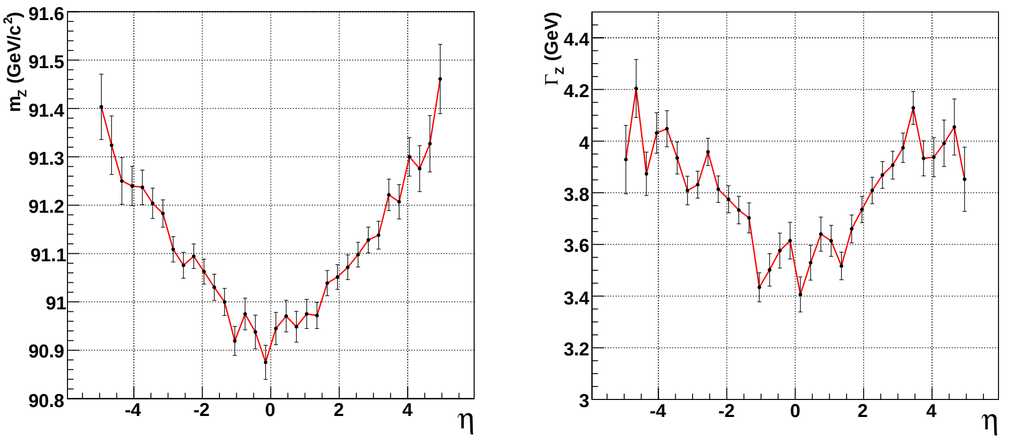

(a) m_Z vs η.

(b) Γ_Z vs η.

Figure 7.18: *Invariant mass and width of the reconstructed Z as a function of the pseudorapidity of the simulated Z.*

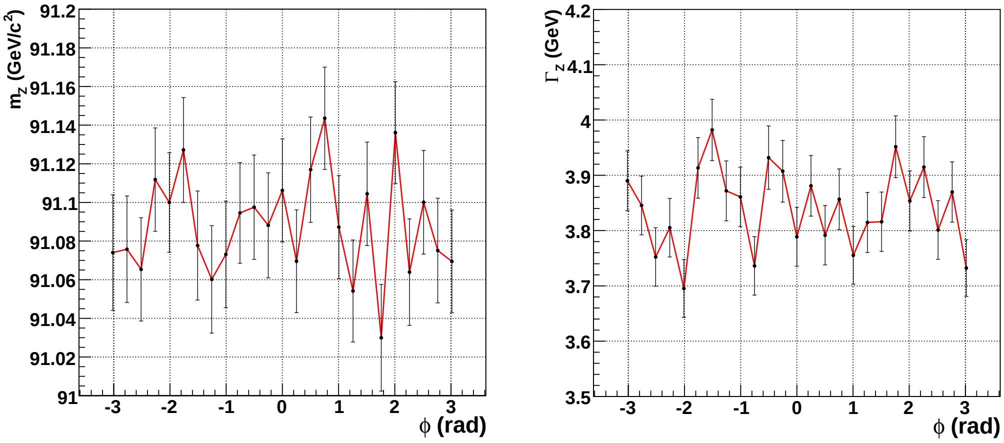

(a) m_Z vs ϕ. (b) Γ_Z vs ϕ.

Figure 7.19: *Invariant mass and width of the reconstructed Z as a function of the ϕ direction of the simulated Z.*

Table 7.3: *m_Z and Γ_Z for the boson reconstructed using the muon spectrometer alone or the global tracking system.*

Muon type	m_Z (GeV/c^2)	Γ_Z (GeV)
Stand-alone muons	88.17 ± 0.03	19.74 ± 0.08
Global muons	91.089 ± 0.005	3.838 ± 0.011

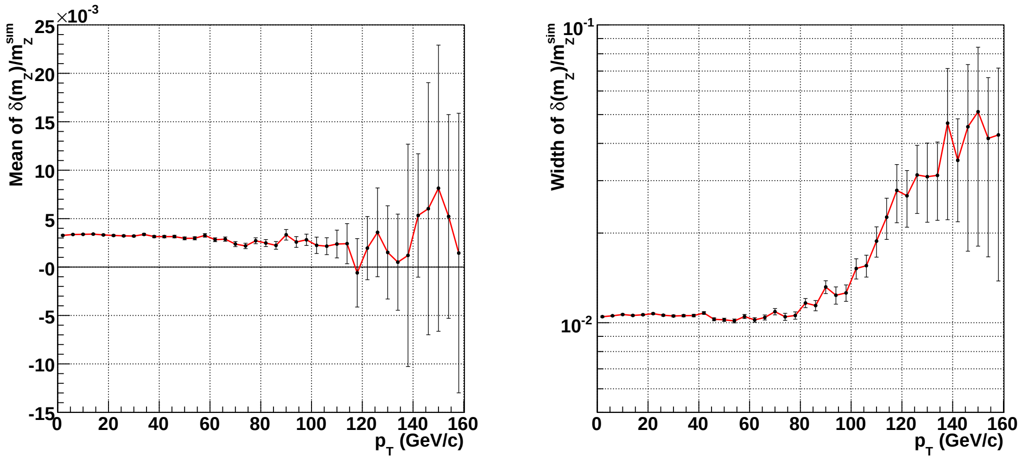

(a) Mean of $\delta(m_Z)/m_Z^{sim}$ vs p_T. (b) Width of $\delta(m_Z)/m_Z^{sim}$ vs p_T.

Figure 7.20: *Resolution on the invariant mass of the reconstructed Z as a function of the transverse momentum of the Z.*

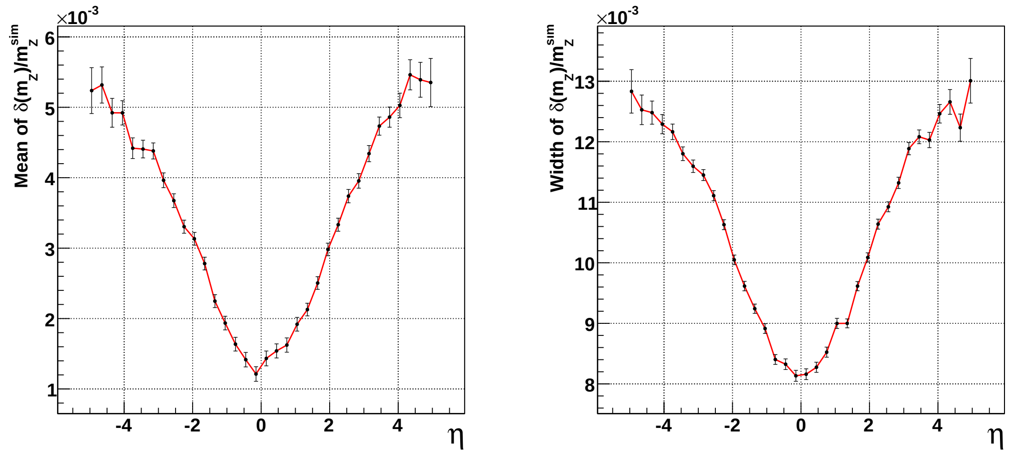

(a) Mean of $\delta(m_Z)/m_Z^{sim}$ vs η. (b) Width of $\delta(m_Z)/m_Z^{sim}$ vs η.

Figure 7.21: *Resolution on the invariant mass of the reconstructed Z as a function of the pseudorapidity of the Z.*

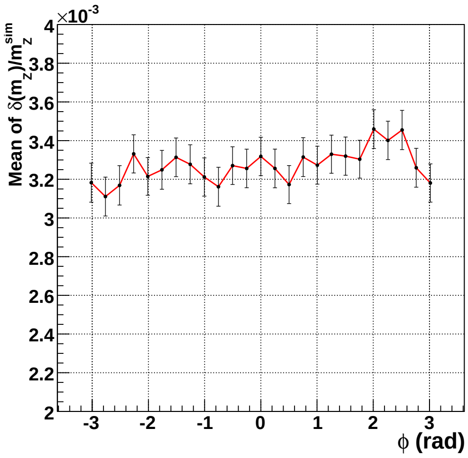

(a) Mean of $\delta(m_Z)/m_Z^{sim}$ vs ϕ.

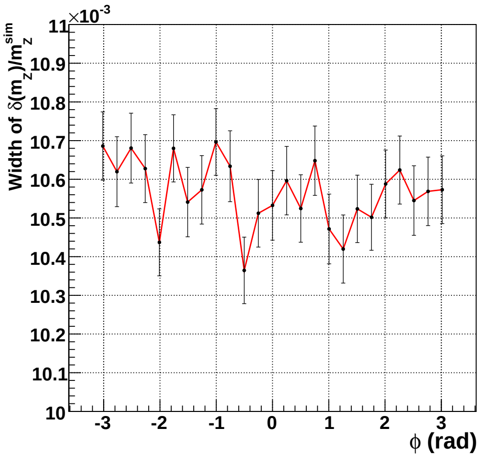

(b) Width of $\delta(m_Z)/m_Z^{sim}$ vs ϕ.

Figure 7.22: *Resolution on the invariant mass of the reconstructed Z as a function of the ϕ of the Z.*

allowing accurate measurements of the relevant quantities of the electroweak bosons [9]. The Z reconstruction efficiency is about 97%, which is compatible with the estimated charge assignment probability and with the muon reconstruction efficiency. The resolution on the Z boson mass is 1.1%, thus obtaining $m_Z = (91.089 \pm 0.005)$ GeV$/c^2$ and $\Gamma_Z = (3.383 \pm 0.011)$ GeV as average values.

In Fig. 7.23 a direct comparison between the algorithm based on ORCA [37] (the old CMS reconstruction software) used for the study in Chapter 6, and the one described in Chapter 5 and here, is shown. The improvement in the efficiency is evident. Improvements in the parameter resolutions, with respect to [37], can also be observed.

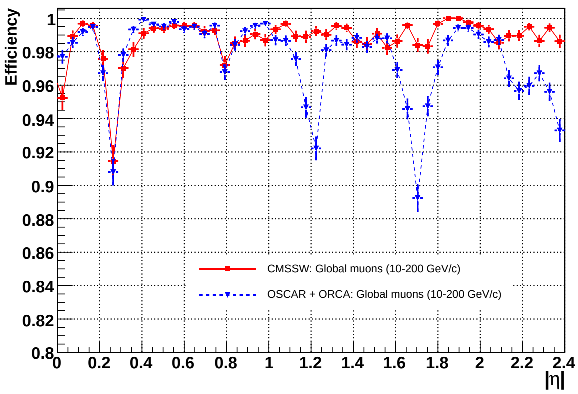

Figure 7.23: *Efficiency as a function of pseudorapidity for the the algorithm used for the analysis discussed in Chapter 6 (blue) and for the current implementation.*

Summary

The Compact Muon Solenoid collaboration designed a robust muon detection system, as muons provide a clear signature for many interesting processes.

The reconstruction of events containing muons requires a deep understanding of the apparatus, thus the output of the simulation should be as close as possible to the real detector response.

The work presented in this thesis covers the description and the performance studies of the muon reconstruction and simulation algorithms which I developed. More specifically: the simulation of the drift tube cell, the muon reconstruction within the DT chamber, the track reconstruction and muon identification with the whole CMS tracking system, have been extensively discussed. The final aim was to obtain a high resolution on the observables of the $Z \to \mu^+\mu^-$ process, because the presence of the Z particle in the final state is one of the important signatures of the $pp \to \mu^+\mu^- jjjj$ vector boson scattering channel.

The main items can be summarised as follow.

In the simulation of the drift tube cell, the response of the detector to the crossing particle is modelled taking into account the particles interaction with material and the electromagnetic properties of the cell. The accuracy of the simulation has been successfully tested comparing its output with the real data collected during the October 2004 test beam.

The muon reconstruction starts at the level of the individual chamber. The tracking algorithms use the information coming from each muon sub-detector to build the tracks within the muon system alone. The final muon tracks are obtained combining the trajectories in the muon spectrometer with the ones in the inner tracking system. The muon reconstruction in CMS has satisfactory performance at each level of the chain and the design requirements [47] are met. Moreover, the muon track reconstruction was tested at the *Magnet Test Cosmic Challenge* [4] held during Summer 2006, where it was proved that it is able to reconstruct real cosmic muons data. This, together with the analysis of the reconstruction performance here presented, demonstrates that the muon reconstruction is ready for the data taking at LHC.

The reconstruction algorithms discussed in this thesis are also the basis of the muon High Level Trigger. The current prototype of the muon HLT is a complete, fully functional system and timing studies show that the CPU time spent in the muon reconstruction is well within the affordable budget.

A study of the $pp \to \mu^+\mu^- jjjj$ channel has been performed in order to assess the possibility of probing the symmetry breaking mechanism through the VV fusion process using the CMS detector, with no assumption on the mechanism which restores the unitarity. Although the results are very encouraging, operation at the full design luminosity of $10^{34}\mathrm{cm}^{-2}\mathrm{s}^{-1}$ is needed in order to reach a significant signal over background ratio.

Finally, the muon reconstruction algorithms have been tested on one of the signatures of the vector boson scattering channel: the reconstruction of the Z boson decaying into two muons. The results show that the $Z \to \mu^+\mu^-$ process can be reconstructed with high precision, thus allowing accurate measurements of the relevant observables related to the electroweak boson.

Appendix A

Kalman Filter Method

The Kalman Filter [76] is a recursive method for the fit of a discrete set of data. This method is particularly suited for track fitting, since it allows implementation of reconstruction code which is independent of the number of measurements available.

The problem consists in the determination of an estimate of a generic state vector $\boldsymbol{x}$ given a set of measurements $\boldsymbol{m}_k$, that are assumed to have the form

$$\boldsymbol{m}_k = H_k \boldsymbol{x}_{k,true} + \boldsymbol{\epsilon}_k. \tag{A.1}$$

where H_k is the transform matrix from the state space to the measurement space and $\boldsymbol{\epsilon}_k$ is the noise that affects the true state.

In the case of track reconstruction, the state vector is defined as the position and momentum relative to a given surface (in the local coordinate frame):

$$\boldsymbol{x} = \begin{pmatrix} q/p \\ \tan\phi \\ \tan\theta \\ x \\ y \end{pmatrix} \tag{A.2}$$

where q is the charge, p is the momentum and ϕ, θ, x and y identify the track direction and position on the surface.

The first step consists in the seed generation. For muon tracks, the seed can either be generated from the parameters of Level-1 candidates or from a approximate state estimation based on the measurements themselves.

Each step is then decomposed into two parts: the prediction of the state vector and of the error covariance matrix on the surface of the next measurement to be included, and the update of the state, *i.e.* the inclusion of the information from that measurement. They are encapsulated in two basic components, called *propagator* and *updator*. The updator includes all the algebra of the filter, so

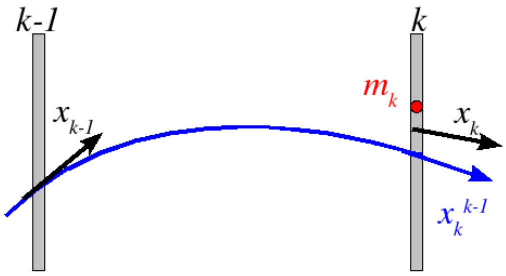

Figure A.1: *Schematic view of the propagation and update of the trajectory state.*

that the complexity of fitting is reduced to providing an analytic or numeric algorithm to propagate tracks and their errors. The propagator used in the muon system is able to extrapolate a state vector and its covariance matrix in a non-constant magnetic field, taking into account the effect of energy loss and multiple scattering in the material traversed by the track.

An external steering code is also needed to look for the measurements to be included in the fit. The algorithm for the hits search in the muon detectors is described in Section 5.

The result of a Kalman filter is a state on the surface of the last measurement, which includes all available information. However, the trajectory parameters calculated at other points of the trajectory do not include the information from all measurements. A special procedure is used to update the parameters at every surface. In the Kalman filter terminology, this procedure is called *"smoothing"*.

Fig. A.1 gives a pictorial view of the iterative process. x_{k-1}, the filtered state on the $(k-1)^{th}$ layer, is propagated to the k^{th} layer using the formulae:

$$x_k^{k-1} = F_{k-1} x_{k-1}, \tag{A.3}$$

$$C_k^{k-1} = F_{k-1} C_{k-1} F_{k-1}^T + Q_{k-1}, \tag{A.4}$$

where x_k^{k-1} is the estimated state on the k^{th}-layer, F_{k-1} is the application to propagate x_{k-1} to the next layer, C_k^{k-1} is the covariance matrix of the predicted state on $k-1$ and Q_{k-1} is the covariance matrix of the process noise (which takes into account the energy loss and the multiple scattering between detectors $k-1$ and k).

On the k layer the pattern recognition can be performed (usually based on a χ^2 criteria) to select the most compatible measurement with the predicted state. Once the best measurement ($\boldsymbol{m}_k$) has been identified, the trajectory is updated with the new information. This task is accomplished by the updator

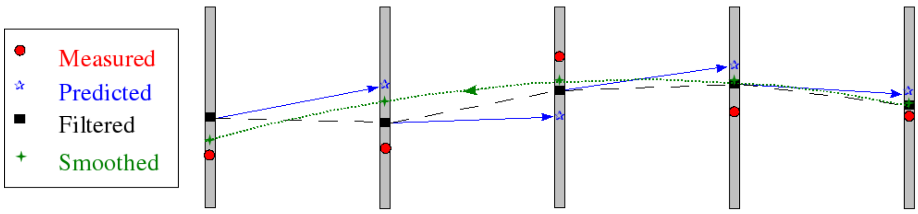

Figure A.2: *Schematic view of the Kalman filter applied to the track fitting.*

using the equations

$$x_k = x_k^{k-1} + K_k(m_k - H_k x_k^{k-1}), \quad (A.5)$$
$$C_k = (1 - K_k H_k) C_k^{k-1}, \quad (A.6)$$

where

$$K_k = C_k^{k-1} H_k^T (V_k + H_k C_k^{k-1} H_k^T)^{-1}$$

is the *gain matrix* and V_k =cov(ϵ_k).

Once all measurement have been filtered, the smoothing step can be performed. Like the filtering step, the smoothing process is iterative (Fig. A.2):

$$x_k^n = x_k + A_k(x_{k+1}^n - x_{k+1}^k), \quad (A.7)$$
$$C_k^n = C_k + A_k(C_{k+1}^n - C_{k+1}^k) A_k^T, \quad (A.8)$$

where

$$A_k = C_k F_k^T (C_{k+1}^k)^{-1}$$

and $n > k$.

The filtered estimate of the state vector is unbiased and has minimum variance among all linear estimates using the same set of measurements. The same is true for the smoothed estimates. Therefore the Kalman filter with a subsequent smoothing is equivalent to a global linear lest-square fit which takes into account all correlation arising from the process noise.

Appendix B

Comparison of μ^+ and μ^- Reconstruction

To perform the comparison two kinds of plots have been chosen: the total efficiency (with respect to the input simulated data) and the resolution of the q/p_T parameter, both evaluated as a function of the pseudorapidity.

The comparison between the two muon charges is shown in the following figures:

- in Fig. B.1 and B.2 for the seed,
- in Fig. B.3 and B.4 for the stand-alone muon reconstruction,
- in Fig. B.5 and B.6 for the tracker alone,
- in Fig. B.7 and B.8 for the reconstruction with the full CMS tracking system.

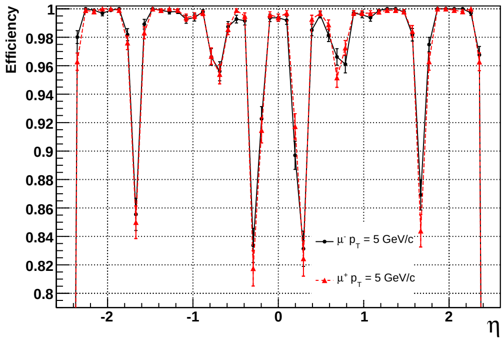

(a) $p_T = 5$ GeV/c. Efficiency.

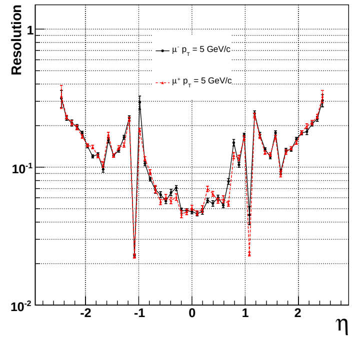

(b) $p_T = 5$ GeV/c. Resolution.

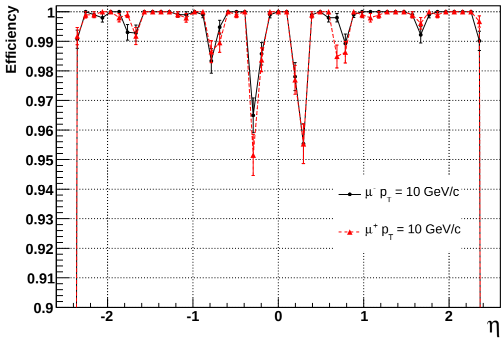

(c) $p_T = 10$ GeV/c. Efficiency.

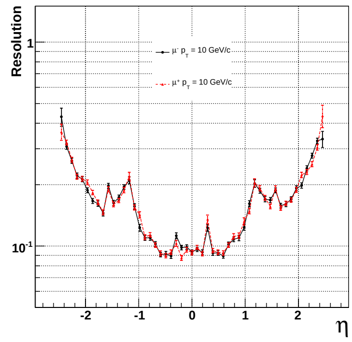

(d) $p_T = 10$ GeV/c. Resolution.

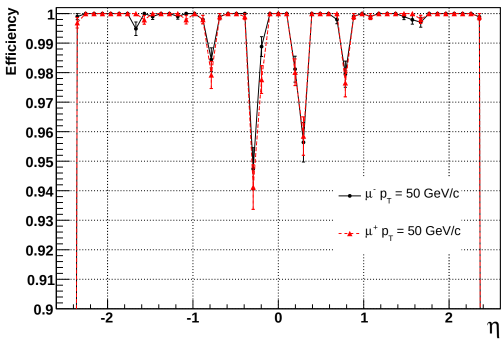

(e) $p_T = 50$ GeV/c. Efficiency.

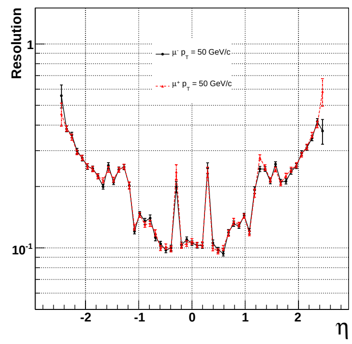

(f) $p_T = 50$ GeV/c. Resolution.

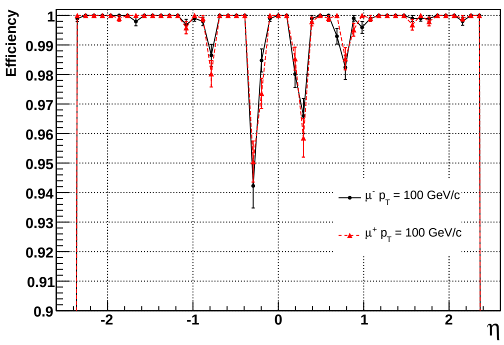

(g) $p_T = 100$ GeV/c. Efficiency.

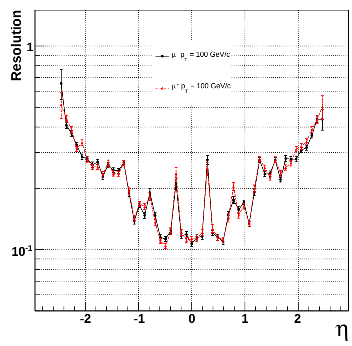

(h) $p_T = 100$ GeV/c. Resolution.

Figure B.1: *Comparison between the muon seed for μ^+ and μ^-.*

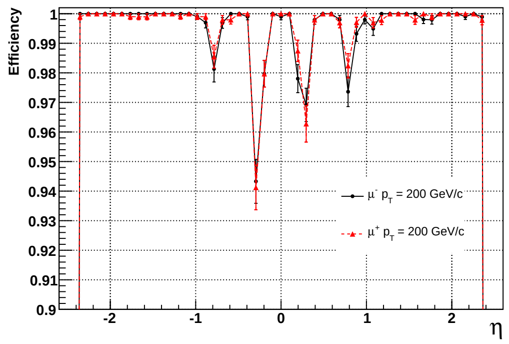

(a) p_T = 200 GeV/c. Efficiency.

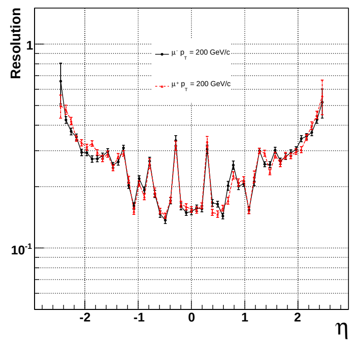

(b) p_T = 200 GeV/c. Resolution.

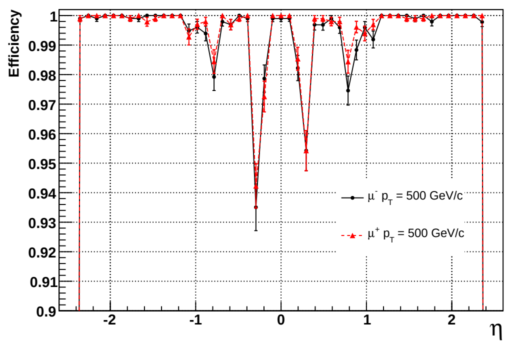

(c) p_T = 500 GeV/c. Efficiency.

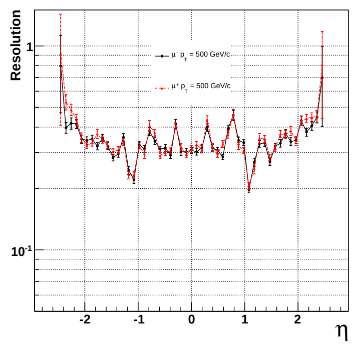

(d) p_T = 500 GeV/c. Resolution.

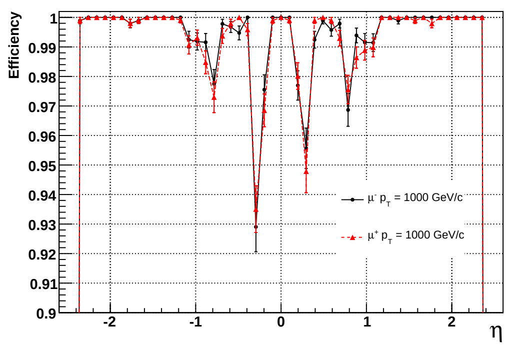

(e) p_T = 1000 GeV/c. Efficiency.

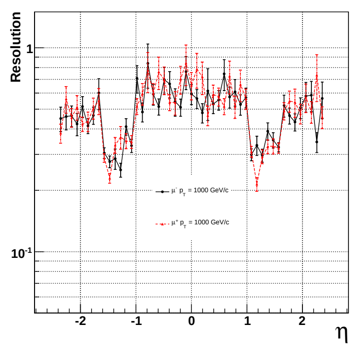

(f) p_T = 1000 GeV/c. Resolution.

Figure B.2: *Comparison between the muon seed for* μ^+ *and* μ^-.

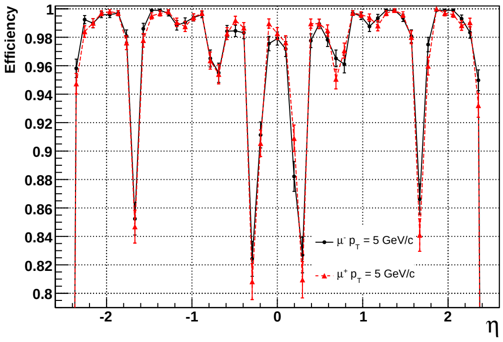

(a) $p_T = 5$ GeV/c. Efficiency.

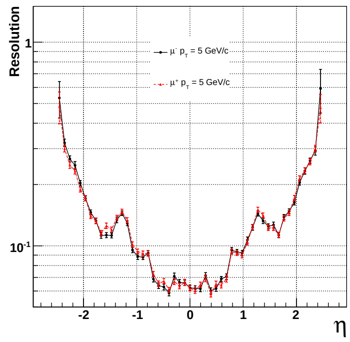

(b) $p_T = 5$ GeV/c. Resolution.

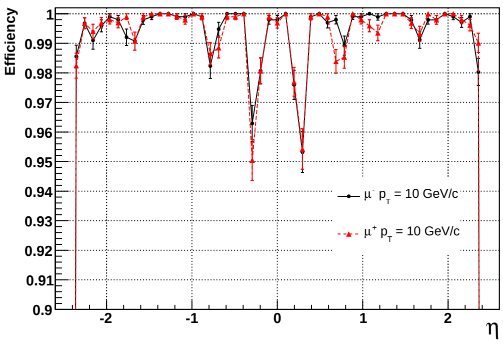

(c) $p_T = 10$ GeV/c. Efficiency.

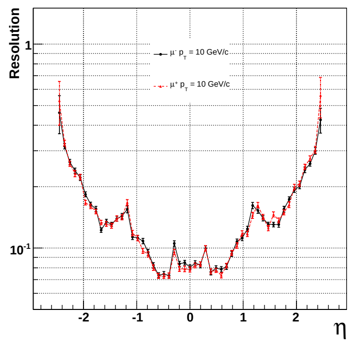

(d) $p_T = 10$ GeV/c. Resolution.

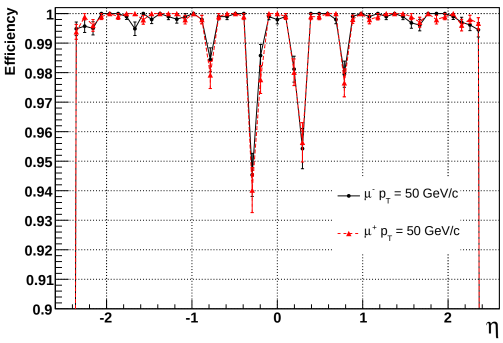

(e) $p_T = 50$ GeV/c. Efficiency.

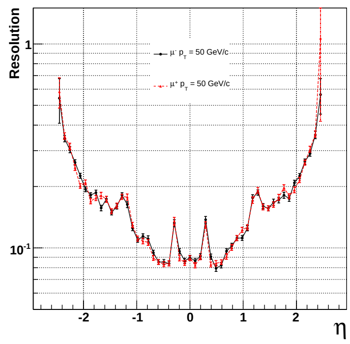

(f) $p_T = 50$ GeV/c. Resolution.

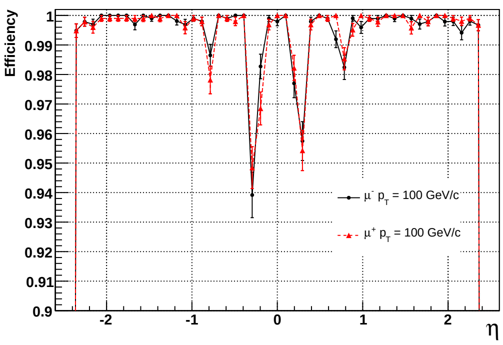

(g) $p_T = 100$ GeV/c. Efficiency.

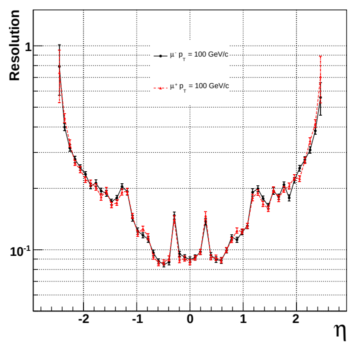

(h) $p_T = 100$ GeV/c. Resolution.

Figure B.3: *Comparison between the reconstruction of μ^+ and μ^- in the muon spectrometer alone.*

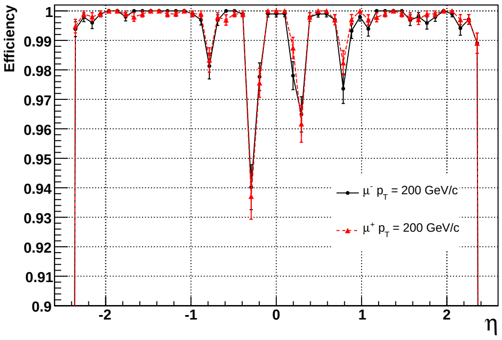

(a) $p_T = 200$ GeV/c. Efficiency.

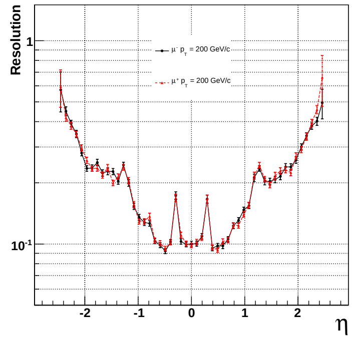

(b) $p_T = 200$ GeV/c. Resolution.

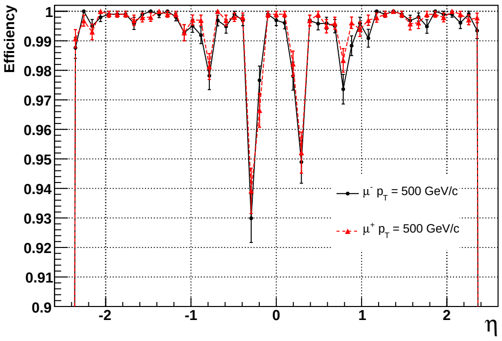

(c) $p_T = 500$ GeV/c. Efficiency.

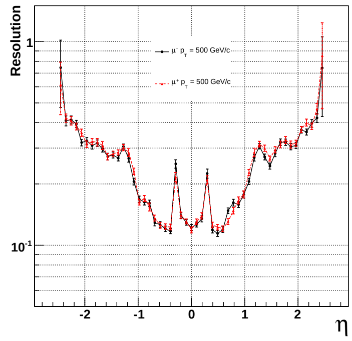

(d) $p_T = 500$ GeV/c. Resolution.

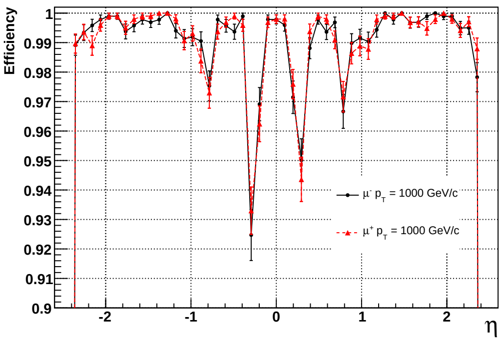

(e) $p_T = 1000$ GeV/c. Efficiency.

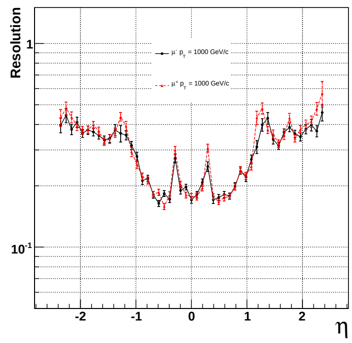

(f) $p_T = 1000$ GeV/c. Resolution.

Figure B.4: *Comparison between the reconstruction of μ^+ and μ^- in the muon spectrometer alone.*

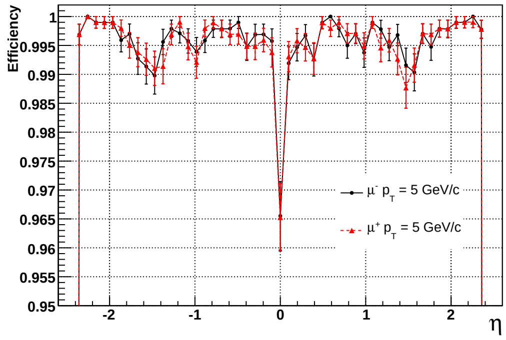

(a) $p_T = 5$ GeV/c. Efficiency.

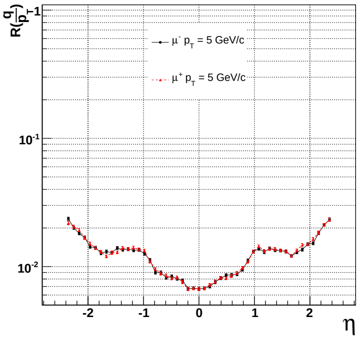

(b) $p_T = 5$ GeV/c. Resolution.

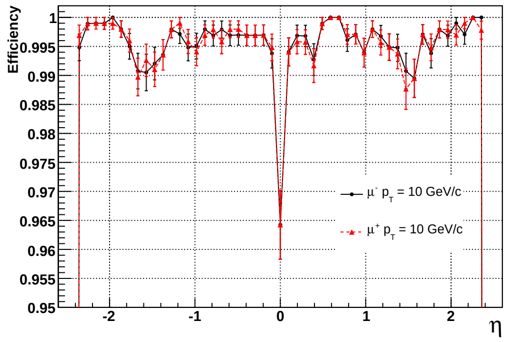

(c) $p_T = 10$ GeV/c. Efficiency.

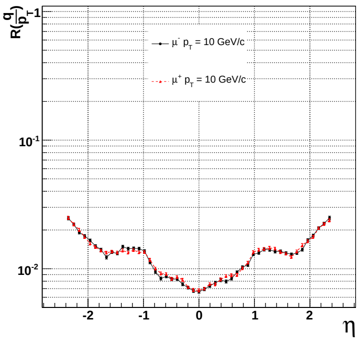

(d) $p_T = 10$ GeV/c. Resolution.

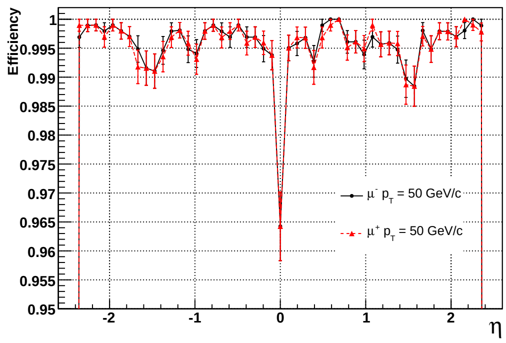

(e) $p_T = 50$ GeV/c. Efficiency.

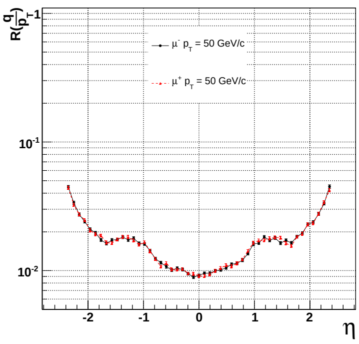

(f) $p_T = 50$ GeV/c. Resolution.

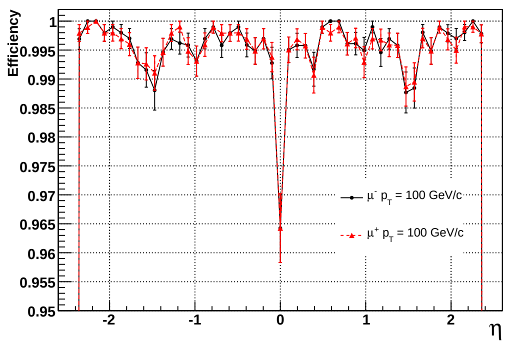

(g) $p_T = 100$ GeV/c. Efficiency.

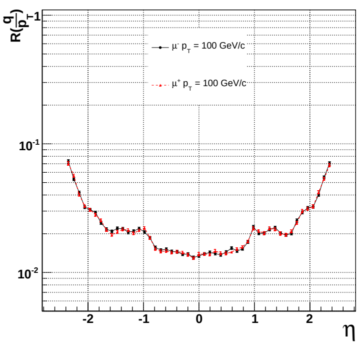

(h) $p_T = 100$ GeV/c. Resolution.

Figure B.5: *Comparison between the reconstruction of μ^+ and μ^- with the inner tracker system alone.*

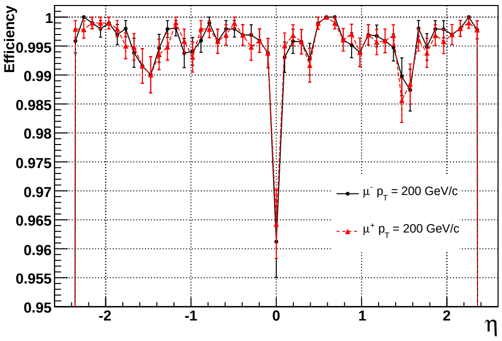

(a) p_T = 200 GeV/c. Efficiency.

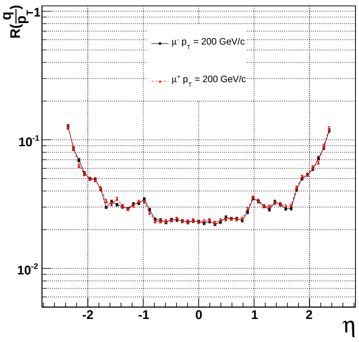

(b) p_T = 200 GeV/c. Resolution.

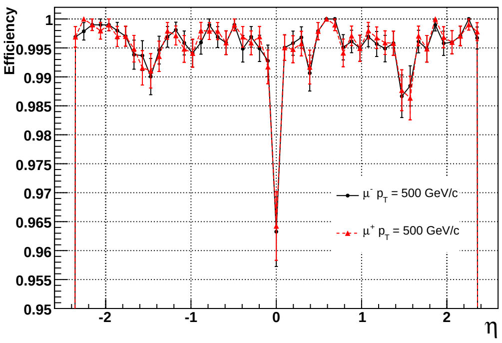

(c) p_T = 500 GeV/c. Efficiency.

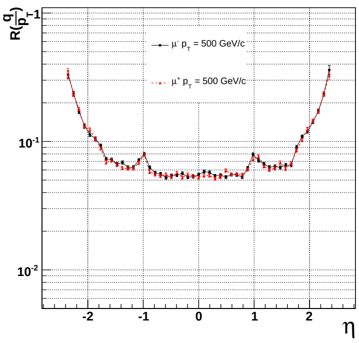

(d) p_T = 500 GeV/c. Resolution.

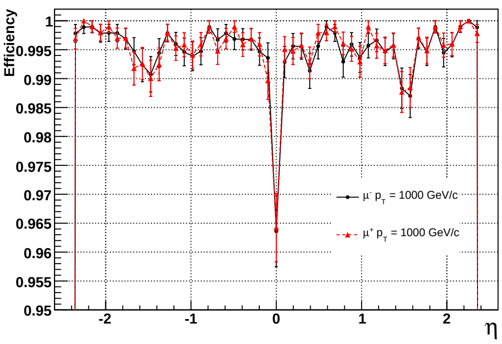

(e) p_T = 1000 GeV/c. Efficiency.

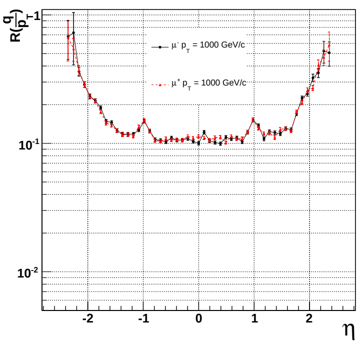

(f) p_T = 1000 GeV/c. Resolution.

Figure B.6: *Comparison between the reconstruction of μ^+ and μ^- with the inner tracker system alone.*

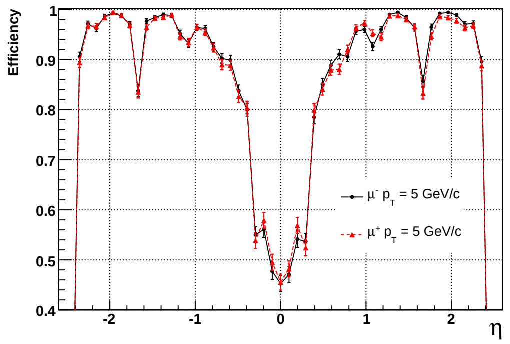

(a) $p_T = 5$ GeV/c. Efficiency.

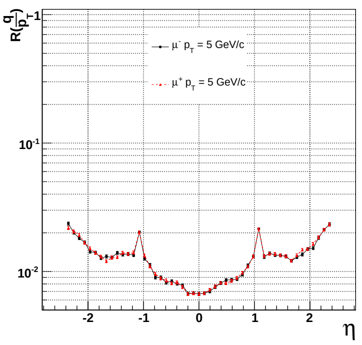

(b) $p_T = 5$ GeV/c. Resolution.

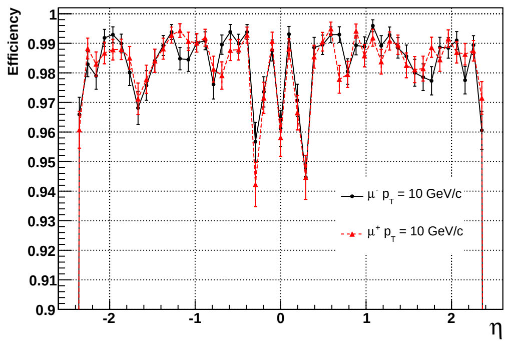

(c) $p_T = 10$ GeV/c. Efficiency.

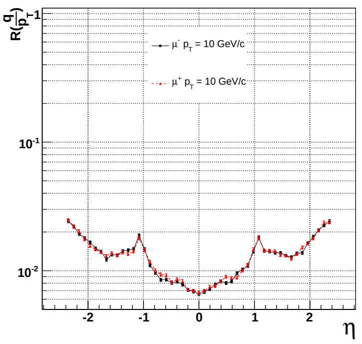

(d) $p_T = 10$ GeV/c. Resolution.

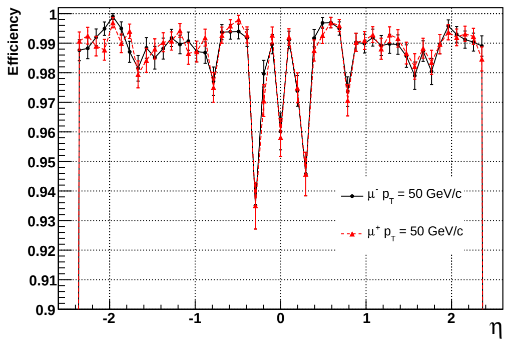

(e) $p_T = 50$ GeV/c. Efficiency.

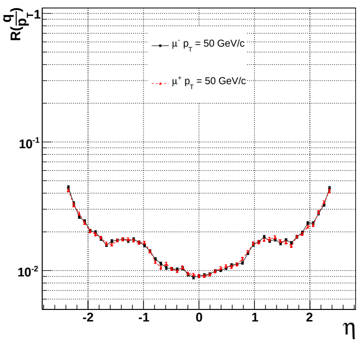

(f) $p_T = 50$ GeV/c. Resolution.

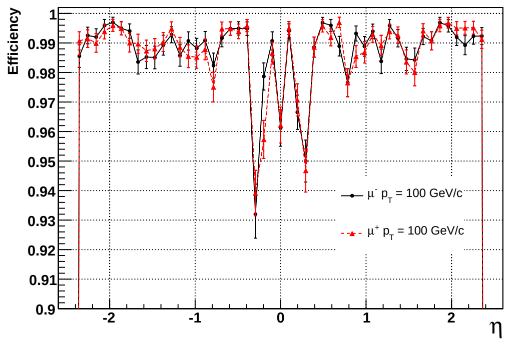

(g) $p_T = 100$ GeV/c. Efficiency.

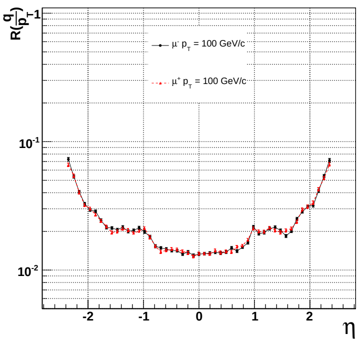

(h) $p_T = 100$ GeV/c. Resolution.

Figure B.7: *Comparison between the reconstruction of μ^+ and μ^- with the whole CMS detector.*

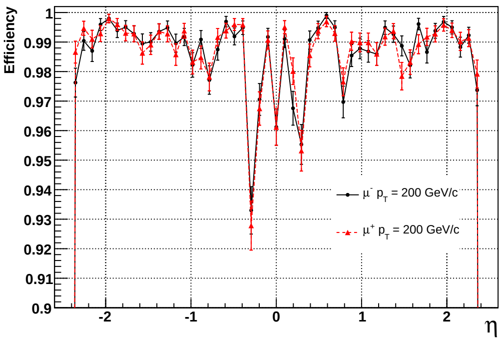

(a) p_T = 200 GeV/c. Efficiency.

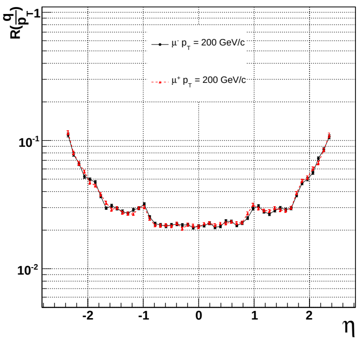

(b) p_T = 200 GeV/c. Resolution.

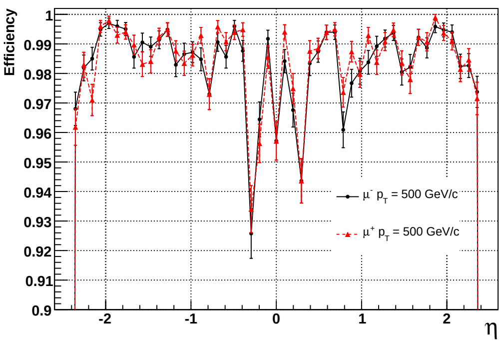

(c) p_T = 500 GeV/c. Efficiency.

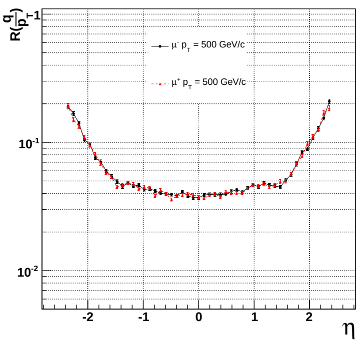

(d) p_T = 500 GeV/c. Resolution.

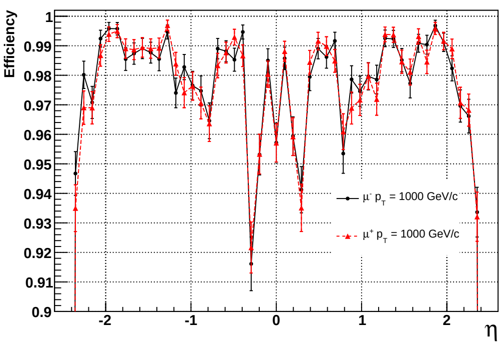

(e) p_T = 1000 GeV/c. Efficiency.

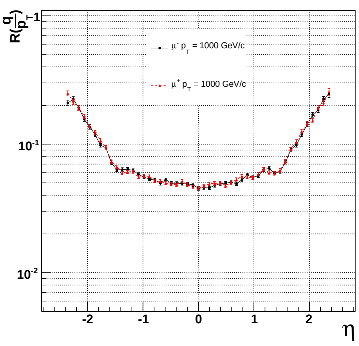

(f) p_T = 1000 GeV/c. Resolution.

Figure B.8: *Comparison between the reconstruction of* μ^+ *and* μ^- *with the whole CMS detector.*

References

[1] N. Amapane, R. Bellan *et al.*, *Simulation of the DT Response*, CMS Note (in preparation).

[2] N. Amapane, R. Bellan *et al.*, *Local Muon Reconstruction in the Drift Tube Detectors*, CMS Note (in preparation).

[3] R. Bellan, *Muon Reconstruction with the CMS Muon Tracking system*, Submitted to Nucl. Phys. B Proc. Suppl. In *Hadron Collider Physics Symposium 2007 proceedings* .

[4] The CMS Collaboration, *The CMS Magnet Test and Cosmic Challenge*, CMS Note (in preparation).

[5] R. Bellan, *VV-Fusion at CMS*, in *Proceedings of the IV International workshop on Frontier Science 2005, new frontiers in subnuclear physics*, volume XL of *Frascati Physics Series*, 2006.

[6] N. Amapane, R. Bellan *et al.*, *Study of VV-scattering processes as a probe of electroweak symmetry breaking*, CMS AN (2007) 2007/005.

[7] S. Alekhin, R. Bellan *et al.*, *HERA and the LHC - A workshop on the implications of HERA for LHC physics: Proceedings Part B*, CERN-2005-014 (2005) 561. hep-ph/0601013.

[8] S. Kraml, R. Bellan *et al.*, *CP Studies and Non-Standard Higgs Physics.*, CERN-2006-009 (2006). hep-ph/0608079.

[9] N. Adam, R. Bellan *et al.*, *Measurement of the inclusive $W \rightarrow \mu\nu$ and $Z \rightarrow \mu^+\mu^-$ cross sections in pp collision at $\sqrt{s} = 14$ TeV*, CMS AN (2007) 2007/031.

[10] G. Altarelli and M. L. Mangano (editors), *Proceedings of the Workshop on Standard Model Physics (and more) at the LHC* (2000) CERN 2000-004.

[11] The LHC Study Group, *The Large Hadron Collider Conceptual Design*, CERN/AC 95-05 (1995).

[12] H. L. Lai *et al.*, *Improved parton distributions from global analysis of recent deep inelastic scattering and inclusive jet data*, Phys. Rev. **D55** (1997) 1280. hep-ph/9606399.

[13] F. Gianotti and M. Pepe-Altarelli, *Precision physics at the LHC*, Nucl. Phys. B Proc. Suppl. **89** (2000) 177. hep-ex/0006016.

[14] M. Arneodo and M. Diehl, *Diffraction for non-believers*, DESY-05-214 (2005) , and references therein. hep-ph/0511047v1.

[15] S. Alekhin *et al.*, *HERA and the LHC - A workshop on the implications of HERA for LHC physics: Proceedings Part B*, CERN-2005-014 (2005) Chapter V. hep-ph/0601013.

[16] M. Spira and P. M. Zerwas, *Electroweak symmetry breaking and Higgs physics*, CERN-TH/97-379 (1997). hep-ph/9803257.

[17] G. Altarelli and G. Isidori, *Lower limit on the Higgs mass in the standard model: An Update*, Phys. Lett. **B337** (1994) 141.

[18] R. S. Willey, *On the Lower Bound for the Higgs Boson Mass*, Phys. Lett. **B377** (1996) 255. hep-ph/9512226.

[19] N. Cabibbo *et al.*, *Bounds on the Fermions and Higgs Boson Masses in Grand Unified Theories*, Nucl. Phys. **B158** (1979) 295.

[20] C. Ford *et al.*, *The Effective potential and the renormalization group*, Nucl. Phys. **B395** (1993) 17. hep-lat/9210033.

[21] R. S. Chivukula *et al.*, *Theory of a strongly interacting electroweak symmetry breaking sector*, Ann. Rev. Nucl. Part. Sci. **45** (1995) 255. hep-ph/9503230.

[22] T. Hambye and K. Riesselmann, *Matching conditions and Higgs mass upper bounds revisited*, Phys. Rev. **D55** (1997) 7255. hep-ph/9610272.

[23] The LEP Electroweak Working Group, *LEP Electroweak Working Group web site*, http://lepewwg.web.cern.ch/LEPEWWG/.

[24] LEP Working Group for Higgs boson searches, *Search for the standard model Higgs boson at LEP*, Phys. Lett. B **565** (2003) 61. hep-ex/0306033.

[25] G. F. Giudice, *Physics beyond the standard model*, Lect. Notes Phys. **591** (2002) 294.

[26] D. I. Kazakov, *Beyond the standard model* (2006). hep-ph/0611279.

[27] J. Lykken, *Introduction to Supersymmetry* (1996). FERMILAB-PUB-96/445-T, hep-th/9612114.

[28] H. Murayama, *Supersymmetry Phenomenology* (2000). UCB-PTH-00/05, hep-ph/0002232.

[29] W. Yao *et al.*, *Review of Particle Physics*, Journal of Physics G **33** (2006). http://pdg.lbl.gov

[30] The CMS Collaboration, *The CMS Physics Technical Design Report, Volume 2*, CERN/LHCC 2006-021, CMS TDR 8.2 (2006).

[31] R. Rattazzi, *Transplanckian collisions at future accelerators* (2002). hep-ph/0205265.

[32] F. Karsch, *Lattice QCD at high temperature and density*, Lect. Notes Phys. **583** (2002) 209. hep-lat/0106019.

[33] The CMS Collaboration, *Technical Proposal*, CERN/LHCC 94-38, LHCC/P1 (1994).

[34] The CMS Collaboration, *The Magnet Project: Technical Design Report*, CERN/LHCC 97-10, CMS TDR 1 (1997).

[35] The CMS Collaboration, *The Tracker Project: Technical Design Report*, CERN/LHCC 98-6, CMS TDR 5 (1998).

[36] The CMS Collaboration, *Addendum to the CMS Tracker Technical Design Report*, CERN/LHCC 2000-016, CMS TDR 5 Addendum 1 (2000).

[37] The CMS Collaboration, *The CMS Physics Technical Design Report, Volume 1*, CERN/LHCC 2006-001, CMS TDR 8.1 (2006).

[38] The CMS Collaboration, *The Electromagnetic Calorimeter Project: Technical Design Report*, CERN/LHCC 97-33, CMS TDR 4 (1997).

[39] The CMS Collaboration, *The Hadronic Calorimeter: Technical Design Report*, CERN/LHCC 97-31, CMS TDR 2 (1997).

[40] F. Gasparini *et al.*, *Bunch Crossing Identification at LHC Using a Mean-timer Technique*, Nucl. Instrum. Meth. **A336** (1993) 91.

[41] The CMS Collaboration, *The Trigger Project, Technical Design Report: The Level-1 Trigger*, CERN/LHCC 2000-038, CMS TDR 6.1 (2000).

[42] M. Aldaya, R. Bellan *et al.*, *Results of the first integration test of the CMS drift tubes muon trigger*, Nucl. Instrum. Meth. **A579** (2007) 951.

[43] H. Sakulin, *Design and Simulation of the First Level Global Muon Trigger for the CMS Experiment at CERN*, PhD thesis (2002).

[44] The CMS Collaboration, *The TriDAS Project Technical Design Report, Volume 2: Data Acquisition and High-Level Trigger*, CERN/LHCC 2002-26, CMS TDR 6.2 (2002).

[45] The Geant4 Collaboration, *GEANT – Detector Description and Simulation Tool* .
http://www.cern.ch/geant/

[46] N. Amapane, R. Bellan *et al.*, *Offline Calibration Procedure of the Drift Tube Detectors*, CMS Note (in preparation).

[47] The CMS Collaboration, *The Muon Project: Technical Design Report*, CERN/LHCC 97-32, CMS TDR 3 (1997).

[48] R. Veenhof, *Garfield, a Drift-Chamber Simulation Program user's guide*, CERN Program Library W5050 (1994).

[49] I. Smirnov, *HEED. Interaction of particles with gases*, CERN Program Library Writeup W5060 .
http://consult.cern.ch/writeup/heed/

[50] J. Puerta-Pelayo, M. C. Fouz and P. Garcia-Abia, *Parametrization of the Response of the Muon Barrel Drift Tubes*, CMS Note (2005) 2005/018.

[51] M. Aguilar-Benítez *et al.*, *Construction and test of the final CMS Barrel Drift Tube Muon Chamber prototype*, Nucl. Instrum. Meth. **A480** (2002) 658.

[52] M. Cerrada *et al.*, *Results from the Analysis of the Test Beam Data taken with the Barrel Muon Protoype Q4*, CMS Note (2001) 2001/041.

[53] T. Zhao *et al.*, *A study of electron drift velocity in Ar-CO_2 and Ar-CO_2-CF_4 gas mixtures*, Nucl. Instrum. Meth. **A340** (1994) 485.

[54] F. Cavallo *et al.*, *Test of MB3 Muon Barrel Drift Chamber with Cosmic Rays*, CMS Note (2003) 2003/017.

[55] N. Amapane *et al.*, *Analysis of the CMS Drift Tube Test-Beam Data*, CMS Note (in preparation).

[56] D. Acosta, R. Bellan *et al.*, *CMS High Level Trigger*, CMS Note (2007) 2007/009.

[57] N. Amapane *et al.*, *High Level Trigger Algorithms for Muon Isolation*, CMS Note (2002) 2002/040.

[58] H. Sakulin, *Methodology for the Simulation of Single-Muon and Di-Muon Trigger Rates at the CMS Experiment in the Presence of Pile-Up*, CMS Note (2002) 2002/042.

[59] M. J. G. Veltman, *Reflections on the Higgs system*, CERN-97-05 (1997).

[60] M. S. Chanowitz, *Strong W W scattering at the end of the 90's: Theory and experimental prospects* (1998). hep-ph/9812215.

[61] S. Dawson, *Introduction to electroweak symmetry breaking* (1998). hep-ph/9901280.

[62] C. Quigg, *Electroweak symmetry breaking and the Higgs sector*, Acta Phys. Polon. **B30** (1999) 2145. hep-ph/9905369.

[63] S. Dawson, *Electroweak symmetry breaking circa 2005*, Int. J. Mod. Phys. **A21** (2006) 1629. hep-ph/0510385.

[64] R. Rattazzi, *Physics Beyond the Standard Model*, PoS **HEP2005** (2006) 399. hep-ph/0607058.

[65] J. Bagger *et al.*, *LHC analysis of the strongly interacting W W system: Gold plated modes*, Phys. Rev. **D52** (1995) 3878. hep-ph/9504426.

[66] A. Dobado *et al.*, *LHC sensitivity to the resonance spectrum of a minimal strongly interacting electroweak symmetry breaking sector*, Phys. Rev. **D62** (2000) 055011. hep-ph/9912224.

[67] J. M. Butterworth, B. E. Cox and J. R. Forshaw, *W W scattering at the LHC*, Phys. Rev. **D65** (2002) 096014. hep-ph/0201098.

[68] E. Accomando *et al.*, *Isolating vector boson scattering at the LHC: Gauge cancellations and the equivalent vector boson approximation vs complete calculations*, Phys. Rev. **D74** (2006) 073010. hep-ph/0608019.

[69] E. Accomando, A. Ballestrero and E. Maina, *PHASE, a Monte Carlo event generator for six-fermion physics at the LHC*, JHEP **07** (2005) 016. hep-ph/0504009.

[70] E. Accomando *et al.*, *Boson boson scattering and Higgs production at the LHC from a six fermion point of view: Four jets + l nu processes at $O(\alpha_{em}^6)$*, JHEP **03** (2006) 093. hep-ph/0512219.

[71] E. Accomando *et al.*, *Boson fusion and Higgs production at the LHC in six fermion final states with one charged lepton pair*, Phys. Rev. **D75** (2007) 113006. hep-ph/0603167.

[72] The CMS Collaboration, *FAMOS, CMS Fast Simulation*, http://cmsdoc.cern.ch/FAMOS/.

[73] M. Mangano *et al.*, *ALPGEN, a generator for hard multiparton processes in hadronic collisions*, JHEP **0307** (2003) 001.

[74] V. Konoplianikov *et al.*, *Jet Calibration using γ+Jet Events in the CMS Detector*, CMS Note (2006) 2006-042.

[75] S. Bityukov *et al.*, *Conference Proceedings of PHYSTAT2005: Statistical Problems in Particle Physics, Astrophysics, and Cosmology*, Unel, Imperial College Press, 2006.

[76] R. Frühwirth, *Application of Kalman filtering to track and vertex fitting*, Nucl. Instrum. Meth. **A262** (1987) 444.

Acknowledgements

In these years I had the pleasure to work with many people that transmitted to me enthusiasm and passion for this work. I hope they know I am grateful to them, although it is impossible to thank all explicitly. I would like to thank in particular the colleagues of the *Muon POG* and *DPGs*, especially T. Cox who gave me a lot of advice for this thesis.

Special thanks go to the CMS Torino group, in which I found a lot of sincere friends, not only colleagues. First of all my supervisor, E. Migliore, whose suggestions were precious for this thesis.

Invaluable support and friendship I have received from N. Amapane and C. Mariotti: Nicola and I started to work together when our new beautiful software was only in our mind. Chiara and I started to work together when the *physicist inside me* was only in our mind... I am glad to be in debt with them.

I would also to thank T. Camporesi for his comments and for the useful discussions on the work presented here.

Finally, the most difficult thanks. Difficult because many thanks are not enough to say how I am grateful to my family, and how I love Sara, not only because she is not (too much) jealous of my love for physics, but simply because I love her. They were my engine in these years, I hope one, true, deep *thanks* can serve for this purpose.